Parametric Interaction in Josephson Junction Circuits and Transmission Lines

by

Hamid Reza Mohebbi

A thesis
presented to the University of Waterloo
in fulfillment of the
thesis requirement for the degree of
Doctor of Philosophy
in
Electrical and Computer Engineering

Waterloo, Ontario, Canada, 2011

Abstract

This research investigates the realization of parametric amplification in superconducting circuits and structures where nonlinearity is provided by Josephson junction (JJ) elements. We aim to develop a systematic analysis over JJ-based devices toward design of novel traveling-wave Josephson parametric amplifiers (TW-JPA). Chapters of this thesis fall into three categories: lumped JPA, superconducting periodic structures and discrete Josephson transmission lines (DJTL).

The unbiased Josephson junction (JJ) is a nonlinear element suitable for parametric amplification through a four-photon process. Two circuit topologies are introduced to capture the unique property of the JJ in order to efficiently mix signal, pump and idler signals for the purpose of signal amplification. Closed-form expressions are derived for gain characteristics, bandwidth determination, noise properties and impedance for this kind of parametric power amplifier. The concept of negative resistance in the gain formulation is observed. A design process is also introduced to find the regimes of operation for gain achievement. Two regimes of operation, oscillation and amplification, are highlighted and distinguished in the result section. Optimization of the circuits to enhance the bandwidth is also carried out.

Moving toward TW-JPA, the second part is devoted to modelling the linear wave propagation in a periodic superconducting structure. We derive closed-form equations for dispersion and s-parameters of infinite and finite periodic structures, respectively. Band gap formation is highlighted and its potential applications in the design of passive filters and resonators are discussed. The superconducting structures are fabricated using YBCO and measured, illustrating a good correlation with the numerical results.

A novel superconducting Transmission Line (TL), which is periodically loaded by Josephson junctions (JJ) and assisted by open stubs, is proposed as a platform to realize a traveling-wave parametric device. Using the TL model, this structure is modeled by a system of nonlinear partial differential equations (PDE) with a driving source and mixed-boundary conditions at the input and output terminals, respectively. This model successfully emulates parametric and nonlinear microwave propagation when long-wave approximation is applicable. The influence of dispersion to sustain three non-degenerate phased-locked waves through the TL is highlighted.

A rigorous and robust Finite Difference Time Domain (FDTD) solver based on the explicit Lax-Wendroff and implicit Crank-Nicolson schemes has been developed to investigate the device responses under various excitations. Linearization of the wave equation, under small-amplitude assumption, dispersion and impedance analysis is performed to explore more aspects of the device for the purpose of efficient design of a traveling-wave parametric amplifier.

Knowing all microwave characteristics and identifying different regimes of operation, which include impedance properties, cut-off propagation, dispersive behaviour and shock-wave formation, we exploit perturbation theory accompanied by the method of multiple scale to derive the three nonlinear coupled amplitude equations to describe the parametric interaction. A graphical technique is suggested to find three waves on the dispersion diagram satisfying the phase-matching conditions. Both cases of perfect phase-matching and slight mismatching are addressed in this work. The incorporation of two numerical techniques, spectral method in space and multistep Adams-Bashforth in time domain, is employed to monitor the unilateral gain, superior stability and bandwidth of this structure. Two types of functionality, mixing and amplification, with their requirements are described. These properties make this structure desirable for applications ranging from superconducting optoelectronics to dispersive readout of superconducting qubits where high sensitivity and ultra-low noise operation is required.

Acknowledgments

Firstly, I would like to thank my supervisor Professor A. Hamed Majedi for introducing me to the world of "superconductivity", giving me a chance to work in this area as a PhD student, and providing me with all opportunities and supports during the course of this research. I am also thankful to my co-supervisor, Professor Sujeet K. Chaudhuri, for his continued support.

I am thankful to my committee members, Professor Safieddin Safavi-Naeini, Professor Raafat R. Mansour and Professor Frank Wilhelm for valuable discussions and reviewing my thesis. I am also grateful to my external examiner, Professor Irfan Siddiqi from University of California, Berkeley, for taking his time to review my thesis.

I owe particular debts of sincere gratitude to Professor Kevin G. Lamb from the Department of Applied Mathematics at the University of Waterloo for his assistance and stimulating discussions on the "Perturbation Theory" part of my research.

I would like to thank all members of the Electromagnetic group at the University of Waterloo, particularly Haig A. Atikian for his help in the experimental part of my thesis, Siamak Fouladi for valuable discussions, Amir Arbabi for fruitful discussions and advice and Amin Eftekharian for his editorial assistance.

I would like to acknowledge Prof. Raymond Laflamme, the Executive Director of IQC, and other IQC members who provide such a stimulating scientific environment in which to conduct cutting-edge research in the field of quantum information.

Outside the scientific community I have had much support from my family and close friends. I would especially like to thank my parents who were my first teachers. Their love and encouragement inspired my passion for learning. Finally, and most importantly, I am deeply indebted to my wonderful wife, Shima, for all her help and patience so that my two sons, Hossein and Javad, never felt my absence during my intense work on the research. Without their love, endless tolerance and unconditional support, I could have never achieved my goals in this journey and I dedicate this thesis to them.

Dedicated to my beloved family:
Shima, Hossein and Javad.

Contents

List of Tables

List of Figures

List of Abbreviations

DJTL	Discrete Josephson Transmission Line
FDTD	Finite Difference Time Domain
HTS	High-Temperature Superconductor
JJ	Josephson Junction
JPA	Josephson Parametric Amplifier
JBA	Josephson Bifurcation Amplifier
JPC	Josephson Parametric Convertor
SQUID	Superconducting Quantum Interference Device
HEMT	High Electron Mobility Transistor
JBT	Junction Bipolar Transistor
LASER	Light Amplification by Stimulated Emission of Radiation
PDE	Partial Differential Equation
TL	Transmissions Line
TW-JPA	Traveling-Wave Parametric Josephson Amplifier
FWHM	Full Wave Half Maximum
QED	Quantum Electrodynamics
CPW	Coplanar Waveguide
SUPARAMP	Superconductive Unbiased Parametric Amplifier
CAD	Computer Aided Design
MASER	Microwave Amplification by Stimulated Emission of Radiation
AFM	Atomic Force Microscopy

List of Symbols

A_i	Complex amplitude associated with the resonant triads
C	Shunt capacitance of a transmission line per unit length
C_J	Shunt capacitance associated with Josephson junction
C_s	Capacitance of the signal filter in lumped JPA
C_i	Capacitance of the idler filter in lumped JPA
C_p	Capacitance of the pump filter in lumped JPA
C_{Je}	Equivalent JJ shunt capacitance
$\tilde{C}$	Normalized capacitance per unit length of a TL
G	Admittance
G_s	Source admittance
G_L	Load admittances
G_i	Idler admittance in voltage-based JPA
G_{fit}	Fit admittance to improve the bandwidth of lumped JPA
G_{neg}	Negative admittance for voltage-based JPA
G_L	Load admittance for voltage-based JPA
I	Current
I_1	Signal current in lumped JPA
I_2	Pump current in lumped JPA
I_3	Idler current in lumped JPA
I_s	Signal current (phasor)
I_p	Pump current (phasor)
I_{stub}	Current running through the open stubs in DJTL
I_i	Idler current (phasor)
I_c	Critical current of Josephson junctions
I_L	Load current
i_J	Current flowing through the JJ
i_s	Signal current in time domain
i_p	Pump current in time domain

i_i	Idler current in time domain
L	Series inductance of a transmission line per unit length
L_{J0}	Zero-current inductance associated with JJ
L_J	Inductance associated with Josephson junction at zero current
L_n	Nth Fourier harmonics of inductance of JJ
L_0	Zeroth Fourier harmonics of inductance of JJ
L_1	First Fourier harmonics of inductance of JJ
J_0	Bessel function of the first kind of order 0
J_2	Bessel function of the first kind of order 2
L_s	Inductance per unit length of associated with the stub
$\tilde{L}$	Normalized inductance per unit length of a TL
$\tilde{L}_J$	Normalized inductance of JJ
R_J	Shunt resistance associated with Josephson junction
R_s	Resistance associated with the source
R_i	Resistance in the idler branch of current-based JPA
R_L	Load resistance
R_{fit}	Fit resistance
R_{neg}	Negative resistance in the current-based JPA
R_{Je}	Effective shunt resistance associated with a junction
P_i	Idler power
P_p	Pump power
P_s	Signal power
P_{in}	Input signal power
P_{out}	Output signal power
P_{mn}	Power of the harmonic at frequency $m\omega_s + n\omega_p$
P_L	Power in the load
P_{av}	Available power
v_J	Voltage dropped on the Josephson junction (in lumped circuits)
V	Voltage
V_g	Group velocity

V_1	Signal voltage (phasor)
V_2	Pump voltage (phasor)
V_3	Idler voltage (phasor)
V_J	Voltage dropped on the Josephson junction (in distributed circuits)
$\overline{V_n^2}$	Noise power
$\hbar$	Plank constant
λ	Wavelength
ω_i	Idler frequency
ω	Angular frequency
ω_p	Pump frequency
ω_s	Signal frequency
ω_n	Nth harmonic frequency
$\mathrm{\omega}_0$	Scaling factor for frequency
ω_1	Signal frequency
ω_2	Pump frequency
ω_3	Idler frequency
f_s	Frequency of the signal source
f_B	Bragg cut-off frequency
φ	Magnetic flux
$\varphi^{(0)}$	Zeroth-order solution for flux (linear solution of the flux) associated with a
φ_p	Flux of associated with a DJTL at pump frequency
φ_s	Flux of associated with a DJTL at signal frequency
φ_i	Flux of associated with a DJTL at idler frequency
φ_J	Magnetic flux due to the inductance associated with the Josephson junction
φ_t	Derivative of flux with respect to the slow-varying variable t
φ_T	Derivative of flux with respect to the slow-varying variable T
φ_X	Derivative of flux with respect to the slow-varying variable X
φ_x	Derivative of flux with respect to the fast-varying variable x
ϕ_s	Josephson flux at signal frequency in lumped JPA
ϕ_i	Josephson flux at pump frequency in lumped JPA

ϕ_p	Josephson flux at idler frequency in lumped JPA
Φ_0	Flux quanta
θ_1	The phase of the signal wave
θ_2	The phase of the pump wave
θ_3	The phase of the idler wave
Z_s	Source series resitance
Z_i	Idler resistance
Z_p	Pump resitsnce
Z_{11}	Entry of the impedance matrix
Z_{12}	Entry of the impedance matrix
Z_{21}	Entry of the impedance matrix
Z_{22}	Entry of the impedance matrix
Z_{neg}	Negative impedance in current-based JPA
Z_{in}	Input impedance
Z_{out}	Output impedance
Z_{stb}	Characteristic impedance of the stub line
Z_0	Characteristic impedance of a TL
Y_{11}	Entry of the admittance matrix
Y_{12}	Entry of the admittance matrix
Y_{21}	Entry of the admittance matrix
Y_{22}	Entry of the admittance matrix
Y_{in}	Input admittance of the voltage-based JPA
Y_{out}	Output admittance of the voltage-based JPA
Y_{neg}	Negative admittance in voltage-based JPA
K_B	Boltzmann constant
τ	Time that TEM wave travels in an open stub
t	Time, fast-varying temporal variable
T	Time, slow-varying temporal variable
T_0	Room tempertaure
DEN.	Denominator of dispersion or group velocity

FWHM	Full wave half maximum of a Gaussian pulse
COEFT. $\partial A/\partial T$	Coefficient of the time slow-varying derivative of complex amplitude
COEFX. $\partial A/\partial X$	Coefficient of the space slow-varying derivative of complex amplitude
COEFNL1.	Coefficient associated with the signal after mixing due to the nonlinearity
COEFNL2.	Coefficient associated with the pump after mixing due to the nonlinearity
COEFNL3.	Coefficient associated with the idler after mixing due to the nonlinearity
RHS	Right hand side of $O(\epsilon)$ equation
PAE	Power added efficiency
Q_s	Quality factor of the signal filter
Q_i	Quality factor of the idler filter
h	Spatial period of discrete Josephson transmission line
u_m^n	Value of quantity u at $t = nk$ and $x = mh$
$\boldsymbol{D}_N$	Spectral differentiation matrix
NL	Nonlinear term
x	Space, length, fast-varying spatial variable
X	Space, slow-varying spatial variable
γ	Complex propagation constant
τ	Time delay due to the stub in DJTL
β	Phase constant
α	Attenuation constant
β_1	Phase constant of the signal wave
β_2	Phase constant of the pump wave
β_3	Phase constant of the idler wave
ϵ	Small perturbation parameter
ξ_i	Coefficients of the coupled amplitude equations
ς_i	Power coefficient
δ_ω	phase-mismatch due to the frequency

Chapter 1

Introduction

Due to the unique advantages such as ultra-low dissipation, high sensitivity and intrinsic accuracy that superconducting materials offer, they have found niche applications in instrumentation, standards, sensors and detectors. Certain applications such as axion detectors [1], radio astronomy amplification [2], nuclear magnetic resonance [3],[4] and quantum information processing devices require high frequency amplifiers with very low noise temperature.

Recently, superconducting circuits have been one of the salient candidates for the implementation and realization of the quantum bits (qubits) which are the basis for quantum information processors whose operation is based on Quantum Electrodynamics (QED). Macroscopic electrical circuits face two related difficulties. First, they are strongly coupled to their environment and they do not behave quantum mechanically. Secondly, any measurement disturbs the quantum state associated with the qubit. However, the Josephson Junction (JJ) was demonstrated as a unique candidate to overcome these difficulties, since it remains both a non-dissipative and a nonlinear inductor at arbitrary low temperatures. Therefore, the future development of quantum information processing using superconducting circuits requires Josephson qubits with long coherence times combined with a high-fidelity read-out section. As a result, superconducting qubits become excellent test-beds for studying the fundamental properties of mesoscopic quantum measurement. As mentioned, one of the outstanding issues in superconducting qubit circuits is to read out the quantum state without introducing excessive noise. Such a read-out scheme requires speed (single-shot read-out), sensitivity and minimal disturbance to the qubit state.

The best performance of a semiconductor amplifier to date is based on High Electron Mobility Transistor (HEMT) which operates at frequencies up to 500 GHz [5] and achieves noise temperatures as low as 1K when cooled down to liquid helium temperature [6].

However, cooling to lower temperatures does not reduce the noise temperature further, as their noise performance is limited by heating of the electrons in the FET channel and recombination noise.

In this regard, substantial progress has been recently achieved using alternative superconductive amplifiers embedded in a microwave on-chip transmission lines. They include superconducting cavity parametric amplifiers [7], [8], microstrip dc SQUID amplifiers [9],[6], Josephson bifurcation amplifiers (JBA) [10], and Josephson parametric amplifiers (JPA) [11],[12].

The mechanism of amplification in dc SQUID amplifiers is based on the flux-to-voltage transfer function of the SQUID. The input signal is converted into the flux and coupled to the SQUID by a superconducting spiral input coil which is a microstrip resonator above the dielectric layer on top of the square-washer SQUID to take advantage of the coil's capacitance. The current-and flux-biased SQUID produces an output voltage in response to a small input flux . The hysteresis in the JJs of the SQUID reduces the performance of the device; therefore a shunt resistor is added to remove the hysteresis effect. This resistor is the source of noise, which has been calculated in [13],[14].

A Josephson bifurcation amplifier consists of a Josephson junction, which behaves as a nonlinear oscillator. The JBA is driven very close to the bifurcation point in order to switch between two states leading to amplification. The advantage of the JBA over the dc SQUID amplifier stems from the fact that no source of dissipation is involved in the latching mechanism. The JBA is a high-speed and ultra-low noise device for application such as readout of the superconducting qubits and microwave magnetometry [15]. In spite of these promising results, they suffer from two main disadvantages. As a consequence of their small dynamic range and narrow-band gain, they are well suited to amplify signals only in a narrow range in both power and frequency, limiting their applications. The JBA is a dispersive biastable detector[15], this limits its performance as a real amplifier .

Josephson parametric amplifier (JPA) is another alternative with different mechanism to realize an ultra-low noise amplifier. JPA is an ultra-low noise microwave amplifier and it has been operated with near quantum-limited sensitivity, less than half a noise above the quantum limit, and it can also used to squeeze both thermal and vacuum noise [11],[12].

As parametric amplification in Josephson junction circuits and transmission lines is the main subject of this thesis, we devote the next section to explain this device.

1.1 Josephson Parametric Amplifiers

Due to inherent nonlinearities in the JJ-based circuits and their similarities to the nonlinear optical crystals, they are potentially suitable for performing nonlinear phenomena similar to ones observed in quantum optics, such as down-conversion and parametric amplification. The name parametric amplifier, in microwave context, has become associated with a class of amplifiers utilizing a nonlinear or time-varying reactance [16],[17], [18]. The semiconductor varactor diode with a nonlinear capacitance was the most widely used parametric amplifier and they are discussed at length in other texts [16],[17].

Travelling wave amplifier is the distributed version of the cascade amplifier. As the name implies the stages of amplifiers are distributed uniformly along a specific waveguide to increase the amplitude of the signal during its travelling. In this case, usually a set of three electromagnetic waves exist in which nonlinear interactions between any two of them resonantly force the third. These three phase-locked waves (or signals) which are referred to as resonant triad are associated with the nonlinearities in the system. In the language of quantum optics, when the media has a quadratic nonlinearity, such an interaction is usually called three photon process [19]. Depending on the nonlinearity of the medium, there is a resonant condition between the wavevectors of triad as well as their frequencies. In a lossless nonlinear media, the power associated with each of triad satisfies the Manley-Rowe relations [16]. This behavior occurs in any parametric amplifier such as optical, mechanical and microwave waves [16],[19],[20]. The nonlinearly-coupled equations for the amplitudes of the three waves can be driven based on slowly varying wave amplitude [21].

In other words, power is supplied by the large pumping signal at frequency ω_p (pump) and a small amplitude signal at frequency ω_s (signal) is also applied simultaneously to the same port, and the output of the amplifier is the amplified signal at frequency ω_s and also another extra output (idler) at a linear combination of frequencies ω_p and ω_s depending on the type of nonlinearity which is denoted by ω_i. In the so-called four-wave or four-photon arrangement, the frequencies are related by $2\omega_p = \omega_i + \omega_s$. In the three-wave or three-photon operation, the relation between the frequencies is $\omega_p = \omega_i + \omega_s$. The possible types of interaction fall into the categories: parametric amplification and parametric frequency conversion. The idler signal is undesirable in amplifiers, but it is the center of attention in the case of down-conversion which is realized in mixers.

To the best of our knowledge, the only theoretical explanation for Josephson parametric amplifier (JPA) is done in frequency domain [22], so we are planning to continue and develop the theoretical framework of parametric amplification in an array of Josephson junctions for traveling microwave signal in a very systematic manner, both in frequency and time domain, leading to a precise design rule to be utilized for integration with either superconducting qubit or the superconductive single photon detector (SSPD).

1.2 Thesis Contribution and Organizations

Although a number of experiments in all varieties of JPAs have been reported, but theoretical part was poorly raised by previous research endeavors. Indeed, this PhD orientation is aimed to provide a systematic approach for the concept of parametric interaction in Josephson junction circuits and transmission lines in order to be used in specific applications through some proposed design rules. Hence, we conduct this research by inclusive study on parametric amplification in lumped and traveling-wave structures to provide a good opportunity to extend the scale of analysis, modeling and developing a set of design rules particularly for TW-JPAs application. By conceptual advances in this area, we come out at the end of this PhD program with some prototype designs that may be utilized in further research projects on related domains.

The major contributions presented in this thesis are as follows and the references in this part are chosen from published papers of the author in his PhD program till time of the thesis writing.

The theoretical framework based on the Manley-Rowe relationship is presented for the case of lumped JPA in full details and clarifications. This suggests two topologies, current- and voltage-based arrangement, for realization of parametric devices. Appropriate model of JJ is chosen and two systematic approaches are used to solve these parametric circuits. In first method, JJ is modeled by the simplified nonlinear equation. The circuit is solved and satisfaction of Manley-Rowe is shown. In the second method, small-signal analysis are used which leads to a time-varying inductor [23]. Doing this method, all frequency components of signal and idler are captured but this method doesn't satisfy Manley-Rowe equation as pump's frequency components are not completely obtained. They are applied to both current- and voltage-based circuits and closed-form equations including voltage-current relationship and device's figure of merits such as transducer power gain, input and output impedance, relative bandwidth and noise temperatures are derived and numerical results are displayed. The distinction between two regimes of operations, oscillation and amplifications are also highlighted [24].

The frequency characteristics of linear microwave propagation in a periodic superconducting TL are studied in the next part and all aspects of microwave engineering is addressed. Due to the lack of availability of any fast CAD (Computer Aid Design) tool in accessible commercial software to account for superconductor plates in design process, a rigorous CAD tool is provided to find all distributed circuit parameters of superconducting TLs [25]. Although we restrict our attention to a specific type of periodic TL, we provide a general, systematic and accessible method of treatment that can be applicable to any linear/nonlinear and infinite/finite periodic waveguide by using transmission line theory in frequency domain. Concepts of complex propagation constant input impedance and scattering parameters of the linear infinite/finite periodic structure have been discussed. Both linear infinite and finite periodic structures have been analyzed in closed form, and the solution has been expressed in a tidy and succinct form [26], [27] . Finally, the prototype of this device is fabricated by YBCO and experimental results are compared with those of our simulations which demonstrates a good agreement.

The nonlinear wave propagation in a series-connected Discrete Josephson Junction Transmission Line (DJTL) is investigated [28]. Having a significant number of junctions per wavelength, the discrete transmission line (TL) can be considered as a uniform nonlinear transmission line. The nonlinear wave equations are solved numerically by Finite Difference Time Domain (FDTD) method with mixed boundary conditions and based on the explicit Lax-Wendroff and implicit Crank-Nicolson schemes. Features and characteristics such as cut-off propagation, dispersive behavior and shock wave formation, which are expected from wave propagation through the nonlinear DJTL, are discussed in this thesis [29]. This nonlinear TL is proposed as a platform to investigate the aspects of traveling-wave parametric interaction and amplification. The dispersion analysis is made to ensure the existence of three non-degenerate time-harmonic waves interacting with each other through the phase matching condition which is imposed by the cubic nonlinearity associated with each junction. As a result, open stubs is periodically added in order to support phase-matching condition. Having weak nonlinearity and slow varying assumptions, we exploit the powerful perturbation theory with the multiple scale technique to derive the three coupled nonlinear partial differential equations to describe their spatial and temporal amplitude variations in this parametric interaction. Cases of perfect phase-matching and slight mismatching are addressed in this work. The numerical analysis based on the spectral method in space and finite difference based on multistep Adams-Beshforth scheme in time domain are used to monitor the gain enhancement, superior stability and bandwidth improvement of the proposed structure. This structure can be used as a mesoscopic platform to study the creation of squeezed states of the microwave radiation. These properties make this structure desirable for applications ranging from superconducting optoelectronics to dispersive readout of superconducting qubits where high sensitivity, fast speed and low-noise operation is required.

The outlook and some suggested areas of research are given in the last chapter to further develop upon the contribution.

Chapter 2

Lumped Josephson Parametric Amplifiers

2.1 Introduction

Emerging applications of Josephson junction (JJ) devices in superconducting integrated circuits relies on its interesting quantum behaviors e.g. nonlinearity with ultra-low dissipation. The development in nanofabrication technology gives rise to the employment of JJs in qubit circuits, circuit cavity quantum electrodynamics and ultra-low noise electromagnetic radiation detectors, oscillators and amplifiers. Among these different devices, Josephson parametric amplifiers (JPA) were a topic of active research with a great interest in microwave applications in the 1960's and 70's [30], [17], [31], [32], [33], [22],[34], [35]. Early microwave solid state amplifiers were dominated by two-terminal devices such as varactor diodes where the parametric amplification stems from varactor's capacitance nonlinearity. Thus, the theory of parametric interaction including frequency conversion and amplification has been developed and fully studied [16], [36], [17], [30], [21], [37], [38], [39]. However, due to the development of high frequency semiconductor transistors, interest in parametric devices declined, and applications of this kind of devices have been merely limited to optical and terahertz devices where no transistor exists at this range of frequencies [19], [40]. Today, due to the inherent advantage of parametric devices particularly low-noise performance, they found a renewed interest in both semiconductor [41],[42],[43] and superconductor technologies [44], [12],[11], [8], [45].

To the best of our knowledge, the first demonstration of JPA is experimentally reported by [31], [46], [32], [47],[34] for doubly and single degenerate mode of a single junction and theoretically followed by [48], [49] for a dc biased Josephson junction. Continuous improvements were made by two-idler JPA with a SQUID configuration [47]. A neat configuration of an array of JJs over a microstrip transmission line was investigated in [22]. Progress was fuelled by introducing traveling-wave JPA in [50], [8], [11] to achieve a broadband distributed JPA. In addition to JPA in which the physics of amplification is based on the concept of negative resistance, different mechanisms for amplification have been also investigated which leads to the SQUID amplifiers [51],[14] and Josephson bifurcation amplifiers [44].

In this chapter, we systematically analyze the parametric amplification in current- and voltage-based JJ circuits where a stable pump signal is used to amplify a low-power signal in the presence of JJ inductor nonlinearity. After reviewing the Manley-Rowe relation for a parametric process in section 2.2, the flux-based model of JJ is explained in section 2.3. The two circuit arrangements for Josephson parametric amplification, namely current- and voltage-based are introduced in section 2.4 and 2.5, respectively. Analysis of these circuits are performed and closed-form equations for the gain characteristics, bandwidth determination and noise temperature are derived. By proposing a design procedure for JJ parametric amplifier, we briefly carry out a numerical simulation of a current-based JPA based on a typical Aluminum JJ in section VI.

2.2 Implementation of Manley-Rowe Relationship in JJ-based Parametric Process

Manley-Rowe relation concisely describes a parametric process between signal, pump and idler based on a lossless nonlinear element. It shows how their power magnitudes and transfer directions are changing. In fact, the Manley-Rowe relation is the manifestation of the energy conservation law for a classical or quantum parametric systems [16], [19],[52], [53].

The Manley-Rowe relations are given in the form of a set of two following equations

$$\sum_{m=0}^{\infty}\sum_{n=-\infty}^{\infty}\frac{mP_{mn}}{m\omega_p+n\omega_s}=0 \qquad (2.1)$$

$$\sum_{n=0}^{\infty}\sum_{m=-\infty}^{\infty}\frac{nP_{mn}}{m\omega_p+n\omega_s}=0 \tag{2.2}$$

where m and n are integers, $\mathrm{m}\omega_p+n\omega_s$ is the harmonic frequency generated by mixing two essential frequencies and P_{mn} represents the reactive power at this harmonic. This chapter is focused on the realization of a parametric process based on the inherent nonlinearity of JJ in current-based and voltage-based configurations as shown in Fig. 2-1 (a) and (b), respectively. These circuits are referred to as typical Josephson parametric amplifiers, since they provide amplification of the signal in the load branch. Power is supplied by two sources, signal and pump, at the frequencies of ω_s and ω_p, respectively. Fig. 2-1 (a) depicts a signal, pump, idler and resistive load in series with the ideal band-pass filters, to make unwanted harmonics open-circuited, and all are connected in shunt with a basic Josephson junction which is treated as a lossless nonlinear inductor. However, in Fig. 2-1 (b), all four essential parts of the circuit are connected in series with the JJ; in addition, filters are set in parallel with circuit components to short-circuit other harmonics generated by the nonlinearity associated with the JJ. Based on the Manley-Rowe equation, the parametric circuit can accommodate an unspecified number of idlers, however, in Fig. 2-1 (a) or (b) only one idler at $2\omega_p-\omega_s$ harmonic is incorporated into the parametric design. Simple manipulation with the Manley-Rowe equations for the circuits in Fig. 2-1 gives the power gain and power added efficiency [54], [55] as

$$G=\frac{P_{out}}{P_{in}}=1+\frac{\omega_s}{2\omega_p}\frac{P_p}{P_{in}} \tag{2.3}$$

$$PAE=\frac{P_{out}-P_{in}}{P_p}=\frac{\omega_s}{2\omega_p} \tag{2.4}$$

where P_{in}, P_{out}, P_p and P_i are input-signal, output-signal, pump and idler powers, respectively. Equation (2.3) gives the maximum power gain possible in the parametric circuit. According to (2.3) the variation of the output-signal versus input-signal is illustrated in Fig. 2-2. As seen in this figure, the line never passes the origin in general; however, by choosing a resistive load (not reactive) and proper design of circuit components, particularly idler impedance and resonators, the parameter P_p/P_{in} might become independent of circuit variables, and equation (2.3) becomes constant over an interval of P_{in} . Saturation effect is not seen in (2.3), as ideal models are used to describe the Josephson junction and resonators.

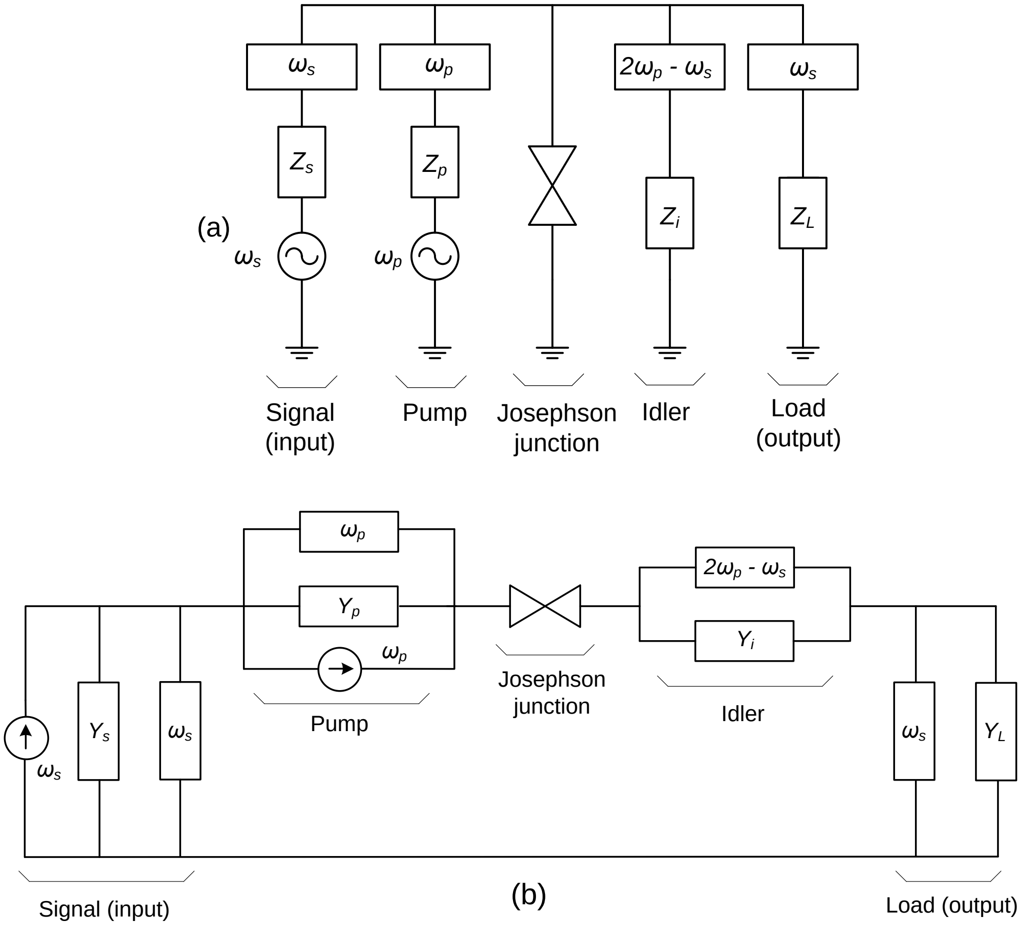

Fig. 2-1 Schematic of a general Josephson parametric amplifier: (a) current-based and (b) voltage-based JPA.

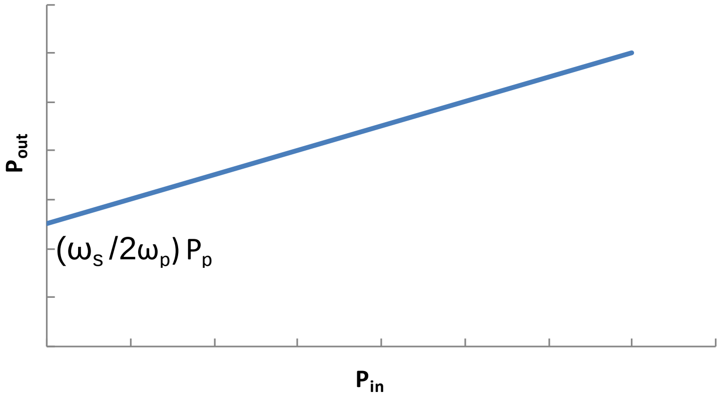

Fig. 2-2 Output-signal power versus input-signal power in a general parametric amplifier shows a jump (nonlinearity) in the gain formula.

Note that when no signal is applied to the circuit ($P_{in} = 0$), pump's photons cannot be broken into the idler and signal photons, as a result, the pump's power would be zero ($P_p = 0$) and the step seen in Fig. 2-2 does not appear. However, once the input signal is applied, this jump is observed. Moreover, in the presence of a white noise source in the circuit, its frequency component corresponding to ω_s can be combined with the pump signal and break the pump's photons at the rate corresponding to $P_p = \left(2\omega_p/\omega_s\right)P_s$ where P_s is the power available at the signal branch.

Closer look at (2.3) shows that the higher gain can be achieved for the smaller input-signal power. Thus, this type of amplifier has a better performance for much lower input power. This fact can be also inferred from Fig. 2-2, where a sharp step jump is observed at zero input-signal power. Therefore, this circuit at low input power acts like a detector rather than an amplifier.

As the parametric process in an unbiased JJ is based on the four photon process, relationship $\omega_s + \omega_i = 2\omega_p$ has to be satisfied. This implies that PAE in (2.4) is less than 50% when $\omega_s < \omega_p < \omega_i$, and it is above the 50% when $\omega_i < \omega_p < \omega_s$.

2.3 Flux-based Model of the Josephson Junction

Before any parametric analysis, an appropriate JJ model is required to fully and accurately describe the nonlinear operation of the JJ. If the current running through the junction is less than its critical current (I_c), the junction can be represented by a nonlinear inductor [22],[56], [28] . The most familiar description of a nonlinear element for the purpose of circuit simulation is in terms of current-voltage characteristics that mathematically written in the form of $f(i, v) = 0$. To obtain such a relationship, the most fundamental description of the junction must be used as a starting point to avoid any possible mistake and unrealistic results. Thus, we employ the primary flux-current ($\varphi - I$) description of the JJ, equation (2.5), instead of using the inductance-current ($L - I$) equation. In the flux-based model of JJ, the development begins by considering the JJ as a device whose flux is a function of the current i flowing through it, as given by

$$\varphi(i) = I_c L_{J0} \sin^{-1}\left(\frac{i}{I_c}\right) \tag{2.5}$$

where I_c is the critical current of the JJ, L_{J0} is a linear inductance (zero-current) associated with the JJ defined by $L_{J0} = \Phi_0/(2\pi I_c)$ and Φ_0 is the flux quanta with the value of $\Phi_0 = 2.0679 \times 10^{-15}\ \mathrm{T.m^2}$. Since the excitations are sinusoidal, we use the phasor notation in the form of

$$a_n(t) = \frac{1}{2}\{A_n e^{j\omega_n t} + A_n^* e^{-j\omega_n t}\} = |A_n|\, cos(\omega_n t + \theta_n). \tag{2.6}$$

to study the steady-state behaviour of the circuit. Basically in (2.6), $a_n(t)$ is a typical circuit variable such as current, voltage, flux,..., A_n is the complex amplitude of $a_n(t)$, θ_n is the phase and index n stands for signal (s or 1), pump (p or 3) and idler (i or 2).

2.4 Current-based JPA

2.4.1 Circuit Arrangement

Fig. 2-3 represents a circuit containing a JJ with three sections corresponding to the signal, pump and idler for the purpose of parametric amplification of the signal. Each signal, pump and idler sections have a voltage source and a simple ideal LC pass-band filter with the center frequency of ω_s , ω_p and ω_i, respectively. In the signal part of the circuit, the load impedance is chosen to be either Z_1 or Z_2. Furthermore, having an auxiliary impedance provide more flexibility to adjust the input impedance in order to avoid possible instability.

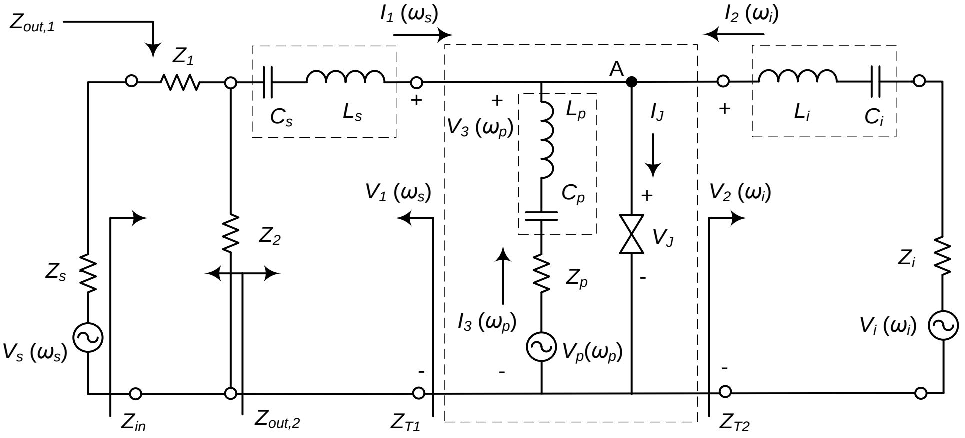

Fig. 2-3 Schematic of the current-based JPA. The JJ with the pump circuit acts like a time-varying inductance.

2.4.2 Voltage-Current Relationship

Using the node analysis at the point A in Fig. 2-3, the current $i_J(t)$ through the junction is found to be $i_J(t) = i_s(t) + i_p(t) + i_i(t)$, where i_s, i_p and i_i are currents through the signal, pump and idler in time-domain. Therefore, only three frequency components of ω_s , ω_p and ω_i can be sustained in the current through the junction. In order to avoid resistive channel of the JJ, the total current $i_J(t)$ should be less than the critical current of the junction. As i_J consists of three components at three different frequencies and phases, this results in the condition of $|I_s| + |I_p| + |I_i| < I_c$ in frequency-domain, where $|I_s|$, $|I_p|$ and $|I_i|$ are their corresponding maximum amplitudes. Then, these frequencies are mixed up due to the nonlinearity of the Josephson junction producing a voltage with all harmonics. Nevertheless, because of the filters in the circuit, only ω_s , ω_p and ω_i components of this voltage can be dropped on the signal, pump and idler branches to proceed the rest of the parametric interaction. To analyze the circuit, the JJ can be treated in two ways: as an independent nonlinear element or combined with the pump to introduce a time-varying reactance.

Method 1: JJ as a nonlinear inductor

The total current $i_J(t) = i_s(t) + i_p(t) + i_i(t)$, which is less than the critical current of the JJ, has to satisfy equation (2.5), we expand the inverse-sinusoidal function in Taylor series about the zero and keep the first two polynomial terms to truncate the series and monitor the harmonic-mixing. Considering frequency relation of $\omega_s + \omega_i = 2\omega_p$, which is the result of cubic nonlinearity associated with the unbiased JJ, using phasor notation in (2.6), and defining V_J as a voltage on the JJ as a time-derivative of the flux, all lead to

$$v_J(t) = \frac{d\varphi(i)}{dt} \cong \frac{d}{dt}\left\{L_{J0}\left(i_p + i_s + i_i\right) + \frac{L_{J0}}{6I_c^2}\left(i_p + i_s + i_i\right)^3\right\}. \tag{2.7}$$

Using (2.6), complex amplitude of the signal (V_1), pump (V_3) and idler (V_2) components of v_J in terms of the their associated complex currents I_1, I_3 and I_2, which all are shown in Fig. 2-3, are given by

$$V_1 = V_J(\omega_s) = j\omega_s L_{J0}\left(I_1 + \frac{I_3^2}{8I_c^2} I_2^*\right) \tag{2.8}$$

$$V_2 = V_J(\omega_i) = j\omega_i L_{J0}\left(I_2 + \frac{I_3^2}{8I_c^2} I_1^*\right) \tag{2.9}$$

$$V_3 = V_J(\omega_p) = j\omega_p L_{J0}\left(I_3 + \frac{I_1 I_2}{4I_c^2} I_3^*\right). \tag{2.10}$$

Accordingly, the time-average real power with associated reference direction at the pair of signal, idler and pump sections are obtained by

$$P_1 = \tfrac{1}{2}\mathrm{Re}\{V_1 I_1^*\} = \frac{\omega_s L_{J0}}{16I_c^2}\mathrm{Re}\{jI_1^* I_2^* I_3^2\} \tag{2.11}$$

$$P_2 = \tfrac{1}{2}\mathrm{Re}\{V_2 I_2^*\} = \frac{\omega_i L_{J0}}{16I_c^2}\mathrm{Re}\{jI_1^* I_2^* I_3^2\} \tag{2.12}$$

$$P_3 = \tfrac{1}{2}\mathrm{Re}\{V_3 I_3^*\} = \frac{-\omega_p L_{J0}}{8I_c^2}\mathrm{Re}\{jI_1^* I_2^* I_3^2\} \tag{2.13}$$

which certainly satisfies the Manley-Rowe equations.

Method 2: JJ as a time-varying inductor

Assuming that the pump current is larger than signal and idler currents, i.e. $i_p(t) \gg i_s(t) + i_i(t)$, a Taylor series approximation about i_p can be made on (2.5) to conduct the small-signal analysis [23]. Thus, the voltage dropped on the junction is found by

$$v_J(t) = \frac{d\varphi(i_J)}{dt} \cong \frac{d}{dt}\left\{\varphi(i_p) + \left.\frac{d\varphi}{di}\right|_{i=i_p}(i_s + i_i)\right\} \tag{2.14}$$

and the time-varying differential inductance is defined by

$$L_J(t) = \left.\frac{d\varphi}{di}\right|_{i=i_p} = \frac{L_{J0}}{\sqrt{1 - 0.5\left|\frac{I_p}{I_c}\right|^2 - 0.5\left|\frac{I_p}{I_c}\right|^2 \cos(2\omega_p t + 2\theta_p)}}. \tag{2.15}$$

where $|I_p|$ and θ_p are the amplitude and phase of the pump current i_p. Since $L_J(t)$ is a periodic function with the period $2\omega_p$, Fourier expansion can be applied on the $L_J(t)$ by

$$L_J(t) = \sum_{n=-\infty}^{\infty} L_n e^{j2n\theta_p} e^{j2n\omega_p t} \cong L_0 + 2L_1\cos(2\omega_p t + 2\theta_p). \tag{2.16}$$

The real-value parameters L_0 and L_1 are the first two Fourier terms of $L_J(t)$ which depends on the amplitude pump current. They are calculated by closed-form equations and also polynomial approximation as follows [57]

$$L_0 = \frac{2L_{J0}}{\pi} F\left(\frac{\pi}{2}, k\right) \approx L_{J0}\left(1 + \frac{1}{4}k^2 + \frac{9}{64}k^4 + \cdots\right) \tag{2.17}$$

$$\begin{aligned} L_1 &= \frac{2L_{J0}}{\pi}\left(\frac{2}{k^2} - 1\right) F\left(\frac{\pi}{2}, k\right) - \frac{4L_{J0}}{\pi k^2} E\left(\frac{\pi}{2}, k\right) \\ &\approx L_{J0}\left(\frac{1}{8}k^2 + \frac{3}{32}k^4 + \cdots\right) \end{aligned} \tag{2.18}$$

where k is the ratio of the pump's maximum amplitude to the critical current of the junction $k = |I_p/I_c|$, $E\left(\frac{\pi}{2}, k\right)$ and $F(\frac{\pi}{2}, k)$ are the complete elliptic integral of the first and second kinds, respectively. The second term in the Taylor series of equation (2.14) is responsible for mixing term and provides power transferring between signal, pump and idlers. This also leads to the necessary condition of parametric amplification which is described by $2\omega_p = \omega_s + \omega_i$, as pointed out before. Even though we have truncated the Taylor series in (2.14) for the purpose of small-signal analysis, the strength of this method lies on the fact that the second term in (2.14) contains all frequency components of ω_s and ω_i due to the nonlinearity in (2.14) and $2\omega_p = \omega_s + \omega_i$ relation. However, to find the exact voltage component at ω_p, we need all other eliminated terms in Taylor series of (2.14) as they still generate ω_p component based on $2\omega_p = \omega_s + \omega_i$. This is the reason that powers calculated by small-signal analysis don't satisfy the Manley-Rowe relations. Therefore, the exact current-voltage characteristics at frequencies ω_s and ω_i of the parametric configuration in Fig. 2-3 can be presented in a linear matrix form

$$\begin{bmatrix} V_1(\omega_s) \\ V_2^*(\omega_i) \end{bmatrix} = \begin{bmatrix} Z_{11} & Z_{12} \\ Z_{21} & Z_{22} \end{bmatrix} \begin{bmatrix} I_1(\omega_s) \\ I_2^*(\omega_i) \end{bmatrix} \tag{2.19}$$

where $I_1(\omega_s)$, $I_2(\omega_i)$, $V_1(\omega_s)$ and $V_2(\omega_i)$ are displayed in

Fig. 2-3, $Z_{11} = j\omega_s L_0$, $Z_{12} = j\omega_s L_1 e^{j2\theta_p}$, $Z_{21} = -j\omega_i L_1 e^{-j2\theta_p}$, $Z_{22} = -j\omega_i L_0$ and θ_p is the phase of the pump current which can be set to zero as a reference for other phases. It should be noted that the coefficients Z_{11}, Z_{12}, Z_{21} and Z_{22} are pump-dependent and are controlled by $|I_p|$ as seen in (2.15) and (2.16) which is expected in a typical parametric interaction. Closer look at the definitions of Z_{11}, Z_{12}, Z_{21}, Z_{22} and comparing equation (2.19) with (2.8) and (2.9) demonstrates that these methods lead to the same voltage-current characteristics, if we approximate L_0 and L_1 by keeping only the first term in (2.17) and (2.18). The complex voltage component at pump frequency ω_p can be found by a better approximation if the quadratic term in the Taylor expansion of $\varphi(i_J)$ about i_p is also taken into account. Fourier analysis of $L_J(t)$ in (2.16) and its derivative yields

$$V_3(\omega_p) \cong j\omega_p\left(L_0 I_3 - L_1 e^{j2\theta_p} I_3^* + \frac{K_1}{2}e^{j\theta_p} I_1 I_2 + \frac{K_1}{2}e^{j\theta_p}|I_1|^2 + \frac{K_1}{2}e^{j\theta_p}|I_2|^2\right) \tag{2.20}$$

where

$$K_1 = \frac{2L_{J0}}{\pi k I_c}\left[\frac{E\left(\frac{\pi}{2},k\right)}{1-k^2} - F\left(\frac{\pi}{2},k\right)\right]. \tag{2.21}$$

2.4.3 Gain, Input and Output Impedance

To find the power gain, the signal and idler sources must be incorporated into the voltage-current characteristics in either (2.8)-(2.10) or (2.19). According to the schematic in Fig. 2-3, the relation between sources and circuit currents and voltage can be written as

$$V_1(\omega_s) + Z_{T1} I_1(\omega_s) = \frac{Z_2}{Z_s + Z_1 + Z_2} V_s(\omega_s) \tag{2.22}$$

$$V_2(\omega_i) + Z_{T2} I_2(\omega_i) = V_i(\omega_i) \tag{2.23}$$

$$V_3(\omega_p) + Z_{T3} I_3(\omega_p) = V_p(\omega_p) \tag{2.24}$$

where Z_{T1}, Z_{T2} and Z_{T3} are total impedances at signal ,idler and pump sections of the circuit, respectively, seen from the pair terminals of the JJ given by $Z_{T1} = j\omega_s L_s + 1/j\omega_s C_s + Z_2(Z_s + Z_1)/(Z_s + Z_1 + Z_2)$, $Z_{T2} = j\omega_i L_i + 1/(j\omega_i C_i) + Z_i$ and $Z_{T3} = j\omega_p L_p + 1/j\omega_p C_p + Z_p$. Voltage sources and their series resistance are denoted by V_s, V_i, V_p, Z_s, Z_i and Z_p for signal, idler and pump parts, respectively. Equations (2.22)-(2.24) together with either (2.8)-(2.10) (method 1) or (2.19)-(2.20) (method 2) constitute a system of six nonlinear equations with six complex unknowns of V_1, V_2, V_3, I_1, I_2, and I_3 which can be solved numerically to find all variables. Nevertheless, I_1 and I_2 can be presented linearly with respect to V_s and V_i with the coefficients parametrically controlled by pump current I_3 as follows

$$\begin{bmatrix} Z_{11} + Z_{T1} & Z_{12} \\ Z_{21} & Z_{22} + Z_{T2}^* \end{bmatrix}\begin{bmatrix} I_1(\omega_s) \\ I_2^*(\omega_i) \end{bmatrix} = \begin{bmatrix} \frac{Z_2 V_s(\omega_s)}{Z_s + Z_1 + Z_2} \\ V_i^*(\omega_i) \end{bmatrix}. \tag{2.25}$$

Coefficients Z_{11}, Z_{12}, Z_{21} and Z_{22} are those found based on either method 1 or 2.

Despite of optical systems, in microwave circuits the amount of the power delivered from the source depends on the two-port network that this source is connected to. Transducer power gain [58] at the frequency ω_s is defined as the ratio of power delivered to the load to the power available from the source which happens when the source is conjugately matched to the two-port network. The maximum transducer gain occurs when the load is conjugately matched to the circuit, which in case is referred to as available gain. Transducer gain is less than the power and available gain [59], and it depends on the real part of the impedance of both source and load as

$$G_T = \frac{P_L}{P_{av}} = \frac{\frac{1}{2}|I_L|^2\mathrm{Re}(Z_L)}{\frac{1}{8}\frac{|V_s|^2}{\mathrm{Re}(Z_s)}} = \frac{4\mathrm{Re}(Z_s)\mathrm{Re}(Z_L)|I_L|^2}{|V_s|^2} \tag{2.26}$$

where Z_L is the load and I_L is the current following through the load. Removing the idler source by substituting $V_i = 0$ in (2.25), a relation between V_s and I_1 is found. Then, by applying current division on the common node between Z_1 and Z_2 in Fig. 2-3, we can find the current running through Z_1 or Z_2. Depending on which one is the load, Z_1 or Z_2, transducer power gain in (2.26) is given by which of two following equations

$$G_T|_{Z_L=Z_1} = 4\mathrm{Re}(Z_1)\mathrm{Re}(Z_s)\left|\frac{Z_2^2 + (Z_s + Z_1 + Z_2)\left(Z_{11} + Z_{T1} - Z_{neg}\right)}{(Z_s + Z_1 + Z_2)^2\left(Z_{11} + Z_{T1} - Z_{neg}\right)}\right|^2 \tag{2.27}$$

$$\begin{aligned} &G_T|_{Z_L=Z_2} \\ &= 4\mathrm{Re}(Z_2)\mathrm{Re}(Z_s)\left|\frac{(Z_s + Z_1 + Z_2)\left(Z_{11} + Z_{T1} - Z_{neg}\right) - Z_2(Z_s + Z_1)}{(Z_s + Z_1 + Z_2)^2\left(Z_{11} + Z_{T1} - Z_{neg}\right)}\right|^2. \end{aligned} \tag{2.28}$$

The term $Z_{neg} = Z_{21}Z_{12}/(Z_{22} + Z_{T2}^*)$ is interpreted as equivalent negative impedance [16], [17], and this type of amplifier is called as a negative resistance Josephson parametric amplifier.

The benefit of this definition lies on the fact that the negative resistance can be determined such that the gain in (2.27) and (2.28) becomes very large. There are two regimes of operation: oscillation and amplification. By proper design of pump and idler sections, the denominator of the gain can be zero which gives an infinite gain. In this case, the circuit operates in oscillation mode as input signal can be removed. If the gain is bounded, but above the unity, the parametric circuit is in the amplification mode.

When instead of one single junction, an array of N identical junctions is placed in the JJ branch in Fig. 2-3, the only modification which must be applied into the final results is to multiply L_{J0} in (2.8)-(2.13), (2.15), (2.17)-(2.18), (2.19) and (2.21) by a factor of N. The input and output impedances seen from the signal source and the load, as illustrated in Fig. 2-3 are

$$Z_{in} = \frac{\left(Z_{11} + Z_{T1}|_{Z_s=0} - Z_{neg}\right)(Z_1 + Z_2)^2}{\left(Z_{11} + Z_{T1}|_{Z_s=0} - Z_{neg}\right)(Z_1 + Z_2) + Z_2^2} \tag{2.29}$$

$$Z_{out}|_{Z_L=Z_1} = \frac{Z_2\left(Z_{11} + j\omega_s L_s + 1/j\omega_s C_s - Z_{neg}\right)}{Z_2 + Z_{11} + j\omega_s L_s + 1/j\omega_s C_s - Z_{neg}} + Z_s \tag{2.30}$$

$$Z_{out}|_{Z_L=Z_2} = \left(Z_{11} + j\omega_s L_s + 1/j\omega_s C_s - Z_{neg}\right) \parallel (Z_1 + Z_s). \tag{2.31}$$

2.4.4 Bandwidth

In previous gain calculation, all filters are assumed to be tuned at the corresponding resonant frequency and negative resistance JPA is designed for the maximum gain achievement, therefore, the bandwidth over which the high gain can be attained is very small. To analyze the bandwidth properties, we consider the circuit arrangement in Fig. 2-3 and also we assume the high-Q filters with certain quality factors that are more realistic compared to the infinite-Q filters. In our analysis we change the signal and idler frequency from ω_s and ω_i to $\omega_1 = \omega_s + \Delta\omega_s$ and $\omega_2 = \omega_i + \Delta\omega_i$ in an attempt to calculate the new gain formula which includes all filters' quality factors as well as signal bandwidth. According to the $2\omega_p = \omega_1 + \omega_2$ and $2\omega_p = \omega_s + \omega_i$, it is straightforward to conclude $\Delta\omega_i = -\Delta\omega_s$. Additionally, we use the relative bandwidth for the signal and idler section of the circuit in our calculation. They are defined by $\delta_s = \Delta\omega_s/\omega_s$ and $\delta_i = \Delta\omega_i/\omega_i$, respectively, and satisfy $\delta_i/\delta_s = -\omega_s/\omega_i$. It simply shows that $\Delta\omega_s$ can be eliminated in the formulation and all equations can be solely expressed in terms of the signal bandwidth. Pump has no influence on the bandwidth, because its role is to convert the JJ into the time-varying inductor whose parameters are determined by the amplitude of the pump. Then, we are able to find the 3-dB bandwidth based on the definition. Afterward, the bandwidth δ_s is found by solving a 4th degree polynomial given by

$$A_4\delta_s^4 + A_3\delta_s^3 + A_2\delta_s^2 + A_1\delta_s + A_0 = 0. \tag{2.32}$$

The coefficients of the polynomial are

$$A_0 = -(1-a)^2 \tag{2.33}$$

$$A_1 = -2a(1-a)(1-r) \tag{2.34}$$

$$\begin{aligned} A_2 = a^2(1-r)^2 + 2r(1-a)(a-4Q_iQ_s) + 4(Q_s+rQ_i)^2 \\ - 8r^2Q_i^2(1-a)^2 \end{aligned} \tag{2.35}$$

$$A_3 = -2ar(1-r)(a-4Q_iQ_s) \tag{2.36}$$

$$A_4 = r^2(a-4Q_iQ_s)^2 \tag{2.37}$$

where Q_s and Q_i are loaded quality factors associated with the signal and idler filters defined by

$$Q_s = \omega_s \frac{L_0+L_s}{(R_s+R_L)\,||\,R_{fit}} = \frac{1}{\omega_s C_s (R_s+R_L)\,||\,R_{fit}} \tag{2.38}$$

$$Q_i = \omega_i \frac{L_0+L_s}{R_i} = \frac{1}{\omega_i C_i R_i}. \tag{2.39}$$

These filters at their resonant frequency are modeled by an LC circuit with resonance conditions of $\omega_s^2 = 1/(L_s+L_0)C_s$ and $\omega_i^2 = 1/(L_i+L_0)C_i$. Moreover, parameters r and a are given by $r{=}\omega_s/\omega_i$ and $a = R_{neg}/[(R_s+R_L)\,||\,R_{fit}] = \omega_s\omega_i L_2^2/R_i[(R_s+R_L)\,||\,R_{fit}]$, where $R_{fit} = Z_2$ in Fig. 2-3 . Equation (2.32) have four real solutions at most, however, the true bandwidth will be the interval including ω_s and the lowest positive answer at right and the first negative answer at left.

In any circumstance, except when $= 1$, there exist at least two plausible real solutions, one positive and one negative, for polynomial (2.32), because $\mathrm{A}_4 > 0$ and $\mathrm{A}_0 < 0$. According to equation (2.27) or (2.28), the maximum gain condition can be achieved when $R_{neg} = R_s + R_L$, because the denominator becomes zero. Evidently, this condition corresponds to the case of $a = 1$. As explained, this condition occurs when all resonators and filters have been tuned at single frequencies which means their bandwidths would be zero. By plugging $a = 1$ into (2.33)-(2.37), it is obvious that we obtain $\delta_s = 0$ which is completely matched by the preceding qualitative explanation. Moreover, by increasing Q_s or Q_i, the coefficients of the polynomial (2.32) corresponding to the higher power terms increase, then the root of the polynomial approaches zero which is expected as explained early. Another interesting point is observed when $r = 1$ or $\omega_s = \omega_i$ (degenerate). In this case, the odd powers of (2.32) disappear and symmetric positive and negative solutions are obtained.

In the derivation of the above formula, we assume that the condition of conjugate matching at the input port is always held unchanged within the whole bandwidth. More importantly, by using the phasor notation, we examine all circuits in our study in the steady state. We have found the bandwidth on the basis of the fact that the frequency of the signal source remains constant, and only at the end of the calculation we allow it to change. Therefore, by changing the frequency of the signal source, we assume that the system has enough time to reach its steady state. In other words, the internal characteristics time of the circuit must be much less than the external time over which the signal frequency changes. This kind of treatment is referred as adiabatic process [60].

2.4.5 Noise Characteristics

In any circuit that internal components dispense noise to the output, noise figure is the best measure to describe the noise performance of such a system. Noise figure associated with the circuit is the ratio of the signal-to-noise ratio at the input to the signal-to-noise ratio at the output [58], provided the input source is matched to the circuit and held at the room temperature, $T_0 = 290\ °\mathrm{K}$. Noise figure can be found by another consistent expression as follows [17]

$$F = \frac{N_{\text{total}}}{G_T k_B T_0 B} \tag{2.40}$$

where N_{total} is the total noise power available at the output, G_T is the transducer gain of the system, $k_B = 1.38 \times 10^{-23} \mathrm{J}/°\mathrm{K}$ is the Boltzmann's constant, $T_0 = 290\ °\mathrm{K}$ is the room temperature and B is the bandwidth of the system. To compute noise figure or equivalent noise temperature of the JPA, we must first recognize the main sources that produce the noise and then we must obtain the available noise power at the output of the JPA. The noise produced by the JPA is the thermal noise in the resistors of the circuits. The first noise is the input noise from R_s at temperature $T_0 = 290\ °\mathrm{K}$ and frequency of ω_s. The second source is the noise contributed by the JPA due to the resistor R_i at the idler frequency ω_i and temperature T_2. With reference to Fig. 2-4., these noisy resistors are replaced with a Thevenin equivalent circuit consisting of noiseless resistors and noise sources shown by voltage sources. The rms value of the voltage noise associated with a resistance R at temperature T in a system with the bandwidth B is given by [58]

$$\overline{V_n^2} = 4k_B TBR. \tag{2.41}$$

Therefore, the maximum noise power that this resistor delivers to the circuit (matched load) is $P_n = k_B TB$. Using the linear impedance matrix in (2.25), we obtain following equations for the noise power N_1 and N_2 at the output due to noise sources at signal and idler branches, respectively,

$$N_1 = \frac{|Z_{22} + Z_{T2}^*|^2}{|(Z_{11} + Z_{T1})(Z_{22} + Z_{T2}^*) - Z_{12}Z_{21}|^2} R_L \overline{V_{ns}^2} \tag{2.42}$$

$$N_2 = \frac{|Z_{12}|^2}{|(Z_{11} + Z_{T1})(Z_{22} + Z_{T2}^*) - Z_{12}Z_{21}|^2} R_L \overline{V_{ni}^2}. \tag{2.43}$$

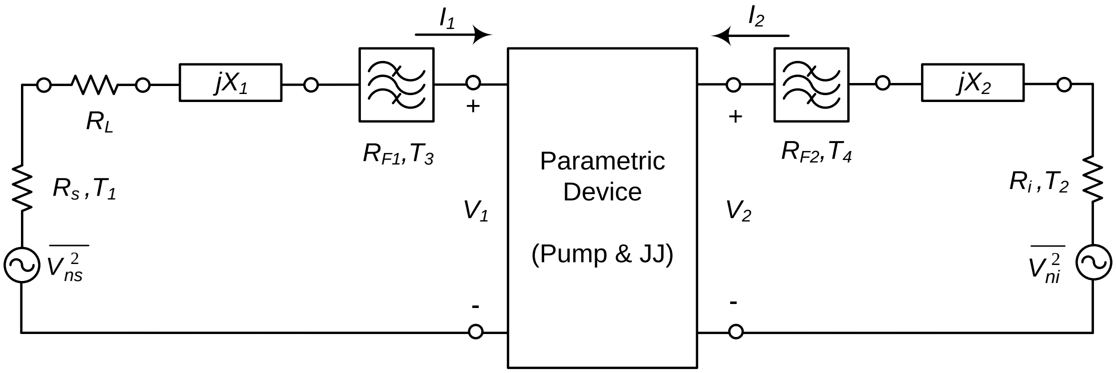

Fig. 2-4 Circuit model used for the thermal noise calculation.

Since these two noises are uncorrelated, the total noise power is the addition of each individual noise power, i.e. $N_{\text{total}} = N_1 + N_2$. Substituting the total noise and also the transducer gain in (2.40), and considering the matching condition of $R_s = R_L$, it yields

$$F = \frac{1}{4R_L k_B T_0 B} \frac{|Z_{22} + Z_{T2}^*|^2 \overline{V_{ns}^2} + |Z_{12}|^2 \overline{V_{ni}^2}}{|Z_{22} + Z_{T2}^*|^2}. \tag{2.44}$$

According to (2.41), we replace $\overline{V_{ns}^2}$ and $\overline{V_{ni}^2}$ by the proper expression, noise figure reduces to

$$F = 1 + \frac{|Z_{12}|^2 T_2 R_i}{|Z_{22} + Z_{T2}^*|^2 R_L T_0}. \tag{2.45}$$

Further simplification is made based on the resonance condition at the idler loop and definition of the negative resonance for (2.45) results in

$$F = 1 + \frac{\omega_s}{\omega_i}\frac{T_2}{T_0}\frac{R_{neg}}{R_L}. \tag{2.46}$$

where R_{fit} is removed. Assuming temperatures and resistances R_{Fs}, T_3 and R_{Fn}, T_4 for the filters, as shown in Fig. 2-4, we can generalize (2.46) and get following equation for the noise figure

$$\begin{aligned} F = 1 + \frac{T_3}{T_0}\frac{R_{Fs}}{R_L} + \frac{T_2}{T_0}\frac{\omega_s}{\omega_i}\frac{R_i^2 R_{neg}}{R_i R_L (R_i + R_{Fi})^2} \\ + \frac{T_4}{T_0}\frac{\omega_s}{\omega_i}\frac{R_i R_{Fi} R_{neg}}{R_L (R_i + R_{Fi})^2}. \end{aligned} \tag{2.47}$$

If the JPA has been designed and optimized for the high-gain achievement, the negative resistance in equations (2.46) and (2.47) can be replaced by $R_{neg} \cong R_s + R_L = 2R_L$.

2.5 Voltage-based JPA

2.5.1 Circuit Arrangement

Fig. 2-5 displays a circuit in which the pump and JJ are connected in series, instead of parallel arrangement. Also, filters associated with signal, pump and idler are modeled by a parallel LC circuit that has been discussed in section 2.2. This schematic fits with the Manley-Rowe configuration illustrated in Fig. 2-1 (b). Writing the KVL around the simple loop containing the JJ implies that $v_J = 0$, for harmonics other than signal, pump, and idler. This is the reason that this kind of arrangement is called a voltage-based JPA, and the topology is considered as a dual configuration for the current-based JPA in the last section. Similar to the current-based JPA, there also exist two admittance Y_1 and Y_2 in Fig. 2-5 to provide general study on the position of the load, as well as adjust the bandwidth of the JPA, as explained later.

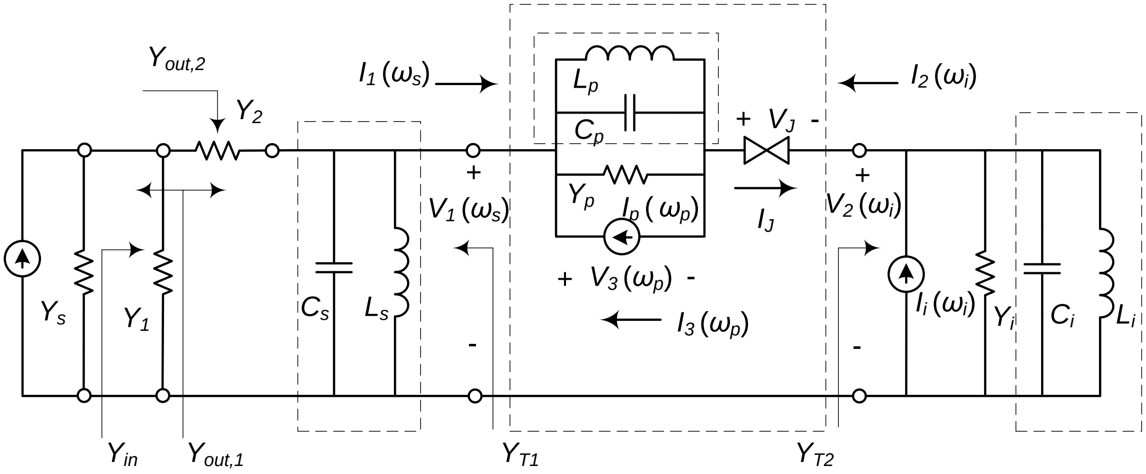

Fig. 2-5 Schematic of the voltage-based JPA.

2.5.2 Voltage-Current Relationship

As pointed out, the voltage of the junction is allowed to only have three frequency components of ω_s , ω_p and ω_i, and it can be written by $v_J(t) = -v_p(t) + v_s(t) - v_i(t)$. According to (2.6), the complex amplitude, angular frequency and initial phase of the signal, pump and idler voltages, respectively, are denoted by V_1, ω_s, θ_s, V_3, ω_p, θ_p, V_2, ω_i and θ_i. According to the Farady's law, we can assign a flux variable to each of $v_s(t)$, $v_p(t)$ and $v_i(t)$ voltages. Scaling the flux by the factor $2\pi/\Phi_0$, we define a phase variable for each of $v_s(t)$, $v_p(t)$ and $v_i(t)$ voltages, similar to the phase difference of two superconductors in a JJ. This is mathematically described by $\varphi(t) = (2\pi/\Phi_0)\int_0^t v(\tau)\,d\tau$. In steady-state, this integral leads to

$$\varphi_i(t) = \frac{-j\pi}{\Phi_0\omega_i}\left(V_i e^{j\omega_i t} - V_i^* e^{-j\omega_i t}\right) = \frac{2\pi|V_i|}{\Phi_0\omega_i}\sin(\omega_i t + \theta_i) \qquad (2.48)$$

where i stands for s, p and i , θ_i is the initial phase, and V_i is the complex amplitude of $v_i(t)$ based on (2.6). The phase difference across the junction can be written as $\varphi_J(t) = -\varphi_p(t) + \varphi_s(t) - \varphi_i(t)$. If the current flowing through the junction is restricted to be less than critical current of the JJ, it will be found by the nonlinear phase-current equation of

$$i_J = I_c \sin\varphi_J. \qquad (2.49)$$

Like the current-based JPA, two methods can be used to relate the current and voltage of each component.

Method 1: JJ as a nonlinear inductor

Expanding the sinusoidal function in (2.49) and keeping the two leading terms, we obtain a nonlinear relation between phase (or flux by scaling factor $\Phi_0/2\pi$) and current associated with the JJ. Inserting φ_J in terms of its components, it gives

$$i_J(t) = I_c\left[-\varphi_p(t)+\varphi_s(t)-\varphi_i(t)\right] - \frac{I_c}{6}\left[-\varphi_p(t)+\varphi_s(t)-\varphi_i(t)\right]^3. \tag{2.50}$$

Following the procedure described in previous section and using (2.48), ω_s, ω_p and ω_i components of the current are obtained by

$$I_1 = I_J(\omega_s) = \frac{-2j\pi I_c}{\Phi_0\omega_s}V_1 - \frac{j\pi^3 I_c}{\Phi_0^3\omega_p^2\omega_i}V_3^2V_2^* \tag{2.51}$$

$$I_2 = I_J(\omega_i) = \frac{-2j\pi I_c}{\Phi_0\omega_i}V_2 - \frac{j\pi^3 I_c}{\Phi_0^3\omega_p^2\omega_s}V_3^2V_1^* \tag{2.52}$$

$$I_3 = I_J(\omega_p) = \frac{-2j\pi I_c}{\Phi_0\omega_p}V_3 - \frac{2j\pi^3 I_c}{\Phi_0^3\omega_s\omega_p\omega_i}V_3^*V_1V_2. \tag{2.53}$$

when $I_J = I_1 - I_2 - I_3$, as seen in Fig. 2-5, and $|I_1| + |I_2| + |I_3| < I_c$. The direction of the currents in Fig. 2-5 are chosen such that all signal, pump and idler terminals have the same reference polarity rule which is important in power calculation. Moreover, the complex current amplitude is defined by $I(t) = \frac{1}{2}\left(Ie^{j\omega t} - c.c.\right)$, as (2.48) implies, where $c.c.$ stands for complex conjugate. Real powers for each section satisfy the Manley-Rowe relation and are given by

$$P_1 = \tfrac{1}{2}\mathrm{Re}\{I_1V_1^*\} = \frac{-\pi^3 I_c}{2\Phi_0^3\omega_p^2\omega_i}\mathrm{Re}\{jV_1^*V_2^*V_3^2\} \tag{2.54}$$

$$P_2 = \tfrac{1}{2}\mathrm{Re}\{I_2V_2^*\} = \frac{-\pi^3 I_c}{2\Phi_0^3\omega_p^2\omega_s}\mathrm{Re}\{jV_1^*V_2^*V_3^2\} \tag{2.55}$$

$$P_3 = \tfrac{1}{2}\mathrm{Re}\{I_3V_3^*\} = \frac{\pi^3 I_c}{\Phi_0^3\omega_s\omega_p\omega_i}\mathrm{Re}\{jV_1^*V_2^*V_3^2\}. \tag{2.56}$$

Method 2: JJ as a time-varying inductor

Like the current-based JPA, the amplitude of the sinusoidal pump source is intended to be much larger than those of the signal and idler, therefore, by expressing the current as a function of phase, equation (2.6), the first two terms of the Taylor expansion about the pump signal are

$$i_J(\varphi_J) \cong i_J(-\varphi_p) + \left.\frac{di_J}{d\varphi}\right|_{\varphi=-\varphi_p} [\varphi_s - \varphi_i]. \tag{2.57}$$

This yields

$$i_J(t) = I_c \sin(\alpha_p \sin \beta_p) + I_c \cos(\alpha_p \sin \beta_p) \sin(\alpha_s \sin \beta_s + \alpha_i \sin \beta_i) \tag{2.58}$$

where $\alpha_p = \frac{2\pi|V_3|}{\Phi_0\omega_p}$, $\alpha_s = \frac{2\pi|V_1|}{\Phi_0\omega_s}$, $\alpha_i = \frac{2\pi|V_2|}{\Phi_0\omega_i}$, $\beta_p = \omega_p t + \theta_p$, $\beta_s = \omega_s t + \theta_s$ and $\beta_i = \omega_i t + \theta_i$. Expanding $\sin(\alpha \sin \beta)$ and $\cos(\alpha \sin \beta)$ in terms of Bessel functions [57], we deduce the condition of $2\beta_p = \beta_s + \beta_i$ which evidently results in $2\omega_p = \omega_s + \omega_i$ and $2\theta_p = \theta_s + \theta_i$. The linear admittance matrix between the current and voltage of the 2-port configuration in Fig. 2-5, is obtained by

$$\begin{bmatrix} I_1(\omega_s) \\ I_2^*(\omega_i) \end{bmatrix} = \begin{bmatrix} Y_{11} & Y_{12} \\ Y_{21} & Y_{22} \end{bmatrix} \begin{bmatrix} V_1(\omega_s) \\ V_2^*(\omega_i) \end{bmatrix} \tag{2.59}$$

where $Y_{11} = -jJ_0/L_{J0}\omega_s$, $Y_{12} = -jJ_2 e^{j2\theta_p}/L_{J0}\omega_i$, $Y_{21} = jJ_2 e^{-j2\theta_p}/L_{J0}\omega_s$, $Y_{22} = jJ_0/L_{J0}\omega_i$ which are more general than those calculated in [22]. Parameters $J_0 = J_0(\alpha_p)$ and $J_2 = J_2(\alpha_p)$ are Bessel's functions of the first kind of order 0 and 2, respectively, for the argument of α_p which can be simplified by polynomial series as

$$J_0(\alpha_p) \approx 1 - \frac{\alpha_p^2}{4} + \frac{\alpha_p^4}{64} - \frac{\alpha_p^6}{2304} + \cdots \tag{2.60}$$

$$J_2(\alpha_p) \approx \frac{\alpha_p^2}{8} - \frac{\alpha_p^4}{96} + \frac{\alpha_p^6}{3072} + \cdots \tag{2.61}$$

Since α_p is a real number, the values of the Bessel's functions are also less than one. Furthermore, Bessel's function has zeros in a oscillatory fashion and the first zeros of $J_0(\alpha_p)$ and $J_2(\alpha_p)$ are located in $2 < \alpha_p < 3$ and $5 < \alpha_p < 6$, respectively.

2.5.3 Gain, Input and Output Impedance

Using the same procedure for the case of current-based JPA to include the current sources in Fig. 2-5 results in

$$I_1(\omega_s) + Y_{T1}V_1(\omega_s) = \frac{Y_2}{Y_s + Y_1 + Y_2} I_s(\omega_s) \tag{2.62}$$

$$I_2(\omega_i) + Y_{T2}V_2(\omega_i) = I_i(\omega_i) \tag{2.63}$$

$$I_3(\omega_p) + Y_{T3}V_3(\omega_p) = I_p(\omega_p) \tag{2.64}$$

which can be used in corporation with current-voltage characteristics obtained in the previous part to solve the circuit. Parameters Y_{T1}, Y_{T2} and Y_{T3} are the total signal, idler and pump conductance seen from the ports illustrated in Fig. 2-5 They are equal to $Y_{T1} = \frac{(Y_s+Y_1)Y_2}{(Y_s+Y_1+Y_2)} + j\omega_s C_s + 1/j\omega_s L_s$, $Y_{T2} = Y_i + j\omega_i C_i + 1/j\omega_i L_i$ and $Y_{T3} = Y_p + j\omega_p C_p + 1/j\omega_p L_p$. Focusing on the voltage and current of signal and idler, they can be presented in a matrix format with pump-dependent coefficients given by

$$\begin{bmatrix} Y_{11}+Y_{T1} & Y_{12} \\ Y_{21} & Y_{22}+Y_{T2}^* \end{bmatrix} \begin{bmatrix} V_1(\omega_s) \\ V_2^*(\omega_i) \end{bmatrix} = \begin{bmatrix} \dfrac{Y_2 I_s(\omega_s)}{Y_s+Y_1+Y_2} \\ I_i^*(\omega_i) \end{bmatrix} \tag{2.65}$$

Disabling the idler source, the transducer gain at the load ($Y_L = Y_1$ or Y_2) in the form of $G_T = 4\mathrm{Re}(Y_s)\mathrm{Re}(Y_L)|V_L/I_s|^2$ is obtained by

$$G_T|_{Y_L=Y_1} = 4\mathrm{Re}(Y_1)\mathrm{Re}(Y_s)\left|\frac{Y_2^2 + (Y_s+Y_1+Y_2)\big(Y_{11}+Y_{T1}-Y_{neg}\big)}{(Y_s+Y_1+Y_2)^2\big(Y_{11}+Y_{T1}-Y_{neg}\big)}\right|^2 \tag{2.66}$$

$$G_T|_{Y_L=Y_2} = 4\mathrm{Re}(Y_2)\mathrm{Re}(Y_s)\left|\frac{(Y_s+Y_1+Y_2)\big(Y_{11}+Y_{T1}-Y_{neg}\big) - Y_2(Y_s+Y_1)}{(Y_s+Y_1+Y_2)^2\big(Y_{11}+Y_{T1}-Y_{neg}\big)}\right|^2 \tag{2.67}$$

The expression $Y_{neg} = Y_{21}Y_{12}/(Y_{22}+Y_{T2}^*)$ in (2.64) and (2.65) introduces the concept of the negative admittance that can be used for oscillation and gain enhancement in amplification mode. The input and output admittance in Fig. 2-5 are given by

$$Y_{in} = \frac{\big(Y_{11} + Y_{T1}|_{Y_s=0} - Y_{neg}\big)(Y_1+Y_2)^2}{\big(Y_{11} + Y_{T1}|_{Z_s=0} - Y_{neg}\big)(Y_1+Y_2) + Y_2^2} \tag{2.68}$$

$$Y_{out}|_{Y_L=Y_1} = \frac{Y_2\big(Y_{11} + j\omega_s L_s + 1/j\omega_s C_s - Y_{neg}\big)}{Y_2 + Y_{11} + j\omega_s L_s + 1/j\omega_s C_s - Y_{neg}} + Y_s \tag{2.69}$$

$$Y_{out}|_{Y_L=Y_2} = \big(Y_{11} + j\omega_s L_s + 1/j\omega_s C_s - Y_{neg}\big) \parallel (Y_1 + Y_s). \tag{2.70}$$

In the case of array of N JJs in series, the Φ_0 in equations (2.51)-(2.56) and L_{J0} in entries of (2.59) must be multiplied by N, and all equations remain unchanged.

2.5.4 Bandwidth

With the reference to the section 2.4.4, we pursue the same argument and calculation which finally leads to the 8-degree polynomial to find the bandwidth δ_s of the circuit in Fig. 2-5 The polynomial has the form of

$$B_8\delta_s^8 + B_7\delta_s^7 + B_6\delta_s^6 + B_5\delta_s^5 + B_4\delta_s^4 + B_3\delta_s^3 + B_2\delta_s^2 + B_1\delta_s + B_0 = 0 \tag{2.71}$$

where coefficients are given by

$$B_0 = -(1-b)^2 \tag{2.72}$$

$$B_1 = -2(1-r)(2b^2 - 3b + 1) \tag{2.73}$$

$$\begin{aligned} B_2 = {} & (1-r)^2 - 2r(1-b)(1-4Q_iQ_s) - 8r^2Q_i^2(1-b)^2 \\ & + 4(Q_s - rQ_i)^2 - 2(1-b)^2(r^2 - 4r + 1) \end{aligned} \tag{2.74}$$

$$\begin{aligned} B_3 = {} & 8r(1-r)(1-b)Q_iQ_s - 2r(1-r)(1-4Q_iQ_s) \\ & - 16r^2(1-r)(1-b)^2Q_i^2 + 8(1-r)(Q_s - rQ_i)^2 \\ & + 4r(1-r)(1-b)^2 \end{aligned} \tag{2.75}$$

$$\begin{aligned} B_4 = {} & -8r^2(1-b)Q_iQ_s + r^2(1-4Q_iQ_s)^2 + 8r(1-r)^2Q_iQ_s \\ & - 8r^2(r^2 - 4r + 1)(1-b)^2Q_i^2 \\ & + 4(r^2 - 4r + 1)(Q_s - rQ_i)^2 - 2r^2(1-b)^2 \end{aligned} \tag{2.76}$$

$$\begin{aligned} B_5 = {} & -16r^2(1-r)Q_iQ_s + 32r^2(1-r)Q_s^2Q_i^2 \\ & + 16r^3(1-r)(1-b)^2Q_i^2 - 8r(1-r)(Q_s - rQ_i)^2 \end{aligned} \tag{2.77}$$

$$\begin{aligned} B_6 = {} & 16r^2(1-r)^2Q_s^2Q_i^2 + 8r^3Q_iQ_s(1 + 4Q_iQ_s) \\ & - 8r^4(1-b)^2Q_i^2 + 4r^2(Q_s - rQ_i)^2 \end{aligned} \tag{2.78}$$

$$B_7 = -32r^3(1-r)Q_s^2Q_i^2 \tag{2.79}$$

$$B_8 = 16r^4Q_s^2Q_i^2. \tag{2.80}$$

and $r = \omega_s/\omega_i$ and $b = G_{neg}(G_s + G_L + G_{fit})/(G_s + G_L)G_{fit}$. The signal and idler filters are tuned at the resonant frequencies $\omega_s^2 = (L_{J0} + L_sJ_0)/C_sL_sL_{J0}$ and $\omega_i^2 = (L_{J0} + L_iJ_0)/C_iL_iL_{J0}$, respectively, and the loaded Q-factors Q_s and Q_i are

$$Q_s = \omega_s \frac{C_s}{\mathrm{Re}(Y_{T1})} = \frac{\left(L_{J0} + L_sJ_0\right)\left(G_s + G_L + G_{fit}\right)}{\omega_sL_sL_{J0}G_{fit}(G_s + G_L)} \tag{2.81}$$

$$Q_i = \omega_i \frac{C_i}{\mathrm{Re}(Y_{T2})} = \frac{L_{J0} + L_iJ_0}{\omega_iL_iL_{J0}G_i}. \tag{2.82}$$

2.5.5 Noise Characteristics

Fig. 2-6 illustrates the voltage-based JPA to study its noise performance. The temperature of each resistor and filter is shown in this figure. The noise sources associated with the generator and idler conductance, G_s and G_i, are displayed based on the Norton equivalent model. Noise powers at the output due to the contribution of G_s and G_i are given by

$$N_1 = \frac{|Y_{22} + Y_{T2}^*|^2}{|(Y_{11} + Y_{T1})(Y_{22} + Y_{T2}^*) - Y_{12}Y_{21}|^2} G_L \overline{I_{ns}^2} \tag{2.83}$$

$$N_2 = \frac{|Y_{12}|^2}{|(Y_{11} + Y_{T1})(Y_{22} + Y_{T2}^*) - Y_{12}Y_{21}|^2} G_L \overline{I_{ni}^2}. \tag{2.84}$$

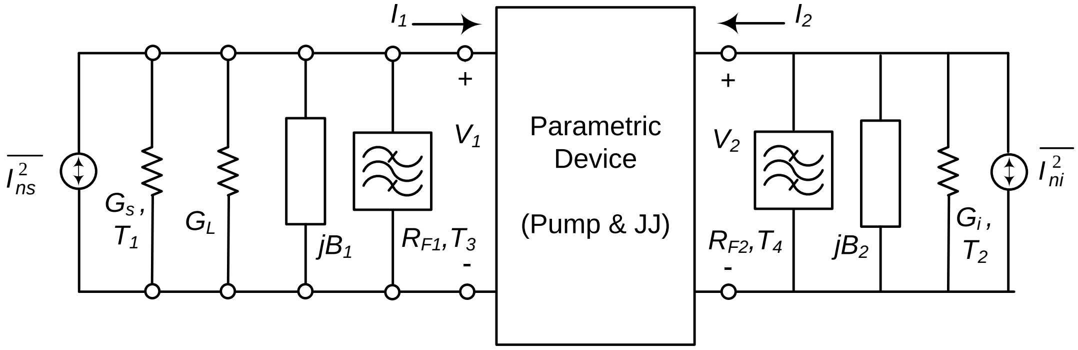

Fig. 2-6 Simplified circuit model of voltage-based JPA for the noise analysis.

Consequently, by the same method that we used for the case of current-base JPA, the noise figure can be found through following equation

$$F = \frac{1}{4G_s k_B T_0 B}\left[\overline{I_{ns}^2} + \left|\frac{Y_{12}}{Y_{22} + Y_{T2}^*}\right|^2 \overline{I_{ni}^2}\right]. \tag{2.85}$$

Substituting noise sources by (2.41), including the filter temperatures into the noise figure based on the Fig. 2-6 and simplifying it according to the resonance condition, the general noise figure for the topology shown in Fig. 2-6 is found by

$$F = 1 + \frac{G_1}{G_s}\frac{T_1}{T_0} + \frac{T_i}{T_0}\frac{\omega_s}{\omega_i}\frac{G_{\text{neg}}G_i^2}{G_s(G_i + G_2)^2} + \frac{T_2}{T_0}\frac{\omega_s}{\omega_i}\frac{G_{\text{neg}}G_2G_i}{G_s(G_i + G_2)^2}. \tag{2.86}$$

when G_{fit} is neglected. By ignoring the filters' resistor s we can simplify (2.86) to get

$$F = 1 + \frac{\omega_s}{\omega_i}\frac{T_2}{T_0}\frac{G_{neg}}{G_L}. \tag{2.87}$$

2.6 Design Procedure

The analysis of current- and voltage-based JPA in two preceding sections has been finally simplified by the gain formulations given by (2.27)-(2.28) and (2.66)-(2.67), respectively. In addition to the signal frequency ω_s, signal source, load and LC filter impedances which emerge in these equations, other parameters such as idler impedance, the current flowing through (or voltage dropped on) the pump section and its frequency implicitly exist in the gain formulas. Due to the presence of the negative resistance (or conductance) in their denominators, the design target is to maximize the gain by setting the denominator to zero, that leads to the proper pump source design and idler impedance. Although dealing with nonlinear equations are complicated, this effort can be easily carried out by plotting the gain contours (in dB) on a 2D graph with pump current (or voltage) vs. pump frequency for different idler impedance. Based on this plot, we are prompted to choose desirable values for the pump frequency, pump current/voltage and idler impedance. Using this information, we can solve the circuit by finding the signal and idler current/voltage based on equation (2.25) or (2.65), depending on the type of JPA configuration. Then, we used (2.10) or (2.53) to compute the total voltage dropped on (or current flowing through) the pump. The design procedure is accomplished, when the pump source amplitude is obtained by (2.24) or (2.64). According to the restriction of $|I_1| + |I_2| + |I_3| < I_c$ on the currents, this condition must be always checked.

Denominators in the gain formula must become real in order to be cancelled by the negative resistance. Hence, the resonant condition for the filter parts are modified to $\omega_s^2 = 1/(L_s + L_0)C_s$, $\omega_i^2 = 1/(L_i + L_0)C_i$ for the current-based and $\omega_s^2 = (L_{J0} + L_s J_0)/C_s L_s L_{J0}$, $\omega_i^2 = (L_{J0} + L_i J_0)/C_i L_i L_{J0}$ for the voltage-based configuration. By proper design of filters, these conditions can be satisfied.

2.7 Numerical Results

We use Nb-AlO$_x$-Nb junction with the size of $3\mu\text{m} \times 3\mu\text{m}$ fabricated by small current density process of $30\,\text{A/cm}^2$ by HYPRES; therefore, the junction's critical current is $I_c = 2.7\,\mu\text{A}$ and its linear inductance is $L_{J0} = 121.9\,\text{pH}$ [61]. Assuming given signal source and load, the design process for maximum gain achievement leads to the determination of ω_p, I_p and Z_i for the current-based and ω_p, V_p and Y_i for the voltage-based JPA, as discussed in design procedure section. The variation of the gain versus amplitude and frequency of the pump are displayed in Fig. 2-7 and Fig. 2-8 for the current-based and the voltage-based configuration, respectively. The source frequency and impedance for both cases are assumed to be $f_s = 10$ GHz and $Z_s = 50\ \Omega$. Both x and y axes of the graphs have been normalized for the purpose of comparison. The contours in Fig. 2-7 and Fig. 2-8 are calculated based on the maximum gain.

Due to the importance of $\omega_s/2\omega_p$ factor in the gain and power added efficiency relations in (2.2) and (2.3), it is desirable to choose the higher value for this factor. Comparison between Fig. 2-7 and Fig. 2-8 reveals the fact that the high-gain curves in current-based configuration are nicely separated in the regime of $\omega_s > \omega_p$, however, in the case of voltage-based these figures are very dense which is not suitable for design purposes. Fig. 2-9 illustrates the effect of number of in-series JJs on the high-gain performance of the current-based JPA. As seen, by increasing the number of JJs the high-gain contours are pushed to the low-current regions with higher value of $\omega_s/2\omega_p$ which results in higher efficiency.

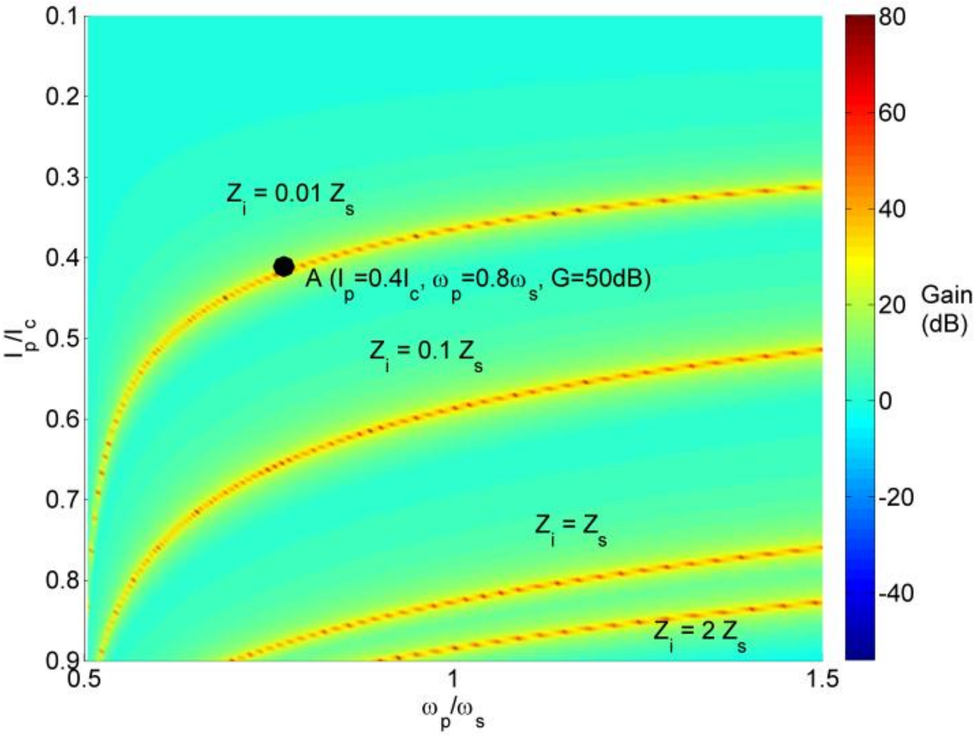

Fig. 2-7 Power gain (dB) of the current-based JPA for different idler impedances for a 50 JJs in series. Other parameters: $Z_s = Z_L$ =50 **Ω**, $Z_1 = Z_L$, $Z_2 = \infty$ **Ω**, f_s =10 GHz and I_c = 2.7 µA.

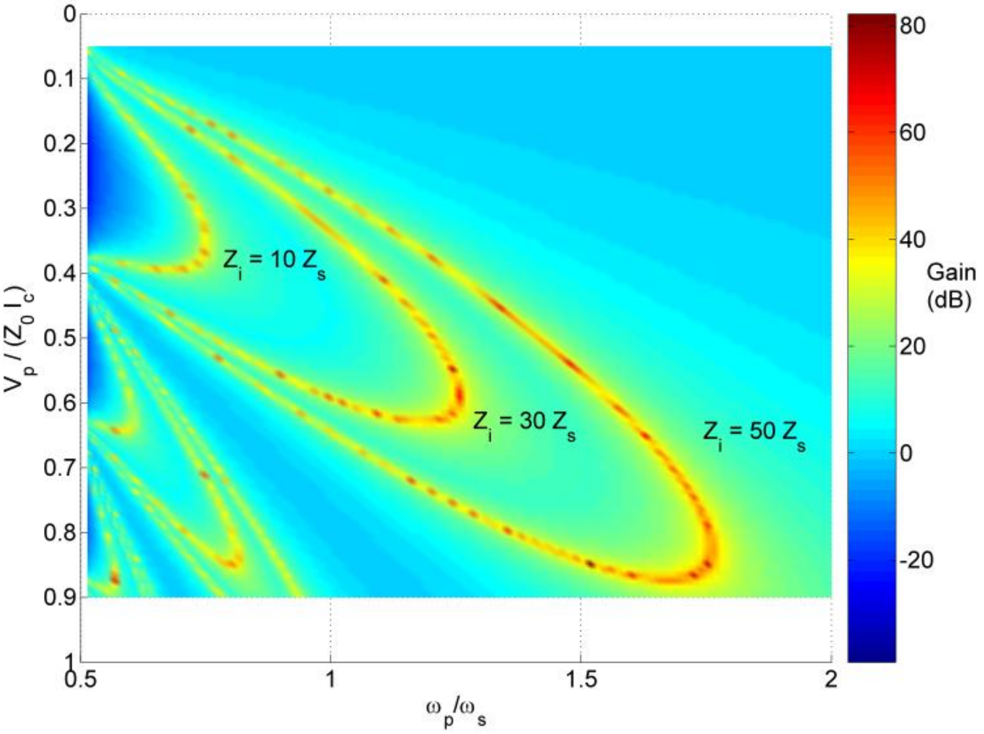

Fig. 2-8 Power gain (dB) of the voltage-based JPA for different idler impedances for 10 JJs in series. . Other parameters are $Z_s = Z_0 = Z_L$ =50 **Ω**, Y_1= Y_L, Y_2 =∞, f_s =10 GHz and I_c = 2.7 µA.

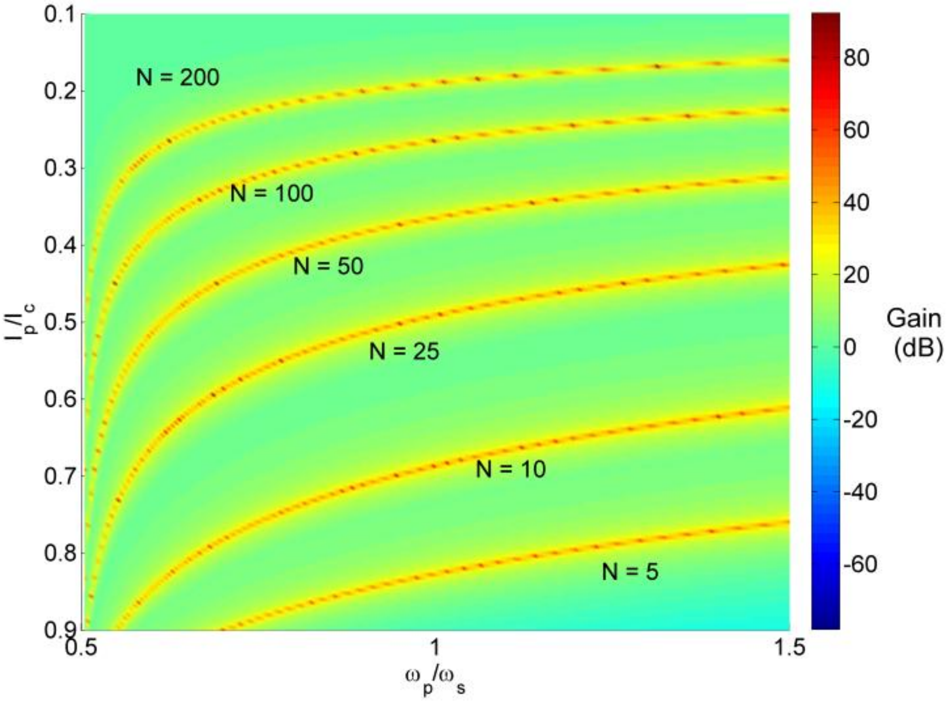

Fig. 2-9 Power gain (dB) for different number of JJs in a current-based JPA, $Z_s = Z_L = 50\ \Omega$, f_s=10 GHz, $Z_i = 0.01\ Z_s$.

As explained in the previous section, these figures can be used to design a parametric amplifier. We select point A in Fig. 2-7 which is located in low-current and high-efficiency operation region. Then, we follow all steps described in the design procedure section to determine the pump source. Table I contains all calculated variables and parameters related to point A by method 1 which have been discussed in section 2.4.2. According to this table, all pump, signal and idler currents are less than the critical current of the JJ. Also, comparison between the values of I_1, I_2 and I_3 in Table I, shows that small-signal analysis is not a suitable method for this circuit. As a phase has not been assigned to the current following through the pump branch, the pump source contains a phase part. This phase can be eliminated by considering a phase for I_3 and sweeping this phase to see when the phase of V_p vanishes.

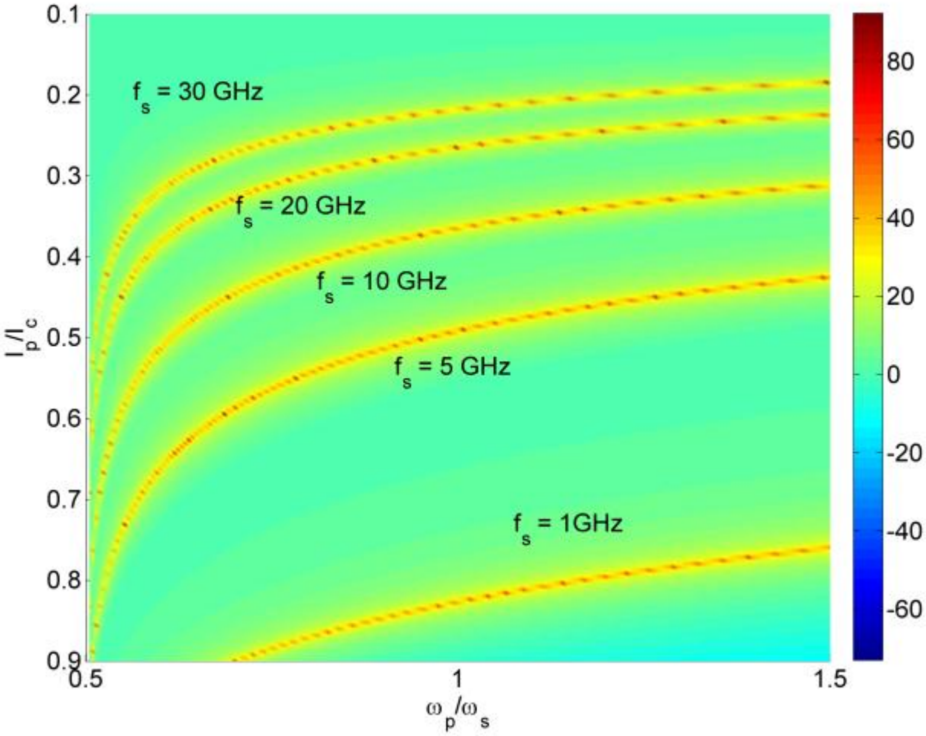

Fig. 2-10 Power gain (dB) versus pump's current and its frequency for different signal frequencies when an array of 50 JJs is placed and Z_i =0.01 Z_s.

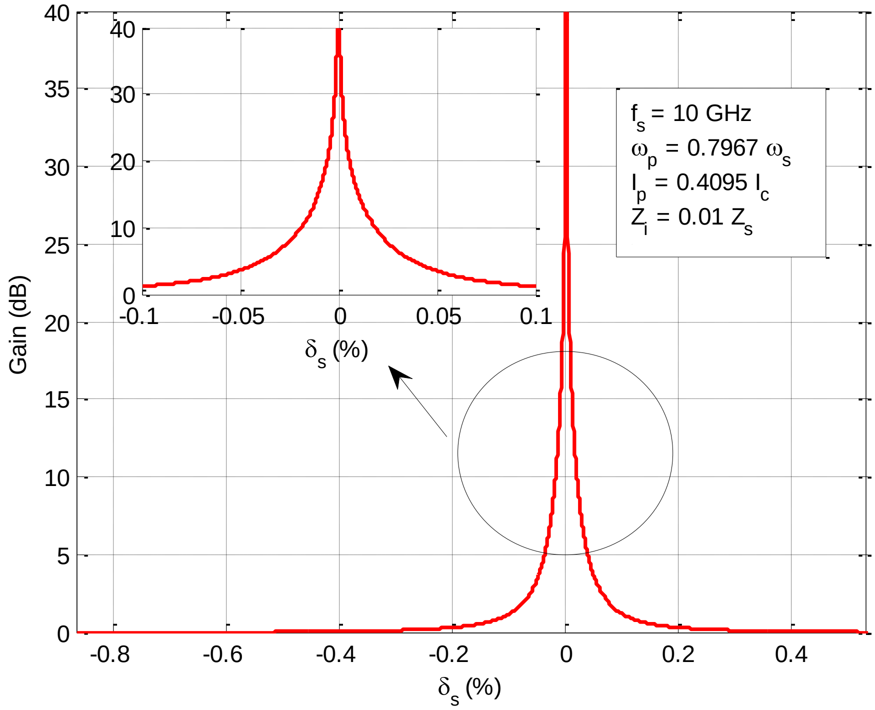

Fig. 2-11 Relative bandwidth (%) of a current-based JPA with $Z_2=\infty\ \Omega$ for 50 Nb-AlO_x-NB junctions in series.

TABLE I

CURRENT-BASED PARAMETERS FOR MAXIMUM GAIN

I_c (μA)	2.7	I_p (or I_3)	$0.4I_c = 1.08$
V_s (μV)	5	L_{J0}(nH)	6.09 (50 JJs)
$Z_s(\Omega)$	50	L_0(nH)	6.36
f_s(GHz)	10	L_1 (nH)	0.1386
$Z_L(\Omega)$	50	L_2 (nH)	0.0045
$Z_p(\Omega)$	50	L_3(nH)	0.0002
N	50	$Z_{11}(\Omega)$	$j382$
$Z_i(\Omega)$	$0.01Z_s = 0.5$	$Z_{12}(\Omega)$	$j7.65$
f_p(GHz)	$0.8f_s$ = 8 GHz	$Z_{21}(\Omega)$	-$j4.6$
f_i(GHz)	6 GHz	$Z_{22}(\Omega)$	-$j230$
L_s(nH)	9.81	I_1(μA)	0.16
C_s(fF)	15.66	I_2(μA)	$1.5\angle-1.57$
L_i(nH)	9.39	V_1(μV)	65.7
C_i(fF)	44.64	V_2(μV)	357
L_p(nH)	1.9	V_3(μV)	$330\angle 1.56$
C_p(fF)	200	V_p(μV)	$335\angle 1.4$

Relative bandwidth, which is defined by $\delta_s = \Delta\omega_s/\omega_s$ to sustain the gain within 3dB below its maximum value, is depicted in Fig. 2-11 for a current-based JPA. By proper design of filter parameters, the resonant conditions for the signal and idler filters occurs at $f_s = 10$ GHz and $f_i = 5.934$ GHz. This plot reveals that the bandwidth is very narrow which is suitable for oscillator design and the device operates in oscillation mode. Based on this fact, Fig. 2-12 demonstrates a pump-controlled oscillator that frequency of oscillation can be adjusted by the amplitude of the AC signal of the pump (I_p) to acquire a subharmonic oscillation from $f_s = 0.5$ GHz to $f_s = 4$ GHz when frequency of the pump is set at $f_p = 10$ GHz.

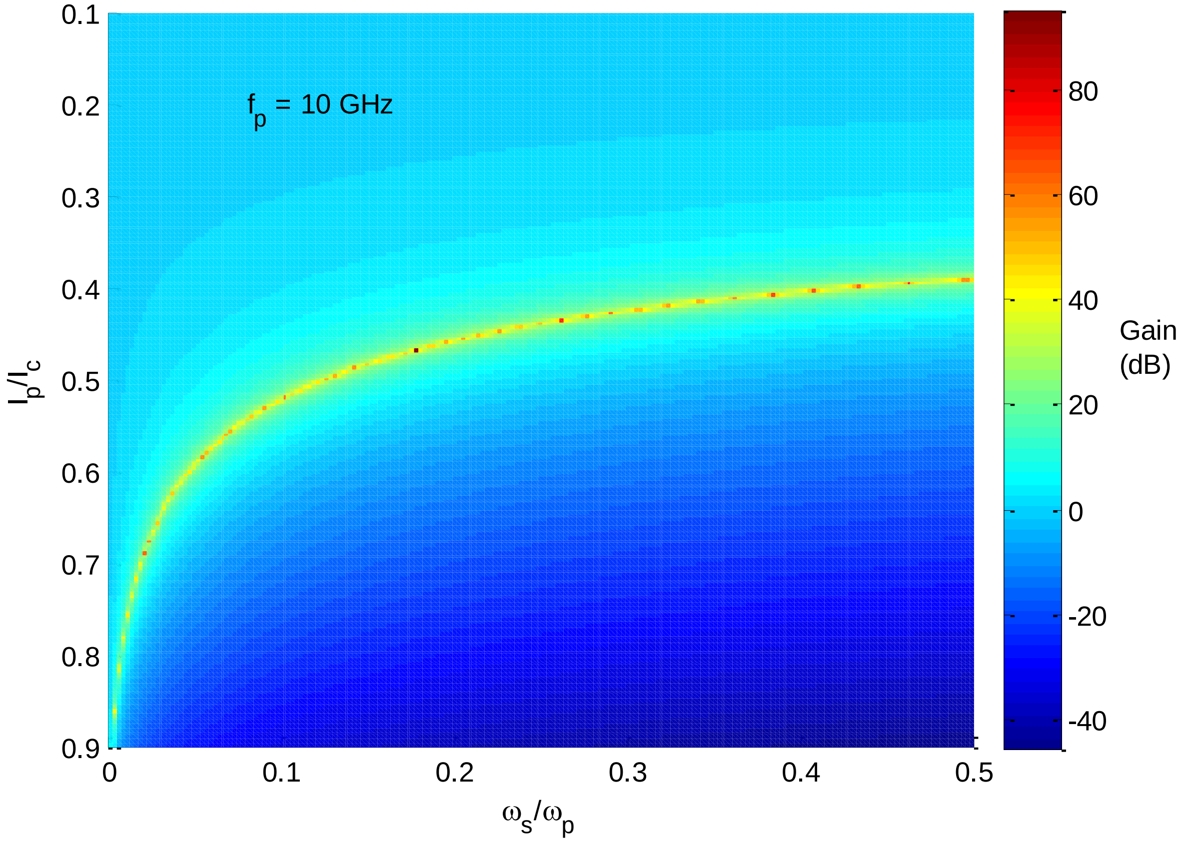

Fig. 2-12 Pump controlled Josephson oscillator demonstration for the current-based configuration when 50 junctions are in series to each other and $Z_{fit} = \infty\ \Omega$.

Oscillation mode happens when the condition of $Z_{in} + Z_s = 0$ or $Y_{in} + Y_s = 0$ is satisfied. As in our simulation, the source impedance is $Z_s = 50\ \Omega$, therefore, Z_{in} must be $-50\ \Omega$ in order that the circuit operates in the oscillation mode. Comparison between Fig. 2-8 and Fig. 2-13 confirms this fact that the condition $Z_{in} = -50\ \Omega$ takes place exactly where the pump source and idler impedance are designed for the maximum gain achievement. This condition causes instability at the signal part of the circuit with a very high gain and extremely narrow bandwidth. In order to change this condition and achieve amplifier mode, the impedance Z_2 in Fig. 2-3 (or Y_2 in Fig. 2-5) can play the role of a fitting impedance (or admittance) in the signal part of the circuit to drift the input impedance slightly from $-50\ \Omega$ and decrease the quality factor of the filters at the cost of lowering the gain. Fig. 2-14 illustrates the profile of the gain with respect to the signal frequency for different values of Y_2. This result shows when $Z_2 = 100\ \Omega$ we obtain a doubly degenerate amplifier ($f_s \sim f_p \sim f_i$) with the gain of 14 dB at $f_s = 12.621$ GHz and the bandwidth of 3MHz. The noise characteristics of these two arrangements don't differ , and the noise temperature of the voltage-based device is depicted in Fig. 2-15 when the device is held at 4K temperature.

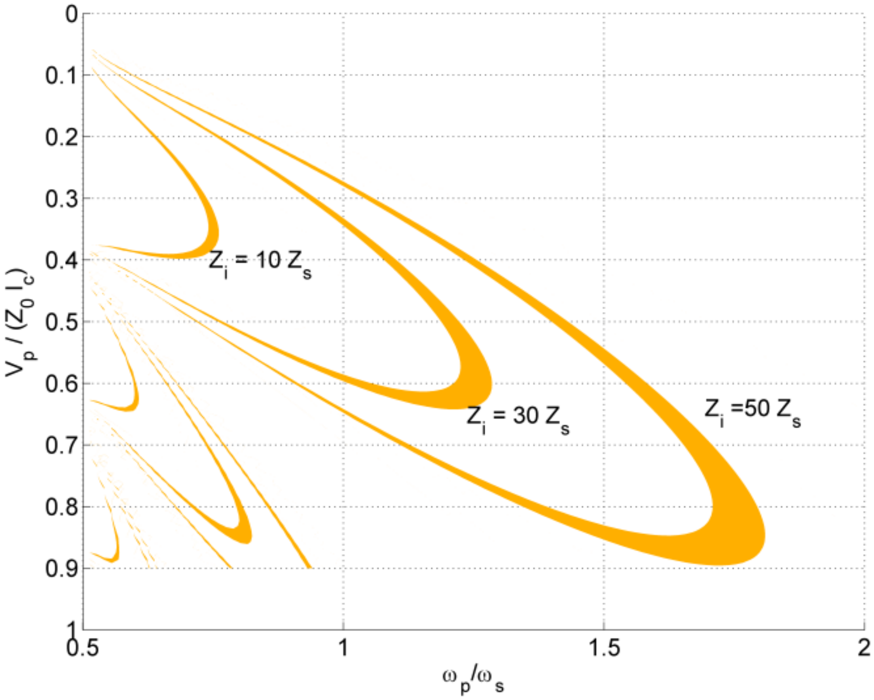

Fig. 2-13 The locus of Zin = -50 Ω for the input impedance with respect to the pump's amplitude and frequency.

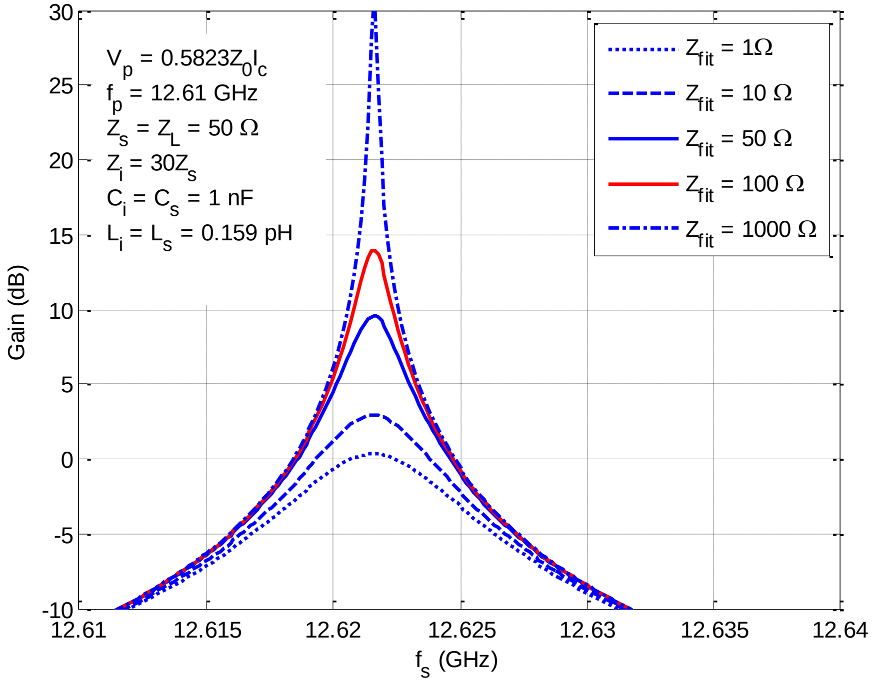

Fig. 2-14 Gain-frequency diagram of a voltage-based JPA, Z_{fit}=Z_2.

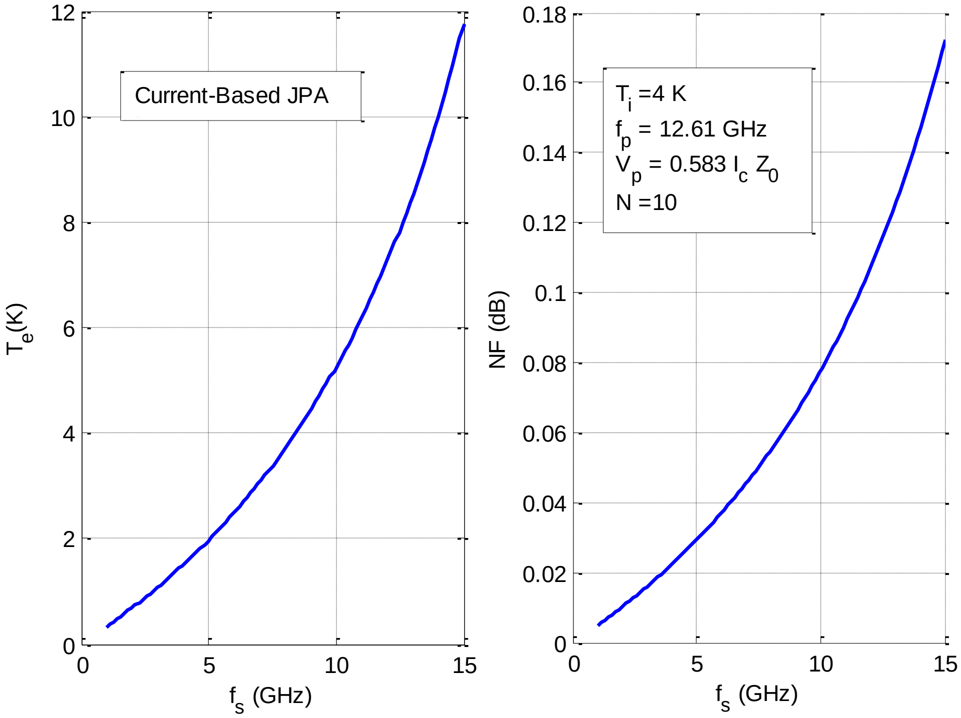

Fig. 2-15 Noise Figure and equivalent temperature for the current-based JPA when the idler is held at 4K.

2.8 Conclusion

In this paper, we studied parametric interaction in two different circuit arrangements containing a series of identical Josephson junctions. We presented a general and systematic method to analyze parametric circuits. Proper modeling of JJ, which is based on the flux-current relation and leads to a linear impedance matrix in a parametric circuit, has been presented. Two methods of analysis have been carried out and their results were compared. One is based on the pure nonlinear treatment of the junction and another is small-signal analysis which leads to the time-varying modeling of the junction. Gain characteristics, the concept of negative impedance and the input/output impedance were discussed. All formulations have been derived in closed-forms and the design rule for two regimes of oscillation and amplification has been addressed.

Chapter 3

Periodic Superconducting Waveguides

3.1 Introduction

Electromagnetic periodic structures remain a subject of great interest, both due to the virtue of the basic theory and numerical computation for the study of the propagation of electromagnetic waves, and because of the potential for practical devices in microwave circuits, antenna systems and photonic components [62],[63],[64], [65][64][66][67][68][69], [70]. The existence of a discrete set of pass-bands separated by stop-bands in periodically loaded transmission lines and guided-wave structures has presented the opportunity of using them for filter purposes [16],[58]. Of these structures, the coplanar waveguide (CPW) has the unique advantages of being uniplanar, requiring simple fabrication processes, and allowing the straightforward connection of series and shunt elements. Moreover, they are suitable for microwave integrated circuits, with the ability to design for a wide range of impedances [71],[72].

High temperature superconductor (HTS) thin-film technology has demonstrated a significant impact on the performance of passive microwave components [14], [73] ,[74]. HTS thin-films support demanding microwave applications by the virtue of their low resistance at high frequencies and extremely low signal dispersion, which are key aspects in microwave circuits[25], [75]. New advances in the technology of cost effective on-site cryogenic refrigeration systems, virtually transparent to the end user, make HTS-based devices highly stable in the temperature range of liquid nitrogen (77 °K or -196 °C) for practical long-term operation.

Superconducting planar resonators have been used to realize filters that provide very low insertion loss with extremely high quality factors, and very sharp frequency roll-off characteristics which is determined by the steepness of the filter skirts and out-of-band rejection [56],[76],[77]. This superior performance can only be realized using conventional filters that are about two orders of magnitude larger in volume and one order of magnitude larger in mass [14],[78],[79],[80]. Therefore, HTS thin-film technology offers reliable products with a lightweight and small form factor. They provide a high-performance platform suitable for microwave integrated circuits for the wide variety of applications such as the front-end receivers in wireless communication systems [81], [76], Josephson parametric conversion/amplification [22],[82],[49],[56], and superconducting terahertz and optoelectronics [83],[84].

In this chapter, we design, analyze, simulate and experimentally characterize an HTS CPW transmission line periodically loaded by dielectric gaps. We develop Computer Aided Design (CAD) equations to model the conventional superconducting CPW [25]. The small dielectric gap is modeled by three capacitors in π-configuration [85],[86], [87],[88]. For an infinitely long periodic structure (open), the method of analysis is based on the ABCD matrix representation of each unit cell in conjunction with the Floquet theorem. Dispersion analysis on the traveling wave and also input impedance calculation for the infinite periodic structure are carried out. In practice, when the periodic structure is finite (closed) and consists of a limited number of unit cells, conventional Floquet theorem does not apply. However, the problem can be solved in a closed form for an arbitrary N unit cells.

S-parameters or the ABCD matrix of the entire structure can be expressed in terms of the parameters associated with a single unit cell. The results obtained by this analysis (closed), is a good approximation for the infinite (open) periodic structure, as demonstrated in this paper. Several devices are fabricated with YBCO and characterized up to 50 GHz. Experimental data for S-parameter measurements are in a good agreement with the analytical results. Multiple band gap formation and rapid roll off filtering properties are highlighted. This device functions as a perfect DC blocker and can also be optimized as a multiple pass-band filter for applications such as the Josephson parametric amplifier, where pass-band filters in different frequency ranges are demanded. Moreover, due to the frequency selectivity in the reflection this device demonstrates, it can be employed as a Distributed Bragg Reflector (DBR) at the ends of a microwave resonator to propose a MASER system.

3.2 Structure

Fig. 3-1 shows a periodically loaded superconducting CPW with dielectric gaps. Each unit cell is comprised of the superconducting transmission line section and a dielectric gap. In this figure, the width of the center strip of the CPW is "s" or "a", the separation between the two semi-infinite ground planes is b, the distance between the outer edges of two ground plates is "c", and the spacing between the center strip and the ground plane which is referred as a slot width is shown by "w". The height of the dielectric spacer is h, and the thickness of the superconductor film is t. Also, the length of each unit cell and the width of the series gap is denoted by l and g, respectively. Indeed, there are various configurations for coplanar waveguides[72], and in this work we study the conventional CPW, where the ground plane is of semi-infinite extent on either side. Although the ground planes of actual CPWs cannot be infinite, if the ratio of c/b is around 3, the CPW with the finite ground plane is considered as a conventional CPW [71].

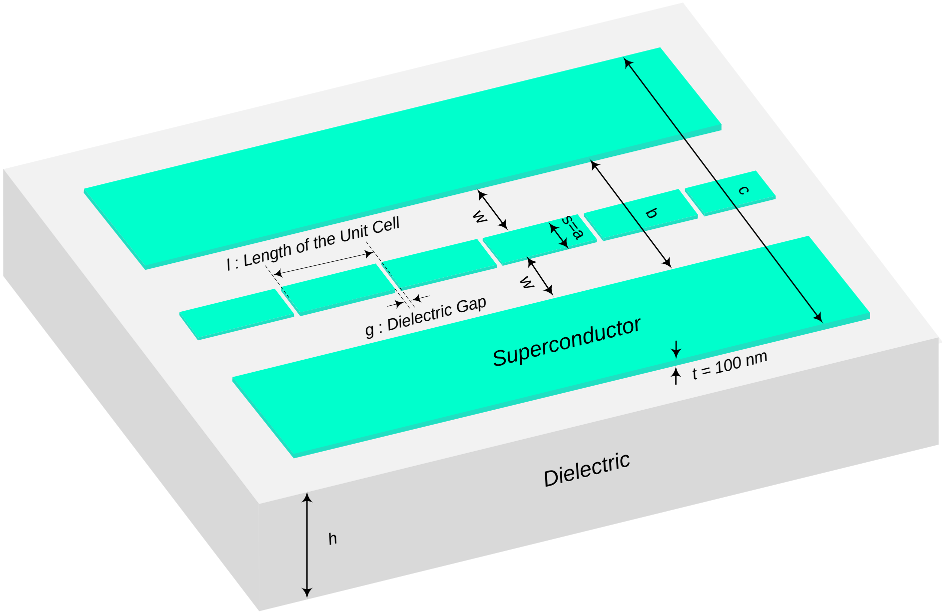

Fig. 3-1. A periodically loaded CPW by dielectric gap.

3.3 Simulation Model

3.3.1 Circuit Parameters of Superconducting CPW

The electromagnetic characteristics of any TEM transmission line such as the phase constant, attenuation constant and characteristic impedance can be determined in terms of the distributed circuit parameters associated with the transmission line [25]. Therefore, the circuit parameters play a significant role into the knowledge of wave propagation, dispersion, and distortion through a transmission line. For fast calculation of distributed circuit parameters it is necessary to develop a CAD tool. For a superconducting CPW transmission line, equations which yield the shunt capacitance and conductance per unit length are taken from [72], as they do not differ from the case when a normal conductor is replaced by superconductor materials [75]. For calculating the capacitance, it is required to use the complete elliptical integral of the first kind as demonstrated in [72]. Since the CPW transmission line is an inhomogeneous transmission line, the effective dielectric constant has to be defined with the consideration of the thickness of the superconducting plates as well as the dispersion behavior of the line, as explained in [85],[89]. The kinetic inductance per unit length for a superconducting CPW is given in [90] and [91]. By calculating the real and imaginary parts of the surface impedance associated with the superconductor plates, the series ohmic resistance per unit length of the line is found [25]. Full details of all equations and other related discussions can be found in [25].

3.3.2 Small Dielectric Gap in CPW

As seen in Fig. 3-2, the discontinuity created by the symmetric series gap can be modeled by a π-capacitive circuit when the gap is small enough compared to the wavelength. The gap on the center strip results in sharp edges at both sides of the discontinuity causing electrical charge accumulation at the corners. Thus, a series capacitor C_s and two shunt capacitors C_p are needed to capture these extra charges, as illustrated in the Fig. 3-2.

There are a number of verified CAD expressions in order to calculate the equivalent capacitors even for the general case of a non-symmetric gap [85],[86],[87], [88]. According to [87] a small coplanar series gap is a dual problem for the twin strip transmission line when they are connected by a shunt narrow strip. We use the relation in [87]to calculate the series coupling capacitance, and choose the closed-form formulation in [88] to determine the parallel capacitors in the π-network. Comparison with the full-wave analysis in [86] reveals that these equations are valid and reliable when the dielectric height is greater than b.

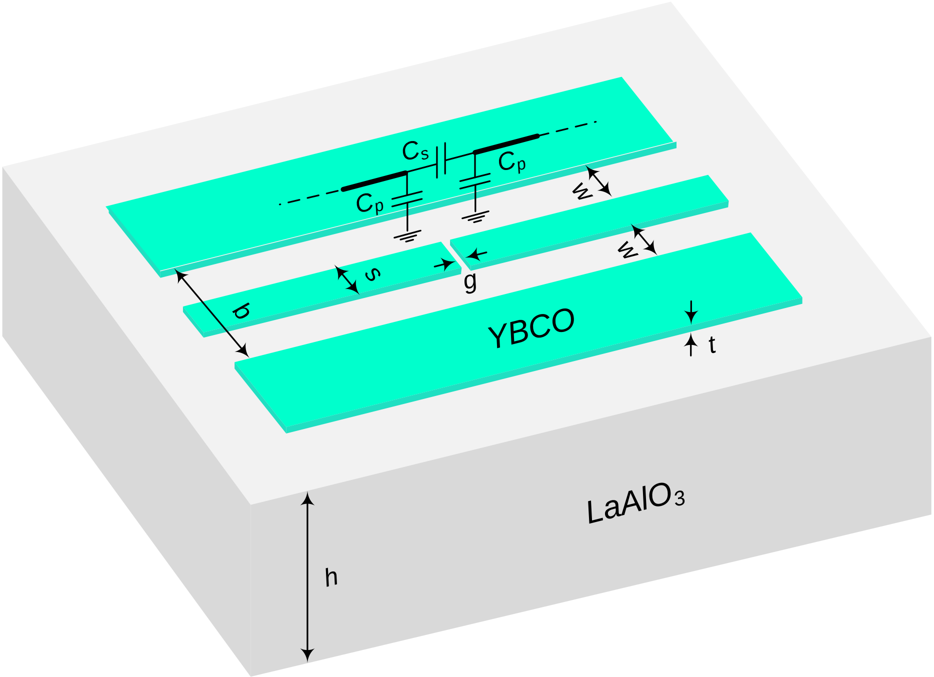

Fig. 3-2 Typical CPW gap and its equivalent π-network model.

3.4 Infinite Periodic Superconducting CPW with Dielectric Gap

3.4.1 Floquet Analysis of the Structure

The circuit representation of the unit cell of the structure is shown in Fig. 3-3. It consists of a cascade connection of two successive sections, a transmission line and the gap. The length of the dielectric gap is g, therefore the length of the transmission line will be

$l_s = l - g$. Considering the small length of the dielectric gap in comparison to the wavelength, this discontinuity can be characterized by an equivalent π-network at the end of the line, as pointed out in previous sections and depicted in Fig. 3-3. Microwave characteristics of the structure can be mathematically described by the ABCD matrix associated with an individual unit cell. This matrix is obtained by multiplying the two ABCD matrices of the constituent sections of the unit cell. The first accounts for the transmission line section and the second represents the π-network [16],[58]. The final ABCD parameters representing the unit cell is given by

$$A = \left(1 + \frac{C_p}{C_s}\right)\cosh(\gamma_s l_s) + j\omega\frac{C_p^2 + 2C_pC_s}{C_s}Z_{0s}\sinh(\gamma_s l_s) \tag{3.1}$$

$$B = \frac{\cosh(\gamma_s l_s)}{j\omega C_s} + Z_{0s}\left(1 + \frac{C_p}{C_s}\right)\sinh(\gamma_s l_s) \tag{3.2}$$

$$C = \left(1 + \frac{C_p}{C_s}\right)\frac{\sinh(\gamma_s l_s)}{Z_{0s}} + j\omega\frac{C_p^2 + 2C_pC_s}{C_s}\cosh(\gamma_s l_s) \tag{3.3}$$

$$D = \frac{\sinh(\gamma_s l_s)}{j\omega C_s Z_{0s}} + \left(1 + \frac{C_p}{C_s}\right)\cosh(\gamma_s l_s) \tag{3.4}$$

where γ_s and Z_{0s} are the complex propagation constant and characteristic impedance associated with the superconducting CPW, respectively. All circuit parameters in (3.1)-(3.4) are shown in Fig. 3-3. Parameter "g", which is the length of the gap, has been absorbed in C_s and C_p [87],[88]. It can be verified that the determinant of this matrix is equal to unity ($AD - BC = 1$), and also $A \neq D$ which shows the basic structure is reciprocal but not symmetric [16], as expected.

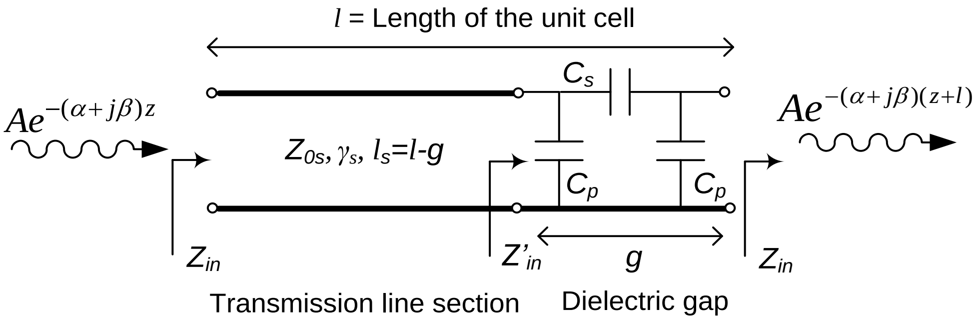

Fig. 3-3 A unit cell's equivalent transmission line model for the infinite periodic structure.

From a theoretical standpoint, the analysis of an open periodic structure, which is formed by the infinite repetition of the unit cell, can be dramatically simplified by applying the Floquet theorem [16], [58]. Applying this theorem, the closed-form dispersion relation for the propagation constant is found by

$$\gamma = \alpha + j\beta = \frac{1}{l}\cosh^{-1}\left\{\left(1+\frac{C_p}{C_s}\right)\cosh(\gamma_s l_s) + j\left[\frac{\left(C_p^2+2C_pC_s\right)\omega^2 Z_{0s}^2-1}{2\omega C_s Z_{0s}}\right]\sinh(\gamma_s l_s)\right\} \tag{3.5}$$

which includes necessary information for the wave propagation through the periodic structure under study. In equation (3.5) parameters α (NP/m), β (rad/m) and ω (rad/s) are attenuation constant, phase constant and angular frequency of the driven TEM electromagnetic wave, respectively. Other parameters in (3.5) have been already explained and illustrated in figures.

3.4.2 Impedance Calculation

Floquet analysis in the previous subsection yields essential information about the wave nature of the periodic structure. As seen, this study results in a dispersion analysis that has been expressed by a closed-form relation (3.5). However, TEM transmission lines can be represented by circuit theory. Also, the structure is ultimately to be connected to other peripheral microwave circuits. Therefore, another source of data such as impedance matching, wave reflection and transmission can be obtained by its input impedance. For the case of an infinitely long periodic structure, the input impedance seen from any interface of two subsequent unit cells is identical as illustrated in Fig. 3-3. This impedance is found by the following quadratic equation

$$CZ_{in}^2 + (D-A)Z_{in} - B = 0 \tag{3.6}$$

where A, B, C and D are ABCD parameters given by equations (3.1)-(3.4). This quadratic equation always has two solutions for Z_{in} with opposite signs in the real parts. Since no active element exists in this structure, the input impedance is the one with the positive real part.

3.5 Finite Periodic Superconducting CPW with Insulator Gap

3.5.1 Finite vs. infinite periodic structures

The number of unit cells in real periodic structures such as filters and metamaterials [92] is always finite, so an open infinite periodic structure is an ideal model which can never exist. However, if the number of unit cells is large enough, a closed finite periodic structure resembles the open infinite periodic structure. The beauty of the Floquet analysis of an infinite periodic structure is that the result of the overall system can be extracted only by considering one single unit cell [16]. Similar to its infinite counterpart, a finite periodic structure with arbitrary number of unit cells and any boundaries at the ends can be solved analytically by a closed-form expression in terms of the parameters of only one single unit cell, provided each unit cell can be represented mathematically by a unitary matrix [93],[69].

A typical periodic structure consisting of N number of unit sections with two boundaries at the ends is depicted in Fig. 3-4 with S-matrix representation. This structure can be regarded as a cavity resonator, and instead of having a continuous dispersion diagram, a set of discrete phase constants is expected [26]. These discrete points on the dispersion diagram are located at the resonant frequencies of the structure. The resonant frequencies can be found by the Transverse Resonance Method or by oscillation condition relation including reflection coefficients. Obviously, a finite periodic transmission line cannot support traveling waves; instead, due to the reflection at the ends, standing waves exist inside of the structure. Hence, the phase constant (β) can be thought of as a wavenumber for the standing waves in this structure. Although the concept of standing waves has been defined for homogenous media, those types of waves can be viewed as Floquet (or Bloch) standing waves. This kind of analysis has been already introduced for optical wave propagation in optical multilayered media [69], superconducting microstripline with metal grating [26], multiple quantum well structures [69], multi-layer stack of Josephson junctions [94] and comprehensive survey was reported in [93].

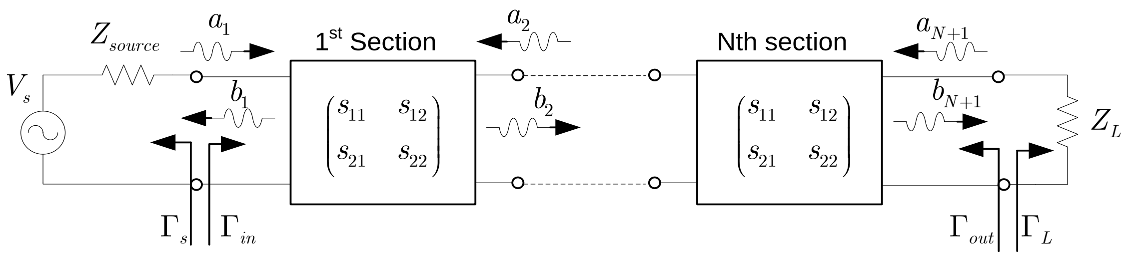

Fig. 3-4 General representation of a finite periodic structure in microwave using S-Matrix.

Basically, the rigorous way of analyzing a closed finite periodic structure in any microwave system is achieved by cascading multiple identical units with two boundaries at the two ends of the network. Similar to any finite electromagnetic structure, the well-known mathematical representation of the ABCD matrix, T-Matrix (Transfer-Matrix) or even S-Matrix (scattering matrix) should be employed. In the following, we use s-parameter analysis to study the microwave characteristics of the finite periodic structure.

3.5.2 Scattering parameter Analysis

As explained before, each unit cell is reciprocal, and as a result its ABCD matrix (or T-Matrix) is unitary. Therefore, the total ABCD matrix of the structure is the nth power of the individual matrix, and it can be expressed in terms of the ABCD matrix associated with the unit cell and periodicity of the system by using the Chebyshev identity [69]. After a little manipulation, the total scattering matrix of the cascading N unit cells can also be found in terms of the scattering parameters of each unit cell in a set of tidy closed-form equations as follows

$$s_{11}^{\text{tot}} = \frac{s_{11}U_{N-1}}{U_{N-1} - s_{21}U_{N-2}} \tag{3.7}$$

$$s_{12}^{\text{tot}} = \frac{s_{12}U_{N-1}^2 + s_{21}U_{N-2}^2 + (s_{11}s_{22} - s_{12}s_{21} - 1)U_{N-1}U_{N-2}}{U_{N-1} - s_{21}U_{N-2}} \tag{3.8}$$

$$s_{21}^{\text{tot}} = \frac{s_{21}}{U_{N-1} - s_{21}U_{N-2}} \tag{3.9}$$

$$s_{22}^{\text{tot}} = \frac{s_{22}U_{N-1}}{U_{N-1} - s_{21}U_{N-2}}. \tag{3.10}$$

As illustrated in Fig. 3-4, s_{11}, s_{12}, s_{21}, s_{22} and s_{11}^{tot}, s_{12}^{tot}, s_{21}^{tot}, s_{22}^{tot} in equations (3.7)-(3.10) are scattering parameters associated with each unit cell and the entire structure, respectively. Parameter U_N is a parameter defined by

$$U_N = \frac{\sinh[(N+1)\gamma l]}{\sinh(\gamma l)}. \tag{3.11}$$

In equation (3.11), l is the spatial period of the periodic CPW shown in Fig. 3-4 and γ is a Floquet propagation constant defined by

$$\gamma = \frac{1}{l}\cosh^{-1}\left(\frac{1 - s_{11}s_{22} + s_{12}s_{21}}{2s_{21}}\right) \tag{3.12}$$

Resonant frequencies can be obtained by applying boundary conditions which are shown in Fig. 3-4. This gives the following constraint equation

$$\Gamma_s\left[s_{11}^{tot} + \frac{s_{12}^{tot}\, s_{21}^{tot}\, \Gamma_L}{1 - s_{22}^{tot}\, \Gamma_L}\right] = 1. \tag{3.13}$$

Equation (3.13) depends only on the angular frequency ω, and its solution can be a general complex frequency at which the real part represents the resonant frequency and the imaginary part accounts for the loss of the system [26].

3.5.3 Impedance Calculation

The input impedance of a finite structure can be found by several techniques. When the total ABCD matrix or S-Matrix of the structure has been calculated, we can simply use

$$Z_{\text{in}} = \frac{(AU_{N-1} - U_{N-2})Z_L + BU_{N-1}}{CU_{N-1}Z_L + DU_{N-1} - U_{N-2}} \tag{3.14}$$

or the following equations in terms of scattering parameters

$$\Gamma_{in} = s_{11}^{\text{tot}} + \frac{s_{12}^{\text{tot}}\, s_{21}^{\text{tot}}\, \Gamma_{\text{L}}}{1 - s_{22}^{\text{tot}}\, \Gamma_{\text{L}}} \tag{3.15}$$

$$Z_{in} = Z_0\frac{1 + \Gamma_{in}}{1 - \Gamma_{in}}. \tag{3.16}$$

Another approach is an iterative method as illustrated in Fig. 3-5. We can start calculating the input impedance from the last unit cell at the right end of the structure and continue the calculation one after another to reach the first unit cell at the left of the structure.

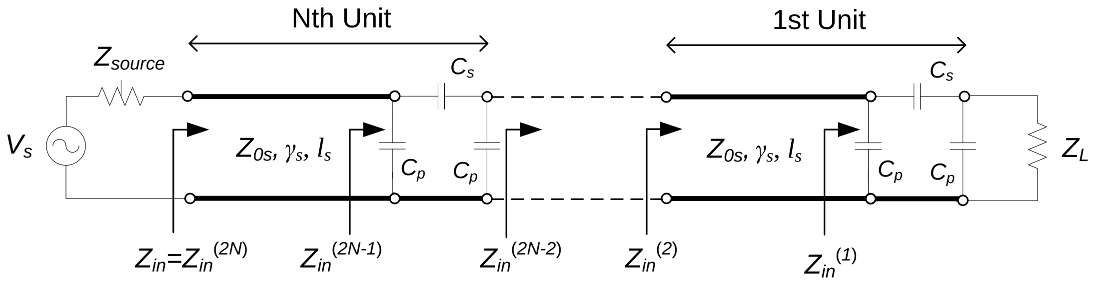

Fig. 3-5 The illustration of the way of calculation the input impedance of N connected unit cells.

3.6 Numerical Results

In this section, YBCO is selected as the HTS material for our simulations since it is one of the most extensively studied HTS, and its existing widespread use in commercial microwave applications. Moreover, firmly established thin film deposition and lithography processing are available for YBCO. The data for this HTS material is taken from the technical data sheet of THEVA [95]. We used the following parameters for YBCO: critical temperature $\mathrm{T_c} = 86$ °K, the penetration depth at zero temperature $\lambda_\mathrm{L}(0) = 120$ nm, and the DC conductivity of a normal channel $\sigma_0 = 10^6$ S/m. The thickness of the HTS film for the center and ground plates of the CPW transmission line is $t = 100$ nm. Liquid nitrogen is used to cool down the structure, so the temperature is held at $T = 77$ °K. The dielectric material is $LaAlO_3$ (Lanthanum aluminate) with the relative dielectric constant of $\epsilon_r = 23.6$ and loss tangent of $\tan\delta = 10^{-5}$at 77 °K. The height of the dielectric substrate is $h = 500$ μm.

To design a CPW with the characteristic impedance of $Z_0 = 50\ \Omega$, we fix the spacing between two ground planes at $b = s + 2w = 280$ μm. Based on the above information, we draw the characteristic impedance versus aspect ratio a/b of the CPW structure in Fig. 3-6at a frequency of 25 GHz. Circuit parameters, propagation constant, attenuation constant and phase velocity have been mentioned in the caption of Fig. 3-6. As a result, a 50 Ω CPW can be achieved with dimensions of $s = 60$ μm and $w = 107$ μm. This will be the platform used to periodically implement dielectric gaps, as illustrated in Fig. 3-7.

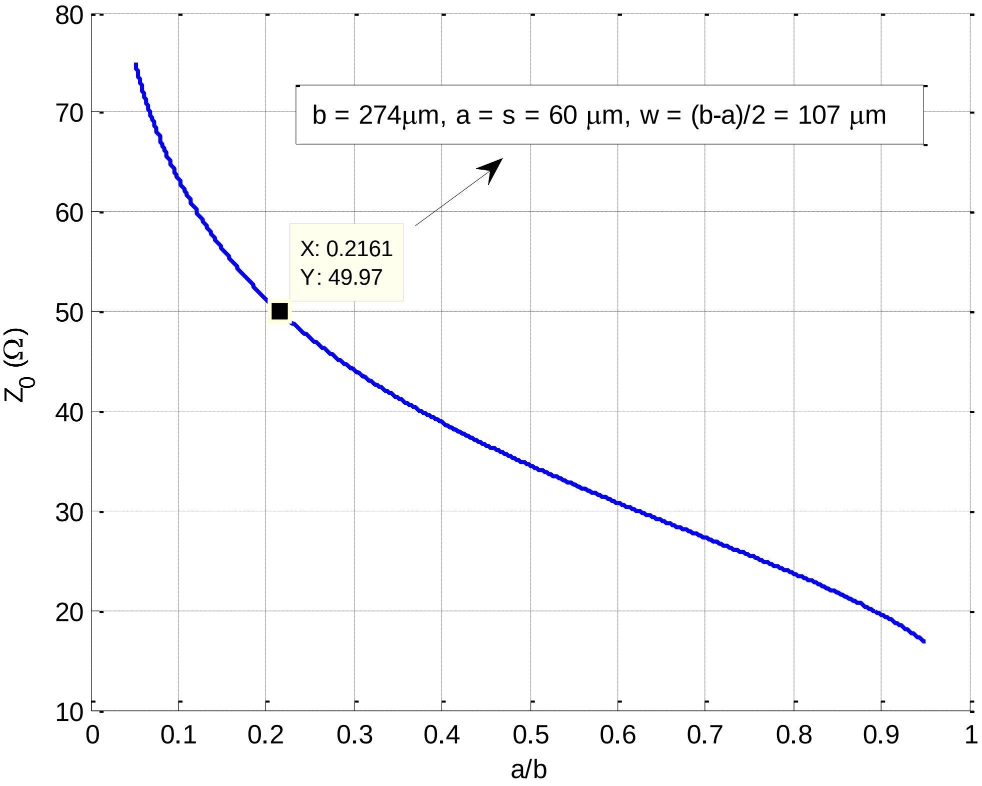

Fig. 3-6 Characteristic impedance of a CPW as a function of aspect ratio for the purpose of 50Ω CPW design at 25 GHz. Other parameters associated with this CPW are $L = 6.06 \times 10^{-7}$ H/m, $C = 2.33 \times 10^{-10}$ F/m, $R = 47\ \Omega/\mathrm{m}$, $\beta = 1860$ rad/m, $\alpha = 4.22$ dB/m, $V_p = 8.5 \times 10^{7}$ m/s.

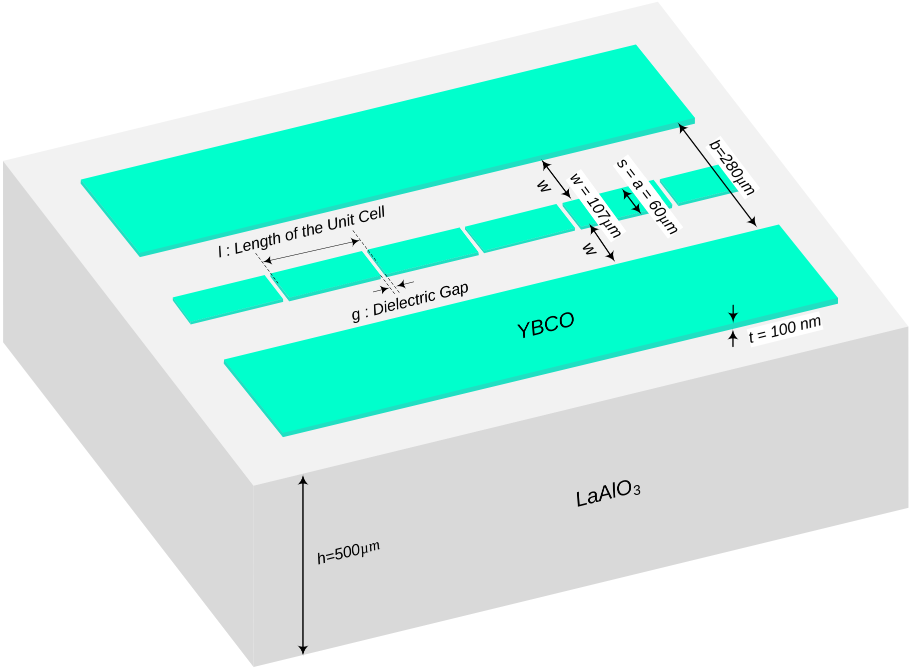

Fig. 3-7 Geometry and all dimensions for a 50Ω CPW with YBCO superconductor on the $LaAlO_3$ substrate.

Two periodically loaded structures with different period lengths will be examined, $l = 1500$ µm and $l = 1250$ µm. In Fig. 8, the first two Brillion zones of the dispersion diagram or variation of phase constant verses frequency (β v.s.ω) associated with the main mode of propagation (TEM mode) are depicted for the two different periods. These curves are drawn based on the results from equation (3.5). Due to the periodic dielectric gaps in the superconducting CPW, the existence of a band-gap is expected as seen in Fig. 3-8. It is obvious that at lower frequencies where the line is disconnected, the structure does not support wave propagation. However, at certain frequencies, wave propagation is allowed. According to Fig. 3-8, the wave suppression occurs at cut-off frequencies of 0 GHz, 29.26 GHz and 58.47 GHz for $l = 1500$ µm. This result can be verified by computing the Bragg frequency given by $f_n = nV_p/2l$, where f_n is the frequency corresponding to the band-edge of the gap, V_p is the phase velocity, l is the length of the unit cell (spatial period) and n is an integer number starting from 0. The phase velocity value can be obtained by dividing ω by β for the CPW transmission line as stated in the caption of Fig. 3-6. Substituting this in $f_n = nV_p/2l$ for the case of $l = 1500$ µm, results in the sequence of Bragg frequencies of 0 GHz, 28.33 GHz and 56.66 GHz, which are close to marked points in Fig. 3-8. The slight deviation in the cut-off frequencies calculated using both methods is due to the dielectric gaps in the CPW. The phase velocity is not a straight line in the pass-band as seen in the dispersion diagram of Fig. 3-8, therefore assuming a constant value is an approximation. This figure also shows that by increasing the width of series gap, the bandwidth associated with the pass-band decreases. Therefore, to have a wider frequency range in the pass-band, the series gap must be made smaller. As a simple justification for this, the gap can be viewed between two limits. One is the complete separation between two parts of the center strip of the CPW such that no frequency component can be passed. The opposite limit is the complete connection such that all frequency components are allowed to pass. By going from the former to the latter limit, the gap width shrinks and the bandwidth of the pass-band is enlarged.

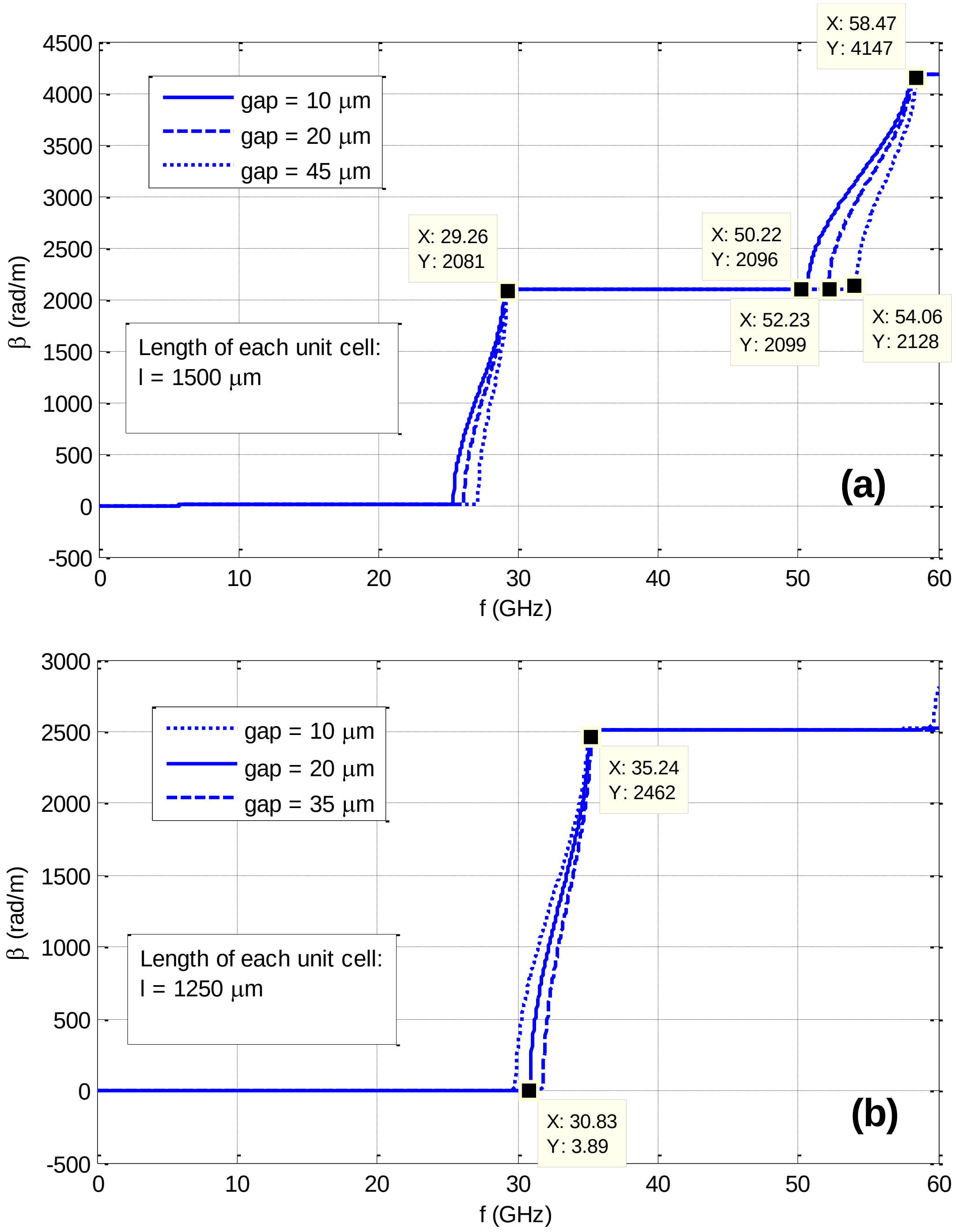

Fig. 3-8 Band diagram of an infinite periodic CPW in Fig. 6. By changing the series gap width, pass-band width can be controlled. Penetration depth is 120nm. (a) period is 1500μm, (b) period is 1250μm,

Using equations (3.5) and (3.6), the attenuation constant (distortion analysis), input reflection coefficient and input impedance (resonance study) of an infinite periodic CPW for varying gap widths and period of $l = 1500$ μm are shown in Fig. 3-9. Comparison between the curves in this figure reveals that the stop-band in the phase constant occurs exactly where the attenuation constant dramatically increases due to the constitutive reflection at Bragg frequencies or where the input impedance rapidly decreases at resonant frequencies. This figure shows that within the bandgap, there is a total reflection and within the pass-band the TEM wave is partially transmitted. Interesting point is that all concepts of band-edge in the phase constant diagram, Bragg frequencies in the attenuation constant or reflection coefficient curve, and resonant frequencies in the input impedance profile, coincide with the same frequency which is referred to as a cut-off frequency.

Although the CPW platform is designed to be used in a $50\,\Omega$ system, numerical calculations in Fig. 3-9 (c) shows that by grating the CPW with dielectric gaps the impedance seen at the beginning of the structure is dramatically changed from $50\,\Omega$. The input impedance is noticeably greater than $50\,\Omega$ creating a mismatching problem when driving this structure. The profile of the input impedance of the infinite periodic structure is depicted in Fig. 3-10, for all possible aspect ratios of a/b when $b = 274\text{nm}$. This figure demonstrates that for lower aspect ratios the input impedance is very large, in addition, the width of the pass-band is narrow. However, for higher aspect ratios, the input impedance decreases closer to $50\,\Omega$, improving the mismatching issue and providing a wider pass-band. Two pass-band channels are clearly seen in Fig. 3-10. As for our case with the aspect ratio of $a/b = 0.21$, based on Fig. 3-9 and Fig. 3-10 we encounter a high mismatching issue with a $50\,\Omega$ system which we address in the s-parameter results in following paragraphs.

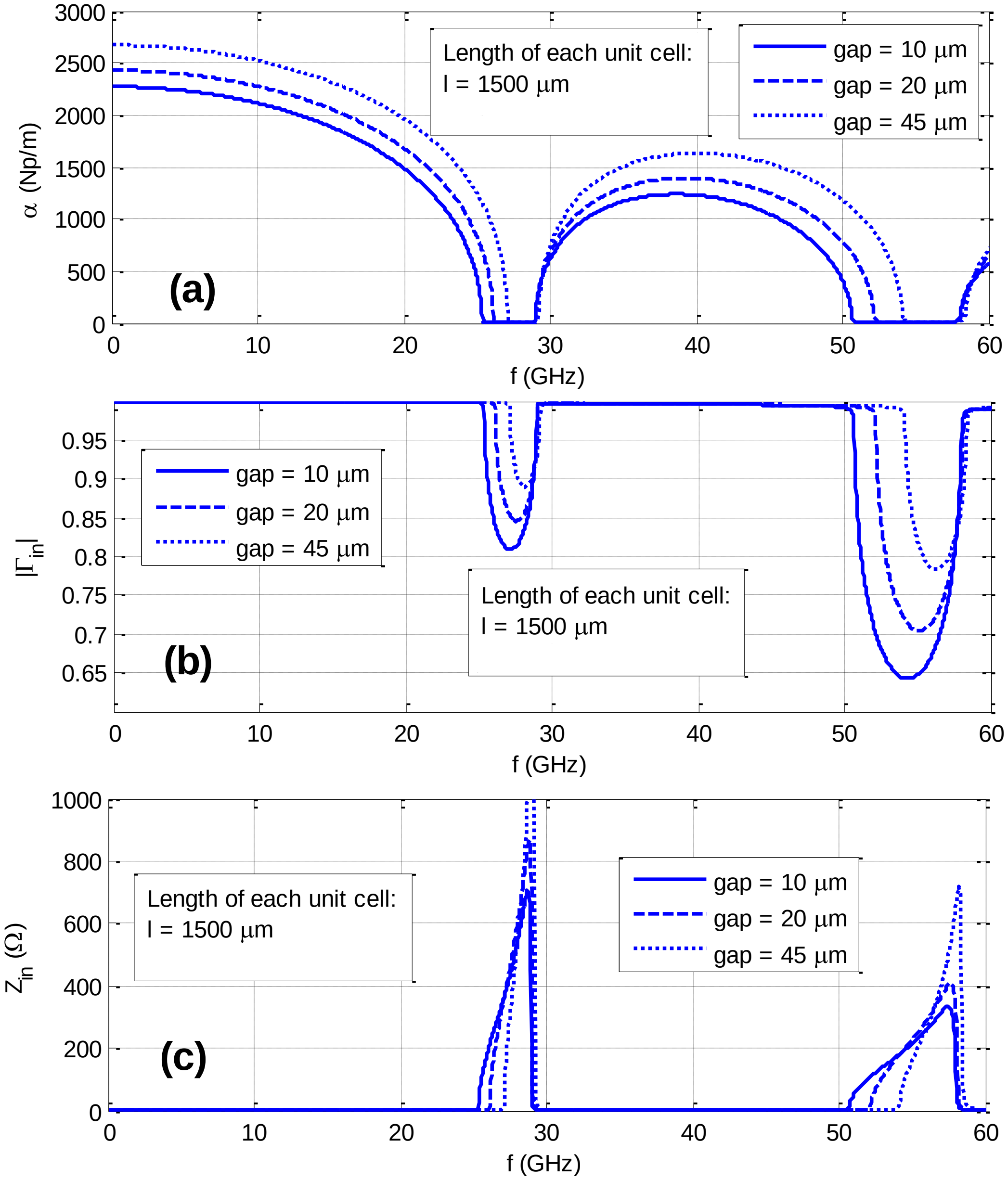

Fig. 3-9 (a) Attenuation constant, (b) Reflection coefficient and (c) Input impedance of an infinite periodic superconducting CPW.

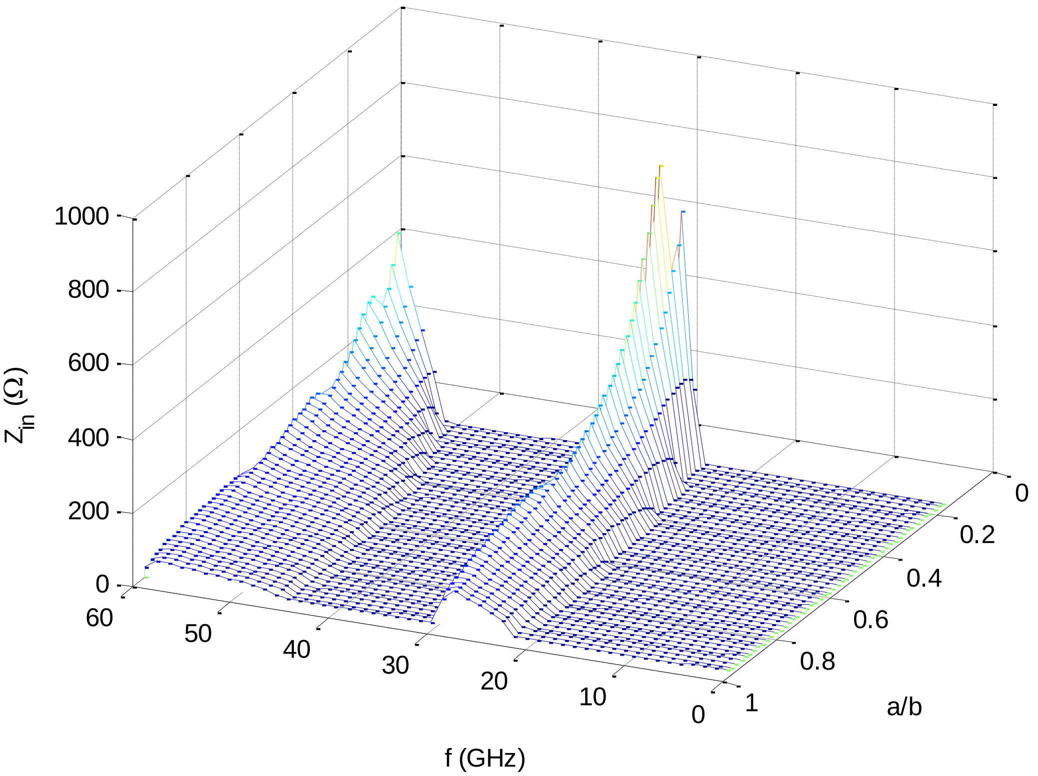

Fig. 3-10 Input impedance of the infinite periodic superconducting CPW when b=274nm, l=1500nm and λ_L=120nm.

Now we consider the finite periodic CPW with 7 or 8 unit cells. Fig. 3-11 shows the forward transmission coefficient or s_{21} in terms of dB for different geometries. As mentioned earlier, due to the large input impedance for an aspect ratio of $a/b = 0.21$, we encounter a mismatching condition with the reference impedance of the system set at 50 Ω. By selecting an aspect ratio of 0.9 as illustrated in Fig. 3-10, we can provide a better match to a 50 Ω system. The resulting S-parameters for a periodically loaded CPW with an aspect ratio of 0.9 is shown in Fig. 3-11. The insertion loss is improved to under 1dB, and the ripples in the pass-band are abated with an increase in the number of unit cells.

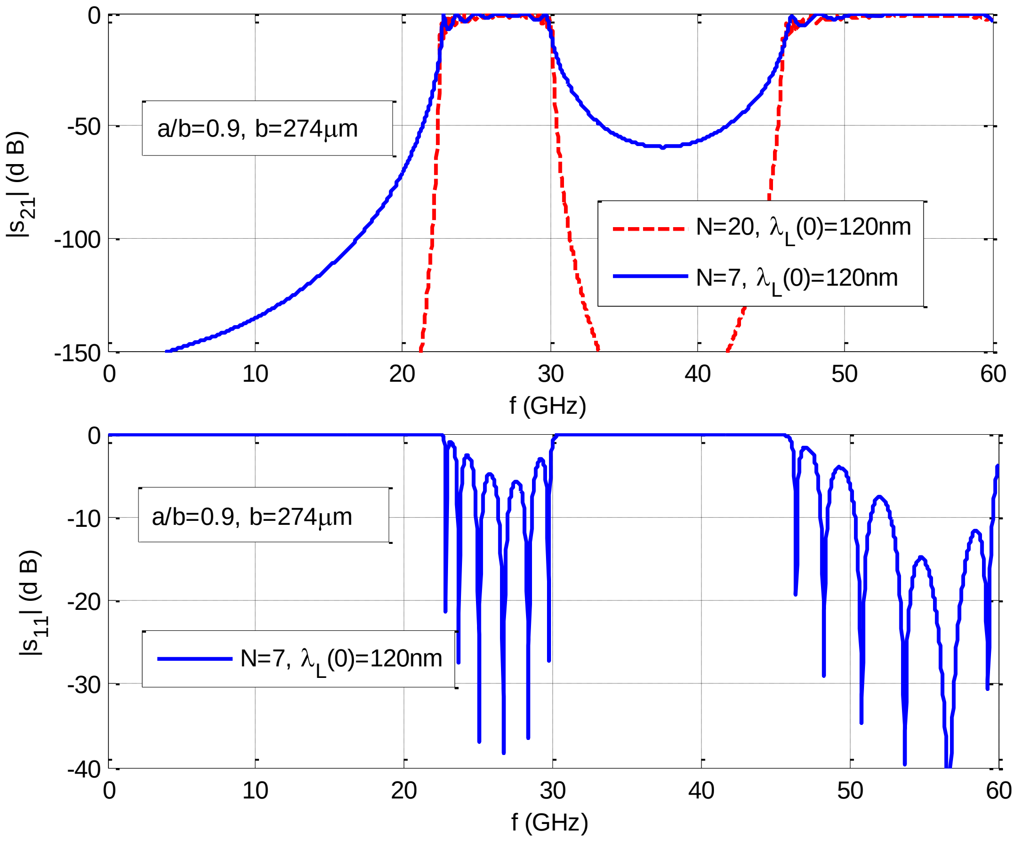

Fig. 3-11 S_{21} and S_{11} for the finite periodic CPW with aspect ratio a/b of 0.9

This mismatch to the $50\,\Omega$ system manifests itself as a greater insertion loss in the pass-band regime of s_{21}. Fig. 3-12 illustrates this issue by plotting s_{21} with a reference impedance of $Z_{\text{ref}} = 50\,\Omega$ and $Z_{\text{ref}} = 200\,\Omega$. By increasing the reference impedance the insertion loss is greatly improved and approaches the zero axis.

Comparison between the results in Fig. 3-8, Fig. 3-9or Fig. 3-12 reveals that the pass- and stop-bands fall exactly on the same interval on the frequency axes, regardless of the analysis performed based on the dispersion diagram, reflection coefficient study, attenuation constant drawing, input impedance behavior or s-parameter analysis. Furthermore, Fig. 3-12 (a) shows that by increasing the number of unit cells, the ripples in pass-band will be modified. Therefore, having a larger number of unit cells is a good implementation for an infinite periodic structure. Moreover, by increasing the penetration depth of the superconductor from $\lambda_L(0) = 120$ nm to $\lambda_L(0) = 240$ nm, a leftward shift in pass-band occurs which we address this issue in experimental section.

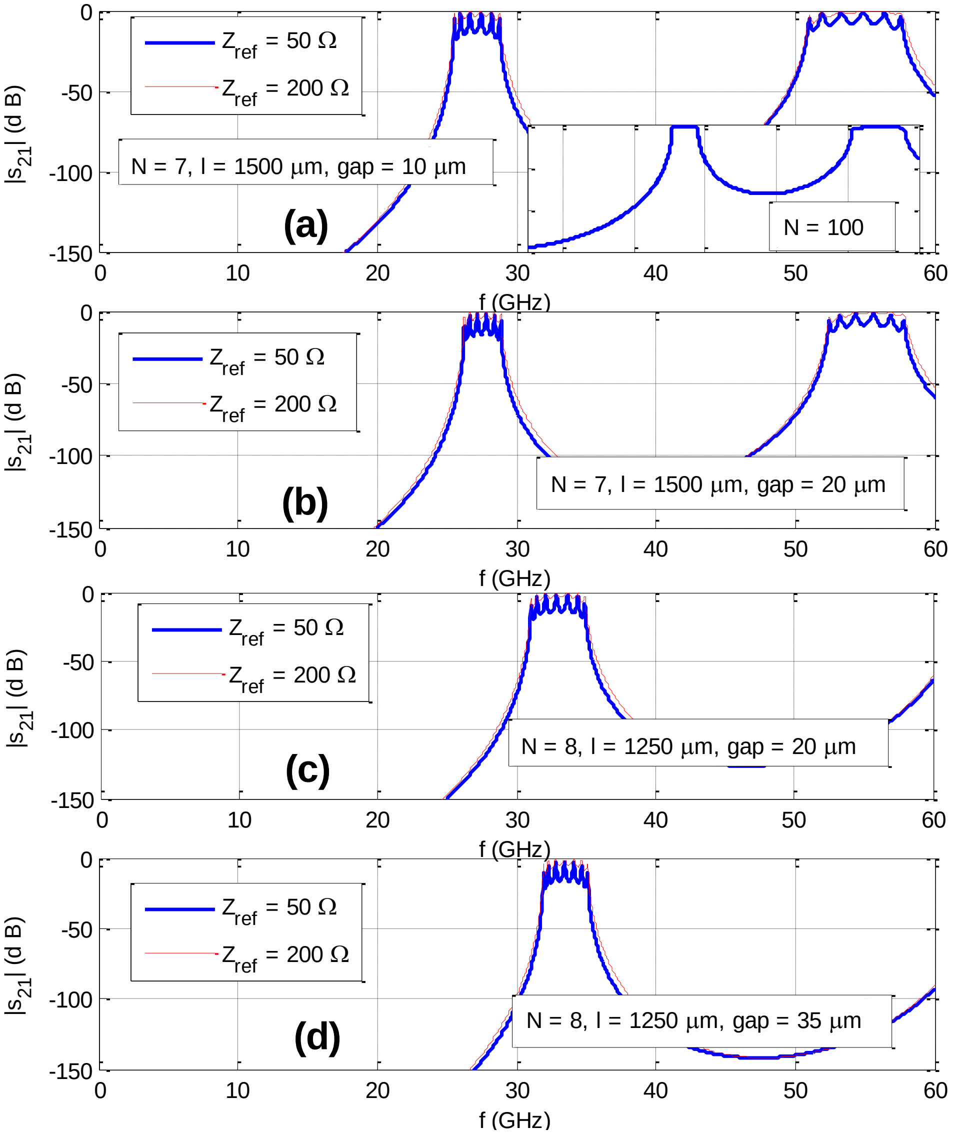

Fig. 3-12 The amplitude of S_{21} for the finite periodic CPW exhibited in Fig. 3.7 with λ_L=120nm and with the load impedance of Z_L=50Ω, but different reference impedance. (a) l=1500nm, gap= 10μm (b) l=1500nm, gap= 20μm (c) l=1500nm, gap= 20μm (d) l=1500nm, gap= 35μm.

3.7 Fabrication

100 nm thick YBCO films have been deposited on (001) LAO substrates by reactive thermal co-evaporation at a temperature of 680°C at THEVA [95]. Details of the deposition process have been described elsewhere [96]. The composition of the film has been optimized to get very smooth films with good superconducting properties. Surface roughness is less than 5nm as measured by AFM (Atomic Force Microscopy). Transition

temperature and critical current density is 87 K and 4 MA/cm^2, respectively. Fig. 3-13 shows the resistance vs. temperature curve for this film. After cool-down in oxygen atmosphere a 200nm gold layer was deposited in situ to serve as contacts.

The YBCO/Au films on LAO substrates were patterned using a resist mask and Ar ion milling. To cool the films during milling, the substrates were clamped to an aluminum puck filled with a salt that undergoes a solid-to-liquid phase change at 38°C. The salt keeps the temperature of the puck at the melting temperature during the milling process. To improve thermal contact with the chuck, the substrates are greased to the chuck using a small amount of thermal grease. After milling through the YBCO/Au film stack, the resist mask is stripped, and a new resist mask is prepared to pattern the top Au layer. The exposed Au is etched using a KI solution. After etching, the Au and resist mask is stripped. Fig. 3-14 shows the four devices to be measured. Two devices with a period $l = 1500$ µm, one with a gap width of 10 µm and the other with 20 µm. Another two with a period of $l = 1250$ µm, one with a gap width of 20 µm and the other with 35 µm

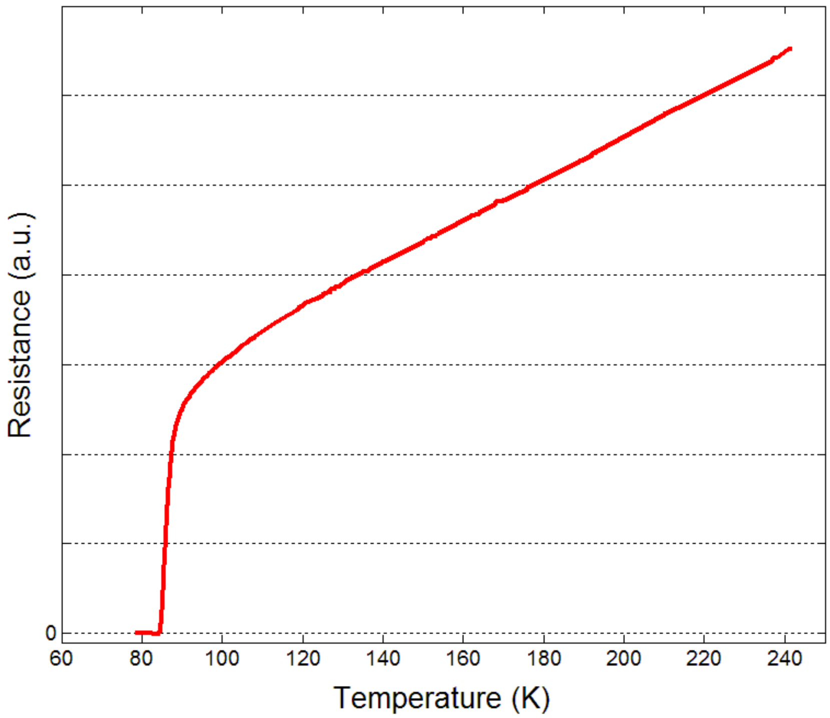

Fig. 3-13 Resistance vs. temperature for 100nm YBCO thin film

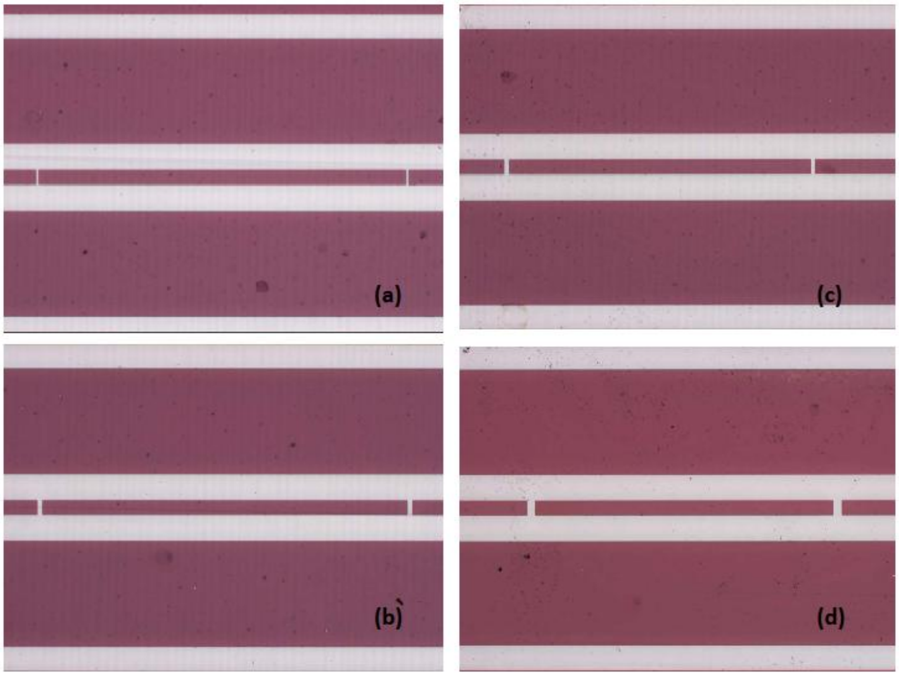

Fig. 3-14 Device images of finite periodic CPWs with (a) period of $l = 1500$ µm and gap 10 µm, (b) period of $l = 1500$ µm and gap 20 µm, (c) period of $l = 1250$ µm and gap 20 µm, and (d) period of $l = 1250$ µm and gap 35 µm.

3.8 Experimental Setup and Measurement

The microwave devices are measured in a vacuum cryogenic probe station as seen Fig. 3-15. It is designed to be used with micro-manipulated coplanar waveguide microwave probes with the frequency capability of 50GHz. The coplanar probes provide a reliable and accurate measurement system for on-wafer characterization of microwave devices, avoiding the need for device packaging or wire bonding. Appropriate considerations should be taken into account when calibrating the network analyzer for on wafer microwave measurements at cryogenic temperatures. The typical Short-Open-Load-Through or SOLT calibration method works well at room temperature, however at cryogenic temperatures the value of the matched load, which consists of a pair of precision 100 ohm thin film resistors, will drift due to its temperature coefficient. A Through-Reflect-Line or TRL calibration is more appropriate at cryogenic temperature, since it does not require the measurement of a matched load. It utilizes the measurements taken from standards based on geometry such as transmission lines of varying lengths. However, due to line dispersion, this calibration method limits the accuracy at the lower frequency range. By using a modified calibration substrate from GGB Industries, namely the CS-5 substrate, we have trimmed the precision loads such that they are exactly 50 ohm at 77K. This provides a more accurate platform to calibrate the network analyzer for cryogenic microwave measurements.

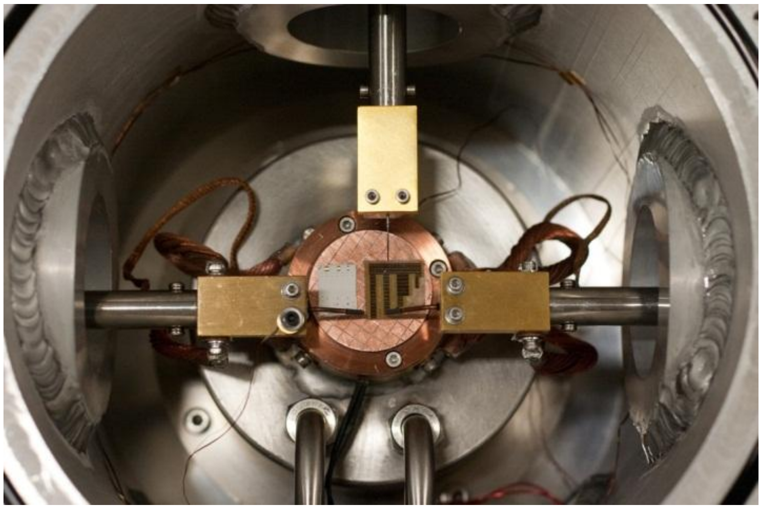

Fig. 3-15 Microwave cryogenic probe station used to measure the YBCO samples.

The s-parameters of the CPW transmission line with dimensions illustrated in Fig. 3-6 are measured using the setup shown above and equation (17) is used to extract the attenuation constant. Fig. 3-16 shows an overlay of the experimental results with the theoretical values. It is shown that increasing the λ_L from 120nm to 240nm in the theoretical simulations provides a better match to the experimental results.

$$\alpha = \frac{-\ln(|s_{11}|^2 + |s_{21}|^2)}{2L} \qquad (3.17)$$

Fig. 3-17 and Fig. 3-18 shows the overlay results of S_{21} and S_{11} of all four devices introduced in Fig. 3-14. We notice a left shift in the passband of the simulated results by adjusting the λ_L from 120nm to 240nm, as seen in Fig. 3-17. This adjustment improves the overlap of the pass-band between the measured and simulated results to approximately 80%. The insertion loss in the pass-band of these devices is roughly 8-10dB. As stated before, this loss is due to the mismatching issue addressed in section 3.6. By selecting an aspect ratio of 0.9 as illustrated in Fig. 3-10, and Fig. 3-11 we can provide a better match to a 50 Ω system.

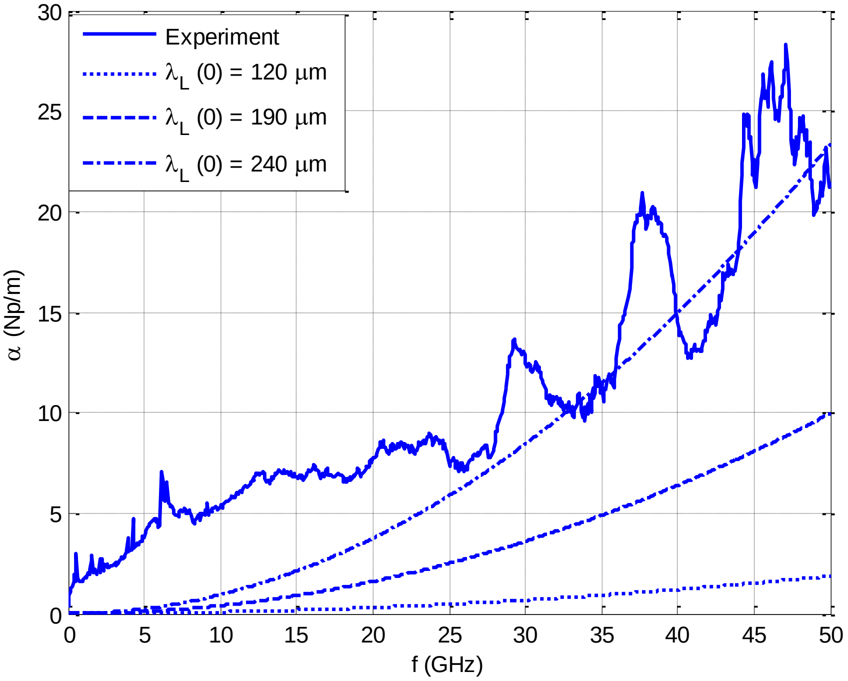

Fig. 3-16 Experimental and theoretical attenuation constant for the YBCO CPW.

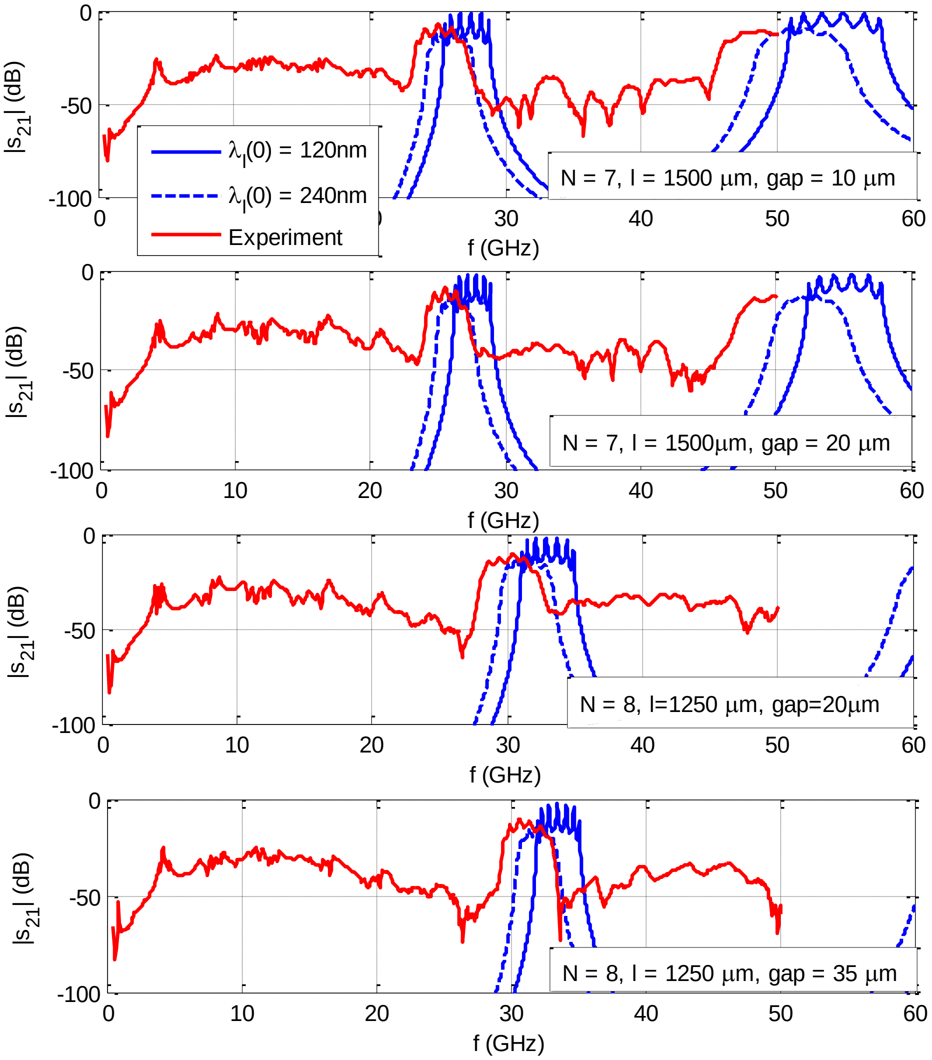

Fig. 3-17 Overlays of S_{21} for the finite periodic CPW with varying λ_L=120nm and 240nm with experimental results.

.

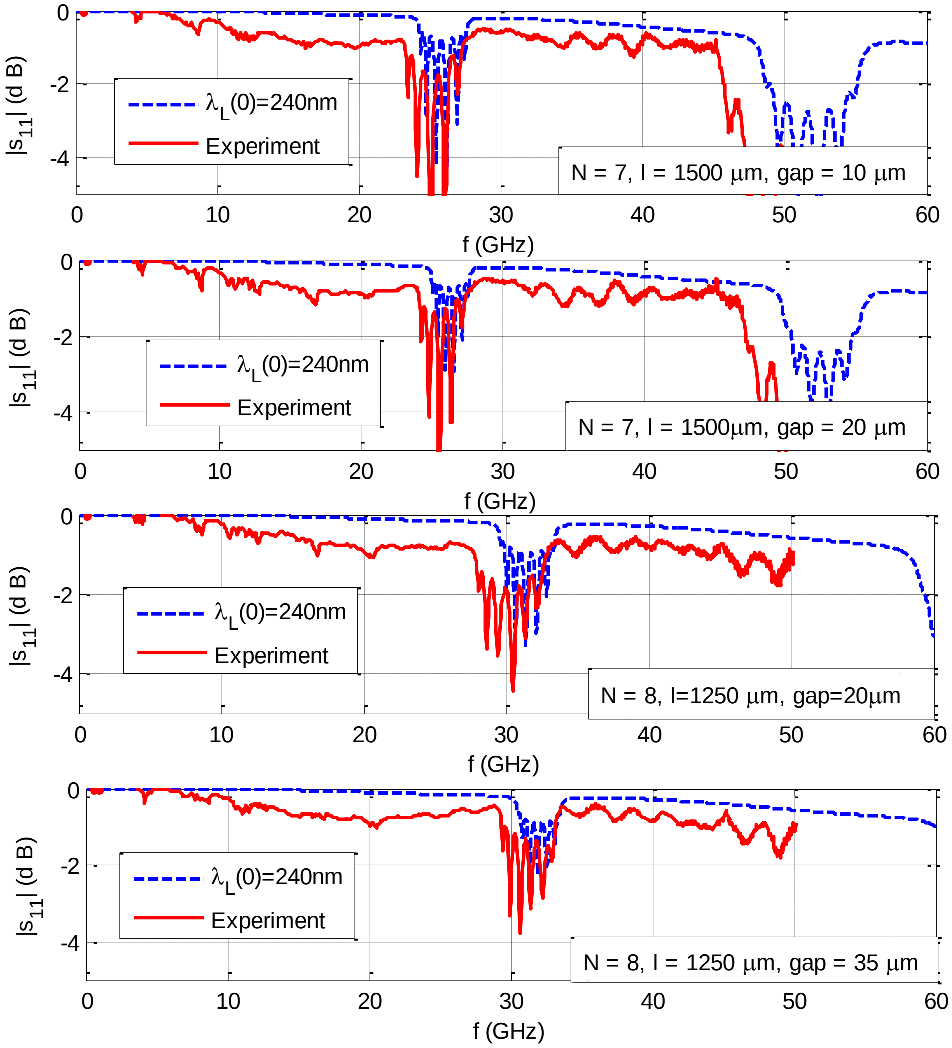

Fig. 3-18 Overlays of S_{11} for the finite periodic CPW with varying λ_L=120nm and 240nm with experimental results.

3.9 Conclusion

We design, simulate, fabricate and charcterized a periodic superconducting CPW based on the transmission line model. Infinite and finite periodic superconducting CPW dielectric gap grating is investigated. Each unit cell is modeled by a simple 2-by-2 matrix. For the case of infinite periodic CPW the Floquet theorem is invoked, and both dispersion diagram and input impedance are obtained. However, for the case of finite periodic CPW, two arbitrary boundary conditions have applied and S-parameters are calculated. The influence of mismaching between the input impedance and refrence impedance is highlighted. All results obtained by dispersion, impedance and S-parameter analysis are completely matched to each other. The beginning of the bandgap occures exactly at Bragg’s frequenies. The finite case goes to the case of infinity, when there is enough number of unit cells. The periodic CPW with dielectric gap demonestrates the filter ptoperty that canbe used to reject low frequenct signals, have multiple band-passes and produce selective reflections in many applications.

Chapter 4

Dispersion Engineering for Parametric Interaction in DJTL Structures

4.1 Introduction

Dispersion is one of the aspects of materials and waveguides which might cause either undesirable or desirable effects on the wave propagation. Separation of the white light into a color spectrum, wave chirping, temporal spreading and shape deformation of the wave pulse are most common consequences of the dispersion that make it a limiting factor in optical imaging and telecommunication applications.

On the other hand, due to its crucial influence on the wave propagation, there are other applications that dispersion is cleverly managed to achieve desired responses. The ability to design a medium with a specific dispersion suggests that one may custom-tailor the wave properties to allow the full control of wave propagation to any requirement. This is because of the strong role that material properties and geometrical parameters of the structured media play on the dispersion relation. The maneuvering of dispersive properties by artificially fabricated structures, which is referred to as dispersion engineering, is similar to the semiconductor technology in which semiconductor materials provide an excellent platform in order to control electrons mobility. They realize highly efficient, compact, easy-to-fabricate, and easy-to integrate microwave and optical devices.

Recent examples of engineered materials include photonic band gap crystals, double negative materials, magnetic metamaterials, electromagnetic band gap structured materials, frequency selective surfaces and complex surfaces such as high-impedance ground plate. Another example, which we refer to Chapter 6, is the traveling-wave parametric amplifier [97]. The case that we studied in this research is a set of three electromagnetic waves at frequencies ω_1 (signal), ω_2 (pump) and ω_3 (idler) with corresponding phase constants β_1, β_2 and β_3 that propagate through a nonlinear waveguide. The aim is to amplify the signal wave with the aid of interaction with the pump and idler waves such that energy transfers to the signal from pump and idler. Firstly, nonlinear interaction between these waves generates unwanted higher order harmonics which must be prevented from propagation to increase the efficiency of propagation and enhance the gain. Therefore, transmission lines with a linear dispersion equation is not suitable for the purpose of parametric amplification because this supports all linear combinations of signal, pump and idler waves. Nonetheless, dispersion engineering enable us to design a proper waveguide to resolve this issue. Secondly, depending on the type of nonlinearity associated with the waveguide specialized for the parametric interaction, there is a resonant condition between their frequencies as well as their phase constants which are together referred to as the phase-matching conditions. Phase-matching condition, in their perfect form, implies that three points on the dispersion curve must satisfy two phase-matching equations simultaneously. Unfortunately, these equations might not have a solution in general. Nonetheless, by designing an appropriate waveguide to harness the dispersion, the phase-matching condition can be fulfilled.

In this chapter we introduce the series-connected DJTL as the simplest and the most natural way to incorporate JJs in a typical superconducting transmission line to make a nonlinear waveguide. In section 2, assuming long-wave approximation, nonlinear wave equations are derived to display the nonlinear wave propagation through the structure. However, when the amplitude of driving signals is small enough such that the current flowing into the junctions is much less than the critical current, DJTL can be regarded as a linear waveguide and dispersion characteristics of the structure can be used to extract propagation characteristics and features. Also, by using a graphical technique, we verified that this structure is not suitable to achieve non-degenerate parametric interaction. In section 3, we introduced an additional open stub to each unit cell to support non-degenerate phase-matching equations based on four-photon interaction. Cut-off condition and input impedance is derived in closed-form expression by using Floquet theorem. Although, we are performing forward engineering, we explore Tichmarsh's theorem to assess the DJTL from analycity, causality and Karmers-Kronig relation. It is demonstrated that our model is achievable and realistic. In section 4, we conduct a design example by tuning the dispersion diagram by realistic Josephson junction and superconducting transmission line parameters.

4.2 Series-Connected DJTL

The structure proposed for the study of parametric interaction in this section is referred to as series-connected discrete Josephson transmission line (DJTL). To realize this device, a superconducting TL, either microstrip line or CPW, is periodically loaded by series of unbiased JJ blocks, as sketched in Fig. 4-1. and Fig. 4-2. This block can be a single junction, N-fold stacked Josephson junctions, array of trilayer junctions or any other combination of junctions with circuit elements such as capacitors and even resistors so that we attain the desired response expected from the structure. The circuit model of the block which is used in our simulation part is depicted in Fig. 4-1. (b). It consists of an array of N identical unbiased junction in parallel to a fit capacitor C_{fit} and also fit shunt resistance R_{fit}. These extra fit elements are used to control the resistance, capacitance and plasma frequency associated with the junction.

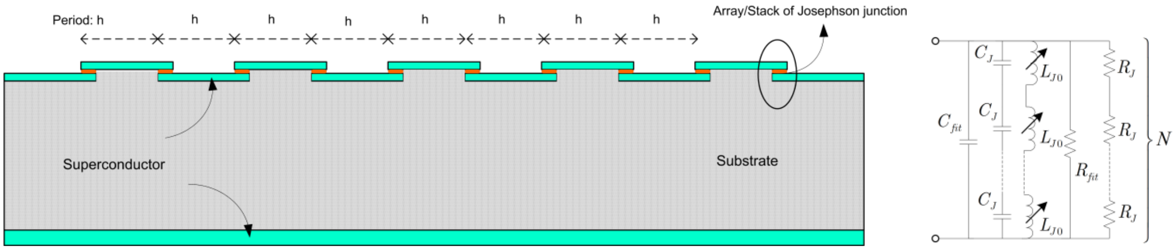

Fig. 4-1 (a) Series-connected DJTL on microstrip line (b) JJ block with RCSJ model of each junction can be presented by a single effective junction.

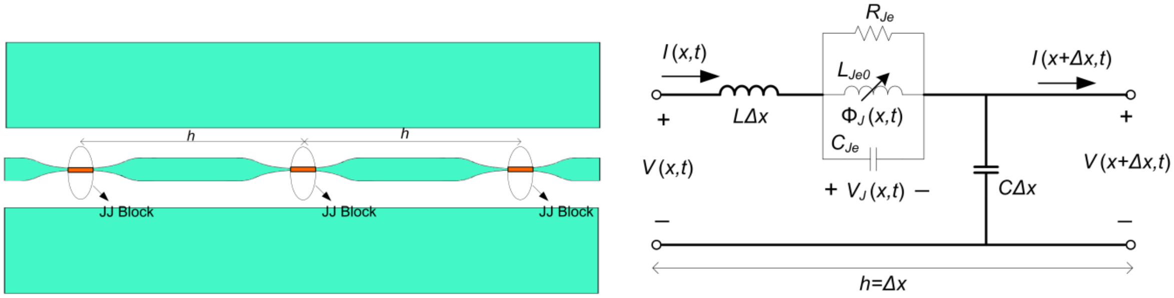

Fig. 4-2 (a) Series-connected DJTL on CPW (b) Unit cell of periodically loaded series-connected DJTL.

The critical currents, capacitances, normal-state junction resistances, and self-inductances are taken to be identical for all junctions. Moreover, like an array of Josephson junction, this Josephson junction block can be represented by a single effective junction.

4.2.1 Transmission Line Model and Wave Equation

The transmission line model of the unit cell of this structure with all variables and circuit parameters are illustrated in Fig 4.2.(b). If the period of the structure ($\Delta x = h$) is much less than the wavelength (λ) of the microwave signal, i.e $\Delta x \leq \lambda/20$, we can exploit the long wave approximation ($\Delta x/\lambda \to 0$) to form a set of differential equations to elucidate the nonlinear microwave propagation through this structure. Therefore, in a low frequency limit, this structure can be described by a system of partial differential equations in the form of

$$\frac{\partial V}{\partial t} + \frac{1}{C}\frac{\partial I}{\partial x} = 0 \tag{4.1}$$

$$\frac{\partial I}{\partial t} + \frac{1}{L}\frac{\partial V}{\partial x} = \frac{-V_J}{Lh} \tag{4.2}$$

$$\frac{\partial V_J}{\partial t} = \frac{1}{C_{Je}} I - \frac{1}{R_{Je} C_{Je}} V_J - \frac{I_c}{C_{Je}} \sin\left(2\pi \frac{\varphi_J}{\Phi_0}\right) \tag{4.3}$$

$$\frac{\partial \varphi_J}{\partial t} = V_J. \tag{4.4}$$

where $I(x,t)$ is the current passing through the series inductor associated with the TL; $V(x,t)$ is the voltage dropped on the shunt capacitor of the line; $V_J(x,t)$ is the voltage dropped on the Josephson junction; $\varphi_J(x,t)$ is the flux related to the nonlinear inductor of the junction and the constant $\Phi_0 = 2.0679 \times 10^{-15}\ \mathrm{T.m^2}$ is the flux quanta . Note that R_{Je} and C_{Je} are lumped elements, but L and C are distributed elements. This is the reason of appearance $h = \Delta x$ in equation (4.2). Also, effective parameters associated with an N-array of JJ are found by $L_{Je0} = NL_{J0}$, $C_{Je} = C_{fit} + C_J/N$ and $R_{Je} = NR_J R_{fit}/(NR_J + R_{fit})$. These equations are derived in a similar manner which is usually used to form state equations in circuit theory.

Equations (4.1) -(4.4) can be reduced to a single equation by eliminating all variables except flux associated with the JJ. Then, by expanding the nonlinear sinusoidal terms in

Taylor series, truncating this expansion and scaling the flux by a dimensionless parameter ϵ as $\varphi_J = \sqrt{\epsilon}\varphi$, all result in

$$\begin{aligned} C\left(1+\frac{Lh}{L_J}\right)\varphi_{tt} - \frac{h}{L_J}\varphi_{xx} - C_J h\varphi_{ttxx} + LCC_J h\varphi_{tttt} \\ + \frac{hLC}{R_J}\varphi_{ttt} - \frac{h}{R_J}\varphi_{txx} = \epsilon J(\varphi) \end{aligned} \tag{4.5}$$

where $J(\varphi)$ include all nonlinear terms and it is given by

$$\begin{aligned} J(\varphi) = \frac{2\pi^2 LCh}{L_J \Phi_0^2}\left(\varphi_{tt} - \frac{1}{LC}\varphi_{xx}\right)\varphi^2 \\ + \frac{4\pi^2 LCh}{L_J \Phi_0^2}\left[(\varphi_t)^2 - \frac{1}{LC}(\varphi_x)^2\right]\varphi. \end{aligned} \tag{4.6}$$

It is evident that by changing $t \to -t$ and $x \to -x$, all terms remain unchanged except dissipation terms which is simply consistent with time reversal property. We will explain more about this important property in the realizibilty section.

It should be noted that the basic model of JJ can be employed by setting $C_J = 0$ and $R_J = \infty$. In this case, the nonlinear expression (4.6) will not change and equation (4.5) reduces to

$$C\left(1+\frac{Lh}{L_J}\right)\varphi_{tt} - \frac{h}{L_J}\varphi_{xx} = \epsilon J(\varphi). \tag{4.7}$$

4.2.2 Dispersion Relation

Equation (4.5) is a nonlinear dispersive wave equation which includes dissipation terms. However, supposing $\varphi_J \ll \Phi_0$, the parameter ϵ becomes very small such that φ becomes comparable to Φ_0. As a result, the nonlinear term $\epsilon J(\varphi)$ on the right hand side of the wave equation (4.5) can be negligible and we get a linear wave equation in order to perform the dispersion analysis under the small amplitude assumption. Then by substitution of elementary solution in the form of sinusoidal wave, which is often so-called time-harmonic waveform, $\varphi_J = Ae^{j(\omega t - \gamma x)}$ into the linear wave equation dispersion characteristics is found. We denote the amplitude by A, angular frequency by ω and complex propagation constant by γ that includes both phase and attenuation constantans, β and α respectively, in the form of $\gamma = \beta - j\alpha$. We can also linearize the original system of equations (4.1)-(4.4) by letting $\sin(2\pi\varphi_J/\Phi_0) \sim 2\pi\varphi_J/\Phi_0$. Then, we insert harmonic solutions given by $Re\{A_i e^{j(\omega t-\gamma x)}\}$, $i = 1, 2, 3, 4$ for all variables of V, I, V_J and Φ_J into the (4.1)-(4.4). This procedure yields a homogenous matrix equation in terms of complex coefficients of A_1, A_2, A_3 and A_4. The determinant of this matrix should vanish in order to have a nontrivial solution. Finally, both methods result in a dispersion relation between complex propagation constant $\gamma = \beta - j\alpha$ and angular frequency ω given by

$$\gamma^2 = \frac{LCL_JC_J\omega^4 - CL\left(1+\frac{L_J}{Lh}\right)\omega^2 - j\frac{LCL_J}{R_J}\omega^3}{L_JC_J\omega^2 - 1 - j\frac{L_J}{R_J}\omega}. \tag{4.8}$$

As we restricted ourselves in the limit of small amplitude, the normal channel in high-quality-fabricated JJ doesn't play a significant role in the device performance. Therefore, loss can be ignored ($R_J \to \infty$) and the phase constant is given by

$$\frac{\beta^2}{LC} = \frac{\omega^4 - \frac{1}{L_JC_J}\left(1+\frac{L_J}{hL}\right)\omega^2}{\omega^2 - \frac{1}{L_JC_J}}. \tag{4.9}$$

According to the dispersion relation (4.9), the group velocity is calculated in a closed-form expression by

$$v_g = \frac{d\omega}{d\beta} = \frac{\beta}{\omega LC} \times \frac{\left(\omega^2 - \frac{1}{L_JC_J}\right)^2}{\left(\omega^2 - \frac{1}{L_JC_J}\right)^2 + \frac{1}{hLL_JC_J^2}}. \tag{4.10}$$

The generic phase constant and group velocity for the lossless case, are plotted in Fig. 4-4 and Fig. 4-5. As frequency increase, both dispersion and group velocity asymptotically resemble the behavior of a regular LC transmission line without the junctions. As shown in Fig. 4-4, there is a clear bandgap between plasma frequency of the JJ which is $\omega_p = 1/\sqrt{L_JC_J}$ and $\omega_q = \sqrt{1+L_J/hL}/\sqrt{L_JC_J} = \omega_p\sqrt{1+L_J/hL}$. This occurs when the right side of equation (4.9) becomes negative. Obviously, the group velocity in this region must be zero as illustrated in Fig. 4-5. It should be noted that for a lossless waveguide the propagation constant β would be either real or pure imaginary. The former gives the propagation condition and the latter situation is referred to as stopband region, bandgap, cut-off condition, or evanescent wave. Taking $\omega \to 0$, the propagation constant also approaches zero as seen in Fig. 4-4. However, Fig. 4-5 shows that the group velocity is nonzero for this case which is consistent with that fact that this structure can support the DC currents.

By taking the shunt resistance R_J into the account, the real and imaginary parts of the propagation constant are illustrated in Fig. 4-3. As the Josephson junction block is modeled by a resonant circuit, the resonance behavior is expected at plasma frequency. At the low frequency domain, the inductive part of the Josephson junction block behaves as a short circuit and at high frequencies the capacitive part of the block exhibits the same behavior. Therefore, in both regimes the effect of the resistive part reduced and we expect low attenuation. On the other hand, at the resonant frequency occurring at plasma frequency, inductor and capacitor components of each block cancel each (open circuit), and the resistance part becomes more prominent by inducing large attenuation. Furthermore, according to Fig. 4-3, we observe nondispersive behavior below plasma frequency (low frequency) and also far above it (high frequency). At low frequencies the inductor elements are dominant components; however, at high frequencies the capacitors of each block become dominant elements. Thus, slow wave propagation is expected at low frequencies in comparison to high frequencies. All the above expectations are observed clearly in the dispersion diagram of Fig. 4-4.

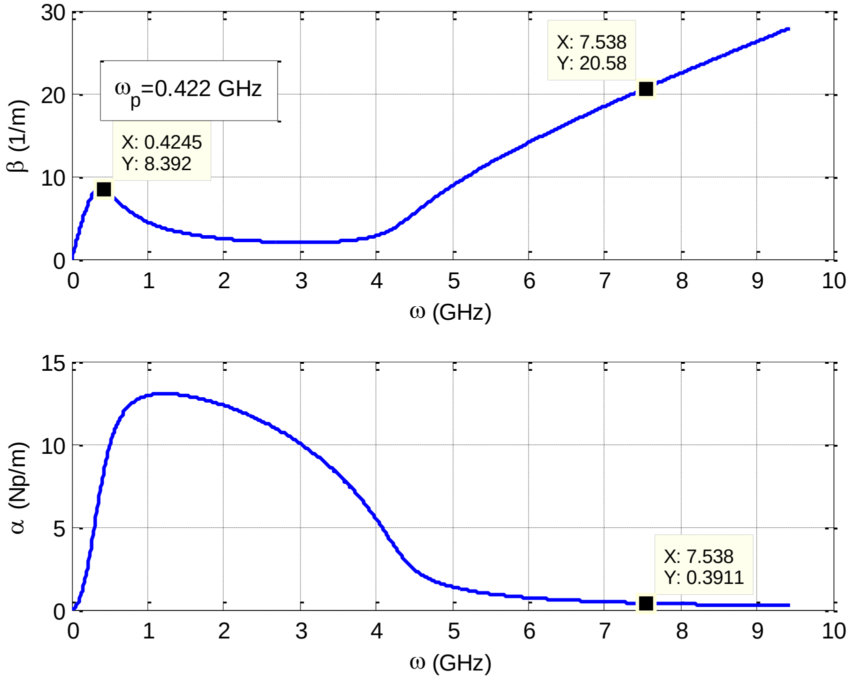

Fig. 4-3 Dispersion Diagram, variation of phase and attenuation constants vs. frequency, of series-connected DJTL with normalized parameters of L_J=1, C_J=0.5, R_J=1, L=C=1, h=0.01.

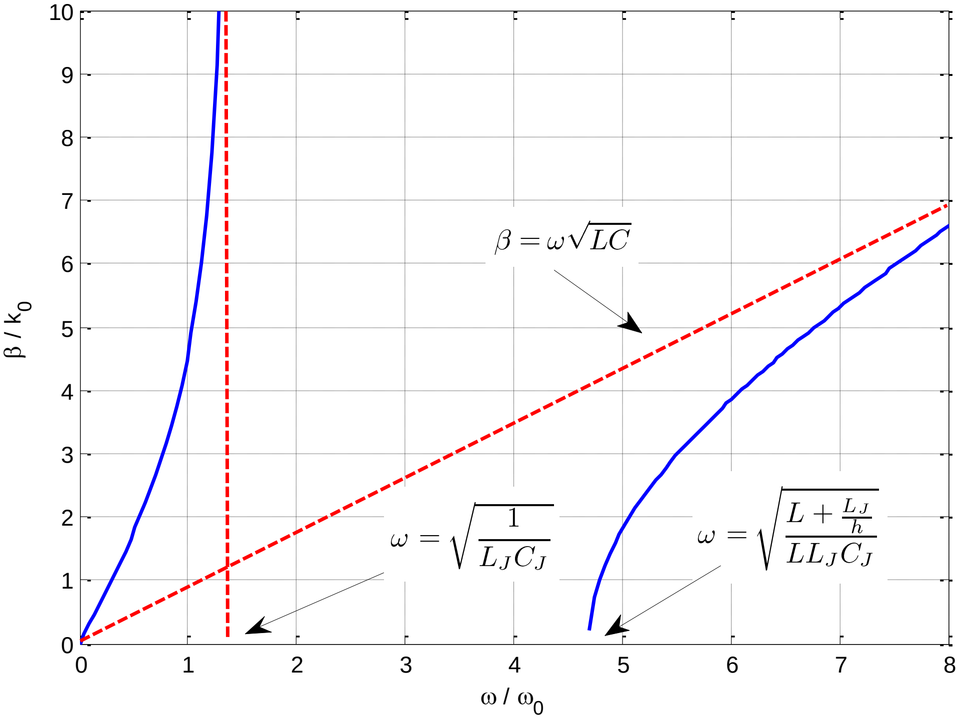

Fig. 4-4 Typical dispersion diagram of a lossless series-connected DJTL

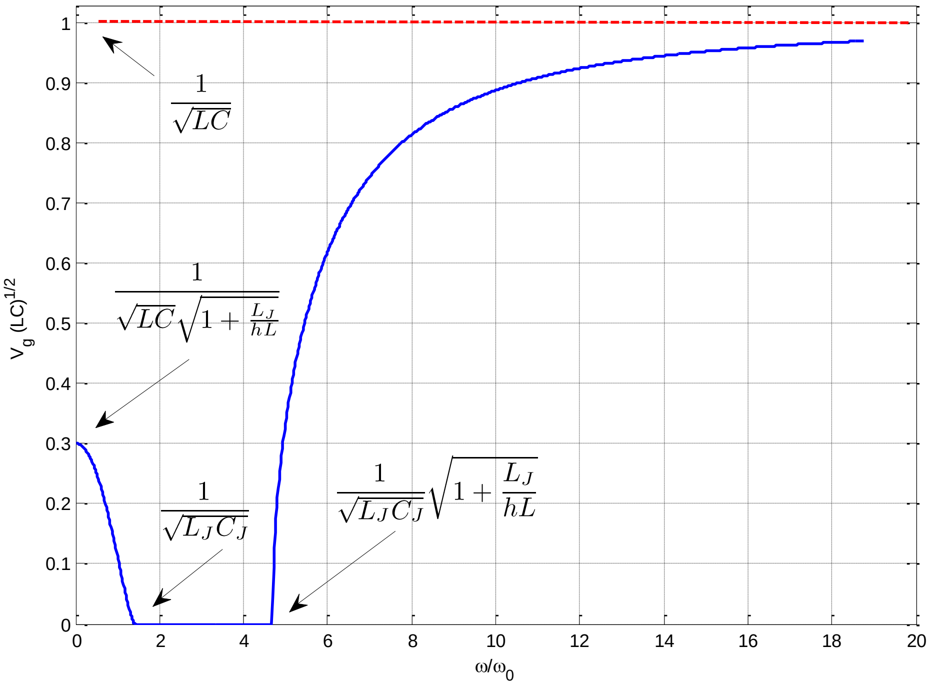

Fig. 4-5 Typical group velocity for a lossless series-connected DJTL.

4.2.3 Supporting Phase-Matching Condition for TW- JPA

Traveling-wave parametric amplification in its simplest form involves the transfer of power between three phase-locked waves in a nonlinear waveguide. A wave with a phase θ_2 interacts with a wave with phase θ_3 to generate a wave with phase θ_1, where $\theta_i = \omega_i t - \beta_i x$ for $i = 1, 2, 3$, ω_i and β_i are angular frequency and propagation constant associated with each wave. Each of the waves is a normal mode of propagation satisfying the dispersion relation and all are copropagating along the same direction. Referring to the dispersion equation (4.9) as $f(\omega, \beta) = 0$, therefore, three nonlinear equations are obtained

$$f(\omega_1, \beta_1) = 0 \tag{4.11}$$

$$f(\omega_2, \beta_2) = 0 \tag{4.12}$$

$$f(\omega_3, \beta_3) = 0. \tag{4.13}$$

Due to the cubic nonlinearity observed in the wave equation (4.6), one can realize that the phase-matching condition for such a resonant interaction between signal, pump and idler waves in the unbiased DJTL is in the kind of four-photon process satisfying the relation $2\theta_2 = \theta_1 + \theta_3$ which leads to the following phase-matching conditions

$$2\omega_2 = \omega_1 + \omega_3 \quad (4.14)$$

$$2\beta_2 = \beta_1 + \beta_3. \quad (4.15)$$

We will return to details of the derivation of the phase-matching condition in chapter 6 section 6.5.4. Assuming the frequency of the signal is given, equation (4.11)-(4.15) forms a system of five nonlinear equations with five unknowns which must be solved. It is clear that solutions in the form of $\omega_3 = \omega_2 = \omega_1$ $\beta_3 = \beta_2 = \beta_1$ always satisfy the phase-matching condition (4.14)-(4.15). This case is referred to as a doubly-degenerate parametric amplifier.

To find any possible non-degenerate solution, we eliminate all variables except the pump's frequency. Thus, a polynomial with degree of ten with respect to ω_2 is obtained to evaluate the frequency of pump for any given signal's frequency. The roots of this polynomial must be positive and real. They must also fall in the proper domain such that all corresponding βs become real. By considering all foregoing facts and solving the polynomial, the DJTL cannot achieve any non-degenerate parametric interaction in accordance with the phase-matching condition (4.14)-(4.15).

Another way to realize if the structure supports the non-degenerate case of phase-matching or not is the graphical visualization by transforming the dispersion diagram in the (ω, β) plane. First, we set the point (ω_1, β_1) on the dispersion curve corresponding to the signal wave. Then we renovate all (ω, β) points in the dispersion curve based on the transformation of $2(\omega, \beta) - (\omega_1, \beta_1)$ to find a new curve. Since this transformation is consistent with the phase-matching equations (4.14)-(4.15), this curve would be the locus for idler wave. On the other hand, the frequency and phase constant of idler, denoted by (ω_3, β_3), must satisfy the dispersion relation, therefore, the idler characteristics can be found by intersection of the new transformed curve with the original dispersion diagram.

This procedure has been applied for two different signal waves in a typical DJTL and the results are illustrated in Fig. 4-6. The solid line is the dispersion curve on which a point corresponding to the signal wave is highlighted. The dashed line is the locus of the idler wave that only intersects the dispersion diagram at the point corresponding to the signal. This confirms the fact that the doubly degenerate case is the only solution satisfying the phase-matching condition for the series-connected DJTL.

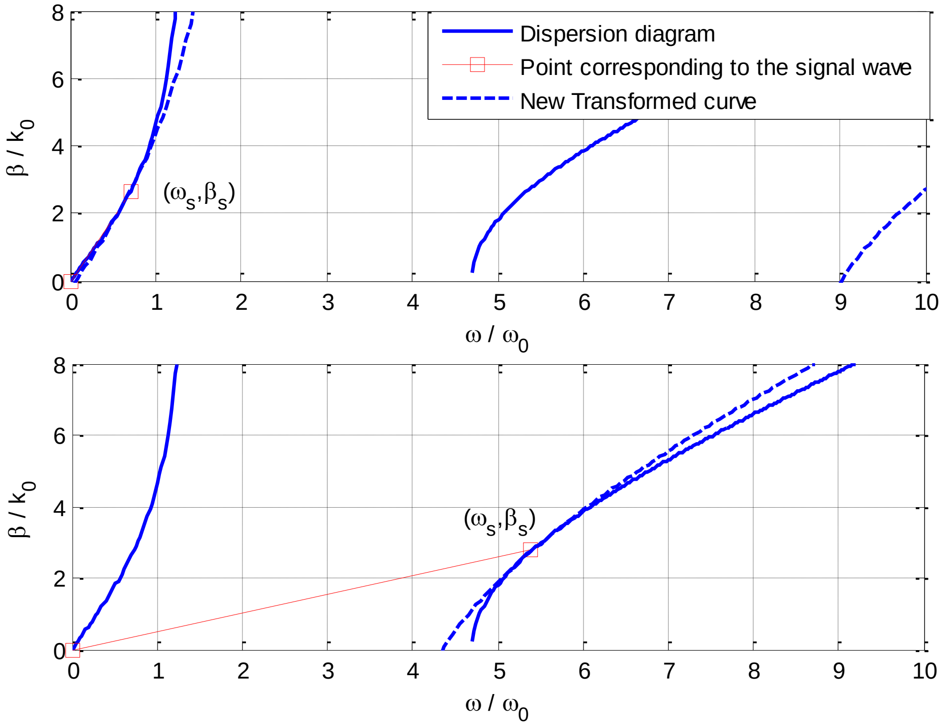

Fig. 4-6 Phase-matching condition cannot be satisfied for three distinct wave characteristics.

If the basic model of JJ is employed, $C_J = 0$ and $R_J = \infty$, the dispersion equation becomes linear

$$\beta = \omega \sqrt{LC\left(1 + \frac{L_J}{hL}\right)} \tag{4.16}$$

and the phase matching relation can be achieved. However, this structure is not suitable for parametric interaction because all harmonics of signal, pump and idler generated due to the nonlinearity can be propagated through the TL.

4.3 Series-Connected DJTL Assisted by Open Stubs

Using dispersion analysis in the preceding section, it was demonstrated that the regular series-connected DJTL is not suitable to guide a non-degenerate resonant triads for parametric amplification. In order to modify the dispersion relation for this purpose two proposals are offered. First, one can replace the host waveguide from TEM transmission line to another microwave waveguide such as ridge waveguides [98], and then embed periodic JJs to create the nonlinearity. Second solution is to insert additional distributed elements such as inclusions to change the wave property of the TL. Due to the simplicity and quick modification that second solution implies, we put a single open-circuited stub at each unit cell. Fig. 4-7 and Fig. 4-8 illustrate the implementation of this structure over a microstrip line and CPW, respectively.

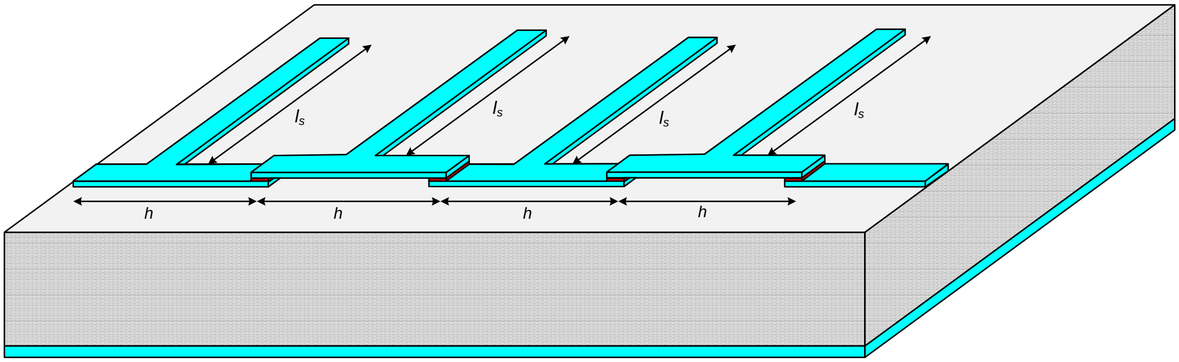

Fig. 4-7 Series-connected DJTL assisted by open-circuited stubs over a microstrip line.

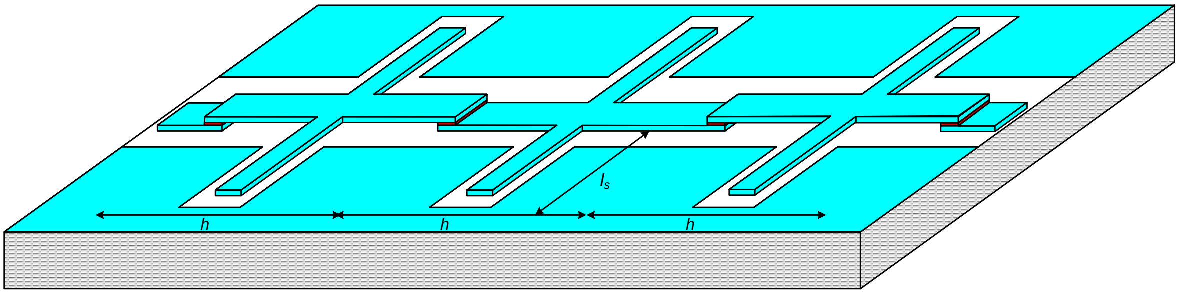

Fig. 4-8 Series-connected DJTL assisted by open-circuited stubs over a CPW.

4.3.1 Wave Equation in Time Domain

Fig. 4-9 shows the circuit model of the DJTL assisted by open stubs. Physically, an open stub is a segment of transmission line with open-circuited end that can be modeled as a shunt impedance. Depending on the length of the stubs, stubs behave like a capacitor, inductor or even resonator. If the characteristic impedance and phase constant associated with the stub's TL are denoted by Z_0 and β_s, the impedance of the open stub is given by

$$Z_{stb} = -jZ_0 \cot(\beta_s l_s) \tag{4.17}$$

where $\beta_s = \omega\sqrt{L_s C_s}$, $Z_0 = \sqrt{L_s/C_s}$ and L_s, C_s are inductance and capacitance per unit length associated with the stub's TL.

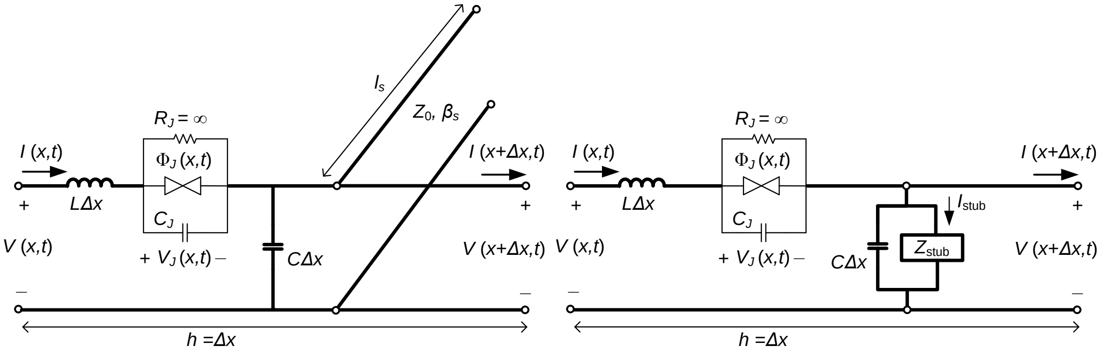

Fig. 4-9 TL model of the series-connected DJTL assisted by open stubs, open stubs are modeled by a shunt impedance.

Equation (4.17) displays the impedance of the open stub in frequency domain which cannot be used in time domain. To describe the wave equation of the structure in time domain, equation (4.17) must be converted in time domain. If the voltage and current seen at the beginning of the stub are denoted by V and I, (4.17) can be revisited as

$$Z_{stb} = \frac{V(\omega)}{I(\omega)} = Z_0 \frac{1 + e^{-j2\omega\tau}}{1 - e^{-j2\omega\tau}} \tag{4.18}$$

where $\tau = l_s\sqrt{L_s C_s} = l_s\beta_s/\omega$ and it has half the time required that the TEM wave travels across the stub and returns. Taking the inverse Fourier transform, (4.18) is written in time domain by

$$V(t) - V(t - 2\tau) = Z_0 I(t) + Z_0 I(t - 2\tau) \tag{4.19}$$

in which the time delay is the impact of the stub in the structure.

Having all variables displayed in Fig. 4-9 and doing the same procedure carried out in section 4.2.1, a system of five nonlinear partial differential equations is obtained

$$\frac{\partial \Phi_J}{\partial t} = V_J \tag{4.20}$$

$$I(x,t) = I_c \sin\left(2\pi \frac{\Phi_J}{\Phi_0}\right) + C_J \frac{\partial V_J}{\partial t} + \frac{V_J}{R_J} \tag{4.21}$$

$$\frac{\partial I}{\partial t} + \frac{1}{L}\frac{\partial V}{\partial x} = \frac{-V_J}{Lh} \tag{4.22}$$

$$Z_0[I_{stub}(x,t) + I_{stub}(x,t-2\tau)] = V(x,t) - V(x,t-2\tau) \tag{4.23}$$

$$\frac{\partial V(x,t)}{\partial t} + \frac{1}{C}\frac{\partial I}{\partial x} + \frac{I_{stub}}{Ch} = 0. \tag{4.24}$$

These equations can be converted into one partial differential equation in terms of one single variable. After sinusoidal terms are expanded in a Taylor series and extra terms are eliminated, equations (4.20)-(4.24) are reduced to a time-delayed PDE as

$$\begin{aligned}
&\left[C\left(1+\frac{Lh}{L_J}\right)+\frac{L}{Z_0R_J}\right]\varphi_{tt}-\frac{h}{L_J}\varphi_{xx}+\frac{1}{Z_0h}\left(1+\frac{Lh}{L_J}\right)\varphi_t \\
&\quad - C_Jh\varphi_{ttxx}+\left[\frac{LC_J}{Z_0}+\frac{hLC}{R_J}\right]\varphi_{ttt}+LCC_Jh\varphi_{tttt} \\
&\quad -\frac{h}{R_J}\varphi_{txx}+\left[C\left(1+\frac{Lh}{L_J}\right)-\frac{L}{Z_0R_J}\right]\varphi_{tt}^{(t-2\tau)} \\
&\quad -\frac{h}{L_J}\varphi_{xx}^{(t-2\tau)}-\frac{1}{Z_0h}\left(1+\frac{Lh}{L_J}\right)\varphi_t^{(t-2\tau)} \\
&\quad - C_Jh\varphi_{ttxx}^{(t-2\tau)}+\left[-\frac{LC_J}{Z_0}+\frac{hLC}{R_J}\right]\varphi_{ttt}^{(t-2\tau)} \\
&\quad + LCC_Jh-\frac{h}{R_J}\varphi_{txx}^{(t-2\tau)}=\epsilon J(\varphi)
\end{aligned} \tag{4.25}$$

where $\varphi^{(t-2\tau)}$ is the flux associated with the JJ at time $t-2\tau$. In equation (4.25), the flux has been scaled through $\Phi_J=\sqrt{\epsilon}\varphi$, where ϵ is a dimensionless parameter. This parameter is used to examine the order of nonlinearity with respect to the amplitude of flux. The left hand side of (4.25) consists of linear terms, however, the right hand side consists of nonlinear $J(\varphi)$ given by

$$\begin{aligned}
J(\varphi) &= \frac{2\pi^2LCh}{L_J\Phi_0^2}\left(\varphi_{tt}-\frac{1}{LC}\varphi_{xx}+\frac{1}{ChZ_0}\varphi_t\right)\varphi^2 \\
&\quad + \frac{4\pi^2LCh}{L_J\Phi_0^2}\left[(\varphi_t)^2-\frac{1}{LC}(\varphi_x)^2\right]\varphi \\
&\quad + \frac{2\pi^2LCh}{L_J\Phi_0^2}\left\{\varphi_{tt}^{(t-2\tau)}-\frac{1}{LC}\varphi_{xx}^{(t-2\tau)}-\frac{1}{ChZ_0}\varphi_t^{(t-2\tau)}\right\}\left[\varphi^{(t-2\tau)}\right]^2 \\
&\quad + \frac{4\pi^2LCh}{L_J\Phi_0^2}\left\{\left[\varphi_t^{(t-2\tau)}\right]^2\right. \\
&\quad \left.-\frac{1}{LC}\left[\varphi_x^{(t-2\tau)}\right]^2\right\}\varphi^{(t-2\tau)}.
\end{aligned} \tag{4.26}$$

4.3.2 Dispersion Relation

Under the small amplitude assumption, the parameter ϵ would be very small and the nonlinearity in (4.25) becomes very weak. Thus, by using the methods described in section 4.2.2, the dispersion characteristics for the lossy structure is found as

$$\gamma^2 = \frac{LCL_JC_J\omega^4 - LC\left(1+\frac{L_J}{Lh}\right)\omega^2 - j\frac{LCL_J}{R_J}\omega^3 - j\frac{LL_J}{hZ_0R_J}\omega^2\tan\omega\tau + \frac{LL_JC_J}{hZ_0}\omega^3\tan\omega\tau - \frac{L}{Z_0h}\left(1+\frac{L_J}{Lh}\right)\omega\tan\omega\tau}{L_JC_J\omega^2 - 1 - j\frac{\omega L_J}{R_J}}. \quad (4.27)$$

where $\gamma = \beta - j\alpha$. Supposing that R_J is large enough in the regime of small amplitude, loss is removed and equation (4.27) is reduced to

$$\frac{\beta^2}{LC} = \frac{\omega^4 + \frac{1}{Z_0Ch}\tan\omega\tau\,\omega^3 - \frac{1}{L_JC_J}\left(1+\frac{L_J}{hL}\right)\omega^2 - \frac{1}{Z_0ChL_JC_J}\left(1+\frac{L_J}{hL}\right)\tan\omega\tau\,\omega}{\omega^2 - \frac{1}{L_JC_J}}. \quad (4.28)$$

Open stubs can be eliminated when we substitute $\tau = 0$ into the (4.28) which must be consistent with the (4.9) when there was no stubs. Doing this, we obtain the dispersion relation in (4.9) as expected.

Derivative of dispersion relation (4.28) gives the group velocity as

$$v_g = \frac{d\omega}{d\beta} = \frac{2\beta}{LC} \times \frac{\left(\omega^2 - \frac{1}{L_JC_J}\right)^2}{\text{DEN.}} \quad (4.29)$$

where DEN. stands for the denominator of the group velocity. DEN. is a lengthy expression as follows

$$\begin{aligned}\text{DEN.} = &\left\{2\omega + \frac{1}{hZ_0C}\left(\tau\omega + \tan\omega\tau + \omega\tau\tan^2\omega\tau\right)\right\}\left\{\omega^4\right.\\ &\left.- \frac{2\omega^2}{L_JC_J} + \frac{1}{L_J^2C_J^2}\left(1+\frac{L_J}{hL}\right)\right\} \\ &- \frac{\omega^2}{h^2LCZ_0C_J}\left(\omega\tau\tan^2\omega\tau - \tan\omega\tau + \tau\omega\right)\end{aligned} \quad (4.30)$$

The dispersion diagram corresponding to (4.28), is displayed in Fig. 4-10. The first asymptotic line and the first bandgap is the result of plasma frequency of JJs. However, due to the asymptotic behavior of tangent function, additional branches and bandgaps are generated. All asymptotic lines and zero-crossing have been calculated in a closed-form expression and written in Fig. 4-10. Removing all stubs by taking $\tau \rightarrow 0$, all vertical asymptotes stemming from tangential functions, go to the leftmost infinite and we get the dispersion diagram of Fig. 4-4. Having extra branches in the dispersion diagram increases the chance of finding three points that satisfies phase-matching conditions (4.14)-(4.15). This is primary benefit of adding open-stubs into the DJTL.

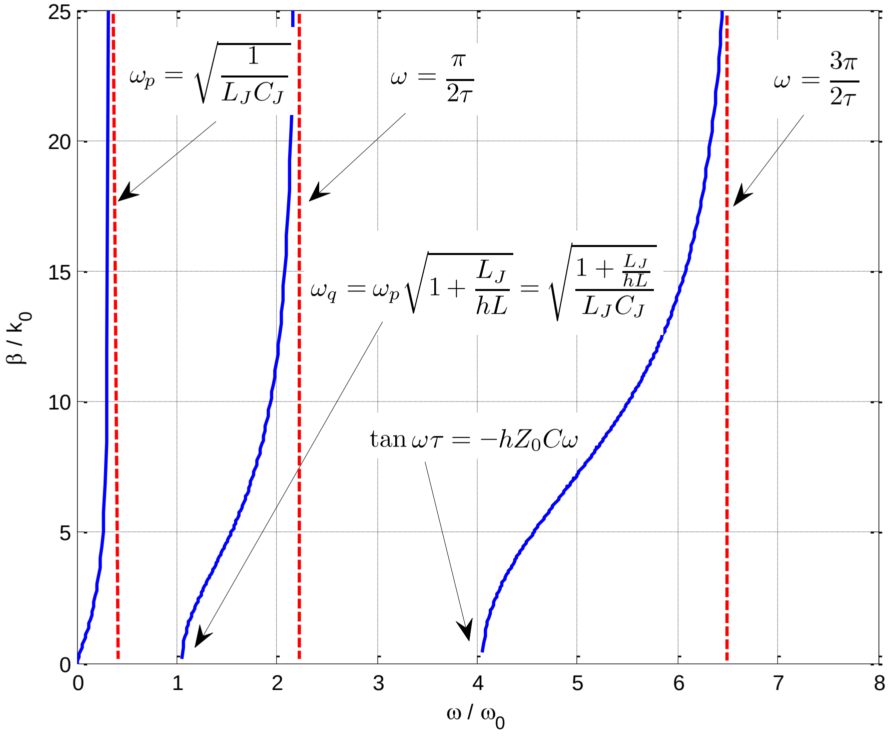

Fig. 4-10 General dispersion diagram of DJTL assisted by open-circuited stubs.

4.3.3 Realizability Assessment

Any engineered electromagnetic medium and waveguides with sophisticated frequency properties must be realistic and physically realizable. To study such a condition, we define the complex unilateral refractive index as $n(\omega) = \gamma / k_0$, where $k_0 = \omega\sqrt{\epsilon_0 \mu_0}$ is the free-space wavenumber. The realizability criteria are conjugate symmetry, passivity and causality [99]. The conjugate symmetry which is expressed by $n^*(\omega) = n(-\omega)$ is a result of the fact that the time-domain impulse response function must be real. Also, for all passive media, $\text{Im}\{n(\omega)\} < 0$ for all $\omega > 0$, otherwise, attenuation constant becomes negative and gain is observed. All physical systems must obey the causality which simply says that the response of the system cannot precede the input. According to the Titchmarsh's theorem, the three concepts of causality, analyticity and Hilbert transform pairs for a linear system are interconnected, assuming one implies the other two [100]. Therefore, the first constraint that causality puts on the system is the analyticity of $n(\omega)$ in the upper half-plane of the complex variable ω in addition to being uniformly square integrable. As a results, $n(\omega)$ approaches to a limit (usually 1) when $\omega \rightarrow \infty$. The second constraint stems from the Hilbert transform or equivalently the Kramers–Kronig relations that control the relationship between the real and imaginary parts of constitutive parameters such as $\epsilon_r(\omega)$ and $\mu_r(\omega)$, effective refractive index $n(\omega)$, and even the impedance of a circuit resonator [101]. We focused on the behaviour of $n^2(\omega) - n^2(\infty)$ for our structure which satisfy the Kramers-Kronig equation

$$\mathrm{Re}\{n^2(\omega_0) - n^2(\infty)\} = \frac{2}{\pi} P \int_0^\infty \frac{\omega \, \mathrm{Im}\{n^2(\omega) - n^2(\infty)\}}{\omega^2 - \omega_0^2} d\omega \tag{4.31}$$

$$\begin{aligned} &\mathrm{Im}\{n^2(\omega_0) - n^2(\infty)\} \\ &\qquad = -\frac{2}{\pi} P \int_0^\infty \frac{\omega_0 \, \mathrm{Re}\{n^2(\omega) - n^2(\infty)\}}{\omega^2 - \omega_0^2} d\omega. \end{aligned} \tag{4.32}$$

According to the dispersion equation (4.28) and definition of effective refractive index, the asymptotic value of n^2 at large frequencies and its DC value at zero frequency are evaluated as

$$n^2(0) = \frac{LC}{\mu_0 \epsilon_0} \left(1 + \frac{L_J}{Lh}\right) \left(1 + \frac{\tau}{Z_0 Ch}\right) \tag{4.33}$$

$$n^2(\infty) = \frac{LC}{\mu_0 \epsilon_0}. \tag{4.34}$$

The loss is related to the imaginary part of the refractive index, therefore, loss is always present in the dispersive materials (or waveguides) but it can be vanishingly small [102]. In other words, any lossless and dispersive medium that has no loss at any frequency interval is a non-causal medium. In [103], a closed-form equation on the bandwidth limitation for both lossy and lossless dispersive media has been discussed, but it is also shown that there are no severe restrictions if just the condition of causality is employed [103],[104].

It should be noted that according to the Titchmarch's theorem the validity of Kramers-Kronig relations depends on the analyticity of the function in the upper half-plane.

Regarding the function of our interest, one pole is present as seen in the dispersion equation (4.9) and (4.28). Due to the different notations used for time harmonic analysis in physics and engineering disciplines, the imaginary unit j must be replaced by $-i$ in our equation which shows that this singularity is located in the lower half-plane.

Fig. 4-11 displays the variation of the real and imaginary parts of $n^2(\omega)$ for the DJTL without stubs. When the real part of $n^2(\omega)$ decreases around the plasma frequency of JJ, a resonance at the same area occurs in the imaginary part. This phenomenon is shown in Fig. 4-11. and called an "anomalous dispersion". Despite the Fourier transform which relates the time domain to the frequency domain, the Hilbert transform is defined in one domain and its effect is seen at the same location where its Hilbert counterparts changes noticeably. Real and imaginary parts of the refractive index is illustrated in Fig. 4-12.

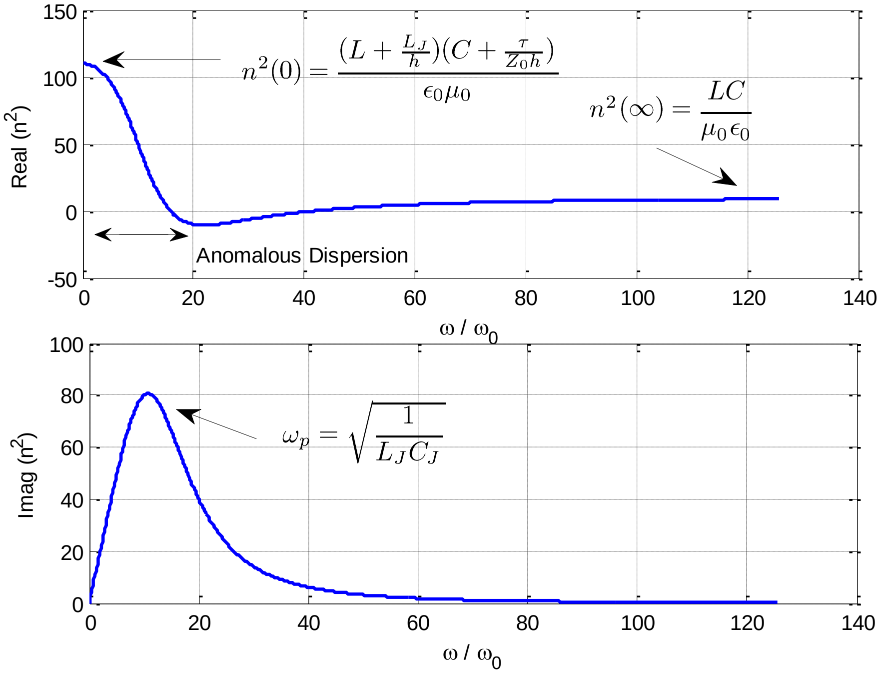

Fig. 4-11 Real and imaginary parts of $n^2(\omega)$ verses frequency for DJTL without stubs.

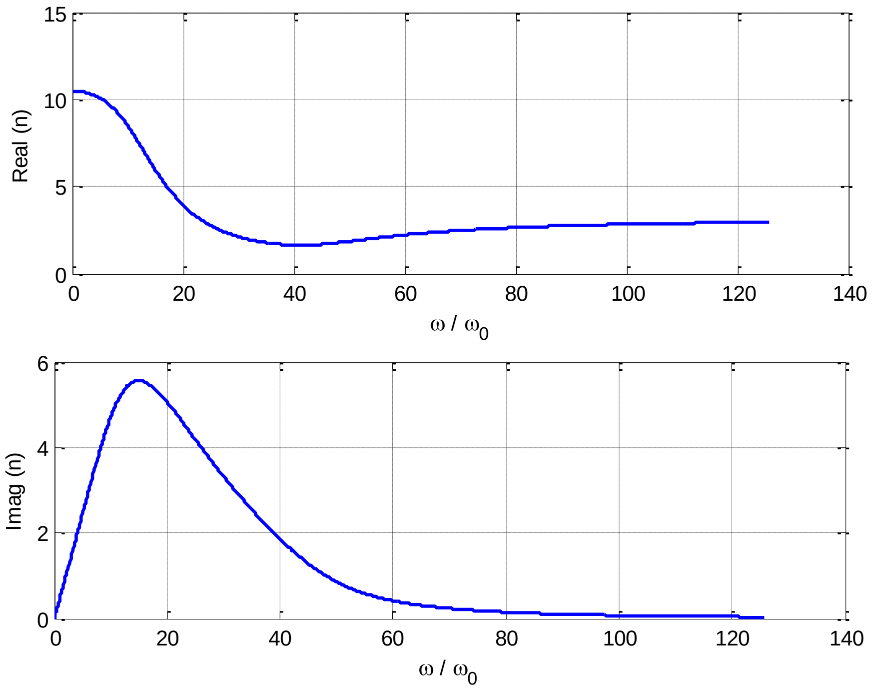

Fig. 4-12 The refractive index of DJTL satisfies the Karmers-Kronig relation and the waveguide is causal.

4.3.4 Floquet Analysis

DJTL falls in the category of one-dimensional periodic structures, in the sense that an array of identical JJs are placed along a TL at equal distance. In this section, we employed the Floquet theorem which is the basis paradigm for the study of linear periodic structures in steady state and in frequency domain to investigate the microwave properties of DJTLs. The goal of this study is the characterization of mode propagation, determination the cut-off condition and inspection of impedance matching. To take a general stand, we begin with the distributed circuit whose unit cell is illustrated in Fig. 4-9. The unit cell consists of a series impedance connected to a shunt admittance. The amount of the series impedance and shunt impedance per unit length is denoted by Z and Y, respectively.

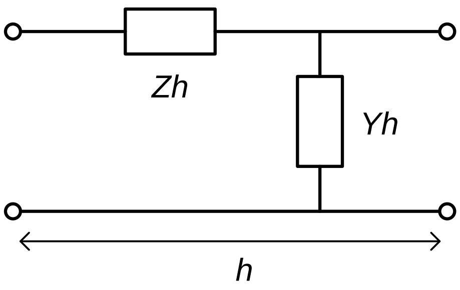

Fig. 4-13 Simplified model of the unit cell of series-connected DJTL.

The total ABCD matrix representing the unit cell is given by

$$\begin{bmatrix} A & B \\ C & D \end{bmatrix} = \begin{bmatrix} 1 & Zh \\ Yh & 1 + ZYh^2 \end{bmatrix}. \tag{4.35}$$

As the determinant of the matrix is unity and the unit cell is reciprocal, application of the Floquet theorem into the structure yields [16],[58].

$$\cosh(\gamma h) = \frac{A + D}{2} = \frac{2 + ZYh^2}{2}. \tag{4.36}$$

Using a mathematical identity, equation (4.36) is reduced to

$$4\sinh^2\left(\frac{\gamma h}{2}\right) = ZYh^2. \tag{4.37}$$

In the case of the lossless structure, attenuation constant is zero, $\gamma = j\beta$, and the hyperbolic function is replaced by regular trigonometric function as

$$4\sin^2\left(\frac{\beta h}{2}\right) = -ZYh^2. \tag{4.38}$$

Equation (4.38) is the dispersion relation which governs the DJTL. However, closer look at the value of sinusoidal function in a trigonometric tables [57] reveals that if the argument of the sine function is less than 0.3, it can be crudely replaced by its argument. Therefore, in the case of long-wave approximation which can be written as $\beta < 0.6/h$ or $h < \lambda/15$, equation (4.38) reduced to

$$\beta^2 = -ZY. \tag{4.39}$$

It should be noted that the same treatment can be given to the sinh $(\gamma h/2)$, when the absolute value of $\gamma h/2$ is small enough. For the DJTL waveguides shown in Fig. 4-9, the series impedance and shunt admittance per unit length are

$$Z = jL\omega + \frac{j\omega R_J \frac{L_J}{h}}{j\omega L_J + R_J\left(1 - \omega^2 L_J C_J\right)} \tag{4.40}$$

$$Y = jC\omega + j\frac{Y_0}{h}\tan\omega\tau. \tag{4.41}$$

Supposing the lossless case by taking $R_J \to \infty$ and substituting (4.40) and (4.41) into equation (4.39), following dispersion equation is obtained

$$\beta^2 = \frac{L\omega^2}{Z_0 h}\frac{\left(Z_0 Ch + \frac{\tan\omega\tau}{\omega}\right)\left(\omega^2 - \frac{1}{L_J C_J}\left(1 + \frac{L_J}{Lh}\right)\right)}{\omega^2 - \frac{1}{L_J C_J}}. \tag{4.42}$$

Equation (4.42) is the same as the dispersion equation found in section 4.3.2. from time-domain analysis. Multiplicative format of this equation is useful to find the zero crossing frequencies and also bandgaps in the dispersion diagram.

Considering two equations (4.38) and (4.39), another limitation on the wave propagation emerges which is because of the discreetness nature of the DJTL. The sinusoidal function in (4.38) is always less than unity, therefore $-ZYh^2/4 < 1$. On the other hand, $\beta^2 = -ZY$ which can be incorporated with the inequality offering another condition for propagation which is $\beta < 2/h$ or $h < \lambda/\pi$ and is called as a Bragg cut-off condition [92],[28]. Another proof for cut-off condition is addressed in the appendix A which is based on the spatial discretization of the structure.

4.3.5 Impedance Analysis

Essential information about the wave propagation through any electromagnetic structure is provided by modal analysis which has been carried out in the previous sections entitled as dispersion analysis. However, when a microwave structure is implemented with a transmission line platform, another source of information for the design purposes can be obtained by the input impedance which inherently is a circuit parameter. Input impedance is a key parameter for calculating the amount of reflection which is a limiting factor in microwave power transfer.

For the case of infinitely long periodic structure, the input impedance is one of the two roots of the following quadratic equation in which its real part is positive

$$CZ_{in}^2 + (D - A)Z_{in} - B = 0. \tag{4.43}$$

Parameters A, B, C and D are entries of the ABCD matrix representing the unit cell. For DJTL with open stubs, these parameters are given by (4.35) when the series impedance and shunt impedance per unit length are substituted by (4.40) and (4.41). Therefore, equation (4.43) reduced to

$$YhZ_{in}^2 + ZYh^2Z_{in} - Zh = 0. \tag{4.44}$$

Considering the fact that $\beta^2 = -ZY$, the discriminant of the equation becomes $\beta^2h^2\,(\beta^2h^2 - 4)$ which is always positive as long as cut-off condition $\beta < 2/h$ is satisfied.

Another approach for any impedance calculation of the structure is to define the characteristic impedance associated with the DJTL as $Z_c = \sqrt{Z/Y}$. Therefore, the input impedance of the DJTL ended by an arbitrary load can be found by using the conventional input impedance formula for a regular TEM transmission line [58].

4.3.6 Stubs' Role for Parametric Interaction

It was demonstrated in section 4.2.3. that a typical DJTL cannot support non-degenerate resonant triad waves satisfying the phase-matching equations (4.14) and (4.15). To overcome this problem, open stubs have been added to the DJTL to change the dispersion diagram. Following the same procedure leading to the graphical illustration in dispersion diagram explained in section 4.2.3., we can verify that embedding open stubs into the DJTL enables this structure to support the phase matching equations described by

$$2\omega_2 = \omega_1 + \omega_3 \tag{4.45}$$

$$2\beta_2 = \beta_1 + \beta_3. \tag{4.46}$$

This technique is carried out on a typical dispersion diagram of the DJTL with open stubs and is shown in Fig. 4-14. The signal wave is chosen by $\widetilde{\omega}_1 = \widetilde{\omega}_s = 21.32$ and $\tilde{\beta}_1 = \tilde{\beta}_s = 163.9$ and we intend to find out the pump and idler waves. All parameters have already been normalized, so they are dimensionless. The normalization rule will be explained in the next section. The dispersion diagram is transformed by

$$\begin{bmatrix} \omega_{new} \\ \beta_{new} \end{bmatrix} = 2\begin{bmatrix} \omega_{old} \\ \beta_{old} \end{bmatrix} - \begin{bmatrix} \omega_s \\ \beta_s \end{bmatrix} \tag{4.47}$$

in order that the locus of idler is obtained. As demonstrated in Fig. 4-14, this new curve which is highlighted by the dashed-line crosses the dispersion diagram at two points. One is located exactly at the same position where the original signal point is, and the second one is a separate solution which has been pointed by an arrow in Fig. 4-14 and designated by (ω_i, β_i). if signal and pump points are connected by a segment, the middle of this segment is inevitably located on the dispersion diagram and marks the pump wave. This procedure is also applied to another dispersion diagram for a different DJTL as shown in Fig. 4-15. The existence of two sets of none-degenerate resonant triads satisfying the phase-matching condition is verified in this figure.

Another virtue that dispersion brings to the DJTL structure for traveling-wave parametric amplification relies on the filter property of the dispersion which prevents other unwanted harmonics from propagating through the structure. If the wave propagation through the structure is ruled out by a linear dispersion relation, any combinations of the resonant triad waves generated by the nonlinearity of the waveguide are allowed to propagate and carry energy. This might result in an inefficient parametric amplifier.

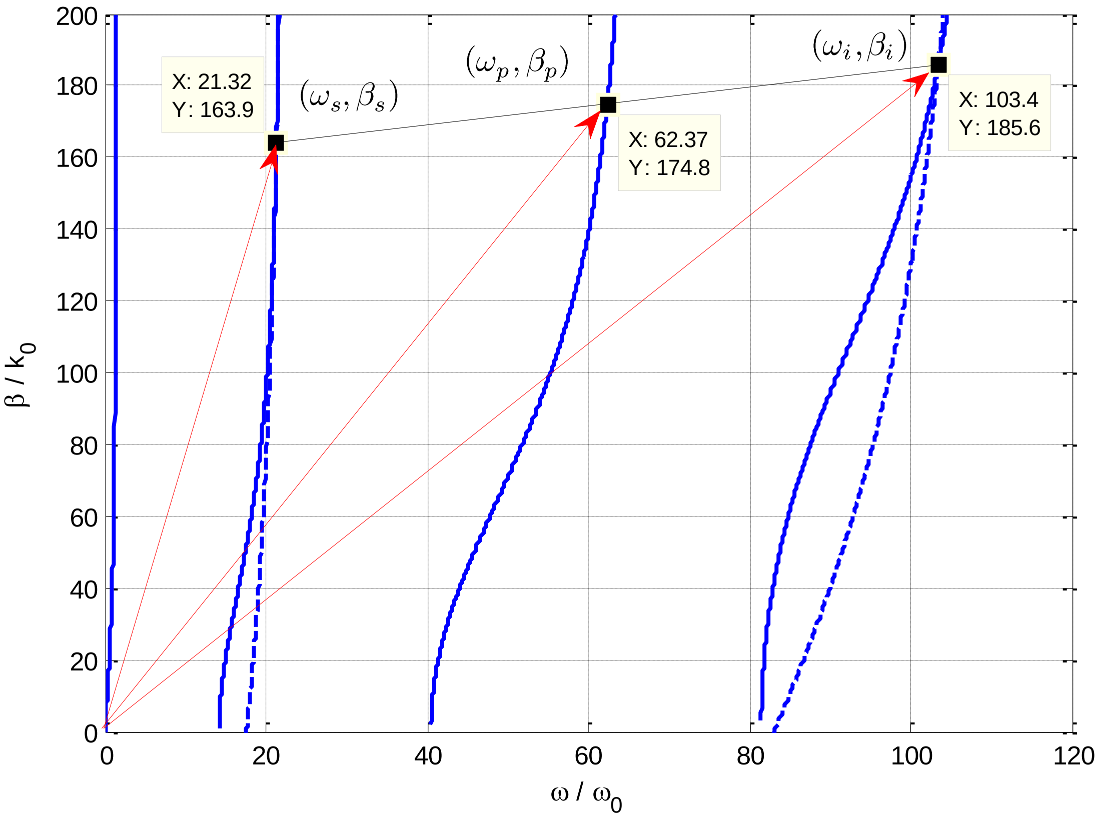

Fig. 4-14 Existence of the non-degenerate resonant triad waves in a DJTL with open stubs. L_J=1, C_J=0.5, L=1, C=1, C_s=1, L_s=0.5, l_s=0.1, h=0.01.

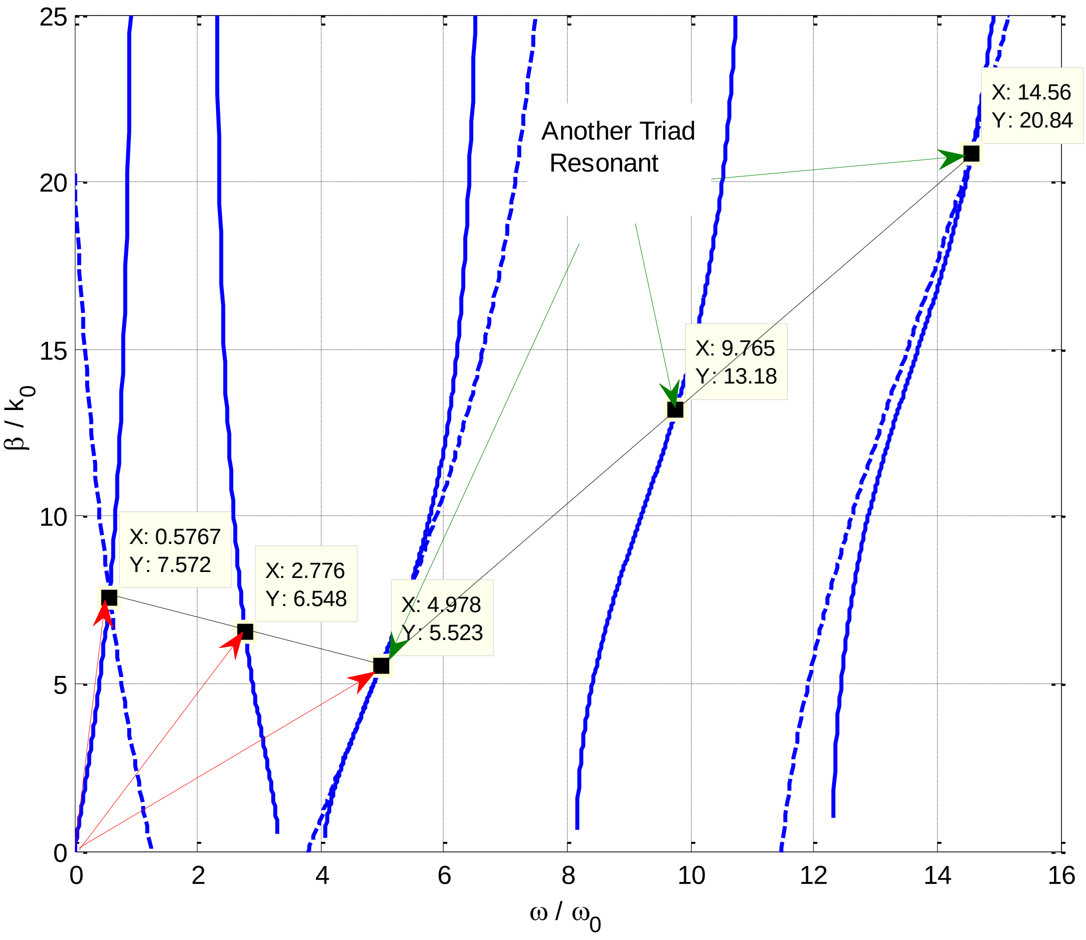

Fig. 4-15 Existence of the non-degenerate resonant triad waves in a DJTL with open stubs. L_J=1, C_J=1, L=1, C=1, C_s=1, L_s=0.5, l_s=1, h=0.1.

4.4 Design Considerations

In previous sections the possibility of supporting phase-matching equations (4.14) and (4.15) in a DJTL assisted with open stubs has been discussed. Nonetheless, there are some assumptions and conditions made at the beginning of our analysis that must be taken into account in the design procedure. Otherwise, the output of the design procedure is not consistent with the early assumptions. The aim of the design scheme in this part, is to find out the proper pump and idler waves for a given signal wave for a feasible DJTL. Moreover, practical limitations in implementing all physical parameters and circuit elements involved in the structure introduce technical restrictions that also need careful attention. Furthermore, fabrication process and their design rules is another restriction for the design flexibility.

4.4.1 Normalization Rule

In order to have more flexibility in design process, all physical parameters and variables are normalized by some arbitrary factors. After getting the desired response in the simulation, then these factors are chosen on the basis of feasibility of the device implementation. In addition, for numerical simulations, when very small or very big numbers are involved, it is often helpful to normalize all parameters and variables to special values. The scaling rules used in our analysis of DJTL are described in Table II.

The concept and formal manipulation by normalizing methods is easy, but the ideas involved seem to be rather deep. Basically, any scaling rule must have this important property that when we substitute new normalized variables and parameters into the set of master equations for the problem, these equations hold the same form as they have for the non-normalized variables and parameters. Hence, in order to establish a normalization rule in our problem, we choose four arbitrary constants namely, ω_0, k_0, R_0 and I_0, to normalize frequency, wavenumber, impedance and current by dividing them by these constants, respectively. Then, all other remaining parameters and variables are normalized into the proper form by using these four assumed parameters, as described in Table II. By putting new normalized variables into the wave equations (4.1)-(4.4), (4.5) or the dispersion relation (4.9), and trying to keep the former format of the equation, we realize that ω_0, R_0, I_0 and k_0 can be taken as arbitrary constants, as long as corresponding parameters are physically realizable. Summary of above process is shown in Table II.

4.4.2 Design Example

Presence of separate branches in the dispersion diagram of DJTL assisted by open-circuited stubs provides a platform to realize the three distinguished waves to satisfy the phase matching equations (4.14) and (4.15). On the other hand, two restrictions on the wavelength and the size of the device's unit cell have been addressed in section 4.3.4. First restriction indicates that no wave can propagate at a phase constant greater than $2/h$ due to the discreteness of DJTL. Second assumption is that the size of the unit cell should be small enough in order that long-wave approximation becomes reasonable. This implies that the phase constant of the wave should be less than $0.6/h$. For DJTL with the spatial period of $h = 0.5$ mm, these two borders have been sketched by thick horizontal lines on the dispersion diagram of Fig. 4-16. Evidently, the design area is below the dashed line as illustrated in the Fig. 4-16.

TABLE II
NORMALIZATION RULE

Parameters and variables	*Normalization rule*
Frequency	$\tilde{\omega} = \omega\, /\omega_0$, i.e. $\omega_0 = 10^9$ rad/s
Propagation constant	$\tilde{\beta} = \beta\, /k_0, \tilde{\gamma} = \gamma\, /k_0,,$ i.e. $k_0 = 1m^{-1}$
Space	$\tilde{x} = x\, k_0$, i.e. $k_0 = 1m^{-1}$
Time	$\tilde{t} = t\, \omega_0$
Impedance	$\tilde{R} = R\, /R_0,\, R_0 = 50\, \Omega$
Inductance	$\tilde{L} = L\, \omega_0/R_0$
Capacitance	$\tilde{C} = C\, \omega_0 R_0$
Inductance per unit length	$\tilde{L} = L\, \omega_0/(R_0 k_0)$
Capacitance per unit length	$\tilde{C} = C\, \omega_0 R_0/k_0$
Current	$\tilde{I} = I\, /I_0,$ i.e. $I_0 = I_c$
Voltage	$\tilde{V} = V\, /(I_0 R_0)$
Flux	$\tilde{\Phi} = \Phi\, \omega_0/(R_0 I_0)$
Velocity	$\tilde{V_g} = V_g/V_{g0} = V_g k_0/\omega_0$
Permittivity	$\tilde{\epsilon} = \epsilon\, R_0 \omega_0/k_0$
Permeability	$\tilde{\mu} = \mu\, \omega_0/\, (R_0 k_0)$

Since the performance of microwave TEM transmission line is degraded at higher frequencies, we focus on the first three branches to conceive signal, pump and idler waves. Each branch is characterized by a vertical asymptotic line and a zero-crossing point that are expressed in terms of the waveguide's parameters as illustrated in Fig. 4-10 from section 4.3.2.. The first asymptotic line is related to the JJ's plasma frequency, $\omega_p = 1/\sqrt{L_J C_J}$, that is to be determined by fabrication process. The second branch has a crossing-point and an asymptotic line at $\omega_q = \omega_p\sqrt{1 + L_J/hL}$ and $\omega_{a1} = \pi/2\tau \ = \pi/(2l_s\sqrt{L_sC_s})$, respectively. Likewise, the third branch has one zero-crossing denoted by ω_{z1} and evaluated by the equation $\tan\omega\tau\,/\omega = -Z_0Ch$ in addition to one asymptotic line referred to by $\omega_{a2} = 3\pi/2\tau \ = 3\pi/(2l_s\sqrt{L_sC_s})$.

The graphical technique explained in section 4.2.3. is used to find three points, corresponding to three waves, on the dispersion diagram satisfying the phase-matching conditions (4.14) and (4.15). If these branches become closer to each other, the chance of getting solutions increases as transformed dispersion curve crosses the original dispersion curve. Thus, as L_J and h are fixed, L can be small in order to decrease the distance between ω_p and ω_q. Moreover, by increasing τ, which leads to an increase in l_s, L_s and C_s, the asymptotic $\omega_{a1} = \pi/2\tau$ moves to the left. Due to the size constraint, l_s cannot be arbitrarily large, but larger values for L_s and C_s are desirable. The roots of equation $\tan\omega\tau\,/\omega = -Z_0Ch$ which gives the zero-crossing points will be shifted to the left when C or Z_0 increases. As a result, lower value of L and larger values for L_s and C are desirable to make branches closer to each other that gives rise to better chance of having solution for phase-matching equations.

The signal wave is given at frequency $\tilde{\omega}_s = 3.48$ and phase constant $\tilde{\beta}_s = 974.3$. It is located on the first branch as seen in Fig. 4-16. Considering above discussions, following parameters are chosen to have a solution in the limit of long-wave approximation; $\tilde{L}_J = 0.2$, $\tilde{C}_J = 0.05$, $\tilde{L} = 250$ $\tilde{C} = 70$, $\tilde{Z}_{LC} = 1.88$, $\tilde{L}_s = 100$, $\tilde{C}_s = 10$, $\tilde{Z}_0 = 3.162$, $\tilde{l}_s = 0.002$ and $\tilde{h} = 0.0005$ where Z_{LC} and Z_0 is the characteristic impedance of LC transmission line given by $Z_{LC} = \sqrt{L/C}$ and $Z_0 = \sqrt{L_s/C_s}$. As demonstrated in Fig. 4-16., these parameters result in pump and idler waves with frequencies $\tilde{\omega}_p = 16.66$, $\tilde{\omega}_i = 29.83$ and phase constants $\tilde{\beta}_p = 966.3$, $\tilde{\beta}_i = 960.8$. According to Fig. 4-16, there is another set of solution as the curves cross each other at another point, but it is outside the region where solutions are acceptable.

To find the parameters from normalized values, we just need to find proper scaling factors k_0, ω_0, R_0 and I_0 to be used based on the normalization rules of Table II. The scaling factor for length and phase constant is chosen as $k_0 = 1\ \mathrm{m}^{-1}$. Concerning practical implementation, we have already set $h = 0.5$ mm, $l_s = 2$ mm. For applications such as superconducting qubits, we used $\omega_0 = 3.7$ Grad/s to cover the frequency range between 2 GHz and 16 GHz. Therefore, signal, pump and idler waves are characterized by $f_s = 2.049$ GHz, $f_p = 9.81$ GHz, $f_i = 17.566$ GHz, $\beta_s = 974.3\ \mathrm{m}^{-1}$, $\beta_p = 966.3\ \mathrm{m}^{-1}$ and $\beta_i = 960.8\ \mathrm{m}^{-1}$. Also, plasma frequency of JJ blocks is evaluated as $\omega_p = 37$ Grad/s or $f_p = 5.888$ GHz. In order to practically realize the TLs, we use the scaling factor $R_0 = 35\ \Omega$ which leads to $L_J = 1.8$ nH, $C_J = 380$ fF, $L = 2.36\ \mu\mathrm{H/m}$ $C = 0.54$ nF/m, $Z_{LC} = 65.8\ \Omega$, $L_s = 0.94\ \mu\mathrm{H/m}$, $C_s = 0.077$ nF/m, $Z_0 = 110.67\ \Omega$. By using Al-Al$_2$O$_3$-Al junctions with parameters [10], [105] $I_c = 2\ \mu\mathrm{A}$, $C_J = 10$ fF, $R_J = 50\ \Omega$, $L_{J0} = 0.17$ nH, an array of 10 junctions and a fit capacitance $C_{fit} = 380$ fF as illustrated in Fig. 4-1, are needed to realize the values of L_J and C_J. The shunt resistance associated with an array of JJs reaches $500\ \Omega$ which can be regarded as open-circuited and ignored.

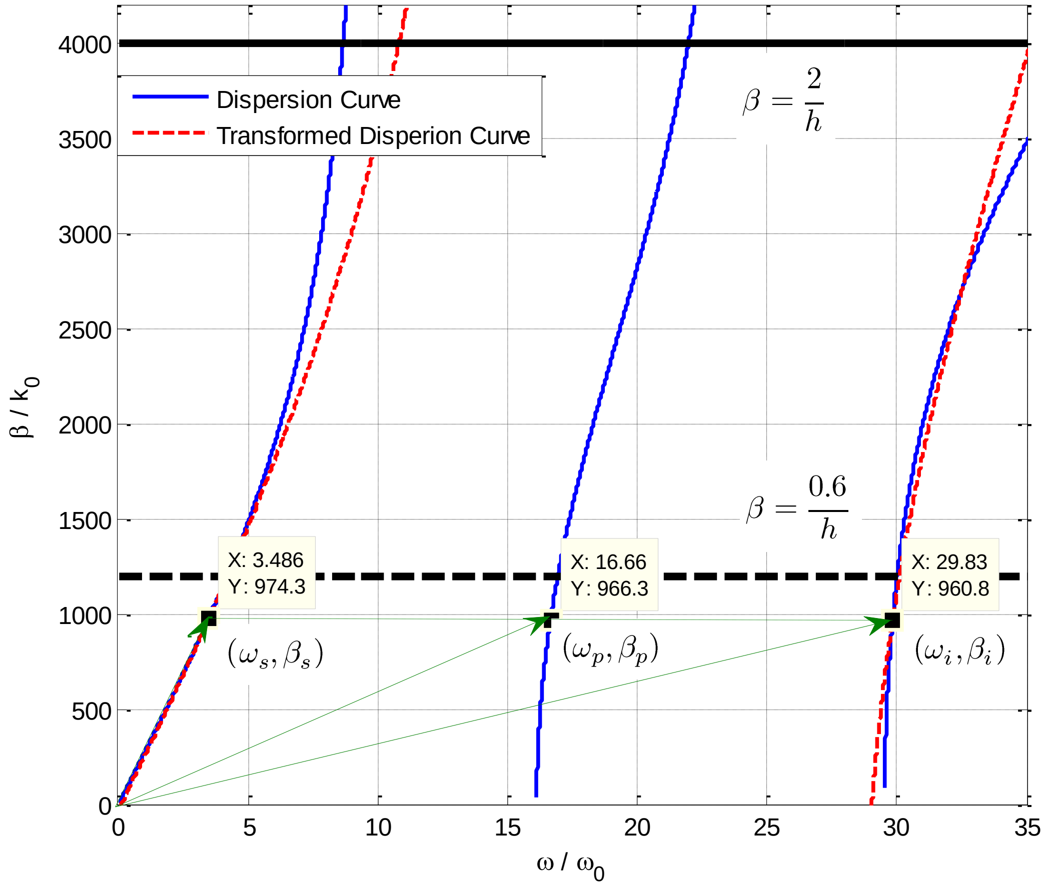

Fig. 4-16 Verification of existence of solutions for phase-matching equations, L_J=0.2, C_J=0.05, L=250, C=70, L_s=100, C_s=10, l_s=0.002, h=0.0005.

The plot of characteristics impedance, inductance and capacitance per unit length associated with a superconducting TL made of Nb versus aspect ratio a/b is shown in Fig. 4-17. Parameter a refers to the width of the center strip and parameter b denotes the distance between two grounds in the CPW configuration. This figure demonstrates that all values mentioned above are realizable over a CPW configuration.

Characteristic impedance associated with the DJTL assisted with open stubs are depicted in Fig. 4-18 and compared with the phase constant profile. When a band gap appears in dispersion diagram, the real part of the impedance dropped to zero which simply shows that maximum reflection occurs in this regime. This graph shows that three different impedances exist at signal, pump and idler frequencies which should be taken into account for impedance matching circuit design.

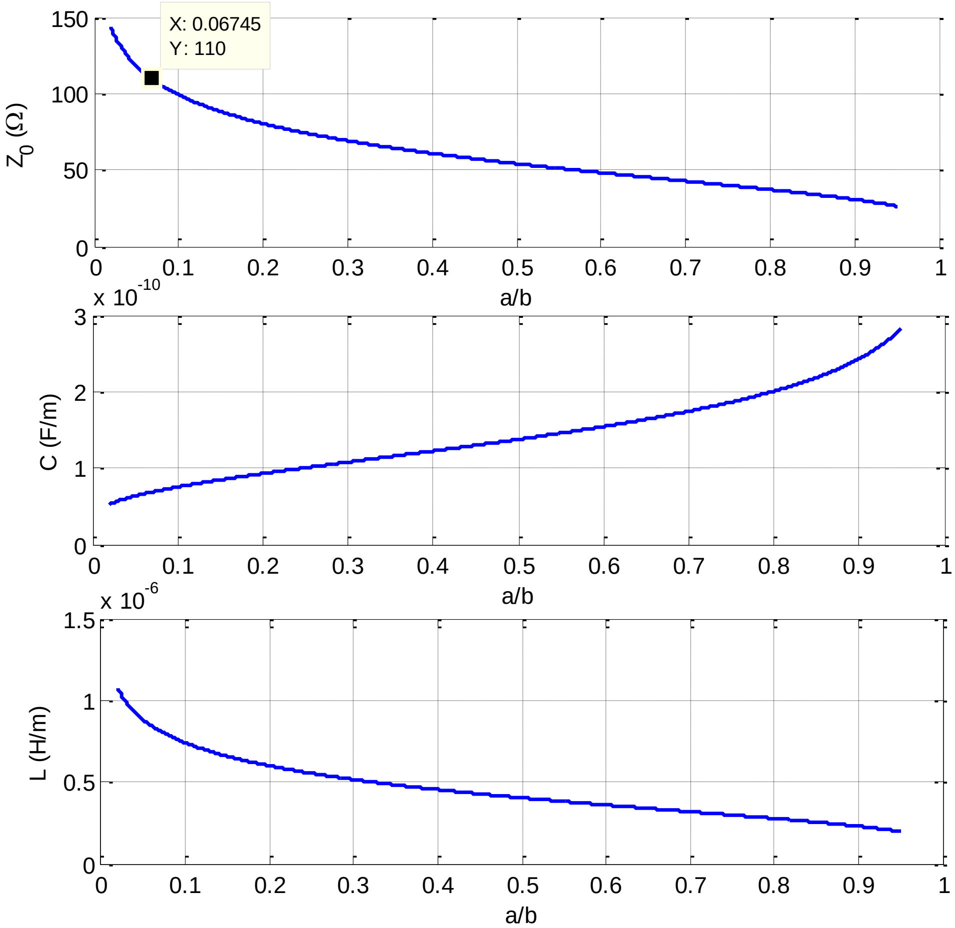

Fig. 4-17 Profiles of circuit parameters of a superconducting CPW made of Nb with thickness o3 400nm. Dielectric constant and thickness are ε_r=9 and 300µm.

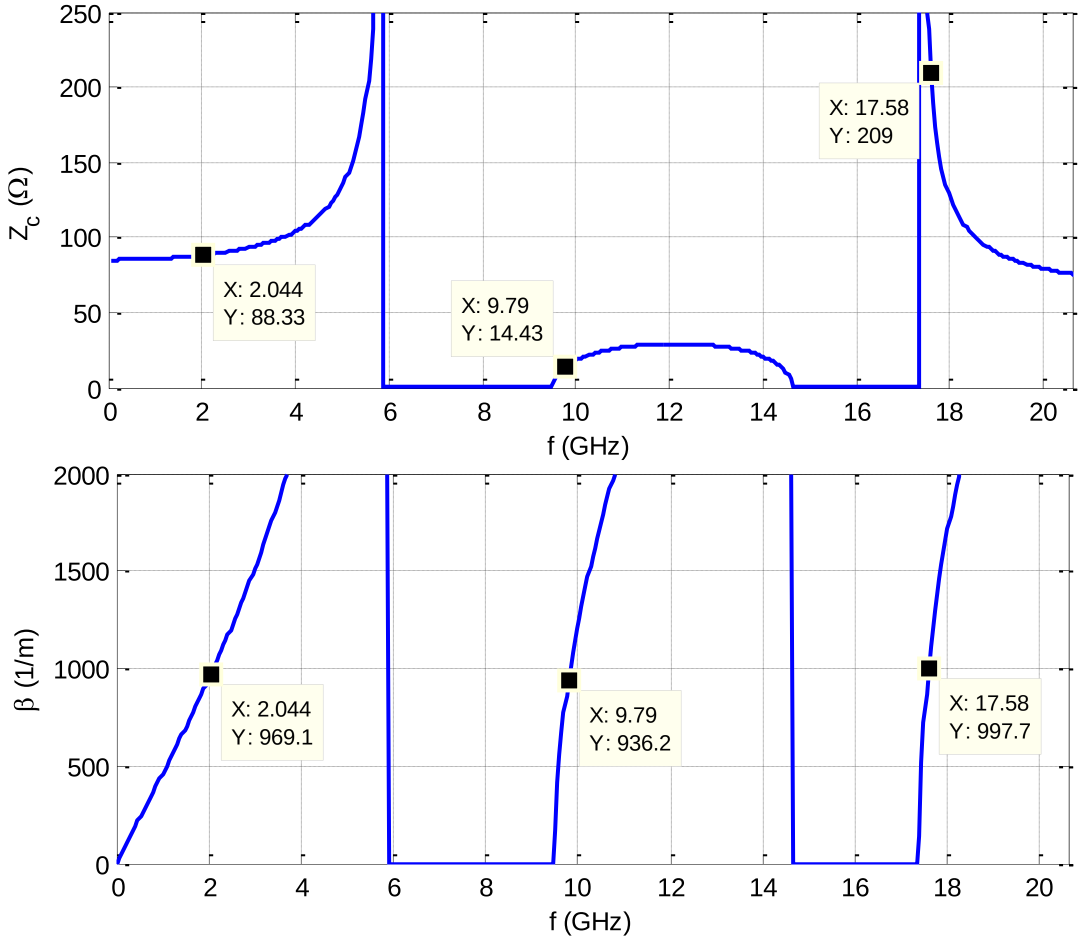

Fig. 4-18 Characteristic impedance (real part) and phase constant of a DJTL with open stubs. JJ blocks consist of 10 array. L_{J0}=1.8nH, C_{fit}=380 fF, L=2.36μH/m, C=0.54nF/m, C_s=0.077 nF/m, L_s=0.94 μH/m, l_s=2mm, h=0.5mm.

4.5 Conclusion

Superconducting transmission line periodically loaded by Josephson junctions was proposed as a nonlinear medium to provide a platform for investigation of nonlinear interaction to achieve a traveling-wave Josephson parametric amplifier. Long-wave assumption was applied to treat the structure as an effectively uniform waveguide and describe it by a nonlinear wave equation based on the transmission line model. In small amplitude regime, this structure, which is referred to as DJTL, exhibited linear behavior. The dominant TEM mode of this structure was engineered to give microwave band gaps. Realizablility of the dispersion relation based on Titchmarsh's theorem has also been assessed. As DJTL is a periodic structure, Floquet theorem has been applied to this structure which gave the cut-off condition and the limit for long-wave assumption. A graphical technique has been described to inspect the support of non-degenerate phase-matching condition based on the four-photon process. As a result, open-circuited stubs have been added to change the dispersion relation in order that DJTL support the phase-matching condition. Concerning microwave implementation of this structure, impedance analysis has been conducted to avoid impedance mismatch issues in practical design stage. A design example leading to realizable parameters was carried out which is useful in fabrication process.

Chapter 5

Finite Difference Time Domain Analysis of Series-Connected DJTL

5.1 Introduction

Using transmission line model in the preceding chapter, the series-connected DJTL is modeled by a set of partial differential equations (PDE) which is boiled down to a single nonlinear wave equation. This system of PDEs with a driving source at the beginning and mixed-boundary condition at the end offers a complete system of PDEs to display the device's performance. As discussed in the previous chapter, by driving DJTL below a limiting frequency, this model is accurate enough to describe the behavior of microwave propagation through the DJTL. This provides a mathematical foundation to investigate the microwave characteristics of the structure to develop devices such as traveling-wave Josephson parametric amplifier.

Due to the nonlinear equations arising from JJs, analytical and also frequency-domain methods fail to provide a solution for this problem, and employing a time-domain analysis is necessary to investigate the response of the device in various circumstances. Finite difference time domain (FDTD) method is a powerful technique to provide a numerical tool to evaluate the temporal and spatial evolution of the DJTL and compute both transient and steady state responses for all kinds of zero, weak, mild and strong nonlinearity associated with the structure [106],[107]. Although enormous computations can be carried out in using FDTD, this method is never regarded as a “brute force” technique, because employing FDTD requires subtle thinking and careful consideration of crucial issues such as choosing a proper scheme, consistency, degree of accuracy, stability criteria, gridding, excitation, numerical boundary conditions, fictitious boundary points and numerical dispersion.

We introduce a systematic approach to develop a rigorous one-dimensional FDTD solver based on the Lax-Wendroff explicit scheme to study the features of DJTL structures [108]. The validity of this tool is justified by comparing the results to those produced by implicit Crank-Nicolson technique, in addition to verifying limiting cases. With this method, one can monitor the time evolution of an incoming signal with any shape such as sinusoidal and Gaussian, during its trip along the DJTL and its interaction with other signals. Also, transient, steady state response of the line, and shape forming/deforming of any pulse can be investigated.

The rest of this chapter is organized as follows. After a brief introduction to FDTD technique in section 2, the numerical implimentation of FDTD accompanying the meticulous algorithm is fully described in section 3. DJTLs with open-stubs, DJTLs with the resistive-capacitive shunted junction (RCSJ) model and DJTLs with the basic model of bare JJ are solved with the robust explicit and implicit schemes of FDTD. Section 4 reports our simulation results based on the FDTD technique. With this new approach, we observe all the features associated with a typical nonlinear TL. They include cut-off propagation, controllable dispersive behavior, and shock wave formation. The propagation of resonant triads designed in previous chapter for signal, pump and idler is also verified in this section. Experimental demonstration of shock-waves in a nonlinear superconducting TL is addressed in section 5.

5.2 Finite Difference Time Domain Method

Finite Difference Time Domain (FDTD) method is a general numerical technique which provides a powerful approach to solve wave propagation in electromagnetic structures and media. These problems are mathematically modeled by a set of Partial Differential Equations (PDE) in terms of time and space variables with proper initial data and necessary boundary conditions, which is usually referred to as initial-boundary value problem [108]. FDTD method proceeds by replacing the derivatives in the differential equations by finite difference approximations on a grid staggered in time and space. Then by time marching, this gives a large number of algebraic equations to be solved in place of the differential equation, something that is easily solved by a computer.

Despite its inherent approximation, there exists some attractive features that arise considerable interest in the FDTD approach. The source of errors in FDTD calculations are well understood, so it can be controlled to permit an accurate model. Furthermore, implementation of FDTD can be done in a systematic approach in a sense that it can be easily applied to other problems. Using wideband sources, the FDTD method can compute a wideband response in one run, whereas frequency domain methods must obviously recompute the system response for each frequency point. Since the method makes no assumption regarding the nature of the solution, both transient and steady-state solution parts of the problem are included in the FDTD method. When the PDE contains nonlinearity, analytical and also frequency-domain methods often fail to provide a solution, but a numerical solution of nonlinear PDE is obtained by FDTD. Moreover, when the region is complex or the boundary conditions are of mixed types, FDTD is a good candidate to solve the problem [107],[106].

FDTD methods can be carried out by either explicit or implicit scheme. Both are based on time stepping on updated equations. In an explicit scheme, the solution at successive time step at each point can be obtained directly in terms of present values or previously computed values of that point and its neighbors. For a one-dimensional problem, an explicit finite difference scheme can be written in the form

$$u_m^{n+1} = \text{a finite sum over } \; u_{\acute{m}}^{\acute{n}} \qquad \acute{n} \leq n \tag{5.1}$$

where u_m^n is a discretized value of variable $u(x,t)$ with time and space step of $\Delta t = k$ and $\Delta x = h$ according to the relation [108]

$$u_m^n = u(mh, nk). \tag{5.2}$$

With an implicit scheme, the next value at a point is a function not only of the current and past values at this and surrounding points, but also the next values of some or all of these points. An implicit method requires the solution of a set of simultaneous equations in order to evaluate the unknowns which generally lead to a highly sparse matrix equation.

Explicit methods don't require matrix solution, so it is computationally simple, but has one serious drawback. The time step $\Delta t = k$ must be necessarily very small, because if it exceeds the certain amount, it produces instability. According to Courant-Friedrichs-Lewy (CFL) theorem [108], for an explicit scheme for the hyperbolic system of equations in the form

$$\frac{\partial \boldsymbol{U}}{\partial t} + \boldsymbol{A}\frac{\partial \boldsymbol{U}}{\partial z} = 0 \quad (5.3)$$

a necessary condition for the stability is

$$|a_i\lambda| \leq 1 \quad (5.4)$$

for all eigenvalues a_i of the matrix $\boldsymbol{A}$, where $\lambda = k/h$ and $\boldsymbol{U}$ is a vector containing all variables. As eigenvalues a_i are the slopes of characteristic lines of the PDE (5.3), they are regarded as phase velocities of the wave propagation in the medium [109]. Note that CFL expresses a necessary, but not sufficient, condition for stability, since numerical boundary conditions can also cause instabilities [108]. Notice that CFL theorem does not extend to implicit schemes, and they are unconditionally stable for every value of λ. Nonetheless, choosing λ arbitrary large for an implicit scheme, we might lose the accuracy of the solution, unless λ is restricted to reasonable values [108].

In addition to the stability issue, a numerical algorithm such as FDTD can introduce numerical dispersion and dissipation, even when waves are propagating in a distortionless and nondissipative medium. They are undesirable effects with numeric origin, but they can be controlled by making the mesh sufficiently fine. On the other hand, the price to be paid is a large number of equations which dramatically reduce the speed of computation. This becomes prohibitive for large practical problems. However, there is another tractable way to avoid such a trouble which is called as a magic time-step [106]. As a general principle, for hyperbolic partial differential equations (5.3), it is best to run the FDTD code as close to the CFL stability limit (take $|a\lambda|$ close to the one) as possible to keep the dispersion and dissipation small. If we are interested in a particular frequency, say ω_0, then we should chose time step k , so that $k\omega_0$is much less than π to get accurate results, both in the speed of the wave (dispersion) and in the amplitude (dissipation).

Numerical boundary condition is another topic in FDTD. In addition to initial data and boundary conditions, many schemes also require additional boundary conditions called numerical boundary conditions to make the PDE well-posed and determine the solution uniquely. Sometimes this can be achieved by inserting extra fictitious points beyond the boundaries. This is due to the fact that the number of equations and unknowns must be equal to each other. It is very important to clearly distinguish between real-imposed and numerical boundary conditions to avoid solving overdetermined or underdetermined problems. As mentioned in the preceding paragraphs, the numerical boundary condition coupled with a particular scheme can give rise to instability, so care should be taken when we want to embed a numerical boundary condition into the problem [108].

5.3 Numerical Implementation of Nonlinear FDTD for Series-Connected DJTLs

In this part, the details of FDTD technique that has been developed to solve various types of DJTL is explained.

5.3.1 DJTL Assisted by Open Stubs

The governing equations representing the physical behavior of the DJTL structure with open stubs, shown in Fig. 4-9, consist of five delay differential equations. Referring to section 4.3.1, there exist five reactive elements in the unit cell depicted in Fig. 4-9, so the state of the structure is determined by five variables satisfying five coupled equations as follows

$$\frac{\partial I}{\partial t}+\frac{1}{L}\frac{\partial V}{\partial x}=\frac{-V_J}{Lh} \tag{5.5}$$

$$\frac{\partial V(x+h,t)}{\partial t}+\frac{1}{C}\frac{\partial I}{\partial x}+\frac{I_{stub}}{Ch}=0 \tag{5.6}$$

$$\frac{\partial \Phi_J}{\partial t}=V_J \tag{5.7}$$

$$I(x,t)=I_c\sin\left(2\pi\frac{\Phi_J}{\Phi_0}\right)+C_J\frac{\partial V_J}{\partial t}+\frac{V_J}{R_J} \tag{5.8}$$

$$\begin{aligned} Z_0[I_{stub}(x+h,t)+I_{stub}(x+h,t-2\tau)] \\ =V(x+h,t)-V(x+h,t-2\tau). \end{aligned} \tag{5.9}$$

All variables and parameters have been described in section 4.3.1.. Putting a voltage source $V_s(t)$ with an associated series resistance R_s and a load impedance R_L at two ends of the DJTL and setting all variables to zero before $t=0$, a set of complete well-posed equations are obtained. This includes a system of partial differential equations (5.5)-(5.9) with mixed boundary conditions and zero initial values in the form of

$$V_s(t) = R_s I(0,t) + V(0,t) \tag{5.10}$$

$$V(x_{max},t) = R_L I(x_{max},t) \tag{5.11}$$

$$V(z,t) = I(x,t) = V_J(x,t) = \Phi_J(x,t) = I_{stub}(x,t) = 0 \;\; t < 0 \tag{5.12}$$

The first step in establishing an FDTD solver is to set up a regular grid in space and time. Time and space steps are denoted by k and h respectively, and the total number of temporal and spatial grids in the interior computational domain is referred by N and M. Because of the modeling approach we chose, the space step h must be equal to the unit cell length of DJTL. The next step is to approximate the differential equations with proper finite difference scheme. We used explicit Lax-Wendroff scheme [110],[108] which can fit well to our problem. This scheme provides a second order accuracy by itself, so there is no need to complicate the implementation by defining additional grids points at half-time and half-space [107],[106],[111]. Using Lax-Wendroff scheme and discrete notation defined by $u_m^n = u(mh, nk)$, this gives five update equations as follows

$$\begin{aligned} V_m^{n+1} + \frac{k}{2Ch} {I_{stub}}_m^{n+1} \\ &= V_m^n - \frac{\lambda}{2C}\left(I_{m+1}^n - I_{m-1}^n\right) + \frac{\lambda^2}{2LC}\left(V_{m+1}^n - 2V_m^n + V_{m-1}^n\right) \\ &+ \frac{k\lambda}{4LCh}\left({V_J}_{m+1}^n - {V_J}_{m-1}^n\right) - \frac{k}{2Ch} {I_{stub}}_m^n \end{aligned} \tag{5.13}$$

$$\begin{aligned} I_m^{n+1} + \frac{k}{2Lh} {V_J}_m^{n+1} \\ &= I_m^n - \frac{\lambda}{2L}\left(V_{m+1}^n - V_{m-1}^n\right) + \frac{\lambda^2}{2LC}\left(I_{m+1}^n - 2I_m^n + I_{m-1}^n\right) \\ &+ \frac{k\lambda}{4Ch}\left({I_{stub}}_{m+1}^n - {I_{stub}}_{m-1}^n\right) - \frac{k}{2Lh} {V_J}_m^n \end{aligned} \tag{5.14}$$

$$\begin{aligned} -\frac{k}{2C_J} I_m^{n+1} + \left(1 + \frac{k}{2C_J R_J}\right) {V_J}_m^{n+1} + \frac{kI_c}{2C_J} \sin\left(2\pi \frac{{\Phi_J}_m^{n+1}}{\Phi_0}\right) \\ = \left(1 - \frac{k}{2C_J R_J}\right) {V_J}_m^n + \frac{k}{2C_J} I_m^n - \frac{kI_c}{2C_J} \sin\left(2\pi \frac{{\Phi_J}_m^n}{\Phi_0}\right) \end{aligned} \tag{5.15}$$

$${\Phi_J}_m^{n+1} - \frac{k}{2} {V_J}_m^{n+1} = {\Phi_J}_m^n + \frac{k}{2} {V_J}_m^n \tag{5.16}$$

$$V_m^{n+1} - Z_0 {I_{stub}}_m^{n+1} = V_m^{n+1-n_0} + Z_0 {I_{stub}}_m^{n+1-n_0} \tag{5.17}$$

where n_0 is the number of time steps between zero and -2τ defined by $n_0 = [2\tau/k]$. The bracket indicates the integer part of the variable. They are necessary in computing the value of variables for the next time step, since a delay differential equation exists in the governing equations. It can be perceived that (5.13)-(5.17) involve five unknowns that are entangled to each other through five nonlinear equations, so at each grid in the computational domain we should solve a system of nonlinear simultaneous equations. By putting all five variables in a vector such as $\boldsymbol{U}_m^n = \left[V_m^n \quad I_m^n \quad {V_J}_m^n \quad {\Phi_J}_m^n \quad {I_{stub}}_m^n\right]^T$, equations (5.13)-(5.17) can be expressed by an implicit nonlinear function such as $\mathbf{F}\left(\boldsymbol{U}_m^{n+1}, \boldsymbol{U}_m^n, \boldsymbol{U}_{m-1}^n, \boldsymbol{U}_{m+1}^n, \boldsymbol{U}_m^{n+1-n_0}\right) = 0$. The goal is to solve $\boldsymbol{U}_m^{n+1}$ when all $\boldsymbol{U}_m^n$, $\boldsymbol{U}_{m-1}^n$, $\boldsymbol{U}_{m+1}^n$ and , $\boldsymbol{U}_m^{n+1-n_0}$ are known. This connection is shown by the computational molecule in Fig. 5-1.

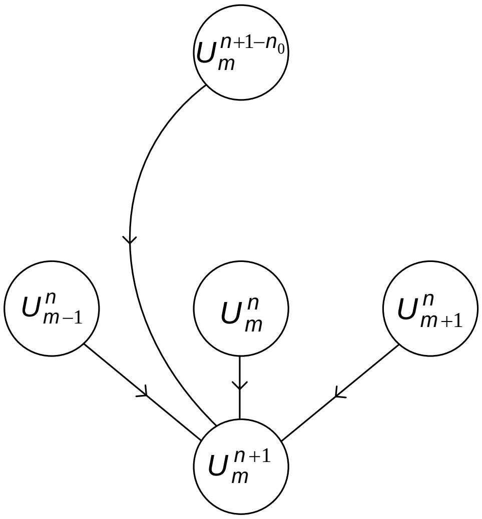

Fig. 5-1 Computational molecule of explicit FDTD for analyzing the DJTL assisted by open stubs.

Fig. 5-2 sheds more light on the implementation of FDTD for DJTL structures. Time and space grids are assigned for each of the five variables, and they are classified into four domains; interior computational domain, initial-value grids, boundary grids, and extra fictitious points. Computational molecule of Fig. 5-1 starts the act of computation at the time step $n = n_0 + 1$ from the top-left point $(m = 3)$ in the interior grids and moves to the right direction up to the last point corresponding to $m = M$. As inferred from the computational molecule, Fig. 5-1 ,the initial-value points at time step $n = 1$ is involved in evaluation grids at time step $n = n_0 + 1$. Then, it goes to the lower and upper boundary points located at $m = 2$ and $m = M + 1$ to update their values. At the boundaries, there exists mixed boundary conditions as pointed out in (5.10) and (5.11). They are discretized by

$$V_2^{n+1} = V_s(t_{n+1}) - R_s I_2^{n+1} \tag{5.18}$$

$$V_{M+1}^{n+1} = R_L I_{M+1}^{n+1}. \tag{5.19}$$

Computing the values of $\boldsymbol{U}$ vector at the boundaries, variable V at time step $n+1$ must be replaced by the expressions in (5.18) and (5.19) that boundary conditions imposes for the beginning and the end boundary points, respectively.

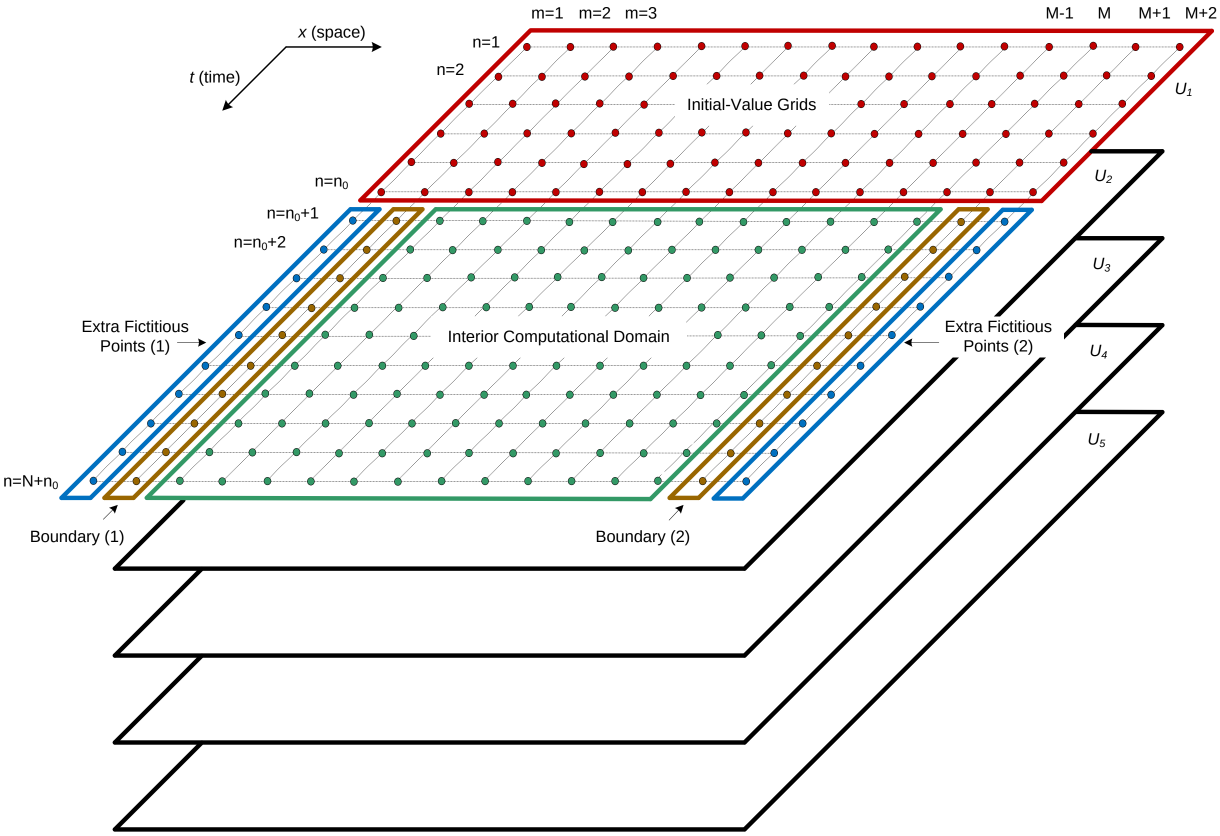

Fig. 5-2 A system of five simultaneously PDEs with five unknowns are descretisized in time-space plane. Four different types of grids are shown: interior computation domain, boundary grids, initial-value grids and extra fictitious points.

Obviously, by applying this computational molecule at points on two boundaries, two fictitious points appear at each time step. Due to the possibility of generating instability, as mentioned before, care should be taken to compute such points. We use the following relations to calculate extra-left and extra-right points respectively [108]

$$\boldsymbol{U}_1^{n+1} = 2\boldsymbol{U}_2^{n+1} - \boldsymbol{U}_3^{n+1} \tag{5.20}$$

$$\boldsymbol{U}_{M+2}^{n+1} = 2\boldsymbol{U}_{M+1}^{n+1} - \boldsymbol{U}_M^{n+1}. \tag{5.21}$$

Complete and detailed procedure is illustrated in the flowchart of Fig. 5-3.

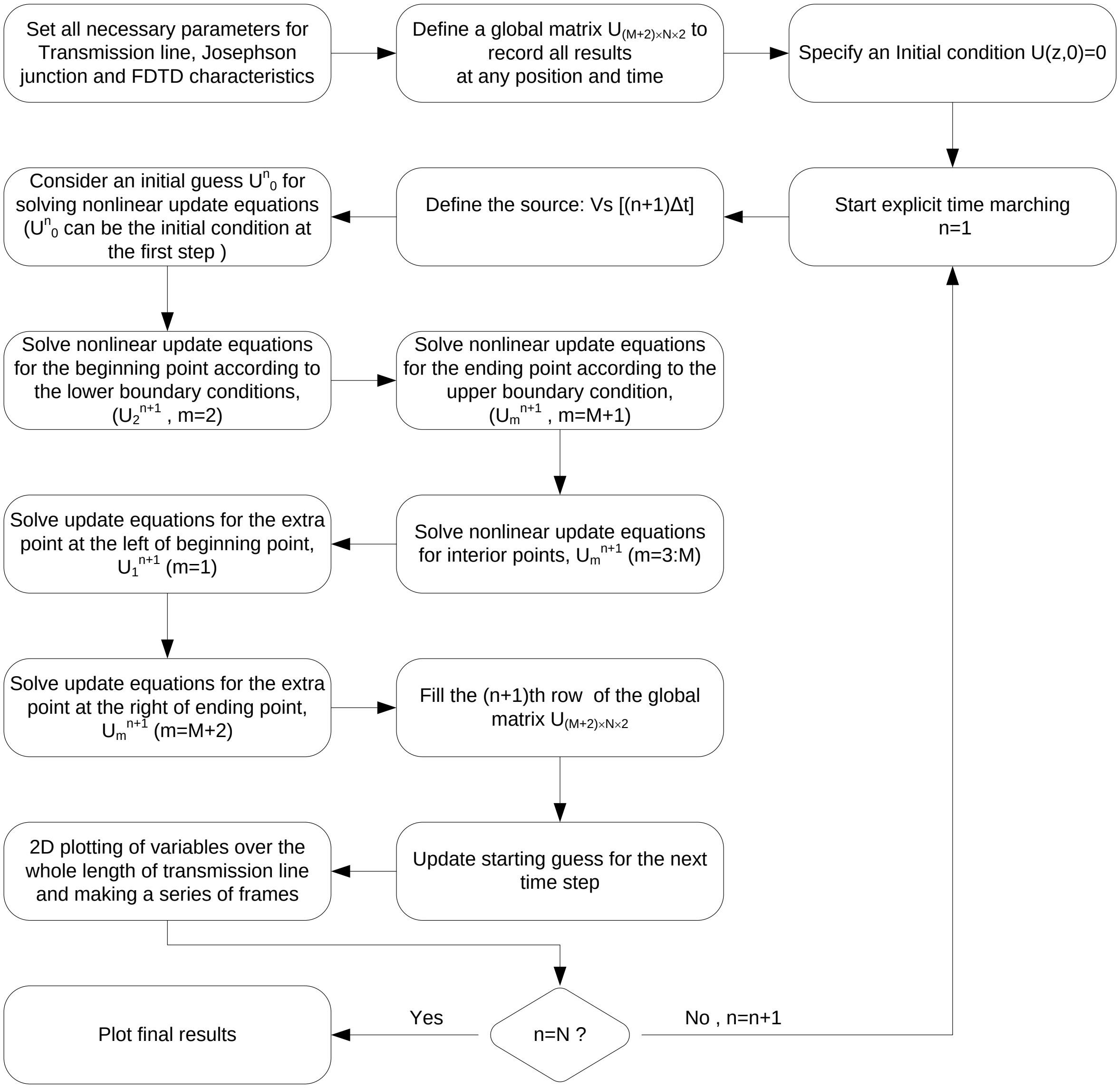

Fig. 5-3 Flowchart including all details for explicit implementation of FDTD to analyze the DJTL.

5.3.2 DJTL without Open Stubs

Equations (5.5)-(5.9) that describe the microwave characteristics of a DJTL without open stubs ($\tau = 0$) are restated in the matrix form

$$\frac{\partial \boldsymbol{U}}{\partial t} = \boldsymbol{f}(\boldsymbol{U}) - \frac{\partial \boldsymbol{F}(\boldsymbol{U})}{\partial x} \tag{5.22}$$

where column vectors $\boldsymbol{U}$, $\boldsymbol{F}(\boldsymbol{U})$ and $\boldsymbol{f}(\boldsymbol{U})$ are defined as $\boldsymbol{U} = [V \quad I \quad V_J \quad \Phi_J]^{\boldsymbol{T}}$, $\boldsymbol{F}(\boldsymbol{U}) = [I/C \quad V/L \quad 0 \quad 0]^{\boldsymbol{T}}$ and

$$\boldsymbol{f}(\boldsymbol{U}) = \begin{bmatrix} 0 \\ \frac{-1}{Lh} V_J \\ \frac{1}{C_J} I - \frac{1}{R_J C_J} V_J - \frac{I_c}{C_J} \sin\left(2\pi \frac{\Phi_J}{\Phi_0}\right) \\ \mathrm{V}_J \end{bmatrix}. \tag{5.23}$$

Note that $\boldsymbol{f}(\boldsymbol{U})$ is a nonlinear function of $\boldsymbol{U}$. Applying Lax-Wendroff scheme, update equation can be obtained as follows

$$\begin{aligned} \boldsymbol{U}_m^{n+1} = \boldsymbol{U}_{\boldsymbol{m}}^{\boldsymbol{n}} - \frac{\lambda}{2}[\boldsymbol{F}(\boldsymbol{U}_{m+1}^n) - \boldsymbol{F}(\boldsymbol{U}_{m-1}^n)] \\ + \frac{\lambda^2}{2}\left\{\boldsymbol{J}\left(\boldsymbol{U}_{m+\frac{1}{2}}^n\right)[\boldsymbol{F}(\boldsymbol{U}_{m+1}^n) - \boldsymbol{F}(\boldsymbol{U}_m^n)]\right. \\ \left. - \boldsymbol{J}\left(\boldsymbol{U}_{m-\frac{1}{2}}^n\right)[\boldsymbol{F}(\boldsymbol{U}_m^n) - \boldsymbol{F}(\boldsymbol{U}_{m-1}^n)]\right\} \\ - k\frac{\lambda}{4}[\boldsymbol{J}(\boldsymbol{U}_{m+1}^n)\boldsymbol{f}_{m+1}^n - \boldsymbol{J}(\boldsymbol{U}_{m-1}^n)\boldsymbol{f}_{m-1}^n] \\ + \frac{k}{2}(\boldsymbol{f}_m^{n+1} + \boldsymbol{f}_m^n) \end{aligned} \tag{5.24}$$

where $\lambda = k/h$, $\boldsymbol{U}_m^n$ is the value of matrix $\boldsymbol{U}$ evaluated at $x = mh$ and $t = nk$ and $\boldsymbol{J}(\boldsymbol{U}_m^n)$ is the 4-by-4 Jacobian matrix whose entries are defined by

$$\boldsymbol{J}_{\boldsymbol{i},\boldsymbol{j}} = \frac{\partial \boldsymbol{F}_{\boldsymbol{i}}}{\partial \boldsymbol{U}_{\boldsymbol{j}}}, \qquad i,j = 1,2,3,4 \tag{5.25}$$

where $\boldsymbol{F}_{\boldsymbol{i}}$ and $\boldsymbol{U}_{\boldsymbol{j}}$ are ith and jth element in column vectors $\boldsymbol{F}$ and $\boldsymbol{U}$. To avoid midpoint evaluations, the Jacobian matrices can be found by

$$\boldsymbol{J}(\boldsymbol{U}_{m+\frac{1}{2}}^n) = \frac{\boldsymbol{J}(\boldsymbol{U}_m^n) + \boldsymbol{J}(\boldsymbol{U}_{m+1}^n)}{2} \tag{5.26}$$

$$\boldsymbol{J}(\boldsymbol{U}_{m-\frac{1}{2}}^n) = \frac{\boldsymbol{J}(\boldsymbol{U}_{m-1}^n) + \boldsymbol{J}(\boldsymbol{U}_m^n)}{2}. \tag{5.27}$$

Equation (5.24) involves four unknowns that are coupled to each other through four nonlinear equations, so at each grid in the computational domain, as shown in Fig. 5-2, a system of nonlinear simultaneous equations must be solved. Also, the computational molecule reduces to one illustrated in Fig. 5-4. Boundary conditions and extra points that numerical scheme imposes on the computation process are the same as those mentioned in the previous section through equations (5.18) and (5.19).

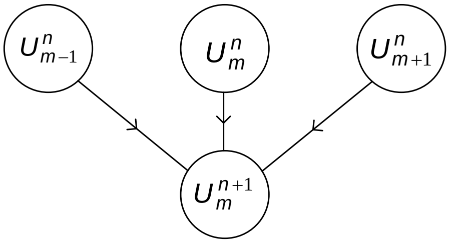

Fig. 5-4 Computational molecule of explicit FDTD for analyzing the DJTL.

It should be noted that by setting $R_J = \infty$ or $R_J = 0$ the shunt resistance associated with JJ becomes open-circuited or short-circuited, respectively, and the two extreme cases are taken into account. The former is the lossless TL and the latter is a linear and normal TL without JJ blocks.

5.3.3 DJTL with the Basic Modeling for JJ

By lowering the temperature far below the critical temperature of superconductors, the normal resistive channel of the junction can be removed, and the basic model of the JJ can be used, provided the flowing current is restricted less than the critical current I_c. The schematic of distributed circuit is shown in Fig. 5-5. Therefore by removing the capacitive and resistive channel in JJ, the nonlinear equations that characterize the propagation of the voltage and current is obtained as

$$\begin{cases} \dfrac{\partial V}{\partial x} = -L\dfrac{\partial I}{\partial t} - \dfrac{NI_cL_J}{h}\dfrac{\partial}{\partial t}\left[\sin^{-1}\left(\dfrac{I}{I_c}\right)\right] \\ \dfrac{\partial I}{\partial x} = -C\dfrac{\partial V}{\partial t} \end{cases}. \tag{5.28}$$

As mentioned in the previous section, instead of a single junction, there exists an array of N junctions at each unit cell, such that the effective mounted inductance will be NL_J instead of L_J, as illustrated in Fig. 4-1(b). Eliminating one of these two coupled variables, i.e. voltage, results in the following nonlinear wave equations for the current

$$\frac{\partial^2 I}{\partial x^2} = LC\frac{\partial^2 I}{\partial t^2} + \frac{NI_cL_JC}{h}\frac{\partial^2}{\partial t^2}\left[\sin^{-1}\left(\frac{I}{I_c}\right)\right]. \tag{5.29}$$

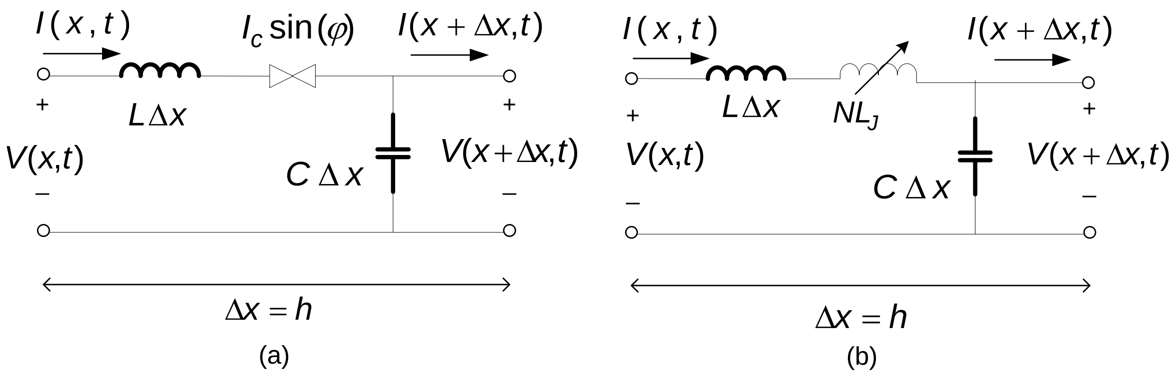

Fig. 5-5 Distributed circuit model of series-connected DJTL with basic JJ (a) and its nonlinear inductor model (b), respectively, for an array of N junctions. The period of the transmission line is denoted by Δx=h.

The system of nonlinear equations in (5.28) can be rewritten in the form

$$\frac{\partial \boldsymbol{U}}{\partial t} + \frac{\partial \boldsymbol{F}(\boldsymbol{U})}{\partial x} = 0 \tag{5.30}$$

where $\boldsymbol{F}(\boldsymbol{U})$ is a nonlinear function of $\boldsymbol{U}$. Moreover, $\boldsymbol{U}$ and $\boldsymbol{F}(\boldsymbol{U})$ are column vectors with two components as follows

$$\boldsymbol{U} = \begin{bmatrix} \Phi \\ V \end{bmatrix} \tag{5.31}$$

$$\boldsymbol{F}(\boldsymbol{U}) = \begin{bmatrix} V \\ \dfrac{g^{-1}(\Phi)}{C} \end{bmatrix}. \tag{5.32}$$

To simplify the formulation, we have used an auxiliary variable Φ, instead of current, with the relation

$$\Phi = g(I) = LI + N\frac{L_J}{h} I_c \sin^{-1}\left(\frac{I}{I_c}\right). \tag{5.33}$$

In fact, Φ represents flux per unit length stored in inductors associated with both transmission lines and Josephson junctions. Hence, based on the inverse relation of $I = g^{-1}(\Phi)$, current at any time and location can be calculated when Φ is known.

Using explicit Lax-Wendroff scheme, it gives the update equations as follows

$$\begin{aligned} \boldsymbol{U}_m^{n+1} = \boldsymbol{U}_m^n - \frac{\lambda}{2}[\boldsymbol{F}(\boldsymbol{U}_{m+1}^n) - \boldsymbol{F}(\boldsymbol{U}_{m-1}^n)] \\ + \frac{\lambda^2}{2}\Big\{\boldsymbol{J}(\boldsymbol{U}_{m+\frac{1}{2}}^n)[\boldsymbol{F}(\boldsymbol{U}_{m+1}^n) - \boldsymbol{F}(\boldsymbol{U}_m^n)] \\ - \boldsymbol{J}(\boldsymbol{U}_{m-\frac{1}{2}}^n)[\boldsymbol{F}(\boldsymbol{U}_m^n) - \boldsymbol{F}(\boldsymbol{U}_{m-1}^n)]\Big\} \quad (3.53) \end{aligned} \tag{5.34}$$

where $\boldsymbol{J}(\boldsymbol{U}_m^n)$ represents a Jacobian matrix that for this problem is a 2-by-2 matrix evaluated by

$$\boldsymbol{J}(\boldsymbol{U}) = \begin{bmatrix} 0 & 1 \\ \dfrac{1}{CL + \dfrac{CNL_{J0}}{h\sqrt{1 - \left(\dfrac{g^{-1}(\Phi)}{I_c}\right)^2}}} & 0 \end{bmatrix}. \tag{5.35}$$

To avoid midpoint evaluations, the Jacobian matrices in the update equation (5.34) is found by equations (5.26) and (5.27) in the previous section. The rest of the explicit FDTD implementation will be similar to what was explained in the previous sections.

Dispersion relation for this structure is

$$\beta^2 = \left(L + N\frac{L_J}{h}\right)C\omega^2 \tag{5.36}$$

and Bragg cut-off frequency and the condition for propagation are given by

$$\omega \leq \frac{2}{\sqrt{LCh^2 + NL_JCh}}. \tag{5.37}$$

Long-wave approximation explained in section 4.4.2 can be obtained by following inequality

$$\omega \leq \frac{0.6}{\sqrt{LCh^2 + NL_JCh}}. \tag{5.38}$$

5.3.4 Implicit FDTD Scheme for DJTL

The execution of the explicit method centers on the way of forming a system of equations whose solution includes all values of variables at all spatial grids at a certain time. Although our explicit method is completely accurate and stable, we tried to solve our problem with the implicit method as well, to demonstrate the validity of our results.

For DJTL with the basic modeling of JJ and M spatial points in the computational domain, we construct a new 2M-by-1 vector at each time step, called $\boldsymbol{X}$**,** by putting all $\boldsymbol{U}$ vectors together as shown in

$$\boldsymbol{X}_{2M\times1}^n = [\boldsymbol{U}_1^n \quad \boldsymbol{U}_2^n \quad \cdots \quad \boldsymbol{U}_{M-1}^n \quad \boldsymbol{U}_M^n]^T \tag{5.39}$$

and described in Table III. Then we apply the Crank-Nicolson scheme [108] to (5.30) in order to derive a discretized expression. This attempt gives

$$\begin{aligned}\frac{\lambda}{4}\boldsymbol{F}(\boldsymbol{U}_{m+1}^{n+1})+\boldsymbol{U}_{m}^{n+1}-\frac{\lambda}{4}\boldsymbol{F}(\boldsymbol{U}_{m-1}^{n+1})&\\ =\frac{-\lambda}{4}\boldsymbol{F}(\boldsymbol{U}_{m+1}^{n})+\boldsymbol{U}_{m}^{n}+\frac{\lambda}{4}\boldsymbol{F}(\boldsymbol{U}_{m-1}^{n})&\end{aligned} \tag{5.40}$$

TABLE III

DEFINING UNKNOWN VECTOR IN IMPLICIT FDTD METHOD

Elements of X vector in implicit scheme	Corresponding U vectors in explicit method	Corresponding flux and voltage variables
$\boldsymbol{X}^n(1)$	$\boldsymbol{U}_1^n(1)$	Φ_1^n
$\boldsymbol{X}^n(2)$	$\boldsymbol{U}_1^n(2)$	V_1^n
…	…	…
…	…	…
$\boldsymbol{X}^n(2m-3)$	$\boldsymbol{U}_{m-1}^n(1)$	Φ_{m-1}^n
$\boldsymbol{X}^n(2m-2)$	$\boldsymbol{U}_{m-1}^n(2)$	V_{m-1}^n
$\boldsymbol{X}^n(2m-1)$	$\boldsymbol{U}_{m}^n(1)$	Φ_{m}^n
$\boldsymbol{X}^n(2m)$	$\boldsymbol{U}_{m}^n(2)$	V_{m}^n
$\boldsymbol{X}^n(2m+1)$	$\boldsymbol{U}_{m+1}^n(1)$	Φ_{m+1}^n
$\boldsymbol{X}^n(2m+2)$	$\boldsymbol{U}_{m+1}^n(2)$	V_{m+1}^n
…	…	…
…	…	…
$\boldsymbol{X}^n(2M-1)$	$\boldsymbol{U}_{M}^n(1)$	Φ_{M}^n
$\boldsymbol{X}^n(2M)$	$\boldsymbol{U}_{M}^n(2)$	V_{M}^n

Relation between variables, vectors used in explicit and implicit FDTD method for DJTL:
$\boldsymbol{X}_{2M\times 1}^{n}=[\boldsymbol{U}_1^n \quad \boldsymbol{U}_2^n \quad \cdots \quad \boldsymbol{U}_{M-1}^n \quad \boldsymbol{U}_M^n]^T$.

By applying this equation to interior points ($m = 2 : M-1$), $2M-4$ equations can be obtained. As the number of unknowns are $2M$, four more equations are required to construct a consistent system of equations with 2M unknowns and 2M equations. Boundary conditions at two ends provides two equations as written in (5.18)-(5.19) and we need two numerical boundary conditions similar to (5.20)-(5.21) to have a system of consistent equations. The flowchart in Fig. 5-6 illustrates the computation flow of this implicit FDTD algorithm.

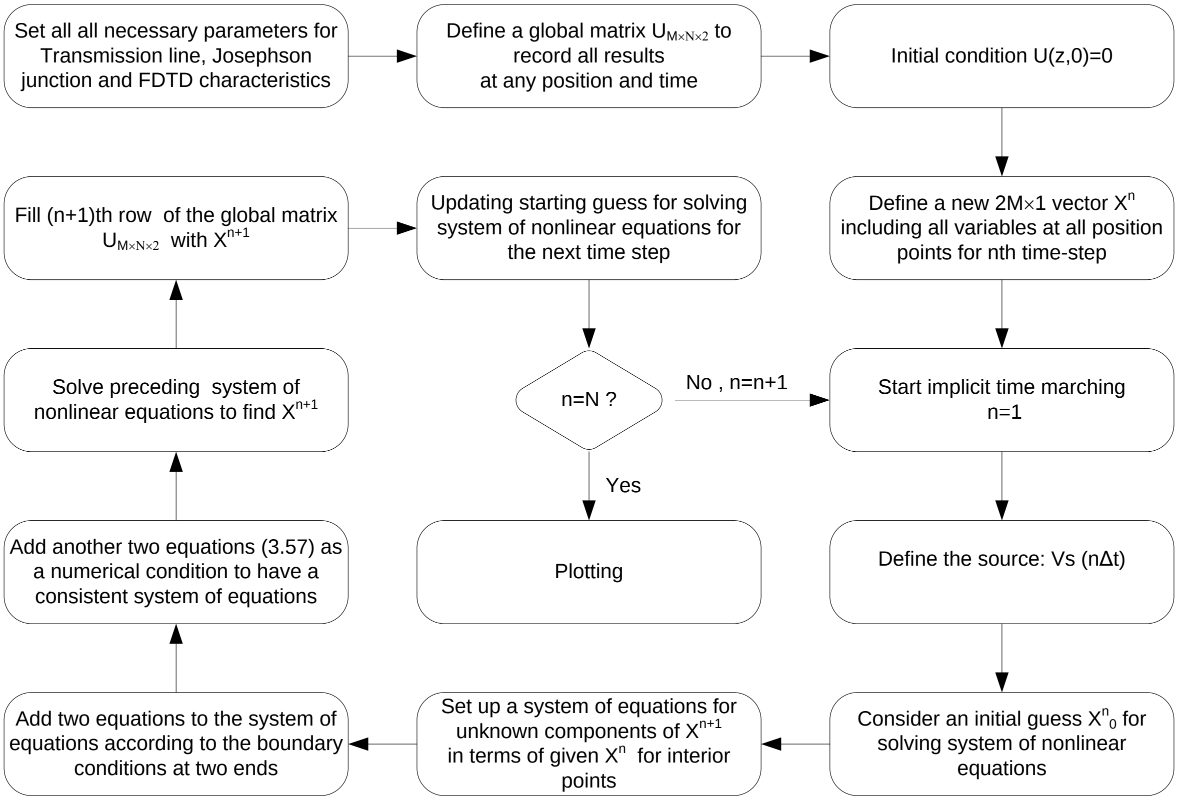

Fig. 5-6 Flowchart describing the full details of the implicit FDTD algorithm to analyze the DJTL.

5.4 Numerical Results

For a $3\mu m \times 3\mu m$ Josephson junction constructed by Nb-AlO$_x$-Nb technology offered by HYPRES in high current density process, the junction's parameters are $I_c = 405\ \mu\text{A}$, $T_c = 9.2\ \text{K}$, $T = 4.2\ \text{K}$, $C_J = 0.531\ \text{pF}$ and $R_J = 3.2\Omega$ [61], [112], which yields zero-current inductance $L_J = 0.812\ \text{pH}$, plasma frequency $\omega_p = 1.522\ \text{Trad/s}$ and Stewart-McCumber parameter $\beta_c = 6.73$. Considering another junction made of Pb-PbO-Pb, the measured junction's parameters are $I_c = 254\ \mu\text{A}$, $T_c = 7.19\ \text{K}$, $T = 4.2\ \text{K}$, $C_J = 5\ \text{fF}$, $R_J = 20\ \Omega$, so $L_J = 1.2\text{pH}$ which is so small [39], [113]. Therefore, arrays or stacks of N identical Josephson junctions are used to increase the total inductance of the structure. This array can be represented by a single junction with N times larger inductance, N times larger resistance, and N times smaller capacitance compared to a single junction. This equivalent model is correct when all junctions are identical. explaining more, there exists three distinct channels for current flow in a typical Josephson junction: inductive channel for cooper pairs, resistive channel for normal electron and capacitive channel for displacement current. The current in the inductive channel, for an array doesn't change as these JJs are in series. The inductive channel can be modeled by a single equivalent JJ by assuming a magnetic flux quanta in all equations which is N times larger than the magnetic flux quanta when only one junction is the case [114].

We consider Al-Al$_2$O$_3$-Al Josephson junctions as they have small critical current which leads to the larger inductance. For Al technology, typically $I_c = 2$ μA, $L_J = 0.17$ nH and $C_J = 5$ fF and $R_J = 50\ \Omega$. As mentioned in section 4.2, it is possible to put an extra shunt capacitance with the JJ to increase the capacitance and reduce the plasma frequency. Doing this, the plasma frequency of junctions fabricated by Al-Al$_2$O$_3$-Al technology reduces to the order of 20-100Grad/s; which is suitable for microwave superconducting electronics.

Fig. 5-7 shows the voltage wave propagation over time and space axes for a DJTL with basic modeling for JJs. The physical parameters of the DJTL for simulation are chosen as $\tilde{L} = \tilde{C} = 1$, $\tilde{L}_J = 0.01$, $h = 0.01$ and a sinusoidal voltage source by $\tilde{V}_s = 0.1.$, $\tilde{f}_s = 4$ drives the DJTL. These values can be converted to the real physical parameters by setting $\omega_0 = 3\ \mathrm{Grad/s}$, $R_0 = 50\ \Omega$ and $I_0 = 2$ μA for normalization constants in the Table II in chapter four which results in having one aluminum JJ in a period of $h = 1$ cm, lossless transmission line with circuit parameters $L = 17\ \mathrm{nH/m}$, $C = 7\ \mathrm{pF/m}$ and a voltage source with amplitude $V_0 = 10$ μV, series impedance $R_s = 50\ \Omega$ and frequency $f_s = 1.9$ GHz. The line is ended with a load impedance of $R_L = 50\Omega$. The effective distributed JJ inductance can be expressed in the unit $\mathrm{nH/m}$ by expression NL_J/h which yields $17\ \mathrm{nH/m}$. Using the right hand side of the inequality (5.37), Bragg cut off frequency is found to be $f_B =$ 95.5 GHz which is above the signal frequency, i.e. $f_s < f_B$, and signal propagates through the DJTL as demonstrated in Fig. 5-7.

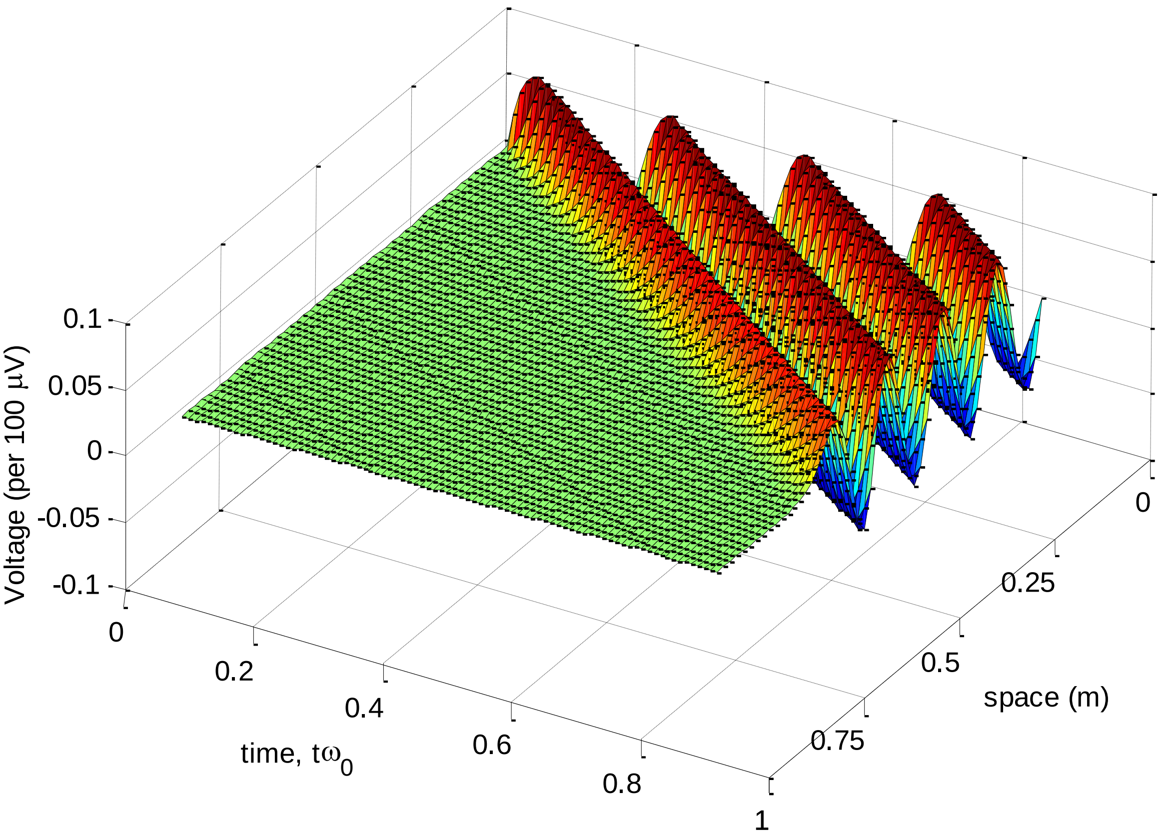

Fig. 5-7 Propagation of sinusoidal wave in a DJTL, L=C=1, L_J=0.01, h=0.01, k=0.001, I_c=1, V_s=0.1, f_s=4.

To justify the validity of the FDTD code, we remove the JJ block by letting $L_J = 0$, put a 50Ω matched load at the end, and drive the DJTL by the matched source at frequency $f_s = 1.9$ GHz. The regular response of linear transmission line is expected, with no reflection at the end. Also, the amplitude of the voltage wave traveling through the waveguide must be one half of the amplitude of the voltage source. Moreover, according to the $\beta = \omega\sqrt{LC}$ formula, wavelength is obtained as $\lambda = 0.25$ m. These are in excellent agreement with the result in Fig. 5-8.

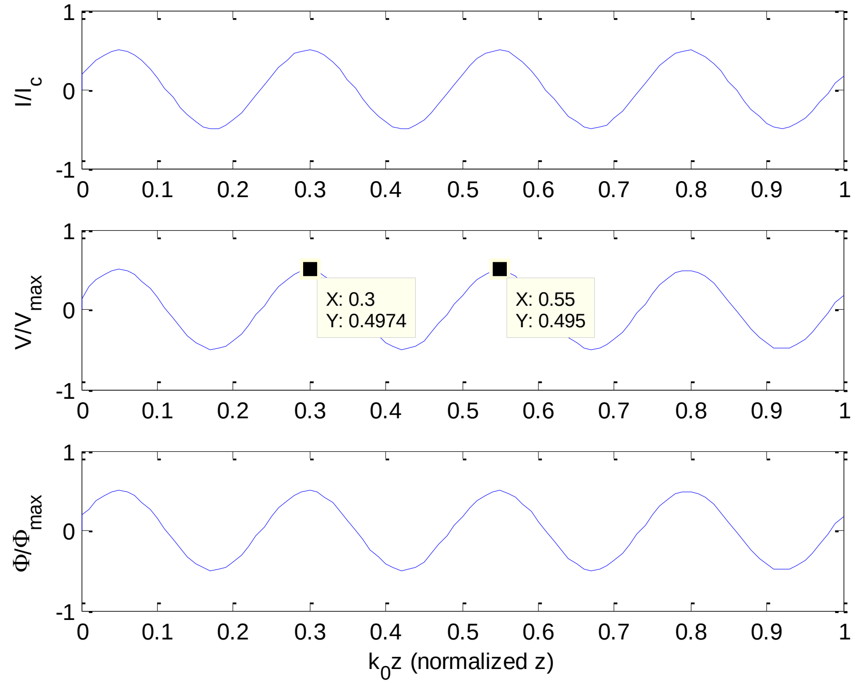

Fig. 5-8 The wave pattern of a regular transmission line (without JJs) connected to the matched load with parameters, L=C=1, L_J=0.01, h=0.01, I_c=1, V_s=0.1, f_s=4**.**

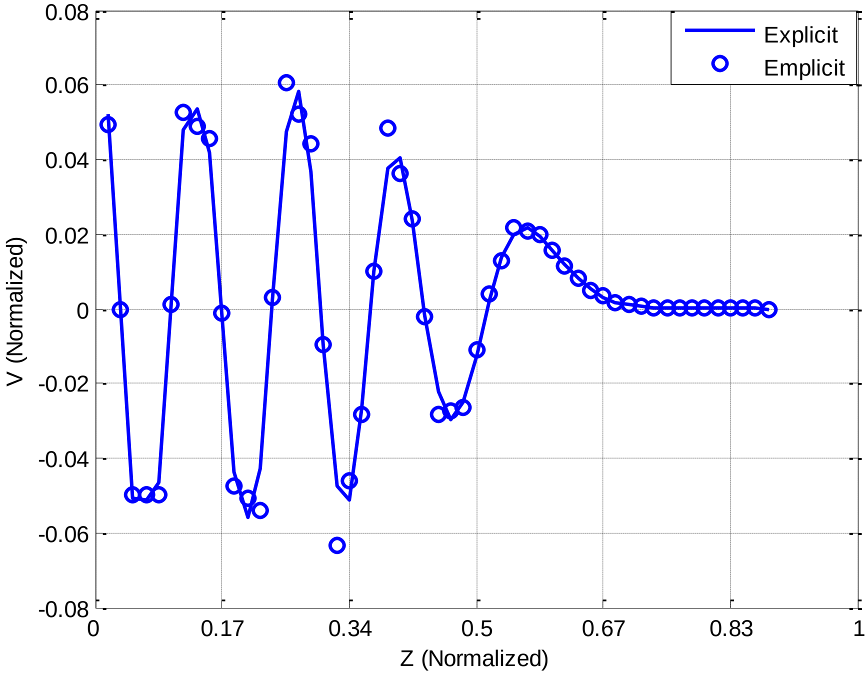

Fig. 5-9 Comparison of results obtained by explicit and implicit method with the same parametrs for the voltage along the TL length, L=C=1, L_J=0.01, h=0.02, I_c=1, V_s=0.1, f_s=4**.**

The profile of voltage along the series DJTL is depicted in Fig. 5-9. This graph compares the solution of FDTD in two different approaches, explicit and implicit. Evidently, both of these approaches provide the same solution, as seen in Fig. 5-9. In such a profile it is seen that the solution consists of transient and steady parts. The transient response is broadened since the phase velocity and group velocity have different values. The leading edge of the signal travels with the group velocity; on the other hand, the crest of the signal travels with phase velocity. The difference between these two speeds gives rise to a dispersive solution which manifest itself by broadening the transient response. This dispersion in transient response is more prounounced in for the case of a Gaussian pulse.

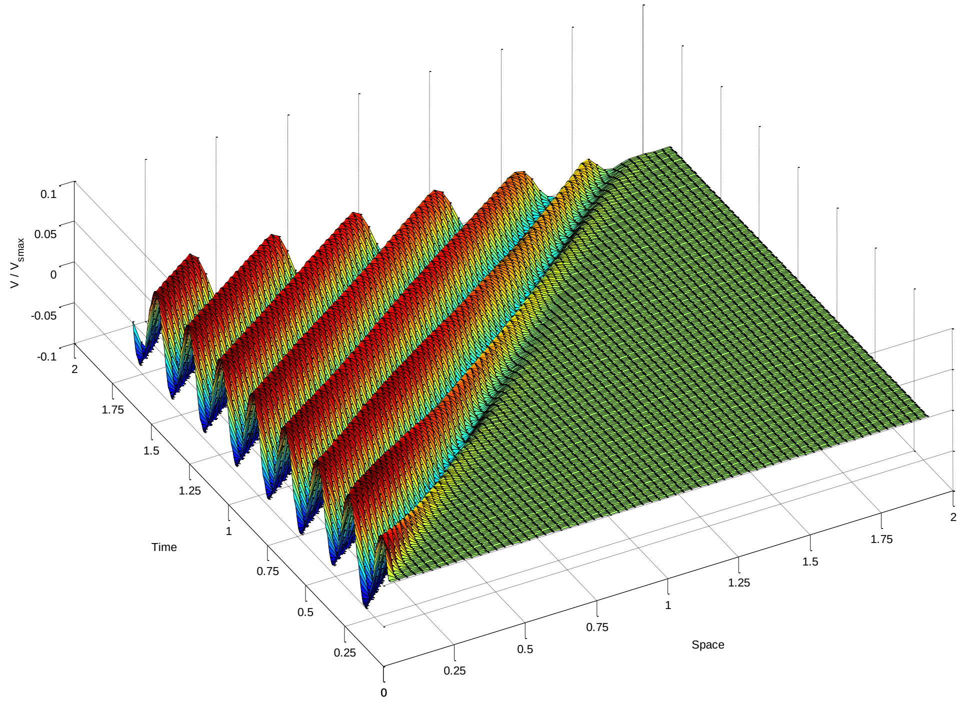

Fig. 5-10 The wave propagation in a DJTL analyzed by the RCSJ model, L=C=1, L_J=1, C_J=0.5, R_J= R_s= R_L=1, h=0.01, I_c=1, V_s=0.1, f_s=4.

Fig. 5-11 illustrates the voltage wave propagation in a series-connected DJTL over both space and time axis when complete RCSJ model is used. We used an array of 100 JJs with fit elements of $R_{fit} = 50\ \Omega$ and $C_{fit} = 3.3$ pF. Due to the abrupt jump from resting initial condition to some values by the voltage source, many Fourier components (frequency components) are excited; hence, we observe dispersive behavior in the forefront of the wave as more clearly shown in Fig. 5-11 which is the top perspective of Fig. 5-10.

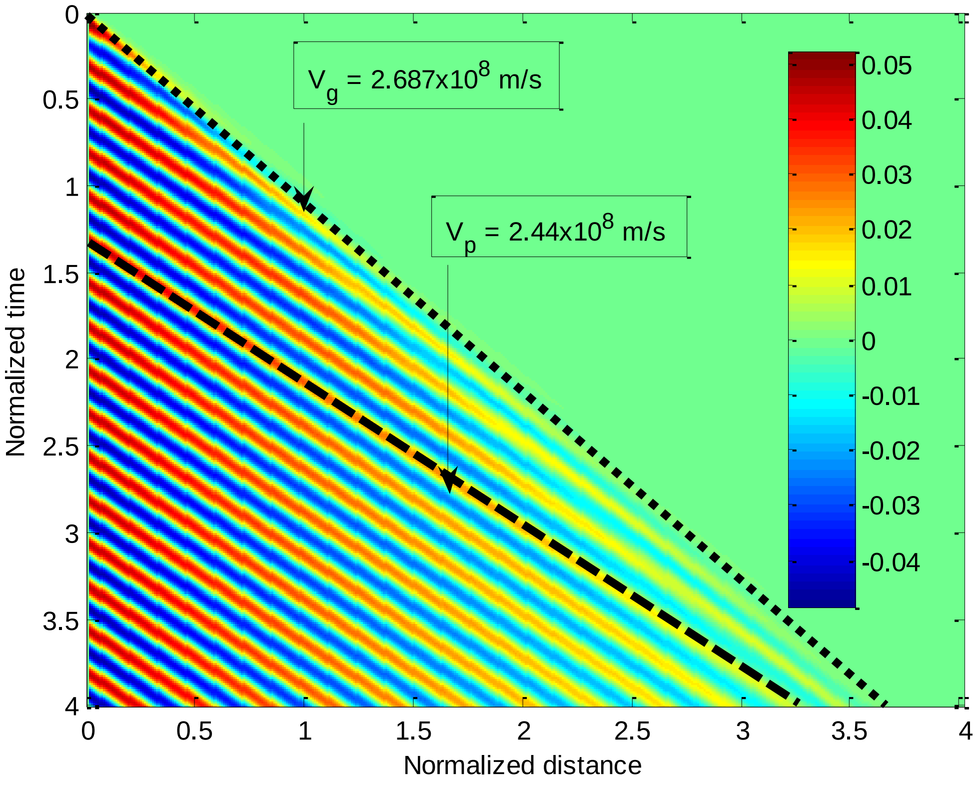

Fig. 5-11 Group and phase velocity for wave propagation in a DJTL based on the RCSJ model.

Because of the normal resistive channel R_J, the wave will attenuate gradually as sketched in the voltage profile of Fig. 5-12. By measuring the distance between two successive crests of the wave depicted in Fig. 5-12 the phase constant of the wave is found to be $\beta = 20.9\ \mathrm{rad/m}$. Moreover, by simple algebraic calculation based on the data of Fig. 5-12, the attenuation constant is given as $\alpha = 0.403\ \mathrm{Np/m}$. Both α and β are in agreement with the result shown in dispersion diagram of Fig. 4-3. The magnitude of the voltage at the beginning of the line is half of the magnitude of the voltage source, as seen in Fig. 5-12, because of the impedance matching between source and the line.

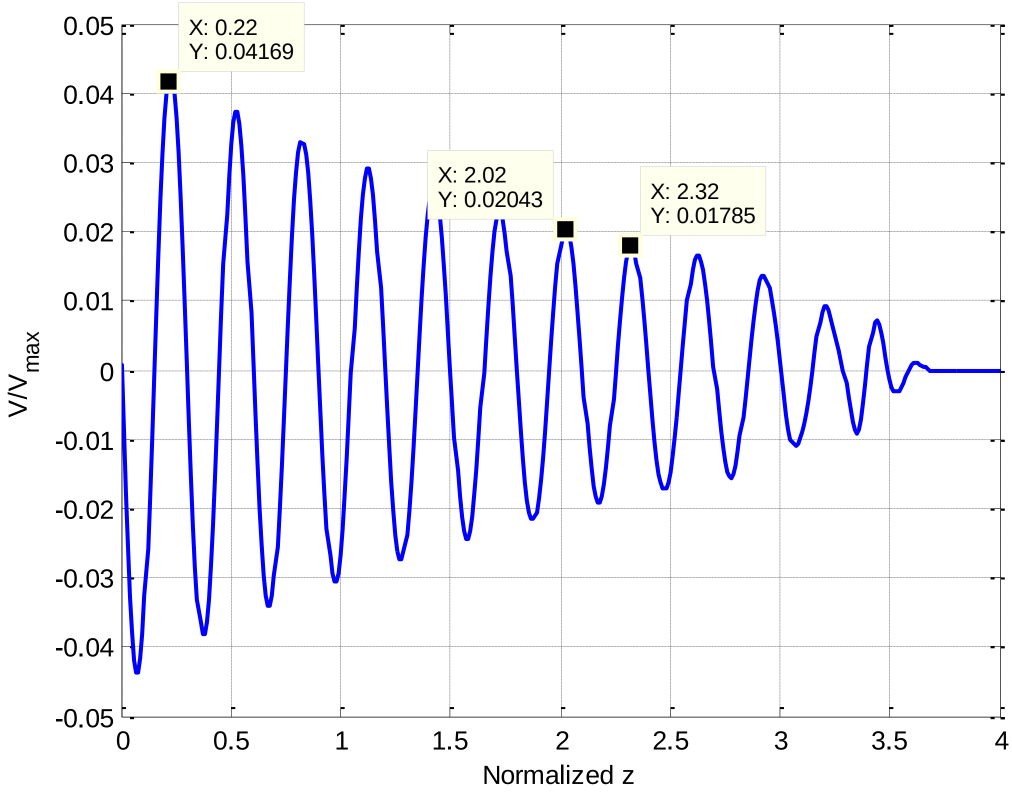

Fig. 5-12 The profile of the voltage pattern in series-connected DJTL. Attenuation and phase constant can be found from this figure.

The study of wave packet introduces another interesting aspect of DJTL. In the generalized RCSJ model of the Josephson junction, the capacitive element causes the dispersion behavior which has already been seen in Fig. 5-10 and Fig. 5-11. This dispersive behavior can be monitored by the wave packet. The wave packet that we use is in the form of

$$V = V_{smax}\sin(\omega_s t)\sin^2(\omega_n t) \tag{5.41}$$

where $\omega_s \gg \omega_n$. The wave $\sin^2(\omega_n t)$ is a relatively smooth function and plays the role of an envelope for the wave function $\sin(\omega_s t)$. The envelope travels at the group velocity and the crests of the wave function moves with phase velocity. As observed in Fig. 5-13, at different zero-crossing points of the envelope, the phase of the wave function changes, this is evidence of dispersive behavior.

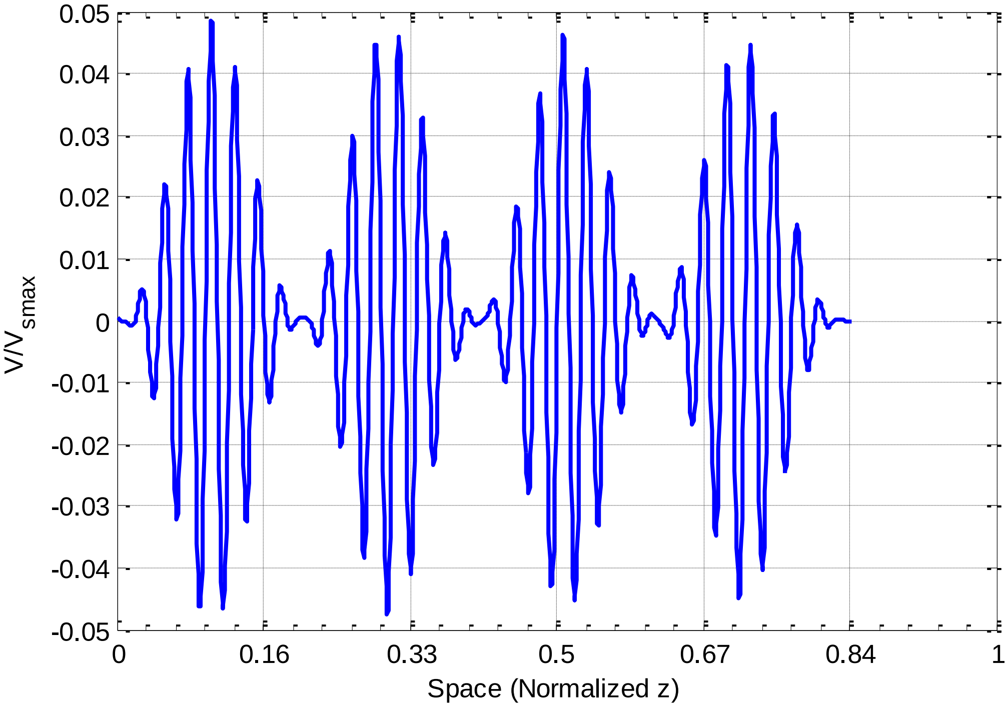

Fig. 5-13 Wave packet propagation in DJTL f_s=32, f_n=2.

As extensively discussed in chapter four, two kinds of cut-off conditions can occur in DJTL structures. One kind of cut-off condition happens when the DJTL is driven by frequencies within the band gap such as those in the dispersion diagrams of Fig. 4-3 or Fig. 4-4. For instance around plasma frequency of JJs, resonance occurs in the series JJ blocks and the line becomes very lossy; therefore, the wave decays very fast. Fig. 5-14 shows cut off propagation when the frequency of the voltage source is $\omega = 2.82\ \mathrm{Grad/s}$. This frequency is located in the interval of the dispersion curve, Fig. 4-3, where attenuation is large.

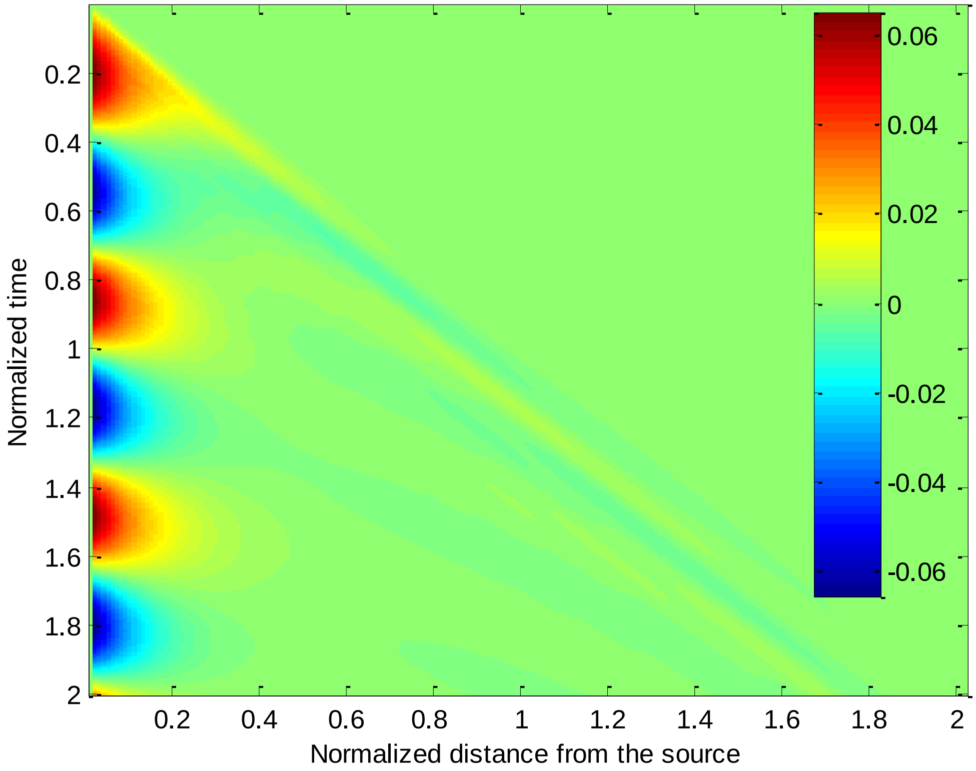

Fig. 5-14 When driving frequency is close enough to plasma frequency, DJTL reveals cut-off propagation.

Another type of cut-off is an effect of spatial discreteness which happens at the Bragg's frequency. This observation is similar to the cut off propagation in the parallel-connected DJTL which has been described by the discreteness factor [115], [116], [117]. This fact has been fully explained in chapter four by using Floquet theorem. We consider the basic model for JJ and we set, $\tilde{L} = \tilde{C} = 1$, $\tilde{L}_J = 10$, $h = 0.02$ and sinusoidal source with frequency $\tilde{f}_s = 4$, these parameters fail to satisfy (5.37) and instead of propagation we have a cut-off propagation in the steady state solution of the analysis as illustrated in Fig. 5-15 for $\tilde{V}_s = 0.2$. According to the cut-off condition (5.37), at a given frequency, by increasing L , C or L_J the cut-off frequency decreases, so for large values of circuit parameters we encounter blocking in wave propagation at lower frequencies. This phenomena has been also reported for parallel-connected DJTL [115],[117].

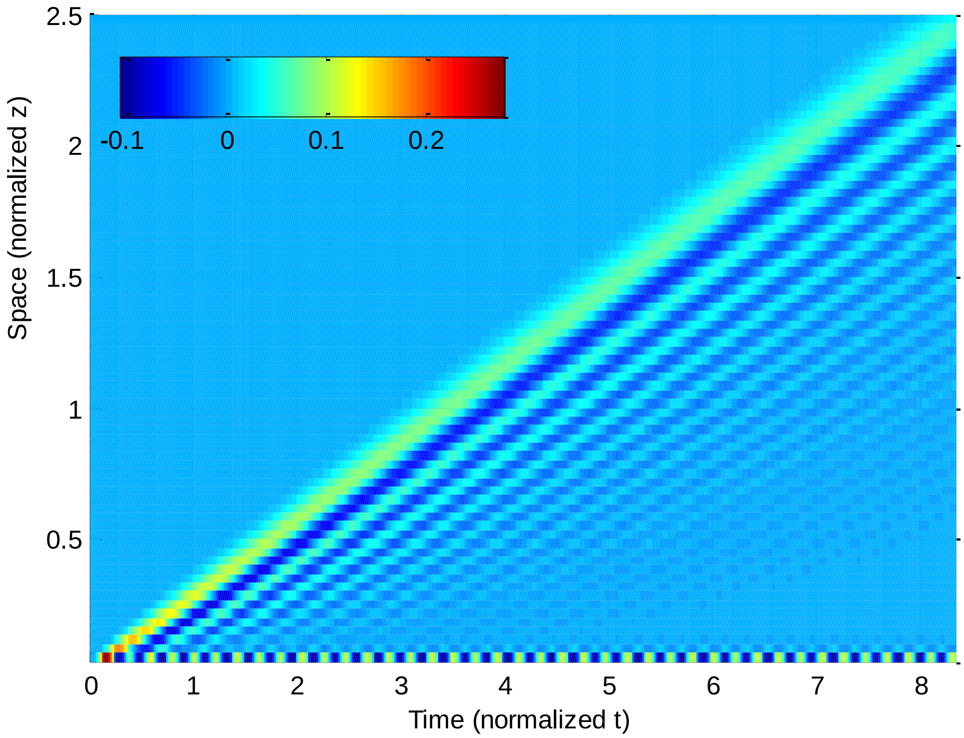

Fig. 5-15 Stopped-propagation of voltage wave through a DJTL, L=C=1, L_J=10, h=0.02, k=0.02, V_s=0.2, f_s=4.

According to the definition of the current dependent Josephson inductance [28], the nonlinear Josephson inductance increases with increasing current, so we expect that high-current sections of the waveform to propagate slower than the low-current sections. Qualitatively, as time evolves the peak of a current (or voltage since both have the same profile) leaves behind the bottom. As a result, a wave with a steeping end can develop which eventually leads to a jump discontinuity [118] as represented in Fig. 5-16. This type of wave which takes the form of a very sharp change is called as a shock wave. Shock-wave formation occurs when the DJTL is excited such that the flowing current is very close to the critical current of the junctions.

To see this, the voltage source is chosen to be a Gaussian pulse in the form of

$$V_s(t) = V_{smax} \exp\left[-0.5\left(\frac{t-t_d}{t_p}\right)^2\right]. \tag{5.42}$$

The FWHM (Full Wave Half Maximum) of the Gaussian pulse has the relation

$$\mathrm{FWHM} = 2\sqrt{2\mathrm{Ln}(2)}\, t_p \cong 2.3548\, t_p. \tag{5.43}$$

We chose $t_p = k/0.125$ [119] where $k = \Delta t$ is a normalized time step which is 2.82×10^{-4} and some other parameters are mentioned under Fig. We have reduced the effect of the numerical dispersion as displayed in Fig. 5-16, by having fine gridding and also running at a rate very close to the stability condition of Courant-Friedrichs-Lewy (CFL).

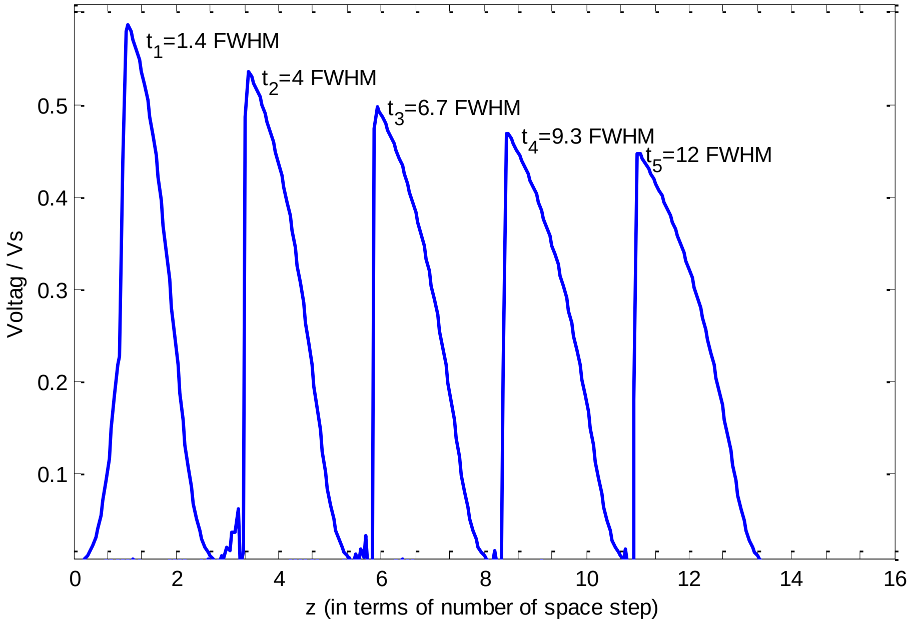

Fig. 5-16 Sketch of the formation of a shock wave in a nonlinear Josephson junction transmission line, h = 2×10^{-4} , FWHM=0.0053, L=C=1, L_J/h=1, k=2.82×10^{-4} such that k/ h=λ=[C(L+ L_J/h)]^{½}.

The propagation of sinusoidal wave along a lossless DJTL assisted by open-stubs is investigated in Fig. 5-17. The structure is driven by a source at frequency $\tilde{\omega} = 4.978$, amplitude $V_s = 0.1$ and series resistance $\tilde{R}_s = 1$. The dispersion diagram and the profile of characteristic impedance beside the time-domain response are depicted in Fig. 5-17. Measuring the distance between two successive crest in Fig. 5-17 leads to the phase constant $\tilde{\beta} = 6$ which is in a good agreement with the data in dispersion diagram of Fig. 5-17. Also, impedance analysis in a loop consisting of the source and the input impedance of the DJTL leads to the wave transfer by the factor 1/3 based on $Z_{in}/(Z_{in} + R_s)$ formula. This is also demonstrated by looking at the maximum amplitude of the wave shown in Fig. 5-17.

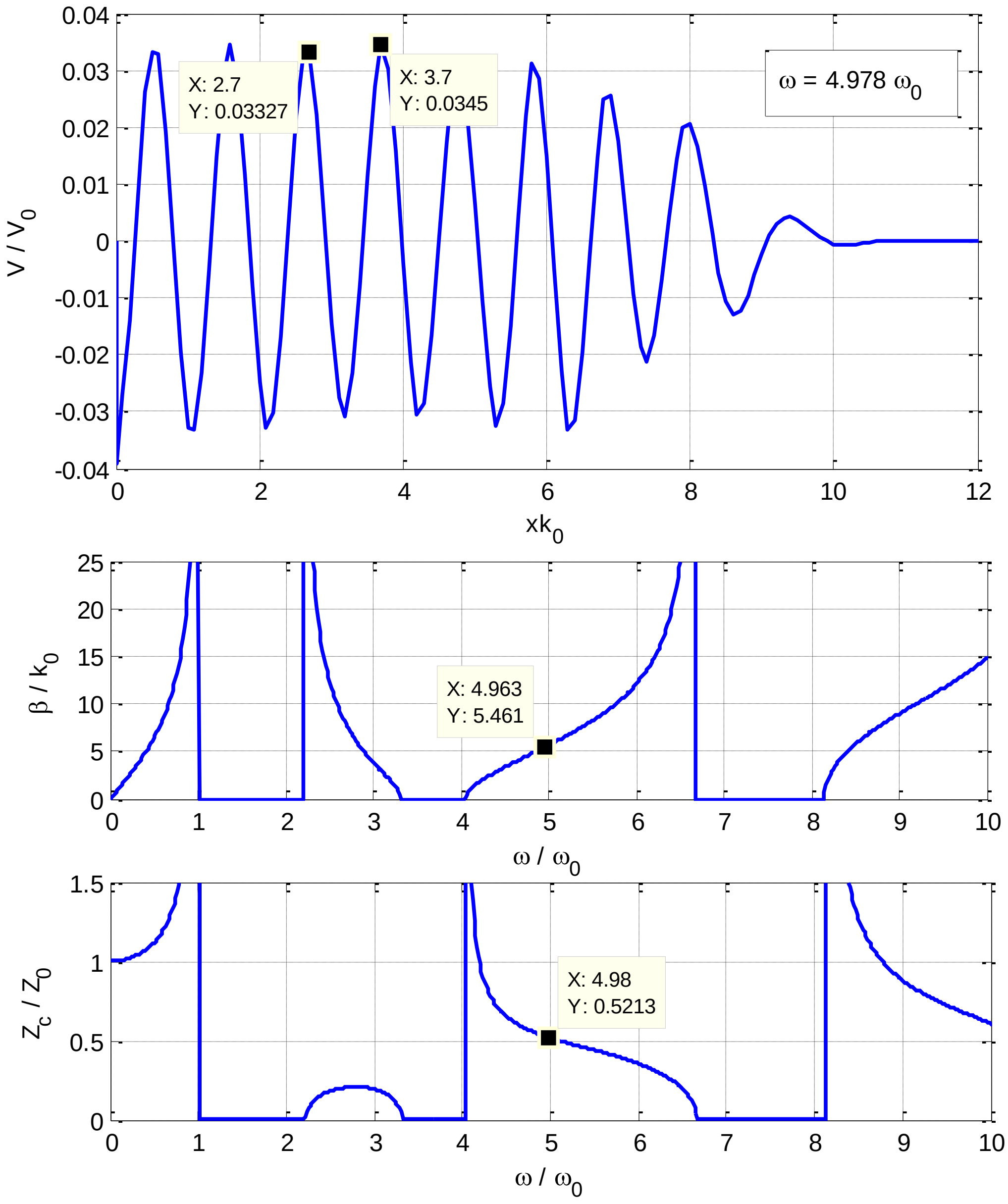

Fig. 5-17 Wave propagation along a DJTL with open stubs driven at ω=4.97with parameters, L_J=1, C_J=1, L=1, C=1, C_s=1, L_s=0.5, l_s=1, h=0.1, R_s=1, V_s=0.1. Time-domain propagation, dispersion diagram and characteristics of impedance are shown.

After justification of the validity of the numerical tool, we return to the design example carried out in section 4.4.2. for realization of non-degenerate parametric interaction in a DJTL. FDTD tool has run for all signal, pump and idler at frequencies $\widetilde{\omega}_s = 3.486$, $\widetilde{\omega}_p = 16.66$ and $\widetilde{\omega}_i = 29.83$, respectively. We used a source with amplitude $\widetilde{V}_s = 0.05$ and series impedance $\widetilde{R}_s = 2.2$, based on the normalizing impedance of $R_0 = 35\Omega$, to be matched with the input impedance of the signal as seen in Fig. 4-18. Therefore, half the signal is transferred to the structure as demonstrated in Fig. 5-18. The wavelength of the signal is calculated $\lambda = 0.0065\mathrm{m}$ based on the phase constant shown in the dispersion diagram of Fig. 4-16, which is in accordance with the distance of two maxima in Fig. 5-18.

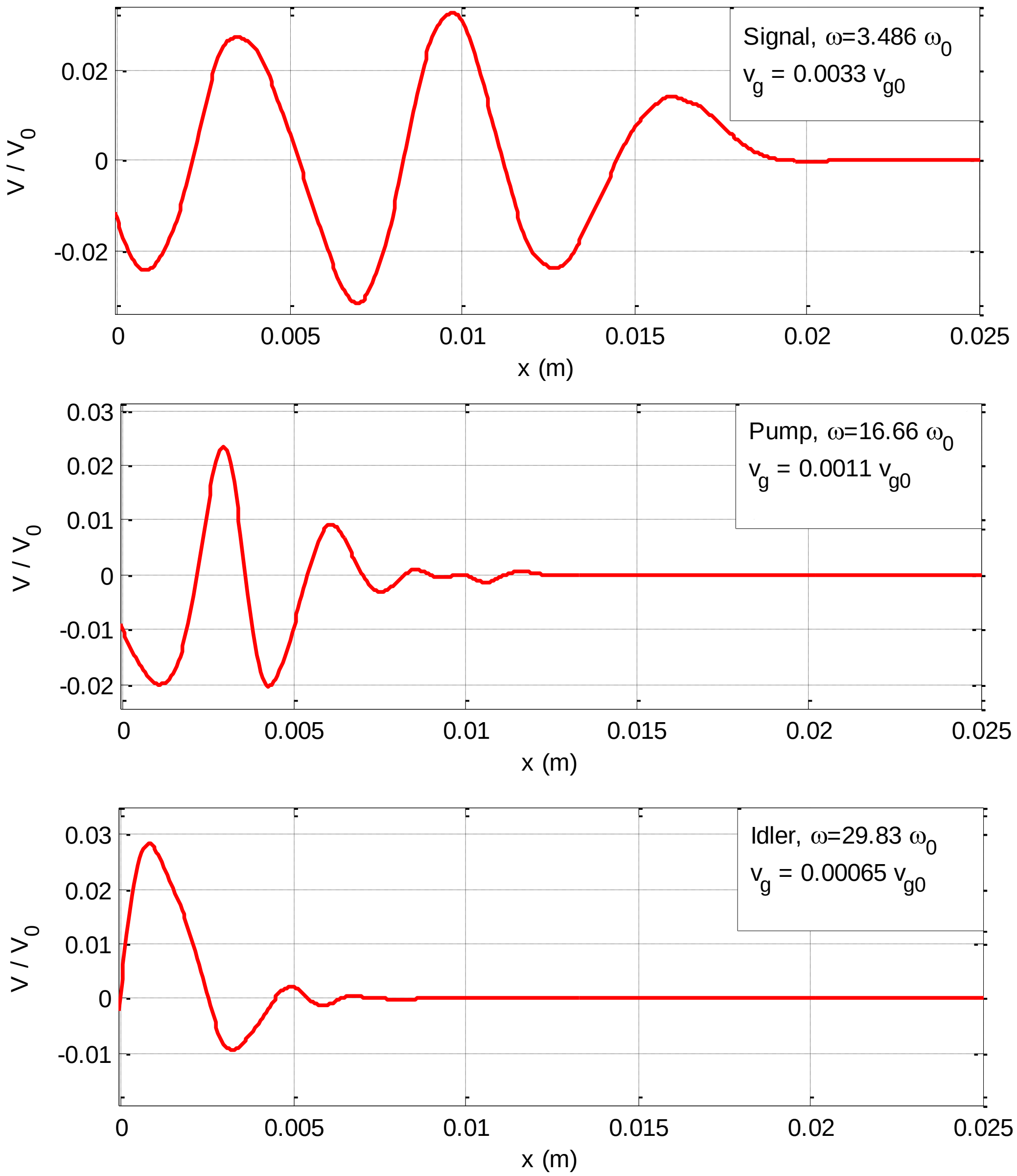

Fig. 5-18 Wave propagation for signal, pump and idler designed in Fig 4.16. with parameters $\omega_0=3\times10^9$ Rad/s, $V_{g0} = 3\times10^9$m/s, V_s =3.5 μV, R_s=80 Ω.

5.5 Observation of Shock-Wave in Experiments

In this part, the shock wave generation is demonstrated in an array of HTS weak-links which are implanted on a CPW transmission line. The geometry of the weak-link with all dimensions of CPW are illustrated in Fig. 5-19. Since we had an access to the facilities of HTS fabrication in THEVA [95], we made the device by YBCO film with the 100nm thickness deposited on a (001) LAO substrate by reactive thermal co-evaporation at a temperature of 680 C. Details of the deposition process have been described in [96]. The composition of the film has been optimized to get very smooth films with good superconducting properties. Surface roughness is less than 5 nm as measured by AFM. The transition temperature and critical current density is 87 K and 4 MA/cm , respectively. After cool-down in an oxygen atmosphere, a 200-nm gold layer was deposited *in situ*.

Fifteen number of such a weak-link are connected periodically to make a DJTL. Since the typical value of the coherence length of YBCO is around 2nm, such a HTS weak-link hardly shows Josephson tunneling. However, a strip of the narrow and thin film of superconductor material exhibit strong nonlinear kinetic inductance as explained in appendix B. This nonlinearity takes the place of the basic JJ in the DJTL which gives rise to the same nonlinear behavior. Moreover, no capacitive element contributes in the weak-link, so the transmission line is dispersionless. Such a lossless, nonlinear and dispersionless waveguide is suitable for making a shock wave, because higher generated harmonics travels at the same velocity as that of the main harmonic and they develop a shock wave[21].

Fig. 5-21 shows deformation of a Gaussian pulse while it travels along the DJTL which finally results to the shock-wave. The DJTL structure is excited with a microwave Gaussian pulse with amplitude of 360mV and FWHM of roughly 50ns. The right pulse shows the Gaussian pulse from the source, and the left trace in Fig. 5-21 shows the pulse after the DJTL structure. All measurements were performed on wafer in the probe station shown in Fig. 5-20 which has been explained in the experimental section of chapter three.

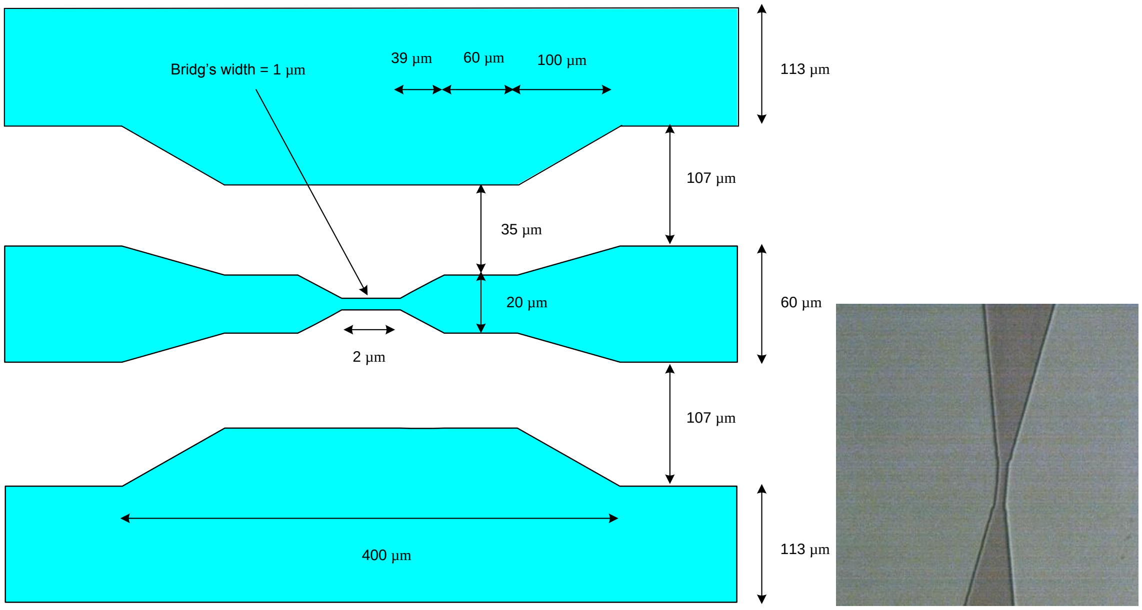

Fig. 5-19 A typical weak-link made of 100nm YBCO (right picture). Dimensions and the real device is shown on the left picture.

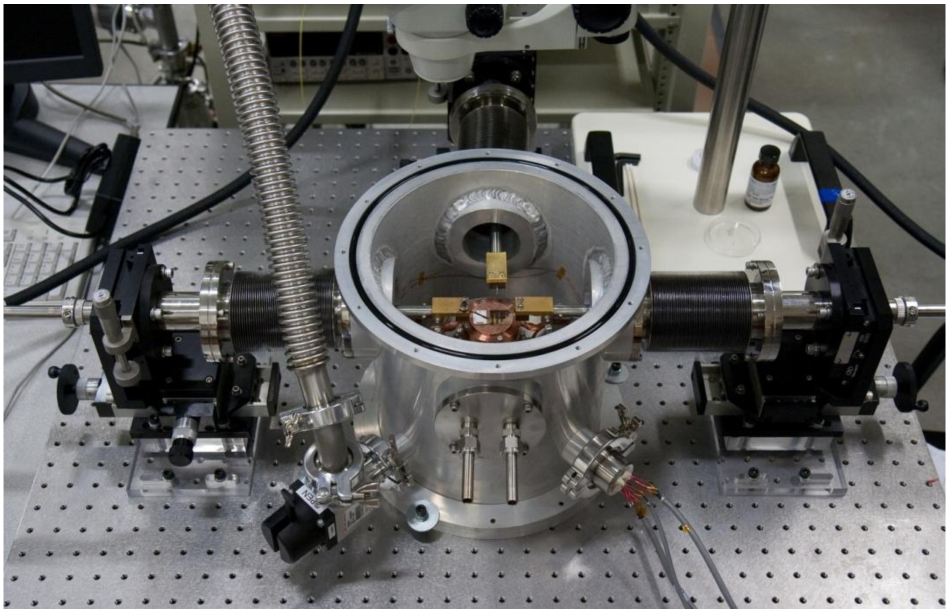

Fig. 5-20 Photograph of probe station for microwave-photonic HTS measurement with the sample stage and probe tips.

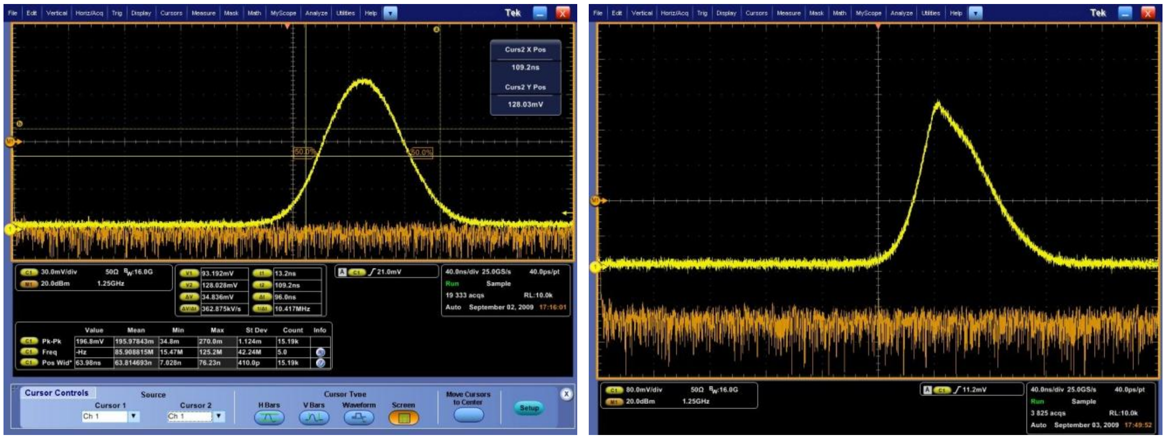

Curs2 X Pos 109.2ns
Curs2 Y Pos 128.03mV

C1 30.0mV/div 50Ω B_W:16.0G
M1 20.0dBm 1.25GHz

V1	93.192mV	t1	13.2ns
V2	128.028mV	t2	109.2ns
ΔV	34.836mV	Δt	96.0ns
ΔV/Δt	362.875kV/s	1/Δt	10.417MHz

A C1 ∫ 21.0mV

40.0ns/div 25.0GS/s 40.0ps/pt
Run Sample
19 333 acqs RL:10.0k
Auto September 02, 2009 17:16:01

		Value	Mean	Min	Max	St Dev	Count	Info
C1	Pk-Pk	196.8mV	195.97843m	34.8m	270.0m	1.124m	15.19k	
C1	Freq	-Hz	85.908815M	15.47M	125.2M	42.24M	5.0	
C1	Pos Wid*	63.98ns	63.814693n	7.028n	76.23n	410.0p	15.19k	

Ch 1
Ch 1

C1 80.0mV/div 50Ω B_W:16.0G
M1 20.0dBm 1.25GHz

A C1 ∫ 11.2mV

40.0ns/div 25.0GS/s 40.0ps/pt
Run Sample
3 825 acqs RL:10.0k
Auto September 03, 2009 17:49:52

Fig. 5-21 Shock-wave formation in an array of YBCO weak-links. Right is the Gaussian pulse at the beginning and left is the deformed pulse at the end.

5.6 Conclusion

In this chapter, a rigorous time-domain analysis was carried out to investigate microwave characteristics of DJTLs. DJTLs have been proposed in chapter four as a platform to realize parametric interaction in microwave signals. Frequency-domain methods such as dispersion analysis performed in chapter four leads to the dispersive behavior, band-gap determination and the cut-off condition arises from discreteness. All have been verified in this chapter under weak nonlinear regime. Nevertheless, frequency-domain techniques are not able to capture some other features of DJTLs such as shock wave formation which is a result of excitation of dispersonless DJTL in a highly nonlinear regime. This sheds light to search for regimes where shock-waves are not built, because shock-wave formation destroys the parametric amplification [21],[120]and mixing. In the next chapter we starts the analysis of four-photon parametric interaction under proper regimes to prevent shock-wave formation.

Chapter 6

Traveling-wave Josephson Parametric Amplifiers

6.1 Introduction

The lumped Josephson parametric devices studied in chapter two, basically used microwave filters and resonators for parametric interaction. As discussed, these devices suffer from certain drawbacks such as dynamic range, stability, gain and bandwidth. The dynamic range issue is an inherent drawback of all parametric amplifiers, as explained by the Manley-Rowe relations in chapter two. However, cascading identical modules of Josephson junctions and replacing microwave filters with suitable waveguides, brings the promise of unilateral gain achievement with improved stability and bandwidth.

In chapters four and five, frequency and time domain analyses have been carried out to study microwave behaviors of a DJTL structure. Microwave compatibility of DJTLs enables design flexibility, impedance and dispersion engineering to realize soliton propagators [121] and traveling wave parametric amplifiers and mixers [50],[12].

Traditional analysis of parametric interaction in a transmission line, periodically loaded by nonlinear elements such as varactor diodes, have been carried out for the simple dispersionless and lossless configurations [21], [21], [122], [123], [124],[125]. These structures consist of a simple LC TLs in which the capacitance (or inductors) are replaced by a nonlinear capacitors (or nonlinear inductors). When the pump wave has a strong power, the effect of the pump is reflected by replacement of nonlinear elements, i.e. unbiased JJ, with the time-varying elements in the analysis. Since the pump power is assumed to be constant along the TL, this results in an exponentially unbounded gain with an exponent of $\alpha = \Delta L/4L_0 \sqrt{\beta_s\beta_i}$ which can be physically valid within bounded distance. Parameters ΔL and L_0 are coefficients in the time-varying model of Josephson junctions. Moreover, β_s and β_i are signal and idler phase constant, respectively. The analysis is improved [21] by letting the pump wave propagate and vary its amplitude along the TL which leads to the bounded hyperbolic gain. However, in both analyses the total solution is imposed by a summation of only signal, pump and idler waves while ignoring all other harmonics. This assumption is justified based on the fact that higher order harmonics are negligible. This is due to having a strong pump in comparison with the signal and idler, and supposing only these three waves are initially injected into the TL. Another approach is based on the normal mode representations of TL. In this approach, coupled conjugate modes are introduced to investigate the parametric interaction [36] which can be extended to the quantum treatment [7]. Modeling each nonlinear element by a pump-modulated time-varying element, the effect of dispersion due to the discreteness has been also taken into account [126],[127] for parametric interaction. Parametric interaction in a TL consisting of both shunt nonlinear capacitor and series nonlinear inductor has been explored when both forward and backward waves exist in the TL [128]. In addition, experimental attempts for observation of parametric interaction have been also reported [50].

A nondispersive waveguide allows all harmonics to propagate. However, dispersive media prevent higher order harmonics from propagating, which leads to high efficiency. Basically, dispersion limits the bandwidth of the traveling wave-based devices, because dispersion plays the same role as filters in lumped parametric devices. However, it is quite manageable by proper design of dimensions and elements of the structures. More importantly, the dispersion engineering is more pronounced for DJTL structures, where three waves have to obey the phase-matching condition imposed by the cubic nonlinearity associated with the junction. As discussed in chapter four, dispersion of the DJTL was engineered to ensure the existence of three non-degenerate time-harmonic TEM waves interacting with each other through the phase-matching condition.

Another benefit leveraged by dispersion is related to the occurrence of shock waves that were demonstrated in the previous chapter. Each level of the wave propagates at different speeds, and gradually they are deformed into shock waves which do not allow steady-state waves to be sustained through the nonlinear dispersionless structure [21]. In [120], it was mathematically explained that the shock waves can form in distances shorter than those where parametric amplification occurs, and impossibility of parametric amplification is concluded in dispersionless TLs. It should be noted that our numerical results in chapter five regarding the shock wave generation were based on the dispersionless DJTL for which the basic model of JJs was used. Moreover, shock wave formation has been observed in our simulation when the DJTL was excited, such that the flowing current was very close to the critical current of the junctions. Therefore, dispersion and weak nonlinearity are crucial properties that a nonlinear TL are required to have for parametric amplification purposes. These assumptions increase the efficiency, provide stability, satisfy the phase-matching conditions, and prevent shock wave formation. Conventional analysis of parametric interaction in a nonlinear media is based on the harmonic balancing between all generated harmonics and keeping only the most significant harmonics. However, this method seems to be too complicated when applied to the more sophisticated and engineered nonlinear TLs. Assuming weak nonlinearity, perturbation collocation methods are the most legitimate techniques to solve the parametric interaction with absolute authority over all approximations and full control on entire harmonics [20],[129], [130].

In this chapter, the well-known Manley-Rowe relation is proposed as a most succinct platform to study parametric interaction in traveling-wave devices. The ideal gain with the power flow of signal, idler and pump are addressed in this section. Then, the basis of the regular perturbation technique and the method of multiple scales are explained as a selection of mathematical methods to study the parametric interaction in the engineered DJTL structures. The spectral method is then introduced as one of the powerful numerical tools to solve nonlinear differential equations which have already been obtained by perturbation methods. All massive calculations by the perturbation technique are finally distilled to three coupled amplitude equations with the condition of phase-matching. These equations describe the evolution of the amplitudes of three phase-locked waves over time and space. Details of these calculation besides important steps are outlined in subsections and some appendices. The coupled amplitude equations are then extended from the perfect phase-matching condition to the slight mismatching in frequency and/or wavenumber equations. These equations are necessary for bandwidth characteristics of the parametric device. Satisfaction of the energy conservation law is shown as a criterion for the validity of coupled amplitude derivation. The numerical tool based on the spectral FDTD with the multistep Adams-Bashforth scheme is developed to solve the nonlinear coupled differential equations with complex variables in time and space. Numerical results are shown in the last section for two different designs which demonstrate superior stability, gain enhancement and bandwidth improvement. Moreover, the significance of the dispersion on the bandwidth and the importance of proper design are highlighted in this section.

6.2 Manley-Rowe Relation for Traveling-wave Interaction

Manley and Rowe [131] developed a mathematical description to show the balance between the energies of all frequencies generated by a nonlinear element. In their original derivation, they used a circuit model for this purpose. However, the Manley-Rowe relation is generally applicable to many nonlinear situations when different photons are present. Fig. 6-1 illustrates three-wave mixing or resonant triads due to the nonlinearity associated with unbiased Josephson junctions in a lossless microwave structure such as DJTL with length x. Each wave is recognized by its frequency and wavenumber (or phase constant) obeying the two phase-matching conditions

$$2\omega_p = \omega_s + \omega_i \tag{6.1}$$

$$2\beta_p = \beta_s + \beta_i. \tag{6.2}$$

We will address their derivation later in the section 6.5.4. Subscripts s, p and i are designated for three signal, pump and idler waves, respectively. The configuration in Fig. 6-1 resembles the lumped JPA shown in Fig. 2-1. Having weak nonlinearity, the dispersion of the waveguide plays the role of microwave filters, because the waveguide is designed such that only three waves are preserved in the structure and other harmonics are supressed in order to enhance the efficiency. We have addressed this topic in chapter four. Therefore, for the structure shown in the Manley-Rowe relations are reduced to

$$\frac{P_p}{\omega_p} + \frac{2P_i}{\omega_i} = 0 \tag{6.3}$$

$$\frac{P_s}{\omega_s} - \frac{P_i}{\omega_i} = 0 \tag{6.4}$$

where P_s, P_p and P_i denote the net powers of electromagnetic waves associated with signal, pump and idler respectively. They can also be written in the form of $P_s = P_s(0) - P_s(x)$, $P_p = P_p(0) - P_p(x)$ and $P_i = P_i(0) - P_i(x)$ to maintain the same sign convention. As the signal is the wave to be amplified, the input and output of the structure are defined just at the signal frequency. Thus, the signal power can also be written by $P_s = P_{in} - P_{out}(x)$. Eliminating the idler power in equations (6.3)-(6.4) and substituting aforementioned power expressions, the power gain at position x is obtained by

$$G(x) = \frac{P_{out}(x)}{P_{in}} = 1 + \left(\frac{\omega_s}{2\omega_p}\right)\left(\frac{P_p(0) - P_p(x)}{P_{in}}\right). \tag{6.5}$$

This formula introduce an upper bound for the maximum achievable gain and is regarded as a figure of merit for the traveling-wave parametric amplifiers. As seen in (6.5), the maximum gain is obtained at position where the pump is completely depleted, i.e. $P_p(x) = 0$. Moreover, when the pump is reconstructed to its original value, i.e. $P_p(x) = P_p(0)$, gain becomes unity. When no signal is injected into the waveguide, the power of the pump doesn't change, i.e. $P_p(x) = P_p(0)$, and no gain can be observed.

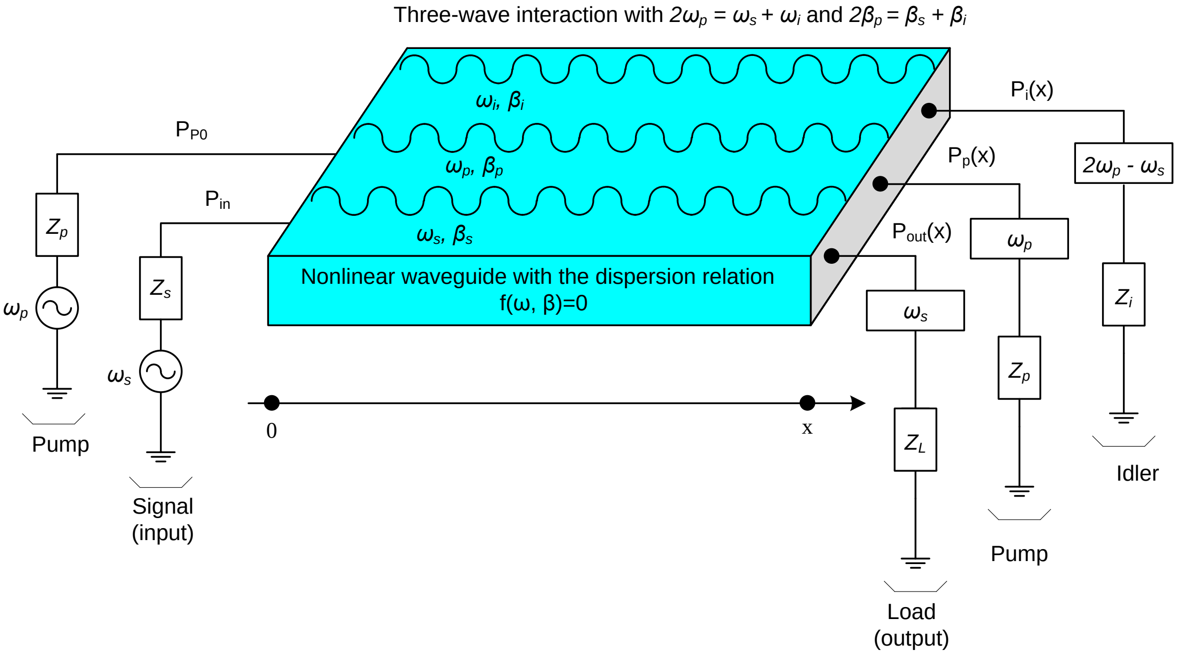

Fig. 6-1 Illustration of Manley0Rowe relation in a general schematic pf three-wave interaction. The dispersion plays the role of the filters.

Parametric interaction and the Manley-Rowe relation can also be viewed from optics and photonics perspective. Two photons are pumped into a virtual energy level above the ground state and then a photon at the signal frequency gives rise to stimulated emission. Therefore, two photons at pump frequency are annihilated and two photons are created, one photon at the signal frequency and one at the idler frequency. The energy diagram for the four-photon parametric process is depicted in Fig. 6-2. For such a photonic process, three conservation laws of "energy", "momentum" and "photon-number" must hold which are reflected by two phase-matching conditions (6.1)-(6.2) and two Manley-Rowe relations (2.1)-(2.2).

Since waves in optics have spatial distribution, Manley-Rowe relations are stated in terms of wave intensity ($\mathrm{W/m^2}$) rather than power which is mostly used in the context of microwave networks [19], [53]. Intensity is denoted by I and is classically defined as the electromagnetic power per area. It is translated in photonic description by equation $I = \hbar\omega\phi$, where ϕ is the photon flux density with the unit of photons/s/m^2. Regarding DJTL which is governed by a four-photon process as explained, we can start by using photon-number conservation law over an incremental length in the nonlinear waveguide. Two photons at frequency of ω_p are broken to produce one photon at frequency ω_s and one photon at ω_i. Therefore, the rate of annihilation is twice the speed of creation which leads to

$$2\frac{d\phi_s}{dx} = 2\frac{d\phi_i}{dx} = -\frac{d\phi_p}{dx}. \tag{6.6}$$

Substituting the photon flux density in (6.6) by $\phi = I/\hbar\omega$, this yields

$$2\frac{d}{dx}\left(\frac{I_s}{\omega_s}\right) = 2\frac{d}{dx}\left(\frac{I_i}{\omega_i}\right) = -\frac{d}{dx}\left(\frac{I_p}{\omega_p}\right). \tag{6.7}$$

Supposing the same cross-sectional are for all three waves and integrating over $[0, x]$ results in the same Manley-Rowe relations mentioned in (6.3) and (6.4).

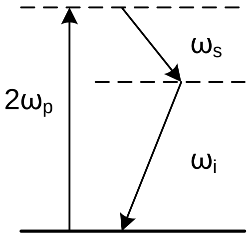

Fig. 6-2 Energy diagram for the four-photon parametric process by $2\omega_p = \omega_s + \omega_i$.

6.3 Perturbation Theory and Method of Multiple Scale

Perturbation theory is a collective name for a group of mathematical methods that are used to derive approximate solutions to a problem which may otherwise not solvable analytically. This is performed by starting from the exact solution of a closely related problem. Perturbation techniques are applicable only to those problems in physics and engineering where an additional small term exists in the mathematical description of a solvable problem. The solutions of such problems evolve smoothly out of the exact initial solution. In contrast, perturbation techniques can fail when a strong transition, rapid evolution or acute deviation occurs in the system. Nonetheless, in many cases, they have highly accurate predictive capability even beyond the range of conditions for which the method is justified. They are beneficial in understanding the underlying process in simple terms and they can serve as references for fully numerical solutions.

In perturbation theory, the solution of the perturbed system is expressed as a series expansion in terms of the powers of a small parameter, denoted by ϵ, that quantifies the deviation from the exactly solvable problem. Indeed, perturbation parameter ϵ acts as a book-keeper to hold the order of each deviation and facilitate comparison for possible approximation. The perturbation parameter ϵ should also exist in the governing equation to connect higher-order deviation to the lower-order terms. If the perturbation solution is denoted by u, then

$$u = u^{(0)} + u^{(1)}\epsilon + u^{(2)}\epsilon^2 + u^{(3)}\epsilon^3 + \cdots. \tag{6.8}$$

The leading term in this power series, i.e. $u^{(0)}$, is the solution of the exactly solvable problem, while higher-order terms $u^{(i)}$, $i = 0,1,2, \ldots$ represent the deviation in the solution and they can be found iteratively by a particular systematic procedure. In brief, perturbation series (6.8) is substituted into the governing equation, and terms of like powers of ϵ are collected to provide a set of equations referred to as $O(i)$ corresponding to the ith power of ϵ. The solution of each $u^{(i)}$ depends on the solution of the lower order terms. In many circumstances, these higher-order terms shrink successively and an approximate perturbation solution is obtained by truncating the series, and usually consists of only the first two terms.

In some perturbative differential equations such as time domain nonlinear cases as seen in a simple pendulum, the solution of the first-order equation, for instance, includes a forcing term which is the resonant solution of the corresponding homogenous problem. Therefore, the total solution contains a secular term which grows in time. For example, when ω_0 is the natural frequency of the zeroth-order term, the $\cos\omega_0 t$ becomes its resonant solution and emerges in the solution as $u^{(0)} = \cos\omega_0 t$. If $u^{(0)}$ (or $\cos\omega_0 t$) is present as a forcing term in the first-order equation, the complete solution includes particular solution in the form of $u^{(1)} = t\sin\omega_0 t + \cdots$. In this notation, we have ignored the unknown coefficients in front of each terms. Therefore, the total perturbative solution can be roughly written as

$$u = \cos\omega_0 t + \cdots + \epsilon[t\sin\omega_0 t + \cdots]. \tag{6.9}$$

It is obvious that the left hand side of (6.9) is a poor approximation to u when t is as large as ϵ^{-1}. If $t > O(\epsilon^{-1})$, the second perturbation term, i.e. $u^{(1)}\epsilon$, grows over the time and becomes greater than the first term $u^{(0)}$. In other words, these effects could be insignificant on short time scales but become important for long times. This leads to a divergent series which is against our basic assumption that successive terms in perturbation series should become smaller. Therefore, the perturbation expansion fails. The problematic "$t\sin\omega_0 t$" term, which is called secular term, arose from the presence of forcing term "$\cos\omega_0 t$" on the right hand side of equation $O(\epsilon)$, which is the so-called resonant forcing term.

One way to modify the perturbation scheme to resolve this issue is the incorporation of regular perturbation technique with the method of multiple scale. The method of multiple scale is useful when the system under study is described by disparate time scales, such as an oscillator or a waveguide where weak nonlinearity or dissipation is modeled by a slow-varying amplitude. Consider a differential equation of the form $D(u, t, \epsilon) = 0$ which models a physical system, where u is a function satisfying the equation and ϵ is a small parameter. Also, suppose the application of regular perturbation theory fails to solve the system over a long time interval due to the appearance of secular terms. If introducing two time scales, e.g. fast for $O(1)$ and slow for $O(\epsilon)$, captures the physics of the system and fits properly to the problem, this engagement to the regular perturbation theory often solves the problem. The procedure is followed by defining a slow time scale "$\tau = \epsilon t$", involved into the problem and treating it as an independent variable. Then, perturbation series to be inserted into the original master equation is given by

$$u(t,\epsilon) = u^{(0)}(t,\tau,\epsilon) + \epsilon u^{(1)}(t,\tau,\epsilon) + \epsilon^2 u^{(2)}(t,\tau,\epsilon) + \cdots. \qquad (6.10)$$

This leads to a sequence of equations for $u^{(i)}$ by equating the coefficients of like powers of ϵ to zero. A pedagogical example is the simple pendulum when nonlinearity results in a slight change in the frequency of oscillation which the leading-order solution in regular perturbation technique cannot capture. However, the method of multiple scale addresses this effect [132],[133].

6.4 Spectral Method

Spectral methods are numerical techniques to solve certain PDEs by focusing on spatial discretization. There are three classes of approaches for the numerical solution of PDEs, which are followed in chronological order of discovery: Finite Difference, Finite Element and Spectral methods. If the PDE is defined on a simple domain and the data attached to the problem is smooth, spectral methods offers high accuracy solutions with excellent speed in convergence which is referred to as an "exponential convergence". Since the numerical precision of spectral methods is so high, the number of spatial grids can be chosen low enough for reasonable computation. Therefore, they are generally less intensive in terms of required computer resources such as memory and CPU time [134]. This property, demanding less computer memory, can be crucial, as the memory allocation of a numerical tool has a significant effect on its performance and runtime. Moreover, there exists many powerful built-in subroutines in many numerical libraries such as Fast Fourier Transform in MATLAB which are required in robust implementation of spectral methods. Another benefit of the spectral methods over FDTD techniques is that the solution from the spectral method remains coherent and clean, but those generated from finite difference discretization rarely look nice. The absence of spurious dispersion, which is inherently a numerical error, is another conspicuous aspect of spectral method.

Assume a set of grid points $\{x_i\}$ and a data set $\{u(x_i)\}$ corresponding to the function values on the grid, are given. The fundamental principle behind all of the spectral collocation methods is to interpolate data by a global interpolant, then evaluate the derivative of the interpolant at the grid points and finally substitute the proper matrix operator for the spatial differential operators in the PDE. For a finite grid $\{x_i\}$ with N points and its corresponding data $\{u_i\}$, consider p as a single continuous function such that $p(x_i) = u_i$ for all i. Then, set $\frac{d}{dx}p(x)|_{x=x_i} = w_i$ and find a differentiation matrix D_N to relate $\{w_i\}$ to $\{u_i\}$ by $W = D_N U$. The choice for function p is arbitrary as long as it fits all the data. Nevertheless, there is only one band-limited interpolant p satisfying all aforementioned conditions, which is the topic of sampling theorem and aliasing issue.

There are two classes of spectral methods, Fourier and Chebyshev methods. For domains with periodic boundaries, the natural choice for p are trigonometric interpolants on an equispaced points, so-called regular grid, and Fourier analysis, which is one of the most extensively worked branches of mathematics, are employed to find differentiation matrix. Table IV summarizes all Fourier techniques including Discrete Fourier Transform (DFT) that is mostly used in spectral methods. For non-periodic problems, algebraic polynomials in uneven spaced points, so-called irregular grid, are the right choice for interpolants, and Chebyshev methods are used for these type of problems.

TABLE IV

FOURIER METHODS

Fourier Methods	Physical variables	Fourier variables	Fourier Analysis	Fourier Synthesis
Fourier transform	Continuous Unbounded $x \in \mathbb{R}$	Unbounded Continuous $k \in \mathbb{R}$	$\hat{u}(k) =$ $\int_{-\infty}^{\infty} e^{-ikx} u(x)\, dx$	$u(x) = \frac{1}{2\pi} \times$ $\int_{-\infty}^{\infty} e^{ikx} \hat{u}(k)\, dk$
Semi-discrete Fourier Transform	Discrete Unbounded $x \in h\mathbb{Z}$	Bounded Continuous $k \in \left[\frac{-\pi}{h}, \frac{\pi}{h}\right]$	$\hat{v}(k) =$ $h \sum_{j=-\infty}^{\infty} e^{-ikx_j}\, v_j$	$v_j = \frac{1}{2\pi} \times$ $\int_{\frac{-\pi}{h}}^{\frac{\pi}{h}} e^{ikx_j} \hat{v}(k)\, dk$
Fourier Series	Continuous Bounded $x \in \left[\frac{-T}{2}, \frac{T}{2}\right]$	Unbounded Discrete $k \in \frac{2\pi}{T}\mathbb{Z}$	$\hat{v}_k = \frac{1}{T} \times$ $\int_{\frac{-T}{2}}^{\frac{T}{2}} e^{-ik_j x} u(x) dx$ $j \in \mathbb{Z}$	$u(x) =$ $\sum_{j=-\infty}^{\infty} e^{ik_j x}\, \hat{v}_k$
Discrete Fourier Transform	Discrete Bounded N (even) points with distance h in $(0,2\pi]$, $\frac{\pi}{h} = \frac{N}{2}$	Bounded Discrete N points at $\frac{-N}{2} + 1, \frac{-N}{2} + 2, \dots, \frac{N}{2}$ or $k \in (\frac{-\pi}{h}, \frac{\pi}{h}]$	$\hat{v}_k =$ $h \sum_{j=1}^{N} e^{-ikx_j}\, v_j$	$v_j = \frac{1}{2\pi} \times$ $\sum_{k=-\frac{N}{2}+1}^{N/2} e^{ikx_j}\, \hat{v}_k$ $j = 1, \dots, N$

At first glance, a periodic boundary condition at the ends of a domain may suggest that the Fourier spectral method has limited applications. However, a periodic grid resembles an infinite grid and it is useful in practice in a sense that many phenomena in physics are either unrelated to the boundaries, described by periodic boundaries or have a geometry which are physically periodic. Furthermore, where real problems in physics are usually studied over a finite range, we consider a bounded periodic domain defined over $(0,2\pi]$ interval. This interval is discretised by even number of points, N points, at equal distances of separation of h, so $\pi/h = N/2$ and DFT can be applied. As mentioned in Table IV, DFT maps out the data set $\{v\}$ corresponding to N number of discrete points $\{x_j\}$ with spacing h in the interval $(0,2\pi]$ or $\{h, 2h, .., 2\pi\}$ to the spectrum of $\{\hat{v}_k\}$ at N distinct wavenumbers $\{k\}$ with spacing as 1 in the Fourier interval of $(-\pi/h, \pi/h]$ or $\{-N/2+1, \ldots, N/2\}$. Note that by increasing the number of discrete points in physical space, i.e. N, we expand the span of the spectrum in the Fourier space. The band-limited interpolant is defined as a continuous function over the inverse DFT of $\{\hat{v}_k\}$ by

$$p(x) = \frac{1}{2\pi} \sum_{k=-N/2}^{N/2^*} e^{ikx} \hat{v}_k \tag{6.11}$$

where $*$ indicates that the terms $k = \pm N/2$ are multiplied by $1/2$ to give the same inverse DFT as the one mentioned in Table IV. Although (6.11) at discrete points $x_j = nh$, $n = 0,1, .., N$ resembles the exact values of the inverse Fourier transform, this change has been done for holding symmetry at end points so that derivative of (6.11) always gives real numbers [134]. Therefore, the interpolant $p(x)$ is a trigonometric polynomial of degree $N/2$, at most.

To calculate the band-limited interpolate $p(x)$ for a grid function $\{v\}$, we can express v as a linear combination of the translated Kronecker delta functions δ_j. Then we need to calculate the DFT of Kronecker delta function based on the formulation in Table IV which gives $\hat{\delta}_k = h$. Then using (6.11), the band-limited interpolant corresponding to the delta function would be a periodic sinc function as follows

$$S_N(x) = \frac{\sin(\pi x/h)}{(2\pi/h)\tan(x/2)}. \tag{6.12}$$

As the original signal is written in the form $v_j = \sum_{m=1}^{N} v_m \delta_{j-m}$, and by using the linear property of Fourier transform, the general band-limited interpolant (6.11) can be written in terms of S_N in (6.12) as

$$p(x) = \sum_{m=1}^{N} v_m S_N(x - x_m). \tag{6.13}$$

After a small calculation to find derivative of $p(x)$ and $S_N(x)$ and inserting grid points into them, the $N \times N$ spectral differentiation matrix is found to be

$$\boldsymbol{D}_N = \begin{bmatrix} 0 & \cdots & -0.5\cot(1h/2) \\ -0.5\cot(1h/2) & \ddots & 0.5\cot(2h/2) \\ 0.5\cot(2h/2) & \ddots & -0.5\cot(3h/2) \\ -0.5\cot(3h/2) & & \vdots \\ \vdots & \ddots & 0.5\cot(1h/2) \\ 0.5\cot(1h/2) & \cdots & 0 \end{bmatrix}. \tag{6.14}$$

Another way to find the spectral differentiation matrix for a give data $\{v\}$ is to start computing the Fourier transform $\{\hat{v}\}$, then find $\hat{w}_k = (ik)^r \hat{v}_k$ at grid points which corresponds to the r^th derivative of the signal, and finally perform an inverse Fourier transform to find w at grid points. Note that for odd derivatives, symmetry cannot hold at the point $N/2$, and we must set $\hat{w}_{N/2}$ zero to get a real function. The calculation of DFT can be accomplished by Fast Fourier Transform (FFT) which is provided by powerful built-in tools in MATLAB.

6.5 Derivation of Nonlinear Coupled Amplitude Equation

In this section, we apply the perturbation technique to derive a system of three PDEs describing the evolution of the complex amplitudes associated with signal, pump and idler.

6.5.1 Weak Nonlinearity and Regular Perturbation Theory

Fig. 6-3 shows a circuit model for a lossless DJTL with open stubs. In chapter four, a series-connected DJTL assisted by stubs was finally modeled by a nonlinear single variable PDE which describes the temporal and spatial evolution of the flux associated with the JJs. Assuming small amplitude for the traveling wave solution of the equation of order $O(\sqrt{\epsilon})$, weak nonlinearity is preserved which leads to the engagement of parameter ϵ into the wave equation as follows

$$
\begin{aligned}
C\left(1+\frac{Lh}{L_J}\right)\varphi_{tt} &- \frac{h}{L_J}\varphi_{xx} + \frac{1}{Z_0 h}\left(1+\frac{Lh}{L_J}\right)\varphi_t - C_J h\varphi_{ttxx} + \frac{LC_J}{Z_0}\varphi_{ttt} \\
&+ LCC_J h\varphi_{tttt} + C\left(1+\frac{Lh}{L_J}\right)\varphi_{tt}^{(t-2\tau)} - \frac{h}{L_J}\varphi_{xx}^{(t-2\tau)} \\
&- \frac{1}{Z_0 h}\left(1+\frac{Lh}{L_J}\right)\varphi_t^{(t-2\tau)} - C_J h\varphi_{ttxx}^{(t-2\tau)} - \frac{LC_J}{Z_0}\varphi_{ttt}^{(t-2\tau)} \\
&+ LCC_J h\varphi_{tttt}^{(t-2\tau)} = \epsilon J(\varphi)
\end{aligned}
\qquad (6.15)
$$

where all parameters and variables have been defined in chapter four and the nonlinear term $J(\varphi)$ is given by

$$
\begin{aligned}
J(\varphi) = \frac{2\pi^2 LCh}{L_J\Phi_0^2}\left(\varphi_{tt} - \frac{1}{LC}\varphi_{xx} + \frac{1}{ChZ_0}\varphi_t\right)\varphi^2 \\
+ \frac{4\pi^2 LCh}{L_J\Phi_0^2}\left[(\varphi_t)^2 - \frac{1}{LC}(\varphi_x)^2\right]\varphi \\
+ \frac{2\pi^2 LCh}{L_J\Phi_0^2}\left\{\varphi_{tt}^{(t-2\tau)} - \frac{1}{LC}\varphi_{xx}^{(t-2\tau)} - \frac{1}{ChZ_0}\varphi_t^{(t-2\tau)}\right\}\left[\varphi^{(t-2\tau)}\right]^2 \\
+ \frac{4\pi^2 LCh}{L_J\Phi_0^2}\left\{\left[\varphi_t^{(t-2\tau)}\right]^2 - \frac{1}{LC}\left[\varphi_x^{(t-2\tau)}\right]^2\right\}\varphi^{(t-2\tau)}.
\end{aligned}
\qquad (6.16)
$$

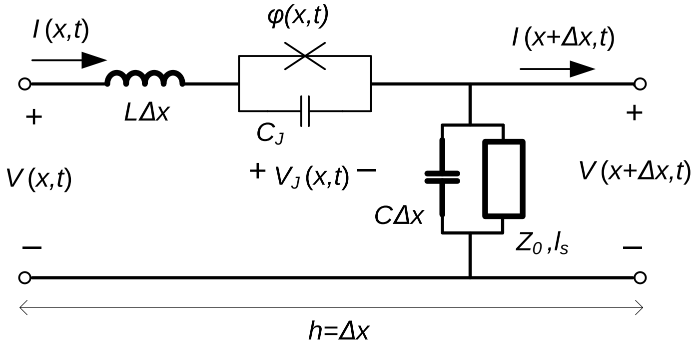

Fig. 6-3 Lossless DJTL assisted by open stubs.

Having weak nonlinearity in the governing equation allows one to use a perturbation scheme to study the parametric interaction. The nonlinearity stems from the sinusoidal phase-current description of JJ, which manifest itself by term $\sin(2\pi\varphi_J/\Phi_0)$ in TL equations (4.21) of DJTL. Taylor expansion gives rise to the presence of cubic nonlinearity in $J(\varphi)$ as seen in (4.21). Note that $J(\varphi)$ is independent of C_J. Furthermore, by $\Phi_0 \to \infty$

this nonlinearity will be removed from all equations and the structure becomes linear. Also, $J(\varphi)$ can be divided into smaller terms as

$$J(\varphi) = \frac{2\pi^2 LCh}{L_J \Phi_0^2}(NL1 + 2NL2 + NL3 + 2NL4) \tag{6.17}$$

where

$$NL1 = \left(\varphi_{tt} - \frac{1}{LC}\varphi_{xx} + \frac{1}{ChZ_0}\varphi_t\right)\varphi^2 \tag{6.18}$$

$$NL2 = \left[(\varphi_t)^2 - \frac{1}{LC}(\varphi_x)^2\right]\varphi \tag{6.19}$$

$$NL3 = \left[\varphi_{tt}^{(t-2\tau)} - \frac{1}{LC}\varphi_{xx}^{(\,t-2\tau)} - \frac{1}{ChZ_0}\varphi_t^{(\,t-2\tau)}\right]\left[\varphi^{(t-2\tau)}\right]^2 \tag{6.20}$$

$$NL4 = \left[\left(\varphi_t^{(\,t-2\tau)}\right)^2 - \frac{1}{LC}\left(\varphi_x^{(\,t-2\tau)}\right)^2\right]\varphi^{(t-2\tau)}. \tag{6.21}$$

Since nonlinearity $J(\varphi)$ is of order $O(\epsilon)$, it can be regarded as a small perturbation to the linear equation and regular perturbation technique can be applied. Now, the dependent variable φ is assumed to be expanded in an asymptotic series of powers of the small parameter ϵ

$$\varphi = \varphi^{(0)} + \epsilon\varphi^{(1)} + \epsilon^2\varphi^{(2)} + \cdots \tag{6.22}$$

$$\varphi^{(t-2\tau)} = \varphi^{(0)(t-2\tau)} + \epsilon\varphi^{(1)(t-2\tau)} + .. \tag{6.23}$$

For our analysis here, only the first two terms $\varphi^{(0)}$ and $\varphi^{(1)}$ are employed to conduct the perturbation technique with a quite good approximation. This series should be substituted into φ in the governing equation (6.15). Then, the resultant equation must be arranged in terms of powers of ϵ such that all terms belonging to the same power of ϵ are collected and equated to zero. This process yields a sequence of PDEs in terms of $\varphi^{(0)}$ and $\varphi^{(1)}$,...

The zeroth-order solution $\varphi^{(0)}$ can be easily found by substituting $\epsilon = 0$ into the original equation (6.15). In this case, the nonlinear term $J(\varphi)$ is eliminated and a linear wave equation is obtained in the form

$$\begin{aligned}
C\left(1+\frac{Lh}{L_J}\right)\varphi_{tt}^{(0)}-\frac{h}{L_J}\varphi_{xx}^{(0)}+\frac{1}{Z_0 h}\left(1+\frac{Lh}{L_J}\right)\varphi_{t}^{(0)}-C_J h\varphi_{xxtt}^{(0)}& \\
+\frac{LC_J}{Z_0}\varphi_{ttt}^{(0)}+LCC_J h\varphi_{tttt}^{(0)}& \\
+C\left(1+\frac{Lh}{L_J}\right)\varphi_{tt}^{(0)(\,t-2\tau)}-\frac{h}{L_J}\varphi_{xx}^{(0)(t-2\tau)}& \\
-\frac{1}{Z_0 h}\left(1+\frac{Lh}{L_J}\right)\varphi_{t}^{(0)(\,t-2\tau)}-C_J h\varphi_{ttxx}^{(0)(\,t-2\tau)}& \\
-\frac{LC_J}{Z_0}\varphi_{ttt}^{(0)(\,t-2\tau)}+LCC_J h\varphi_{tttt}^{(0)(\,t-2\tau)}=0.&
\end{aligned} \tag{6.24}$$

As three time-harmonic waves are initially used in the DJTL to study their interaction, the solution for the linear wave equation will be in the form of

$$\varphi^{(0)}=\frac{1}{2}\sum_{i=1}^{3}\left\{A_i e^{j(\omega_i t-\beta_i x)}+c.c.\right\} \tag{6.25}$$

where A_i is the complex amplitude, pairs (ω_i, β_i) satisfy the dispersion equation (4.28) calculated in chapter four, and $c.c.$ stands for the complex conjugate.

6.5.2 Method of Multiple Scale

In reality, the effect of a weak nonlinearity in the solution of the problem is just a slight deviation from the linear solution. For the problem of our interest, the nonlinear term results in slow variation in the complex amplitude. Therefore, the solution consists of two parts, slow-varying in amplitude and fast-varying in phase component. Hence, the method of multiple scale should be incorporated with the regular perturbation technique in order to capture this effect and provide a concrete perturbation scheme as explained in section.

We begin with defining new slow-varying variables X and T in the order $O(\epsilon)$

$$X=\epsilon x,\qquad T=\epsilon t \tag{6.26}$$

which modifies the zeroth-order solution (6.25) to

$$\varphi^{(0)}=\frac{1}{2}\sum_{i=1}^{3}\left\{A_i(X,T)e^{j(\omega_i t-\beta_i x)}+c.c.\right\}. \tag{6.27}$$

Dependence of the complex amplitudes on the spatial variable X is a result of weak nonlinearity that makes the solution slightly deviate from the linear solution. Besides, its dependence on the temporal variable T is due to the excitation of DJTL by amplitude modulated waves. As a result, four variables X, T, x, t are involved in the problem and original φ is described by these variables $\varphi(X, T, x, t)$. Time delay parameter τ is also multiplied by ϵ and yields a slow time delay by $\theta = \epsilon\tau$ which apperas in the equation. The connection between these variables and φ is shown in Fig. 6-4. Getting insight from Fig. 6-4, derivatives of φ are computed as

$$\frac{d\varphi}{dt} = \varphi_t + \epsilon\varphi_T \tag{6.28}$$

$$\frac{d\varphi}{dx} = \varphi_x + \epsilon\varphi_X. \tag{6.29}$$

$$\frac{d\varphi^{(t-2\tau,T-2\theta)}}{dt} = \varphi_t^{(t-2\tau,T-2\theta)} + \epsilon\varphi_T^{(t-2\tau,T-2\theta)} \tag{6.30}$$

$$\frac{d\varphi^{(t-2\tau,T-2\theta)}}{dx} = \varphi_x^{(t-2\tau,T-2\theta)} + \epsilon\varphi_X^{(t-2\tau,T-2\theta)} \tag{6.31}$$

Other higher derivative of φ are given in the appendix C which are necessary in our analysis.

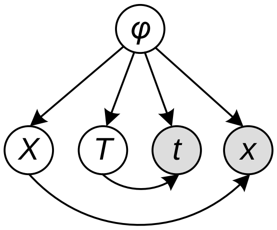

Fig. 6-4 Interconnection between φ and four slow- and fast-varying variables.

Slow time delay 2θ which appears in the equation is in order of $O(\epsilon)$ and it can be eliminated by simple Taylor expansion as follows

$$\varphi^{(t-2\tau,T-2\theta)} = \varphi^{(t-2\tau,T)} - 2\theta\varphi_T^{(t-2\tau,T)} + \cdots \cong \varphi^{(t-2\tau,T)} - 2\epsilon\tau\varphi_T^{(t-2\tau,T)}. \tag{6.32}$$

This Taylor expansion is incorporated in the asymptotic series (6.23) to give the resultant asymptotic expression by keeping only the first two terms

$$\varphi^{(t-2\tau,T-2\theta)} = \varphi^{(0)(t-2\tau,T)} + \epsilon\left[-2\tau\varphi_T^{(0)(t-2\tau,T)} + \varphi^{(1)(t-2\tau,T)}\right]. \tag{6.33}$$

Combining asymptotic and derivative expansions that all include small parameter ϵ and keeping only the first two terms gives expressions such as

$$\varphi_t \cong \varphi_t^{(0)} + \epsilon\left(\varphi_t^{(1)} + \varphi_T^{(0)}\right) \tag{6.34}$$

$$\varphi_x \cong \varphi_x^{(0)} + \epsilon\left(\varphi_x^{(1)} + \varphi_X^{(0)}\right) \tag{6.35}$$

$$\varphi_t^{(t-2\tau)} \cong \varphi_t^{(0)(t-2\tau,T)} + \epsilon\left[\varphi_T^{(0)(t-2\tau,T)} - 2\tau\varphi_{tT}^{(0)(t-2\tau,T)} + \varphi_t^{(1)(t-2\tau,T)}\right] \tag{6.36}$$

$$\varphi_x^{(t-2\tau)} \cong \varphi_x^{(0)(t-2\tau,T)} + \epsilon\left[\varphi_X^{(0)(t-2\tau,T)} - 2\tau\varphi_{xT}^{(0)(t-2\tau,T)} + \varphi_x^{(1)(t-2\tau,T)}\right]. \tag{6.37}$$

The complete list is given in appendix D. Substituting expressions (6.34)-(6.37) and the rest of those appendix into the governing equation (6.15) yields

$$\begin{aligned}
&\left(1+\frac{Lh}{L_J}\right)C\left[\varphi_{tt}^{(0)} + \epsilon\varphi_{tt}^{(1)} + 2\epsilon\varphi_{tT}^{(0)}\right] - \frac{h}{L_J}\left[\varphi_{xx}^{(0)} + \epsilon\left(\varphi_{xx}^{(1)} + 2\varphi_{xX}^{(0)}\right)\right] \\
&\quad - C_J h\left[\varphi_{ttxx}^{(0)} + \epsilon\varphi_{ttxx}^{(1)} + 2\epsilon\left(\varphi_{xXtt}^{(0)} + \varphi_{xxtT}^{(0)}\right)\right] \\
&\quad + \frac{LC_J}{Z_0}\left[\varphi_{ttt}^{(0)} + \epsilon\left(\varphi_{ttt}^{(1)} + 3\varphi_{ttT}^{(0)}\right)\right] \\
&\quad + LCC_J h\left[\varphi_{tttt}^{(0)} + \epsilon\left(\varphi_{tttt}^{(1)} + 4\,\varphi_{tttT}^{(0)}\right)\right] \\
&\quad + \frac{1}{Z_0 h}\left(1+\frac{Lh}{L_J}\right)\left[\varphi_t^{(0)} + \epsilon\varphi_t^{(1)} + \epsilon\varphi_T^{(0)}\right] \\
&+C\left(1+\frac{Lh}{L_J}\right)\left[\varphi_{tt}^{(0)(t-2\tau,T)} + \epsilon\left(-2\tau\varphi_{ttT}^{(0)(t-2\tau,T)} + 2\varphi_{tT}^{(0)(t-2\tau,T)} + \varphi_{tt}^{(1)(t-2\tau,T)}\right)\right] \\
&\quad - \frac{h}{L_J}\Big[\varphi_{xx}^{(0)(t-2\tau,T)} \\
&\quad + \epsilon\left(2\varphi_{xX}^{(0)(t-2\tau,T)} - 2\tau\varphi_{Txx}^{(0)(t-2\tau,T)} + \varphi_{xx}^{(1)(t-2\tau,T)}\right)\Big] \\
&\quad - C_J h\Big[\varphi_{ttxx}^{(0)(t-2\tau,T)} \\
&\quad + \epsilon\Big(2\varphi_{ttxX}^{(0)(t-2\tau,T)} + 2\varphi_{xxtT}^{(0)(t-2\tau,T)} - 2\tau\varphi_{ttTxx}^{(0)(t-2\tau,T)} \\
&\quad + \varphi_{ttxx}^{(1)(t-2\tau,T)}\Big)\Big] \\
&\quad - \frac{LC_J}{Z_0}\Big[\varphi_{ttt}^{(0)(t-2\tau,T)} \\
&\quad + \epsilon\left(3\varphi_{ttT}^{(0)(t-2\tau,T)} - 2\tau\varphi_{tttT}^{(0)(t-2\tau,T)} + \varphi_{ttt}^{(1)(t-2\tau,T)}\right)\Big] \\
&\quad + LCC_J h\Big[\varphi_{tttt}^{(0)(t-2\tau,T)} \\
&\quad + \epsilon\left[4\varphi_{tttT}^{(0)(t-2\tau,T)} - 2\tau\varphi_{ttttT}^{(0)(t-2\tau,T)} + \varphi_{tttt}^{(1)(t-2\tau,T)}\right]\Big] \\
&\quad - \frac{1}{Z_0 h}\left(1+\frac{Lh}{L_J}\right)\Big[\varphi_t^{(0)(t-2\tau,T)} \\
&\quad + \epsilon\left(\varphi_T^{(0)(t-2\tau,T)} - 2\tau\varphi_{tT}^{(0)(t-2\tau,T)} + \varphi_t^{(1)(t-2\tau,T)}\right)\Big] = \epsilon J\left(\varphi^{(0)}\right).
\end{aligned} \tag{6.38}$$

The zeroth-order term $O(1)$ gives the solution for the linearized form of the master equation (6.15). The equation and its solution has been mentioned in (6.24) and (6.25), respectively. The next order $O(\epsilon)$ terms are arranged such that the right and left hand side of the equation are expressed in terms of zeroth-order $\varphi^{(0)}$and first-order $\varphi^{(1)}$ solutions, respectively

$$
\begin{aligned}
&\left(1+\frac{Lh}{L_J}\right)C\varphi_{tt}^{(1)}-\frac{h}{L_J}\varphi_{xx}^{(1)}-C_Jh\varphi_{ttxx}^{(1)}+\frac{LC_J}{Z_0}\varphi_{ttt}^{(1)}+LCC_Jh\varphi_{tttt}^{(1)}\\
&\quad+\frac{1}{Z_0h}\left(1+\frac{Lh}{L_J}\right)\varphi_t^{(1)}\\
&+C\left(1+\frac{Lh}{L_J}\right)\varphi_{tt}^{(1)(t-2\tau,T)}-\frac{h}{L_J}\tilde{\varphi}_{xx}^{(1)(t-2\tau,T)}-C_Jh\varphi_{ttxx}^{(1)(t-2\tau,T)}\\
&-\frac{LC_J}{Z_0}\varphi_{ttt}^{(1)(t-2\tau,T)}+LCC_Jh\varphi_{tttt}^{(1)(t-2\tau,T)}-\frac{1}{Z_0h}\left(1+\frac{Lh}{L_J}\right)\varphi_t^{(1)(t-2\tau,T)}\\
&=J\left(\varphi^{(0)}\right)-2\left(1+\frac{Lh}{L_J}\right)C\varphi_{tT}^{(0)}+2\frac{h}{L_J}\varphi_{xX}^{(0)}+2C_Jh\left(\varphi_{xXtt}^{(0)}+\varphi_{xxtT}^{(0)}\right)\\
&\quad-\frac{3LC_J}{Z_0}\varphi_{ttT}^{(0)}-4LCC_Jh\,\varphi_{tttT}^{(0)}-\frac{1}{Z_0h}\left(1+\frac{Lh}{L_J}\right)\varphi_T^{(0)}\\
&\quad-2C\left(1+\frac{Lh}{L_J}\right)\left(-\tau\varphi_{ttT}^{(0)(t-2\tau,T)}+\varphi_{tT}^{(0)(t-2\tau,T)}\right)\\
&+\frac{2h}{L_J}\left(\varphi_{xX}^{(0)(t-2\tau,T)}-\tau\varphi_{Txx}^{(0)(t-2\tau,T)}\right)\\
&\quad+2C_Jh\left(\varphi_{ttxX}^{(0)(t-2\tau,T)}+\varphi_{xxtT}^{(0)(t-2\tau,T)}-\tau\varphi_{ttTxx}^{(0)(t-2\tau,T)}\right)\\
&+\frac{LC_J}{Z_0}\left(3\varphi_{ttT}^{(0)(t-2\tau,T)}-2\tau\varphi_{tttT}^{(0)(t-2\tau,T)}\right)\\
&\quad-2LCC_Jh\left(2\varphi_{tttT}^{(0)(t-2\tau,T)}-\tau\varphi_{ttttT}^{(0)(t-2\tau,T)}\right)\\
&\quad+\frac{1}{Z_0h}\left(1+\frac{Lh}{L_J}\right)\left(\varphi_T^{(0)(t-2\tau,T)}-2\tau\varphi_{tT}^{(0)(t-2\tau,T)}\right).
\end{aligned}
\tag{6.39}
$$

Closer look at (6.39) reveals this fact that the derivatives in the left hand side are with respect to the fast-varying variables t and x. Moreover, the derivatives relative to the slow-varying variables T and X are first-order derivatives that only seen in the right-hand side. Also, nonlinear term $J\left(\varphi^{(0)}\right)$ which only depends on $\varphi^{(0)}$ appears in the right hand side of

(6.39). From now on we focus on the first-order perturbation equation (6.39), particularly on its right hand side to extract all information regarding parametric interaction.

By defining the phase of each wave as $\theta_i = \omega_i t - \beta_i x,\ i = 1, 2, 3$, the solution of $\varphi^{(0)}$ can be restated as

$$\varphi^{(0)} = \frac{1}{2}\sum_{i=1}^{3}\{A_i e^{j\theta_i} + c.c.\} \tag{6.40}$$

where A_i is a function of slow-varying variables X and T. Also, the time delay 2τ in $\varphi^{(0)(t-2\tau,T)}$ gives rise to a phase shift as follows

$$\varphi^{(0)(t-2\tau,T)} = \frac{1}{2}\sum_{i=1}^{3}\{e^{-j2\omega_i\tau} A_i e^{j\theta_i} + c.c.\}. \tag{6.41}$$

Solutions in the form of (6.40) and (6.41) must be replaced for $\varphi^{(0)}$ and $\varphi^{(0)(t-2\tau,T)}$at the left hand side of (6.39). This substitution into the right hand side of (6.39) can be done for the linear and nonlinear parts separately.

6.5.3 Substitution of Zeroth-Order Solution to the First-Order Equation

In order to substitute (6.40) and (6.41) into the right hand side of (6.39), all derivatives of $\varphi^{(0)}$ with respect to x, t, X and T must be calculated. Appendix E summarizes all necessary derivatives for this substitution. After substitution and simplification, the right hand side of (6.39) is written as

$$\text{RHS} = J\left(\varphi^{(0)}\right) + \sum_{i=1}^{3}\left(\text{COEFT.}\frac{\partial A_i}{\partial T} + \text{COEFX.}\frac{\partial A_i}{\partial X}\right) e^{j\theta_i} \tag{6.42}$$

where

$$\text{COEFX.} = \left(1 + e^{-j2\omega_i\tau}\right)\left(-j\frac{h}{L_J}\beta_i + jC_J h\omega_i^2\beta_i\right) \tag{6.43}$$

$$\begin{aligned}\text{COEFT.} = {} & \left[-j\omega_i C\left(1+\frac{Lh}{L_J}\right) - jC_J h\omega_i\beta_i^2 + j2LCC_J h\,\omega_i^3\right]\left(1+e^{-j2\omega_i\tau}\right) \\ & + \left[\frac{3}{2}\frac{LC_J}{Z_0}\omega_i^2 - \frac{1}{2Z_0 h}\left(1+\frac{Lh}{L_J}\right)\right]\left(1-e^{-j2\omega_i\tau}\right) \\ & + e^{-j2\omega_i\tau}\left[-C\left(1+\frac{Lh}{L_J}\right)\tau\omega_i^2 + \frac{h}{L_J}\tau\beta_i^2 + j\tau\frac{LC_J}{Z_0}\omega_i^3\right. \\ & \left. + LCC_J h\tau\omega_i^4 - \frac{j\tau\omega_i}{Z_0 h}\left(1+\frac{Lh}{L_J}\right) - \tau C_J h\omega_i^2\beta_i^2\right].\end{aligned} \tag{6.44}$$

The nonlinear part $J\left(\varphi^{(0)}\right)$ is very important as this is the only place where three waves mixing with each other being responsible for phase-matching condition and parametric interaction. The mathematical treatment of the nonlinear term will be presented in the next section.

6.5.4 Phase-Matching Condition

As (6.16) implies, the nonlinearity associated with the structure is a cubic-type nonlinearity. As mentioned in section 6.5.1, the nonlinear $J\left(\varphi^{(0)}\right)$ is divided into four parts. The solution of zeroth-order perturbation terms which is a summation of three waves must be replaced in the $J\left(\varphi^{(0)}\right)$ which causes these terms to be mixed and produce 54 higher order terms, including their complex conjugate, such as θ_1, θ_2, θ_3, $\theta_1-\theta_2+\theta_3$, $-\theta_1+2\theta_2$, $2\theta_2-\theta_3$, $3\theta_1$, $3\theta_2$, $3\theta_3$,.....

In order to have energy transferred between these waves, if some simple relations between the phases of these three waves are preserved, some of higher harmonics become equal to one of the original waves. This kind of relation is called "phase-matching" relation which is crucial for the purpose of parametric interaction and these three phased-locked waves are referred to as "resonant triads" [20],[130]. For DJTL this relation is in the form of

$$2\theta_2 = \theta_1 + \theta_3 \tag{6.45}$$

which cause harmonics $\theta_1-\theta_2+\theta_3$, $2\theta_2-\theta_1$, $2\theta_2-\theta_3$become θ_2, θ_3 and θ_1, respectively. Condition (6.45) must hold for all x and t, so it can be expressed in terms of frequency and phase constant as stated before in chapter four

$$2\omega_2 - \omega_1 - \omega_3 = 0 \tag{6.46}$$

$$2\beta_2 - \beta_1 - \beta_3 = 0. \tag{6.47}$$

In quantum description of a parametric process, this process is called a "four-photon process", since two photons from pump interact with one photon from signal and one from idler frequency.

6.5.5 Nonlinear Interaction of Three Waves

Application of phase-matching relation to the coefficients of harmonics generated from nonlinear interaction leads to the new coefficients for the resonant forcing terms of θ_1, θ_2 and θ_3. These coefficients are presented in tabular format in appendix F. They are combined based on the relation

$$J\left(\varphi^{(0)}\right) = \frac{\pi^2 LCh}{4L_J\Phi_0^2}(8NL1 + 16NL2 + 8NL3 + 16NL4) \tag{6.48}$$

which yields

$$\begin{aligned} J\left(\varphi^{(0)}\right) = \mathrm{COEFNL1}.\, e^{j\theta_1} + \mathrm{COEFNL2}.\, e^{j\theta_2} + \mathrm{COEFNL3}.\, e^{j\theta_3} \\ + \text{higher order terms} \end{aligned} \tag{6.49}$$

where

$$\mathrm{COEFNL1}. = R_1\{A_1|A_1|^2 + 2A_1|A_2|^2 + 2A_1|A_3|^2 + A_2^2A_3^*\} \tag{6.50}$$

$$\mathrm{COEFNL2}. = R_2\{2A_2|A_1|^2 + A_2|A_2|^2 + 2A_2|A_3|^2 + 2A_1A_2^*A_3\} \tag{6.51}$$

$$\mathrm{COEFNL3}. = R_3\{2A_3|A_1|^2 + 2A_3|A_2|^2 + A_3|A_3|^2 + A_1^*A_2^2\} \tag{6.52}$$

and

$$R_i = \frac{\pi^2 LCh}{4L_J\Phi_0^2}\left[\left(\frac{\beta_i^2}{LC} - \omega_i^2 + \frac{j\omega_i}{ChZ_0}\right) + e^{-j2\omega_i\tau}\left(\frac{\beta_i^2}{LC} - \omega_i^2 - \frac{j\omega_i}{ChZ_0}\right)\right] \tag{6.53}$$

for $i = 1, 2, 3$.

6.5.6 Elimination of Resonant Forcing Terms

When we explained the method of multiple scale in section 6.3, we mentioned that existence of resonant forcing terms in the $O(\epsilon)$ of perturbation scheme results in secular terms in the solution of $\varphi^{(1)}$ which are unphysical in long term processes. These terms exist in the right hand side of $O(\epsilon)$ in equation (6.39) as follows

$$\mathrm{RHS} = \sum_{i=1}^{3}\left(\mathrm{COEFT.}\frac{\partial A_i}{\partial T} + \mathrm{COEFX.}\frac{\partial A_i}{\partial X} + \mathrm{COEFNL.}\right) e^{j\theta_i} + \text{higher order terms} \tag{6.54}$$

where COEFNL. can be either COEFNL1. , COEFNL2. or , COEFNL3. depending on the index i. All of the resonant forcing terms can be eliminated by setting their coefficients equal to zero, separately, as follows

$$\mathrm{COEFT.}\frac{\partial A_i}{\partial T} + \mathrm{COEFX.}\frac{\partial A_i}{\partial X} + \mathrm{COEFNL.} = 0 \tag{6.55}$$

.

It should be noted that if the media were not dispersive, all higher order harmonics would become resonant forcing terms and their coefficients must then be set to zero which makes the analysis more complicated.

6.5.7 Coupled Amplitude Equations

Vanishing all resonant forcing terms, as stated in above paragraph, leads to a three nonlinear coupled equations with complex amplitude which shows the temporal and spatial evolution of complex amplitudes associated with the three waves:

$$\frac{\partial A_1}{\partial T} + v_{g1}\frac{\partial A_1}{\partial X} = -j\xi_1\{|A_1|^2 A_1 + 2|A_2|^2 A_1 + 2|A_3|^2 A_1 + A_2^2 A_3^*\} \tag{6.56}$$

$$\frac{\partial A_2}{\partial T} + v_{g2}\frac{\partial A_2}{\partial X} = -j\xi_2\{2|A_1|^2 A_2 + |A_2|^2 A_2 + 2|A_3|^2 A_2 + 2A_1 A_2^* A_3\} \tag{6.57}$$

$$\frac{\partial A_3}{\partial T} + v_{g3}\frac{\partial A_3}{\partial X} = -j\xi_3\{2|A_1|^2 A_3 + 2|A_2|^2 A_3 + |A_3|^2 A_3 + A_2^2 A_1^*\} \tag{6.58}$$

where v_{g1}, v_{g2} and v_{g3} are group velocities satisfying (4.29) for the waves traveling through a DJTL with open stubs. Parameters ξ_i for $i = 1, 2, 3$ are real and given by two following equivalent equations

$$\xi_i = \frac{\pi^2}{4hLL_J C_J^2 \Phi_0^2} \times \frac{v_{gi}}{\left(\omega^2 - \frac{1}{L_J C_J}\right)\left[\omega^2 - \frac{1}{L_J C_J}\left(1 + \frac{L_J}{Lh}\right)\right]}. \tag{6.59}$$

$$\xi_i = \frac{\pi^2 L_J C}{4h\Phi_0^2} \times \frac{v_{gi}\omega_i}{\beta_i} \times \frac{\left(\omega_i + \frac{1}{Z_0 hC}\tan\omega_i\tau\right)}{\left(1 - L_J C_J \omega^2\right)^2}. \tag{6.60}$$

Looking at the system of governing wave equations in chapter four, one realizes that the origin of nonlinearity which is the term $\sin(2\pi\varphi/\Phi_0)$ in equations (4.20)-(4.24), can be removed by setting $\Phi_0 \to \infty$. This is another view to the small amplitude assumption that the ratio of φ/Φ_0 becomes very small. Therefore, the parameter ξ_i and the right hand side of (6.56)-(6.58) originate from the nonlinearity in the DJTL, because ξ_i goes to zero when $\Phi_0 \to \infty$ as seen in (6.59). The left hand side of (6.56)-(6.58) simply shows that the amplitude of the wave is travelling at the speed of group velocity v_{gi}. The right hand side, which result from nonlinearity, acts as a source in evolution of the amplitude. The parameter ξ_i is very important for amplification and we will discuss more about this in results section of this chapter.

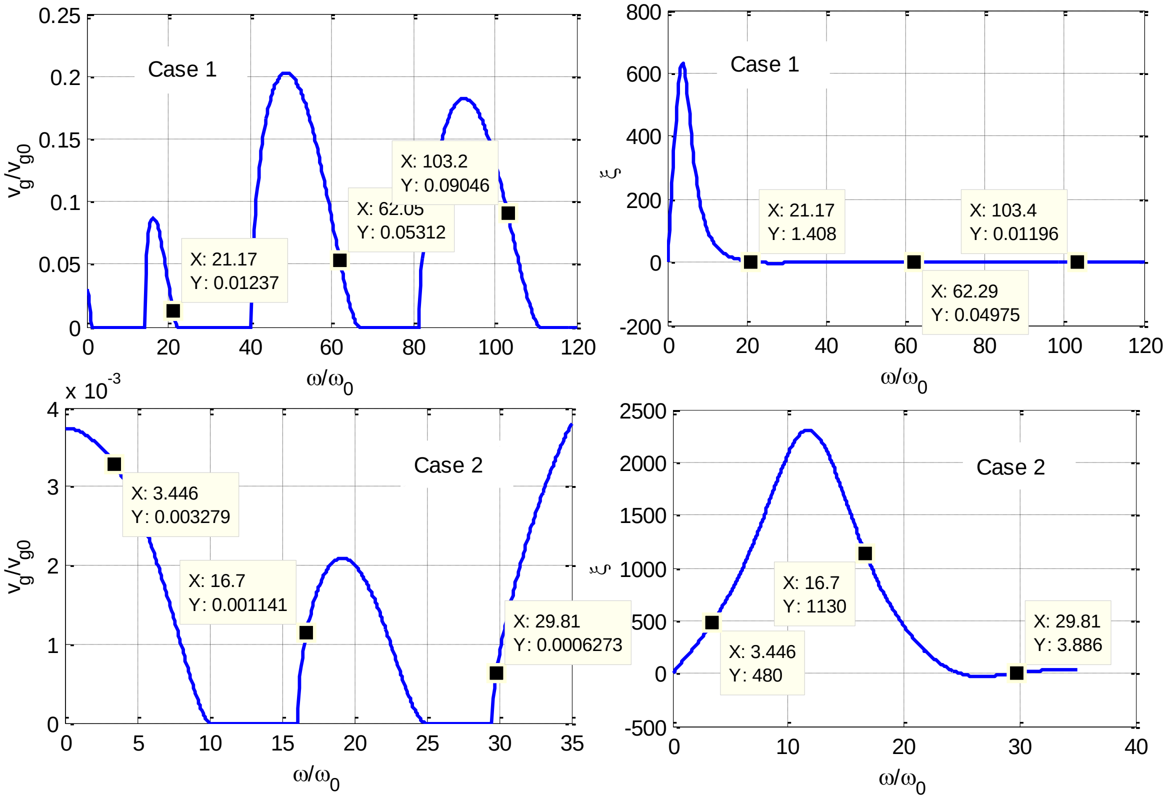

Fig. 6-5 Group velocity vg and nonlinear parameter ξ versus frequency. The top is related to the DJTL (case1) with parameters LJ = 1,CJ = 0.5,L = 1,C = 1,Ls = 0.5,Cs = 1,ls = 0.1, h = 0.01; and the bottom is for DJTL (case2) with parameters LJ = 0.2,CJ = 0.05,L = 250,C = 70,Ls = 100,Cs = 10,ls = 0.002,h = 0.0005.

In addition, the right hand side of each equation consists of two parts. For instance, the first part of (6.56) is $-j\xi_1 A_1(|A_1|^2 + 2|A_2|^2 + 2|A_3|^2)$ and only changes the phase of A_1 by 90 degree. The second part is $-j\xi_1 A_2^2 A_3^*$ which is the mixing term between pump and idler. This term changes the amplitude of the signal A_1 and is responsible for the gain achievement. As a result, pump's and signal's photons mixed together to generate the idler photon and, in turn, the idler and pump are combined to produce the signal's photon.

Closer look at the coupled amplitude equation (6.56)-(6.58), reveals the fact that by initially setting any two of the waves zero, the third wave can propagate. This is because of the first three terms on the right hand side which makes a 90 degree phase change. These terms don't exist in the case of quadratic nonlinearity [19]. Variation of group velocity and nonlinear parameter ξ over frequency are depicted in Fig. 6-5. for two example cases explained in chapter four.

6.6 Conservation of Energy in Parametric Amplification

In section 6.2, Manley-Rowe relations have been explained as an alternative form for the conservation of photon numbers. In addition to the conservative quantity of photon numbers, energy conservation law is also satisfied in parametric interaction in DJTL. According to the PDEs (4.20)-(4.24), the first order voltage $V^{(0)}$ and current $I^{(0)}$ associated with the DJTL can be found in terms of the flux solution of $\varphi^{(0)}$ in equation (6.24) as follows

$$V^{(0)} = \frac{1}{2}\sum_{i=1}^{3}\left[\frac{L\omega_i}{L_J\beta_i}\left(\frac{L_J}{Lh} + 1 - L_J C_J \omega_i^2\right) A_i e^{j\theta_i} + c.c.\right] \tag{6.61}$$

$$I^{(0)} = \frac{1}{2}\sum_{i=1}^{3}\left[\left(\frac{1}{L_J} - C_J \omega_i^2\right) A_i e^{j\theta_i} + c.c.\right]. \tag{6.62}$$

Defining electrical power as $P = V^{(0)} I^{(0)}$, we get power associated with each resonant triad A_i as

$$P_i = \varsigma_i |A_i|^2, \qquad i = 1, 2, 3 \tag{6.63}$$

where ς_i is a coefficient defined by

$$\varsigma_i = \frac{1}{4}\frac{L\omega_i}{L_J^2\beta_i}\left(1 - L_J C_J \omega_i^2\right)\left(1 + \frac{L_J}{Lh} - L_J C_J \omega_i^2\right) \tag{6.64}$$

to be multiplied by $|A_i|^2$ in order to give the power. Taking conjugate from each coupled equation, multiplying by corresponding A_i or A_i^*, adding them together and a little mathematical manipulation yields

$$\begin{aligned} &\frac{\partial}{\partial T}\left(\frac{\varsigma_1}{v_{g1}}|A_1|^2+\frac{\varsigma_2}{v_{g2}}|A_2|^2+\frac{\varsigma_3}{v_{g3}}|A_3|^2\right) \\ &\qquad +\frac{\partial}{\partial X}\left(\varsigma_1|A_1|^2+\varsigma_2|A_2|^2+\varsigma_3|A_3|^2\right) \\ &\qquad =j\frac{\pi^2}{8hL_J\Phi_0^2}(\omega_1-2\omega_2+\omega_3)\mathrm{Im}\left(A_1{A_2^*}^2A_3\right) \end{aligned} \tag{6.65}$$

where the right hand side is zero because of the phase-matching condition. Equation (6.65) can be interpreted as

$$\frac{\partial}{\partial T}(\text{Stored energy in the unit length})+\frac{\partial}{\partial X}(\text{Power})=0 \tag{6.66}$$

which is another statement for the energy conservation law. The energy per unit length is referred to as "energy density". Multiplying both sides of equations by ∂X and taking integral with respect to X over the whole interval of $(-\infty,+\infty)$, we extract the simple form of energy conservation law that energy is constant over time. We assumed that the power at positions $X=\pm\infty$ is zero. Satisfaction of energy conservation law is a necessary condition to verify the validity of our derivation as well as simulation. When there exist a slight mismatch such that $\omega_1-2\omega_2+\omega_3\neq 0$, above procedure leads to the equation of

$$\begin{aligned} \text{Stored energy} &= \frac{\varsigma_1}{v_{g1}}|A_1|^2+\frac{\varsigma_2}{v_{g2}}|A_2|^2+\frac{\varsigma_3}{v_{g3}}|A_3|^2 \\ &= j\frac{\pi^2}{8hL_J\Phi_0^2}(\omega_1-2\omega_2+\omega_3)\int_0^T\int_{-\infty}^{\infty}\mathrm{Im}\left(A_1{A_2^*}^2A_3\right)dTdX. \end{aligned} \tag{6.67}$$

According to [20], the total energy oscillates periodically with frequency $\Delta\omega=\omega_1-2\omega_2+\omega_3$.

6.7 Slight Phase Mismatch

The perturbation analysis that led to the coupled wave equations (6.56)-(6.58) in the previous sections was based on the assumption of exact phase-matching condition. In this section, a slight mismatch in order of ϵ is considered in phase constant or/and frequency to perform a general treatment and study the bandwidth of the DJTL. In many cases, the phase-matching condition corresponding to the frequency is exactly held but the phase mismatch is considered only in the phase constant as follows

$$2\beta_2 - \beta_1 - \beta_3 = \delta_\beta \epsilon \tag{6.68}$$

$$2\omega_2 - \omega_1 - \omega_3 = 0. \tag{6.69}$$

When idler is set zero at the starting time, any slight frequency shift in the signal frequency leads to the same frequency shift with opposite sign about the idler frequency and they canceled each other. Doing the same perturbation procedure which is carried out for the perfect phase matching condition, following modified coupled amplitude equations are obtained

$$\frac{\partial A_1}{\partial T} + v_{g1}\frac{\partial A_1}{\partial X} = -j\xi_1\{|A_1|^2A_1 + 2|A_2|^2A_1 + 2|A_3|^2A_1\} - j\mu_1 A_2^2 A_3^* e^{-j\delta_\beta X} \tag{6.70}$$

$$\begin{aligned}\frac{\partial A_2}{\partial T} + v_{g2}\frac{\partial A_2}{\partial X} \\ &= -j\xi_2\{2|A_1|^2A_2 + |A_2|^2A_2 + 2|A_3|^2A_2\} \\ &\quad - j\mu_2 2A_1 A_2^* A_3 e^{j\delta_\beta X}\end{aligned} \tag{6.71}$$

$$\frac{\partial A_3}{\partial T} + v_{g3}\frac{\partial A_3}{\partial X} = -j\xi_3\{2|A_1|^2A_3 + 2|A_2|^2A_3 + |A_3|^2A_3\} - j\mu_3 A_2^2 A_1^* e^{-j\delta_\beta X} \tag{6.72}$$

where ξ_i is a parameter defined in (6.59) or (6.60) and μ_i is a real parameter defined by

$$\mu_1 = \frac{\pi^2 LC}{4\Phi_0^2}\frac{v_{g1}}{\beta_1}\frac{\frac{(2\,\beta_2 - \beta_3)^2}{LC} - \omega_1^2 - \frac{\omega_1}{ChZ_0}\tan\omega_1\tau}{1 - L_J C_J \omega_1^2} \tag{6.73}$$

$$\mu_2 = \frac{\pi^2 LC}{4\Phi_0^2}\frac{v_{g2}}{\beta_2}\frac{\frac{(\beta_1 - \beta_2 + \beta_3)^2}{LC} - \omega_2^2 - \frac{\omega_2}{ChZ_0}\tan\omega_2\tau}{1 - L_J C_J \omega_2^2} \tag{6.74}$$

$$\mu_3 = \frac{\pi^2 LC}{4\Phi_0^2}\frac{v_{g3}}{\beta_3}\frac{\frac{(2\,\beta_2 - \beta_1)^2}{LC} - \omega_3^2 - \frac{\omega_3}{ChZ_0}\tan\omega_3\tau}{1 - L_J C_J \omega_3^2}. \tag{6.75}$$

6.8 Numerical Basis to Solve Nonlinear Coupled Amplitude Equations

Coupled amplitude equations (6.56)-(6.58) and (6.70)-(6.72) describes the interaction of three waves in a nonlinear DJTL in time and space. Because of the nonlinearity, there is no analytical or frequency domain method to solve this system of PDEs. We numerically solve equations by using spectral differentiation in space and finite differences in time. Moreover, we carry out the time stepping by using explicit four-step Adams-Bashforth scheme. In implementation of finite difference by multistep methods the values of the function u that already computed in previous time steps are reused to obtain higher order accuracy and better numerical stability [135]. The Adams-Bashforth formula for numerically computation of the autonomous equation $du/dt = f(u)$ can be written in a four-step finite difference as

$$u^{n+4} = u^{n+3} + \frac{k}{24}[-9f^{n} + 37f^{n+1} - 59f^{n+2} + 55f^{n+3}] \tag{6.76}$$

where $f^n = f(u^n)$.

To obtain a numerical formulation for solving coupled amplitude equations, they are written in the form of three equations

$$\frac{\partial A_i}{\partial T} + v_{gi}\frac{\partial A_i}{\partial X} = G_i \quad i = 1, 2, 3 \tag{6.77}$$

where G_i is the algebraic function of A_i. Then we decompose all complex variables to real and imaginary parts as $A_i = B_i + jC_i$ and $G_i = F_i + jF_{i+1}$ for $i = 1, 2, 3$. Hence, the system of the complex amplitude equations reduces to a real system with six equations and six unknowns written in a matrix representation form of

$$\frac{\partial \boldsymbol{A}}{\partial T} + \boldsymbol{V_g}\frac{\partial \boldsymbol{A}}{\partial X} = \boldsymbol{F} \tag{6.78}$$

where $\boldsymbol{A} = [B_1 \quad C_1 \quad B_2 \quad C_2 \quad B_3 \quad C_3]^T$, $\boldsymbol{F} = [F_1 \quad F_2 \quad F_3 \quad F_4 \quad F_5 \quad F_6]^T$ and $\boldsymbol{V_g}$ is a six-by-six diagonal matrix containing group velocities. For the case of perfect phase matching condition, components of $\boldsymbol{F}$ are given by

$$\begin{aligned} F_1 = \xi_1(&C_1^3 + C_1B_1^2 + 2C_1C_2^2 + 2C_1B_2^2 + 2C_1C_3^2 + 2C_1B_3^2 + C_3C_2^2 + 2C_2B_2B_3 \\ &- C_3B_2^2) \end{aligned} \tag{6.79}$$

$$F_2 = -\xi_1(B_1^3 + B_1C_1^2 + 2B_1B_2^2 + 2B_1C_2^2 + 2B_1B_3^2 + 2B_1C_3^2 + B_3B_2^2 \\ + 2B_2C_2C_3 - B_3C_2^2) \tag{6.80}$$

$$F_3 = \xi_2(C_2^3 + C_2B_2^2 + 2C_2C_1^2 + 2C_2B_1^2 + 2C_2C_3^2 + 2C_2B_3^2 + 2C_1C_2C_3 \\ + 2B_1B_2C_3 + 2C_1B_2B_3 - 2B_1C_2B_3) \tag{6.81}$$

$$F_4 = -\xi_2(B_2^3 + B_2C_2^2 + 2B_2B_1^2 + 2B_2C_1^2 + 2B_2B_3^2 + 2B_2C_3^2 + 2B_1B_2B_3 \\ + 2C_1C_2B_3 + 2B_1C_2C_3 - 2C_1B_2C_3) \tag{6.82}$$

$$F_5 = \xi_3(C_3^3 + C_3B_3^2 + 2C_3C_2^2 + 2C_3B_2^2 + 2C_3C_1^2 + 2C_3B_1^2 + C_1C_2^2 + 2C_2B_2B_1 \\ - C_1B_2^2) \tag{6.83}$$

$$F_6 = -\xi_3(B_3^3 + B_3C_3^2 + 2B_3B_2^2 + 2B_3C_2^2 + 2B_3B_1^2 + 2B_3C_1^2 + B_1B_2^2 \\ + 2B_2C_2C_1 - B_1C_2^2) \tag{6.84}$$

and this can be generalized to other cases with the phase mismatch.

If the number of spatial and temporal grids are denoted by N_x and N_t, a three dimensional global matrix $\boldsymbol{A}$ with the size of 6-by-N_x-by-N_t is defined to hold all values of the six variables. Combining spectral and Adams-Bashforth schemes leads to the update equation in the form of

$$\begin{aligned} \boldsymbol{A}^{n+4} = \boldsymbol{A}^{n+3} + \frac{\Delta t}{24}\Big\{ & -9\left[\boldsymbol{F}^{n} - \boldsymbol{V_g}\left(\boldsymbol{D}\boldsymbol{A}^{n^T}\right)^T\right] + 37\left[\boldsymbol{F}^{n+1} - \boldsymbol{V_g}\left(\boldsymbol{D}\boldsymbol{A}^{n+1^T}\right)^T\right] \\ & - 59\left[\boldsymbol{F}^{n+2} - \boldsymbol{V_g}\left(\boldsymbol{D}\boldsymbol{A}^{n+2^T}\right)^T\right] \\ & + 55\left[\boldsymbol{F}^{n+3} - \boldsymbol{V_g}\left(\boldsymbol{D}\boldsymbol{A}^{n+3^T}\right)^T\right]\Big\} \end{aligned} \tag{6.85}$$

where the time and space steps are denoted by Δt and $\Delta x = 2\pi/N_x$, and $\boldsymbol{D}$ is the N_x-by-N_x spectral differentiation matrix obtained by the spectral methods.

The coupled wave equations (6.56)-(6.58) are first order partial differential equations, therefore one initial condition and one boundary condition is sufficient to avoid an overdetermined system of equations during the numerical computation. As the observation of parametric interaction is a major goal of this chapter, we excite the structure by initial condition at some point of the waveguide and we use the periodic boundary condition in order to resolve numerical issues related to the transient response and reflections at the end. The periodic boundary condition can be physically realized by a circle-shape transmission line or an infinitely long transmission line.

6.9 Numerical Results and Discussions

(1) Wave Mixing (Down-Conversion)

The structure that we used to study the parametric interaction of three phase-matched waves is a DJTL with open stubs with the dispersion diagram illustrated in Fig. 4-14 of chapter four. The normalized TL, stubs and JJ parameters associated with this structure are $L = 1, C = 1$, $h = 0.01$, $L_s = 0.5$, $C_s = 1$, $l_s = 0.1$, $L_J = 1$, $C_J = 0.5$. The three non-degenerate signal, pump and idler waves satisfying the phase-matching conditions are found in Fig. 4-14 with angular frequencies $[\,21.32 \quad 62.37 \quad 103.42]$, phase constants $[\,163.9 \quad 174.8 \quad 185.6]$ and group velocities $[\ 0.0099 \quad 0.0480 \quad 0.0868]$, respectively. Applying the normalization rule described in chapter four and using normalizing factors $k_0 = 20\ m^{-1}$, $\omega_0 = 10^9\ \mathrm{rad/s}$, $R_0 = 50\ \Omega$ and $I_0 = 0.2\ \mu\mathrm{A}$, these parameters are converted to the real physical parameters as $L = 1\ \mu\mathrm{H/m}$, $C = 0.4\ \mathrm{nF/m}$, $h = 0.5\ \mathrm{mm}$, $L_s = 0.5\ \mu\mathrm{H/m}$, $C_s = 0.4\ \mathrm{nF/m}$, $l_s = 5\ \mathrm{mm}$, $L_J = 50\ \mathrm{nH}$, $C_J = 10\ \mathrm{pF}$. By using a lumped array of Al-Al_2O_3-Al junctions with the current density around 1μA per 1μm^2 area [136] and adding a fit capacitance in parallel with the JJ, these parameters are physically realizable as explained in chapter four. Moreover, the normalized flux quanta is obtained as $\widetilde{\Phi}_0 = 0.206$. We have assumed at the beginning that the structure is driven in a weakly nonlinear regime in order to apply perturbation method. The order of nonlinearity is ϵ, whereas the order of small amplitude assumption is $\sqrt{\epsilon}$, therefore we always limit the driving signals less than $0.5\widetilde{\Phi}_0$ in order to have an accurate perturbation scheme.

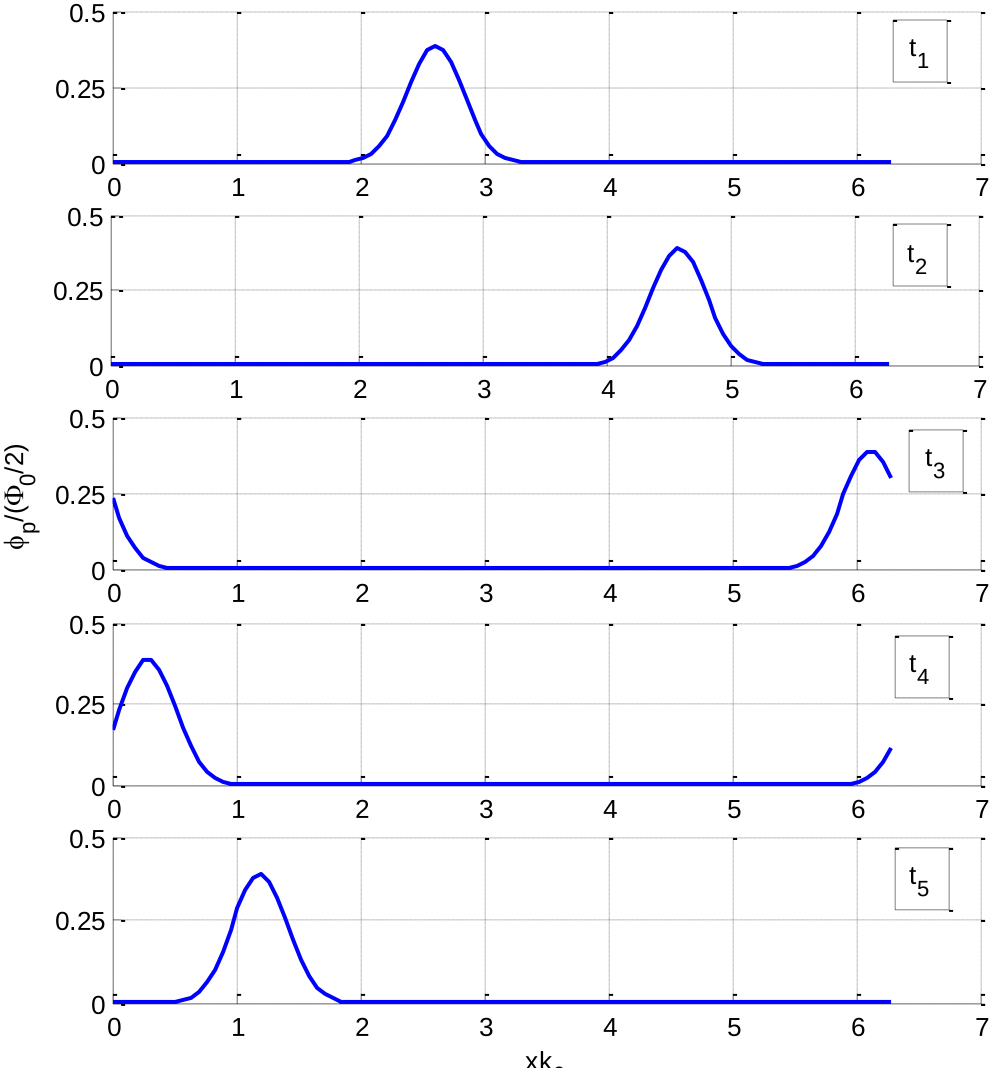

Fig. 6-6 Propagation of a Gaussian pulse modulated at $\omega=62.37\omega_0$ over a DJTL with parameters $L_J = 1, C_J = 0.5, L = 1, C = 1, L_s = 0.5, Cs = 1, l_s = 0.1$, $h = 0.01$;

Fig. 6-6 shows the propagation of a Gaussian pulse modulated at the pump frequency $\widetilde{\omega} = 62.37$ and traveling at the group velocity $\tilde{v}_g = 0.0487$ when both signal and pump waves are set to zero. As explained in section 6.5.7, if two of the three waves are zero, the third one can propagate as demonstrated in this figure. When the pulse reaches the end, it returns at the beginning which is the demonstration of a periodic boundary condition.

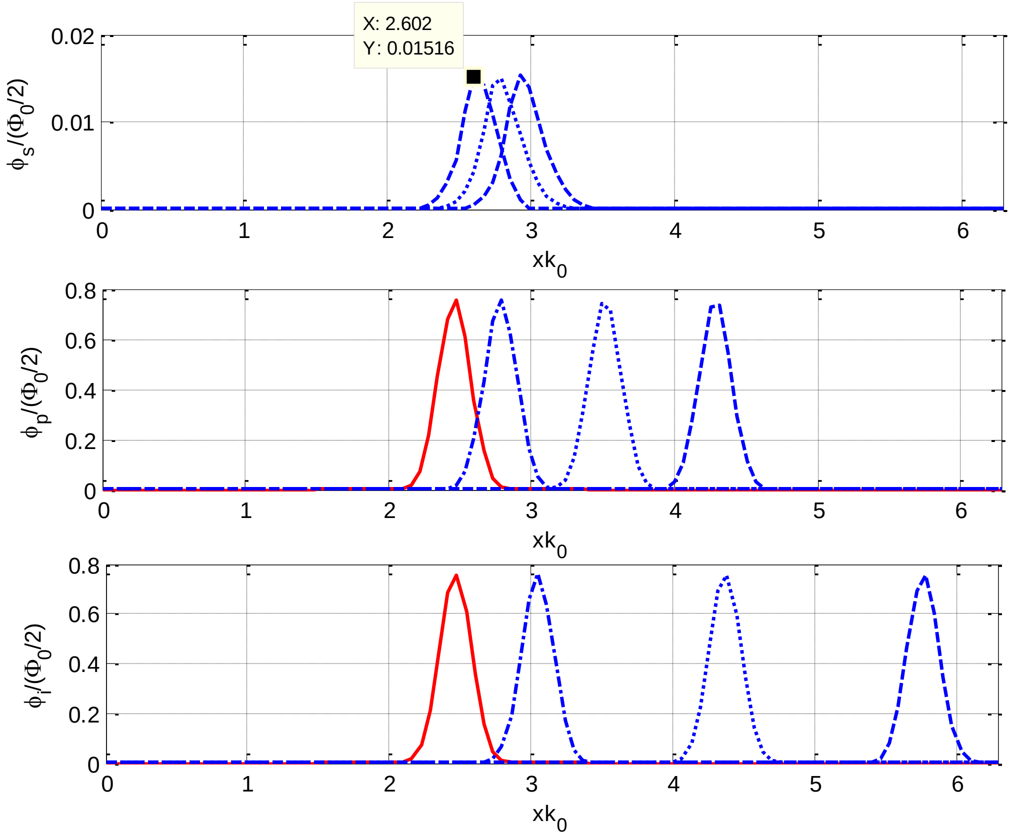

Fig. 6-7 Pulse generation over the signal wave by parametric interaction between three phase-locked pulses of signal (φ_s), pump (φ_p) and idler (φ_i).

Fig. 6-7 shows the interaction of pump and idler pulses which leads to the pulse generation over the signal wave. After all pulses pass each other, the grown signal travels with the amplified value. Each pulse consists of a Gaussian envelope in the form of

$$A(x) = A_0 \exp[-a(x - x_0)^2] \sin(\pi x / x_{\max}) \qquad (6.86)$$

modulated at signal, pump or idler frequencies. Since the tails of a Gaussian pulse extend to infinity, a half-wave sinusoidal term has been multiplied to satisfy the periodic boundary conditions and prevent numerical error which finally leads to the instability in the spectral method. The coefficient a determines the width of the pulse. The FWHM (Full Wave Half Maximum) of the pulse is evaluated by the simple formula of $\text{FWHM} = 2\sqrt{\text{Ln}(2)/a}$. Choosing $a = 40$ in Fig. 6-7., we obtain spatial $\text{FWHM} = 0.2633$. The width of the pulse in time can be easily found by multiplying the corresponding space span by the group velocity. Therefore, the temporal FWHM is obtained as 0.0026. Between signal, pump and idler waves, the group velocity of the signal is the lowest and the group velocity of the idler is the highest, so the signal pulse travels slower compared with pump and idler pulse.

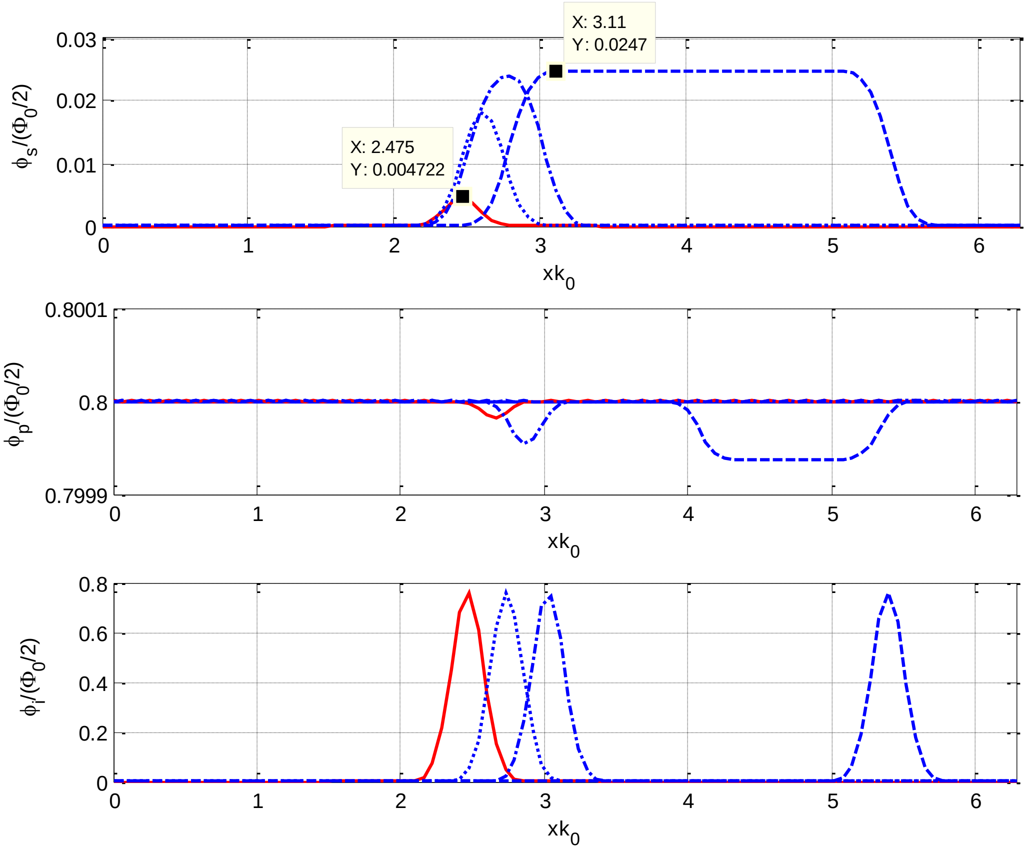

Fig. 6-8 Parametric interaction between a pulse at signal's frequency, continuous wave at pump's frequency and another pulse at the idler frequency which cause the signal pulse to grow with the amplitude gain =14 dB. Leading edge of pulses travels at idler's group velocity.

In Fig. 6-8. the pump is replaced by a continuous wave with the amplitude of $\varphi_p = 0.4\Phi_0$ and the idler is Gaussian pulses with the same FWHM as the one in Fig. 6-7. The amplitude of the pulse generated over the signal has a 4dB improvement compared with the pulse interactions in Fig. 6-7. At the points they start to interact with each other, the level of the pump slightly decreases which give rise to the grow in signal pulse. The left rising edge and the right falling edge of the signal pulse is traveling at two different speeds. The former travels at the group velocity of the signal wave, but the latter travels at the group velocity of the idler wave.

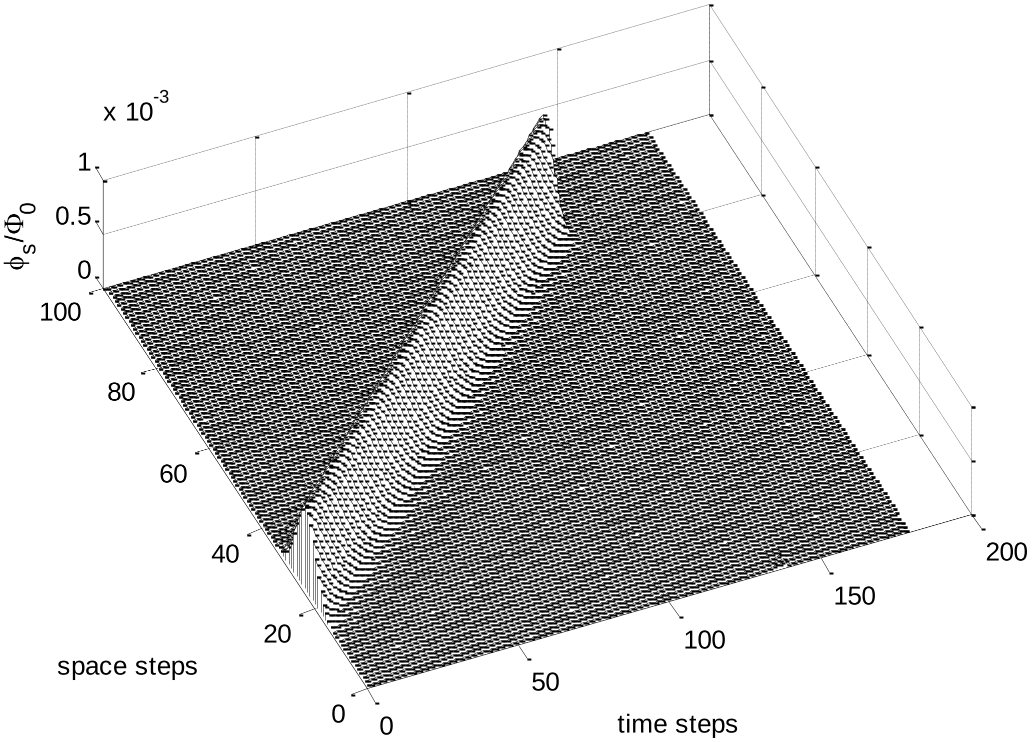

Fig. 6-9 The signal pulse propagate without amplification when idler is zero.

In Fig. 6-9 we investigate the parametric interaction by considering a zero idler at the beginning. The signal pulse has an initial amplitude of $0.01\Phi_0$ and the pump consists of a continuous wave with a constant envelop of $0.4\Phi_0$. According to the coupled amplitude equations (6.56)-(6.58), interaction between the signal and the pump generates an idler wave and interaction between the pump and the idler must also result in increasing the signal. However, the generated idler wave does not attain enough power to contribute in the signal gain. As a result, the signal pulse is propagating with the same amplitude through the DJTL, as shown in Fig. 6-9. We will explain more about this later in this section.

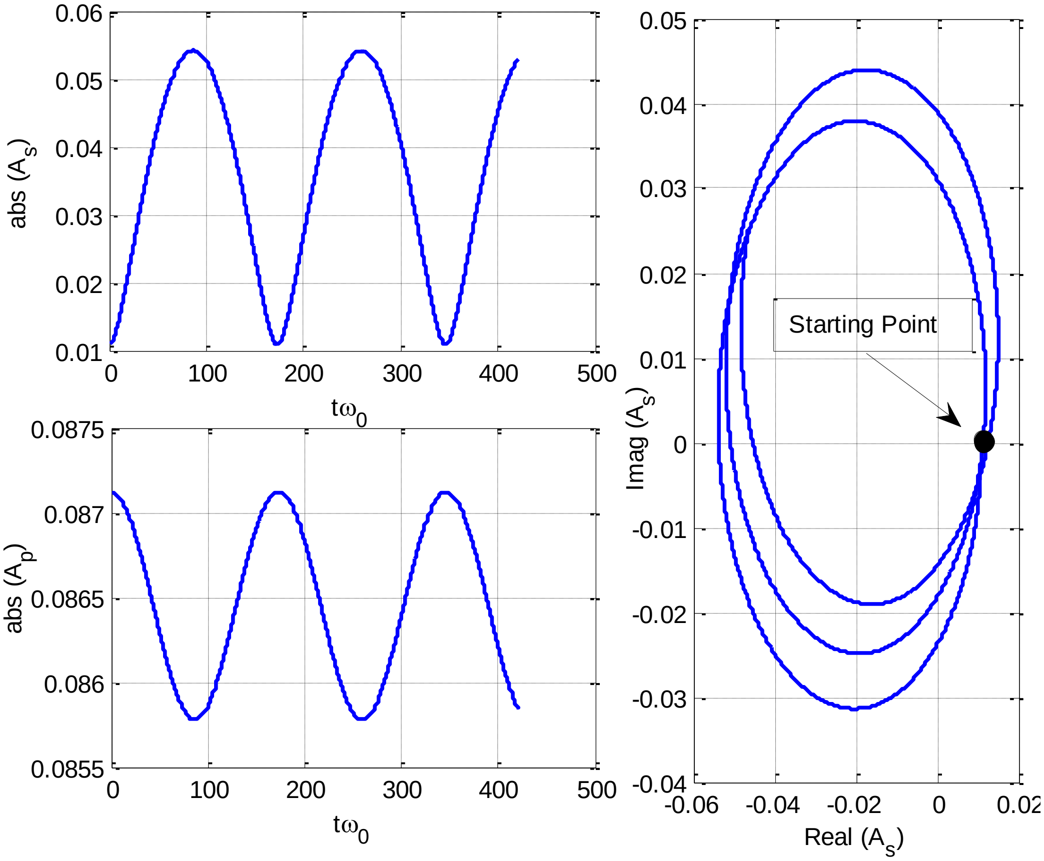

Fig. 6-10 Two sinusoidal pump and idler with $\varphi_p = 0.4\Phi_0$, $\varphi_i = 0.4\Phi_0$ interact that generate a sinusoidal signal wave at the signal frequency . The profile of the signal and pump are shown on the left and the time-varying phase of the generated signal in the right side.

The profile of the signal and pump are depicted in Fig. 6-10 when all three waves are continuous waves with the constant envelope. The signal grows and reaches its maximum, then it returns to its initial value and this process continues. It should be noted that at points when signal reaches its maximum, the pump has its minimal value which is expected by the Manley-Rowe relations as discussed by (6.5) in section 6.2. Moreover, the quadratures of the signal (the real and imaginary parts of the signal) are depicted on the right part of Fig. 6-10. The starting point is highlighted in this figure. The variation on the quadratures starts from this point and traces continuously in the anti-clockwise direction at circles with a growing radius, until it approaches the starting point and this process repeats. The growing radius is an indication for the gain in amplitude and tracing in a circle in an anti-clockwise is due to the first three terms on the right hand side of the coupled amplitude equations

(6.56)-(6.58) which impose a rotation at -90 degree. This results shows that the quadratures are not increasing by the same factor.

The total energy of the three waves is depicted in Fig. 6-11 versus time for several cases of mismatching conditions. In the case of the perfect matching condition the total energy of the system is a constant for all time, as seen in equation (6.67). For the case of mismatch condition, energy oscillates with frequency of $\Delta\omega = \omega_1 - 2\omega_2 + \omega_3$ [53], and this fact can be clearly seen in Fig. 6-11.

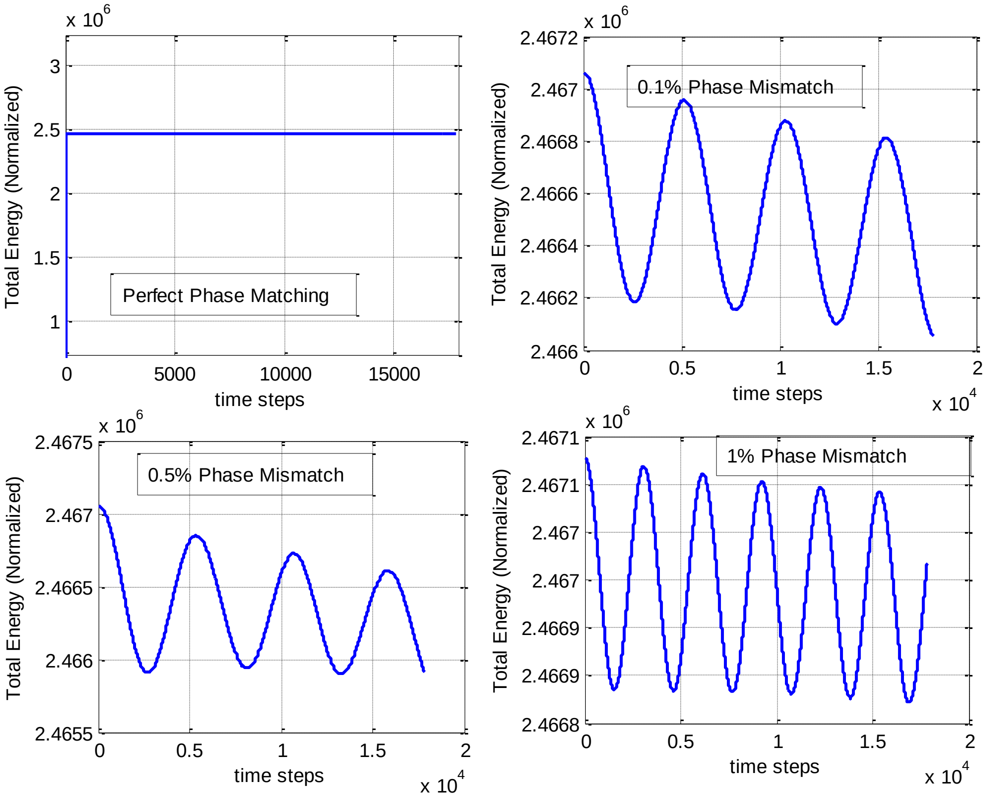

Fig. 6-11 Total energy in the DJTL for cases of perfect matching condition and several cases of mismatching conditions, Time step is dt=0.0314.

(2) Amplification:

In the case of amplification, two waves at signal frequency ω_1 and pump frequency ω_2 are traveling through the DJTL and the idler wave is initially zero. The complex amplitude of the signal, pump and idler waves are A_1, A_2 and A_3. The interaction between the pump and the signal through the $A_2^2 A_1^*$ term on the right side of (6.58) produces the idler wave at frequency ω_3. The idler wave grows over time and space, so that it becomes significant in amplitude to increase the signal wave through the mixing $A_2^2 A_3^*$ term on the right hand side of (6.56). However, the term $A_2^2 A_3^*$ should be significant compared with the term $|A_1|^2 A_1 + 2|A_2|^2 A_1 + 2|A_3|^2 A_1$, which only change the phase of A_1 at -90 degree, to make signal's amplitude A_1 grow. To satisfy this condition, the coefficients ξ_3 and ξ_1 must be quite large in order to influence A_3 and A_1. In the above case, with normalized parameters $\tilde{L} = 1$,$\tilde{C} = 1$, $\tilde{h} = 0.01$, $\tilde{L}_s = 0.5$, $\tilde{C}_s = 1$, $\tilde{l}_s = 0.1$, $\tilde{L}_J = 1$, $\tilde{C}_J = 0.5$, the variation of ξ versus frequency, depicted in Fig. 6-5, shows that ξ_3 is very small. Therefore, the idler wave remains small and doesn't give rise to the signal amplification. Therefore, we reconsider another design with the following normalized parameters $\tilde{L} = 1$,$\tilde{C} = 0.5$, $\tilde{h} = 0.1$, $\tilde{L}_s = 0.5$, $\tilde{C}_s = 1$, $\tilde{l}_s = 1$, $\tilde{L}_J = 0.25$, $\tilde{C}_J = 0.5$. By setting the scaling factors $k_0 = 100\ \mathrm{m}^{-1}$, $\omega_0 = 2\pi \times 10^9$ rad/s, $R_0 = 50\ \Omega$ and $I_0 = 2$ μA, we obtain physical parameters of $L = 0.8$ μH/m, $C = 0.16$ nF/m, $h = 1$mm , $L_s = 0.4$ μH/m, $C_s = 0.31$ nF/m, $l_s = 10$ mm, $L_J = 2$ nH, $C_J = 1.8$ pF.

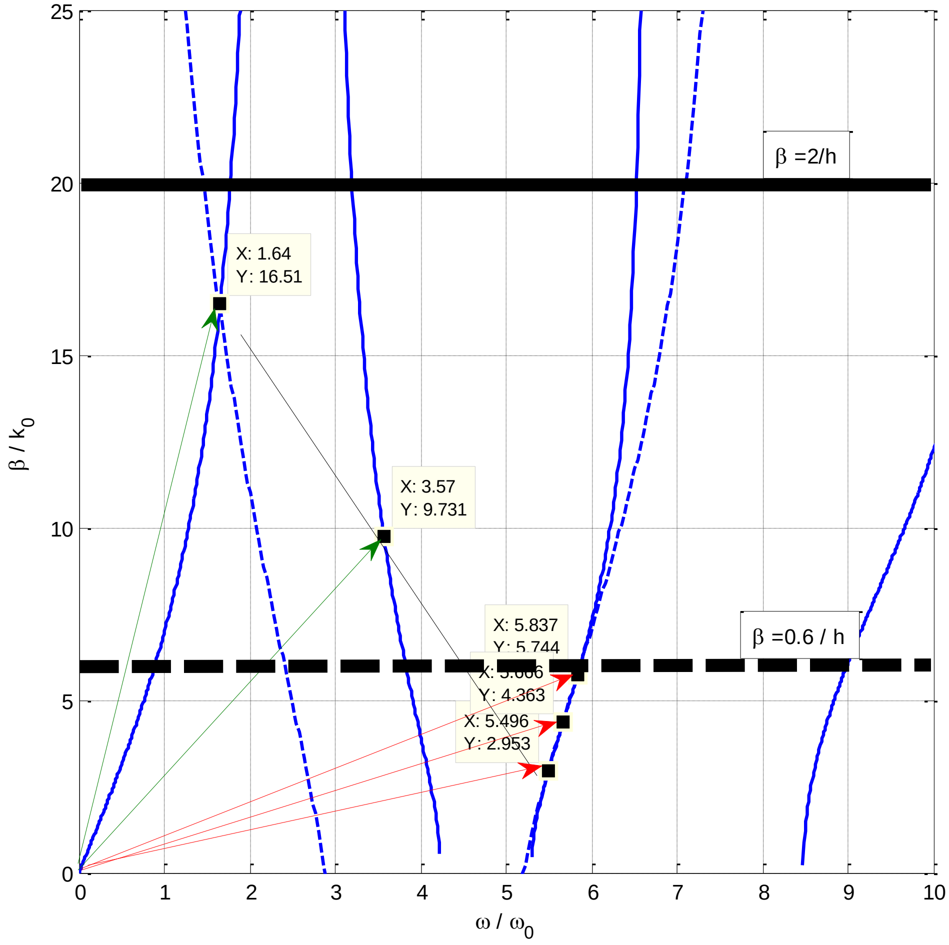

Fig. 6-12 Dispersion diagram of , L_J =0.25, C_J = 0.5, L = 1, C = 0.5, L_s = 0.5, C_s = 1, l_s = 1, h = 0.1. Two sets of three phase-matched waves are found in this diagram.

The dispersion diagram with three phase-matched waves are shown in Fig. 6-12. The group velocity and nonlinear parameter ξ are depicted in Fig. 6-13. For resonant triads with $\widetilde{\omega}_1 = 5.5$, $\widetilde{\omega}_2 = 5.66$ and $\widetilde{\omega}_3 = 5.83$, we find $\tilde{\xi}_1 = 68.42$, $\tilde{\xi}_2 = 52.79$ and $\tilde{\xi}_3 = 41.5$ which are much better than the previous case.

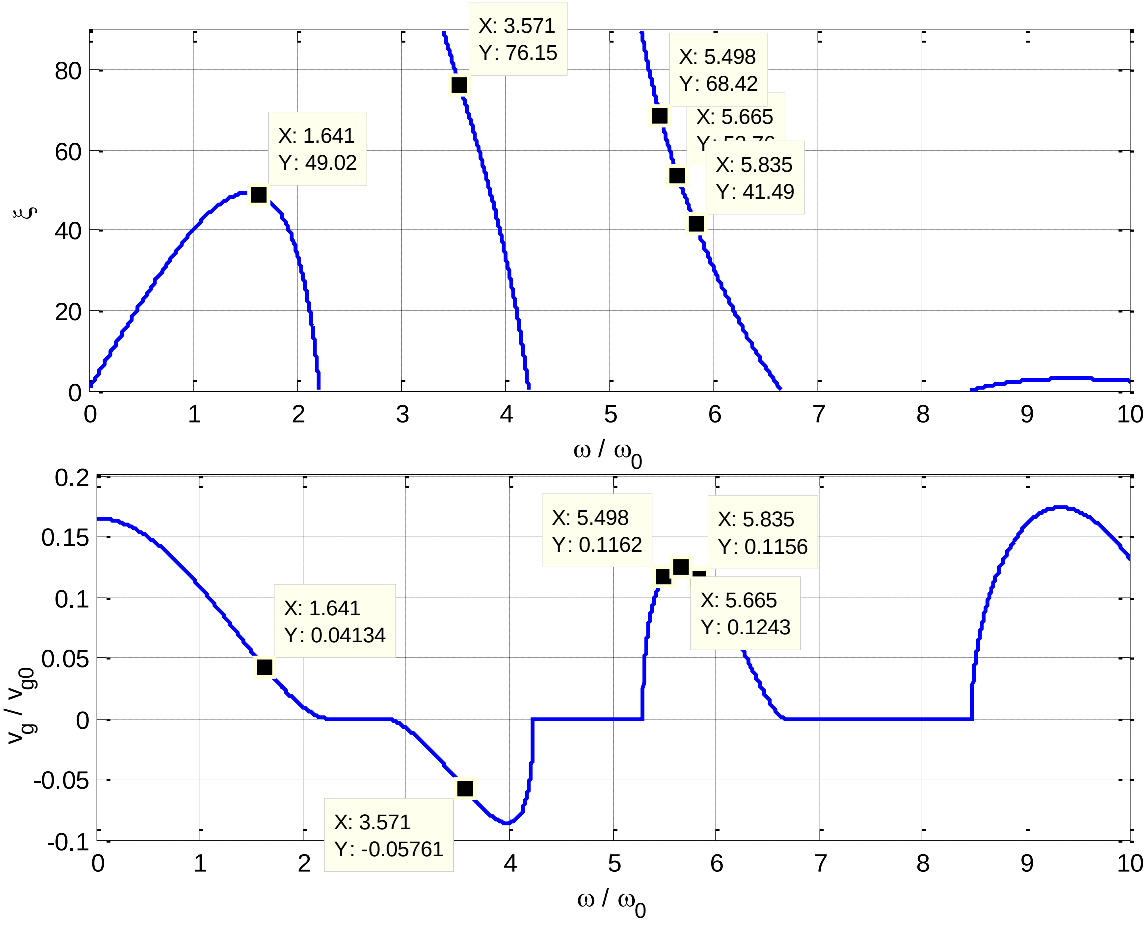

Fig. 6-13 Parameter ξ and group velocity of a DJTL with following parameters L_J =0.25, C_J = 0.5, L = 1, C = 0.5, L_s = 0.5, C_s = 1, l_s = 1, h = 0.1.

Fig. 6-14 displays the results of parametric amplification of the Gaussian pulse with FWHM=0.5266 modulated at the signal frequency by interaction with the continuous-wave pump with an amplitude of $\varphi_p = 0.8\Phi_0$. The signal grows and shrinks to its initial level and this process repeats, as illustrated in Fig. 6-14. At those locations where the signal is amplified, the pump wave is depleted and the idler reaches its maximum. The results of parametric amplification for the Gaussian pulses are illustrated in Fig. 6-15 and Fig. 6-16 with respect to time and space. The contour of Fig. 6-15 is related to the Fig. 6-14. The FWHM of the wider Gaussian pulse of Fig. 6-16 is 2.35. Both pulses receive the same amplification factor, a gain of 8.2 dB. The ratio of the vertical (along y-axis) and horizontal (along x-axis) length of each pulse equals the normalized group velocity at the signal frequency which is 0.116 as seen in Fig. 6-13. Moreover, by dividing the total distance and the total time over which the signal travels, the normalized group velocity of 0.116 is confirmed.

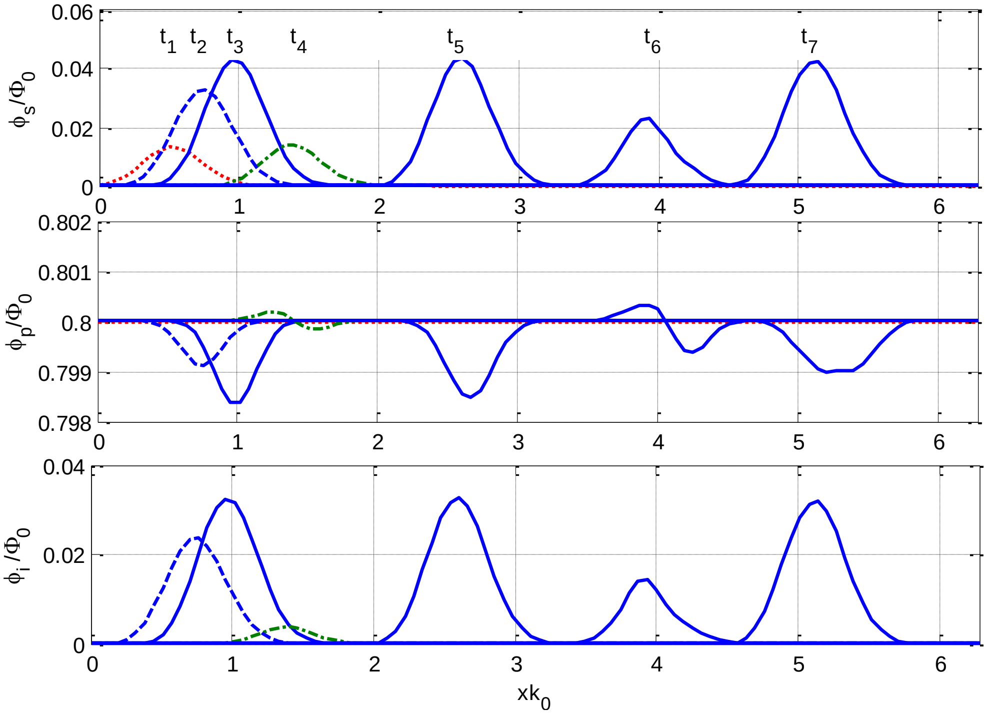

Fig. 6-14 Amplification of the Gaussian signal pulse with FWHM=0.5266 initially at $\varphi_s=0.05\Phi_0$, with the continuous-wave pump at $\varphi_p=0.8\Phi_0$ leads to a gain of 8.2dB.

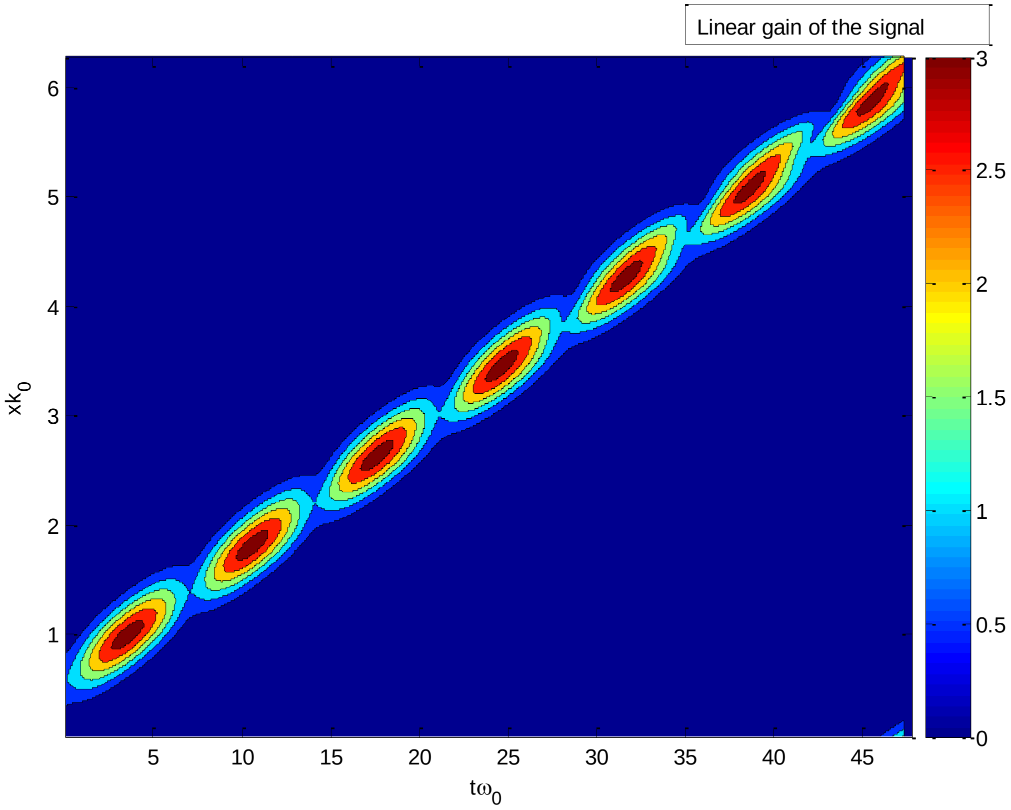

Fig. 6-15 The contour of the Gaussian signal pulse, corresponding to Fig. 6-14 with respect to time and space. The process of amplification occurs in a periodic fashion.

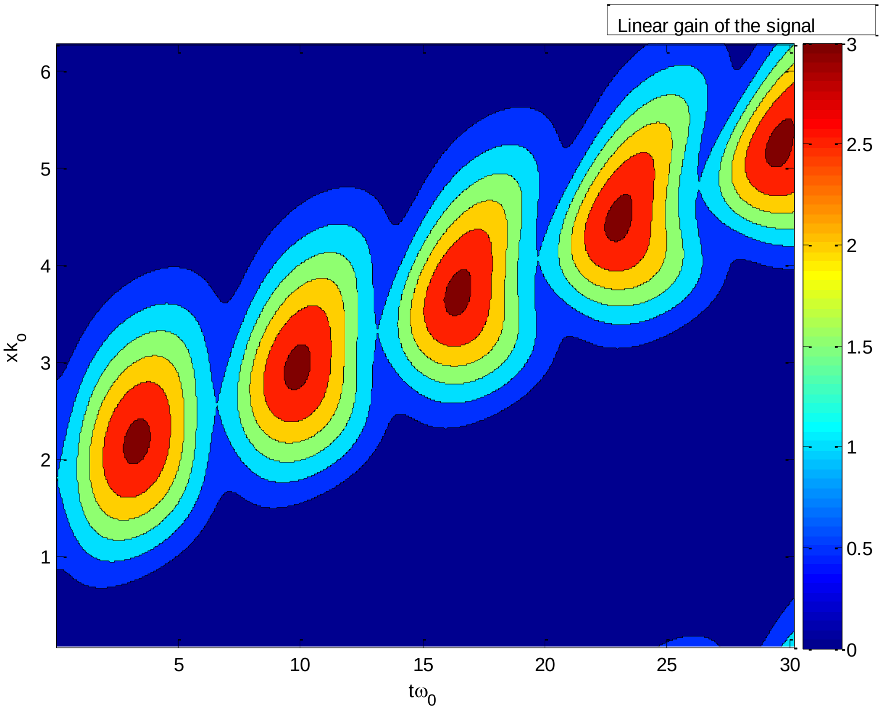

Fig. 6-16 The result of parametric amplification for a Gaussian signal pulse with FWHM=2.35 leads to a gain of 8.2dB.

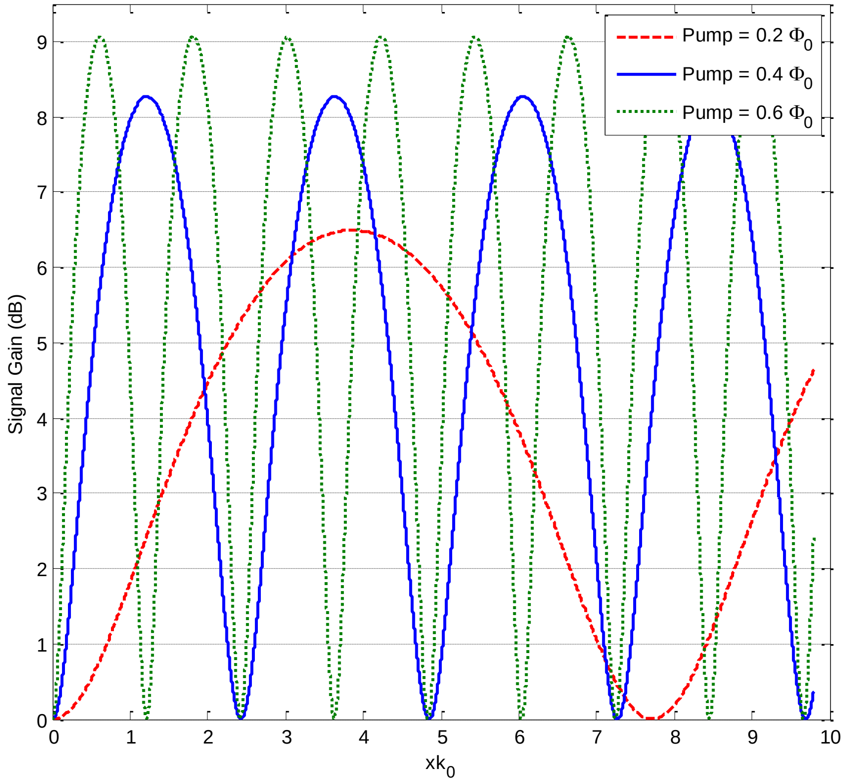

Fig. 6-17 The effect of the pump on amplification gain for the sinusoidal signal wave with an amplitude of $\varphi_s=0.05\Phi_0$.

In Fig. 6-17, the signal and pump waves are assumed sinusoidal and the gain for different pump waves are plotted over the length of the DJTL. As we increase the pump level, the length of the amplifier to achieve the maximum gain becomes smaller, in addition, the gain increases. In other words, the gain density which is the ratio of the maximum gain to the length of maximum gain achievement is increased when the level of the pump wave increases.

Dynamic range is investigated in Fig. 6-18. In this figure for a fixed continuous-wave pump wave at $\varphi_p = 0.4\Phi_0$, the gain of the continuous-wave signal wave for different levels are depicted. As the Manley-Rowe relation (6.5) predicts, when the amplitude of the signal increases, its corresponding gain decreases. If we design the length of the amplifier at the normalized length $\Delta L = 1.1$, the dynamic rage based on the 1-dB compression point covers signals from $\varphi_s = 0.05\Phi_0$ to $\varphi_s = 0.07\Phi_0$ which is very limited. For this length. 11 unit cells are necessary and each contributes 0.74dB in the total gain.

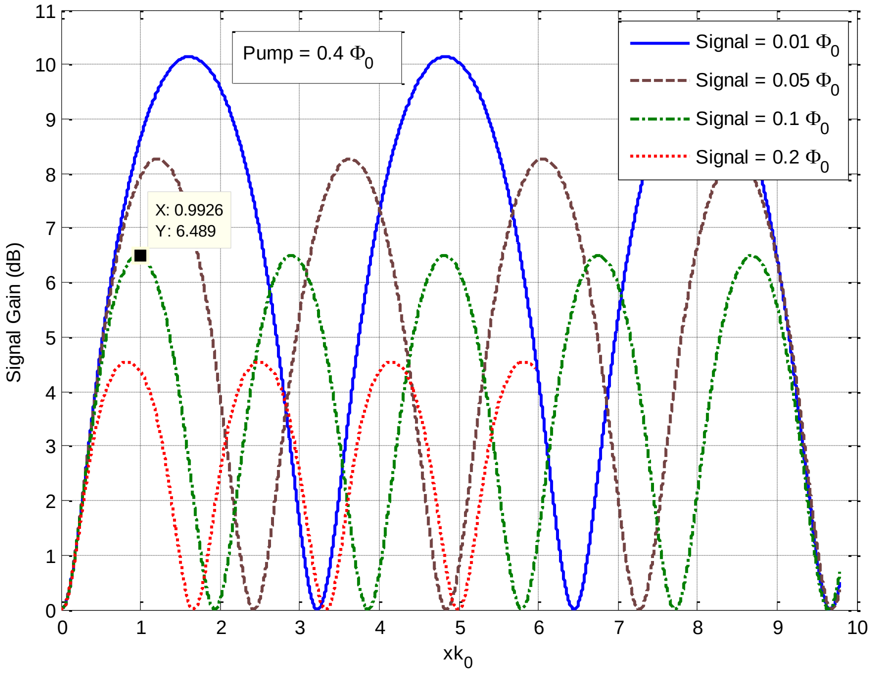

Fig. 6-18 Investigation on the dynamic range of the TW-JPA. The signal gain for different signal levels are depicted and compared.

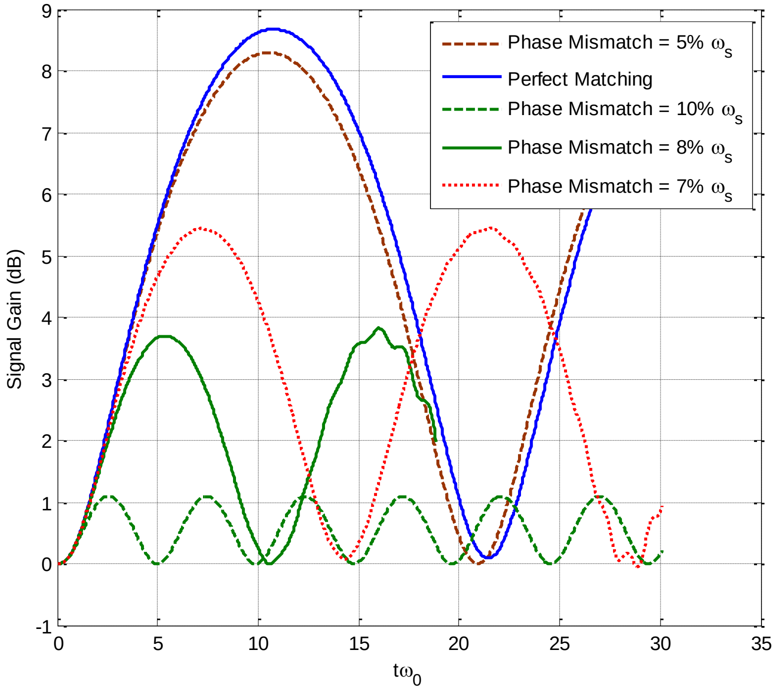

Fig. 6-19 Bandwidth calculation for a TW-JPA leads to the study of the mismatch effect.

Fig. 6-19 studies the bandwidth of the amplifier. Signal and pump waves are continuous waves with amplitudes of $\varphi_s = 0.05\Phi_0$ and $\varphi_p = 0.4\Phi_0$, respectively. According to this figure the relative bandwidth for this design is about 7%.

The bandwidth characteristic of traveling-wave parametric device can be studied by fixing the length of the device (particularly amplifier) and calculating the gain dropped at this point by assuming a certain mismatch. As mentioned in section 6.7, when the pump is fixed in frequency, the slight frequency shift at the signal is compensated by a similar opposite shift at idler, and there is only mismatch of the phase constant. The solid line is the gain profile for the perfect matching case that a gain of 8.6dB is achieved at $\tilde{t} = 15$. This is the time interval between the initial interaction and the maximum gain achievement. Multiplying this time interval by the group velocity of the signal wave, the time duration $\Delta\tilde{t} = 12$ can be converted into the length over which this gain is achieved. This yields $\Delta\tilde{x} = 1.394$ which is the length of the device. Since the length of each unit cell is $h = 0.1$, this parametric device consists of 14 numbers of unit cells. Each unit cell contributes a gain of 0.6143 dB so that the total gain with 14 unit cells becomes 8.6 dB.

Bandwidth is related to the mismatch caused by a deviation from the perfect phase-matching condition, therefore, bandwidth is determined by the dispersion diagram of the structure. As seen in Fig. 6-12, the bandwith is limited by two bandgaps just before and after the branch where the resonant triads are located. According to the dispersion diagram of Fig. 4-14, the signal wave is located at the very sharp part of the dispersion curve, so a slight deviation from this point results in a large deviation in the phase constant which destroys the bandwidth. However for the structure with the dispersion diagram in Fig. 4-15 of chapter four with the three non-degenerate waves at frequencies $[4.978 \quad 9.765 \quad 14.56]$, the signal wave is located in a linear-like part of the dispersion curve and typical values for the phase constant are rather high. Therefore, by a slight change around the signal point, the relative variation in the phase constant becomes small. To have a more accurate analysis, the frequency mismatch should be on the order of ϵ as our derivation for the formula (6.70)-(6.75) was based on this assumption. The pump signal is set at $0.4\Phi_0$, therefore we limit the frequency variation to $\pm 0.2\omega_s$.

6.10 Conclusion

A mathematical treatment based on the regular perturbation technique and method of multiple scales has been applied to the nonlinear wave equation which describes microwave propagation through DJTL structures assisted by open stubs. DJTLs have been driven in a weakly nonlinear regime, so perturbation methods are applicable. This process leads to three coupled amplitude equations which describe the spatial and temporal evolution of the complex amplitudes of the three phased-locked signal, pump and idler waves. Assuming a slight phase mismatch in frequency and phase constants, more general coupled wave equations have been obtained. The incorporation of two numerical techniques: the spectral method in space and the multistep Adams-Bashforth scheme in time domain, have been employed to solve the coupled amplitude equations. Based on the coupled amplitude equations, we have investigated different aspects of the parametric interaction of the resonant triads in a TW-JPA such as energy conservation, gain, stability, dynamic range and the bandwidth. Designing proper DJTL structures, numerical results have shown that DJTLs act as parametric amplifier and they exhibit superior stability, unilateral gain and a large bandwidth.

Chapter 7

Concluding Remarks

7.1 Summary and Conclusion

Investigation of different aspects of parametric interactions and amplifications between microwave signals in structures involving Josephson junctions is the main theme of this thesis. Conceptual framework, basic ideas and common terminology around the parametric process and amplification have been briefly explained in the first introductory chapter.

We began our study with the lumped JPA with two configurations, which are referred to as current- and voltage-based. Manley-Rowe relation predicted the ideal gain and also the "power added efficiency" of the system. Application of Manley-Rowe relations to the JPA, revealed that parametric amplifiers can have serious issue regarding the dynamic range which might limit their performance. For both cases, the transducer power gain was obtained in a closed-form and the negative resistance was observed in the denominators of the gain formula. When gain is very large, the circuit is unstable, the bandwidth is very small and the JPA operates in the oscillation regime. Having a new design for the maximum gain achievement and using an additional fit resistor, the regime of the device operation moved to the stable amplification regime where gain decreased and bandwidth was improved. The bandwidth of the lumped JPA was hindered by microwave filters and resonators. The thermal noise analysis of the device has been carried out and it was shown that it was reduced to as low as 35 photons above the quantum limit when the device was held at 4K. We concluded that a current-based configuration seems more promising as it is less sensitive to the pump source. A design procedure with an example for the current-based JPA was outlined, which led to the proper pump source and filter characteristics.

In chapter three, we presented our analytical and experimental work regarding the filter properties of a superconducting periodic structure where a series of dielectric gaps were periodically placed on the TL. We have assumed both an finite and infinite number of unit cells. Each requires a different method of analysis, but as the number of unit cells increases, it was shown that both approaches would merge to the same result. Due to the lack of availability of any CAD (Computer Aid Design) tool in accessible commercial software to account for superconductor plates, a rigorous CAD tool was provided to find all distributed circuit parameters of superconducting transmission lines such as parallel plate, microstrip line and CPW (Coplanar Waveguide) [25]. The Dispersion diagram, attenuation constant, s-parameters, input impedance and filter properties of the periodic TL were discussed. It is quite interesting that for both finite and infinite periodic structures, all wave and circuit variables such as propagation constant, s-parameters, input impedance and resonant frequencies are expressed in closed-form equations in terms of the parameters of a single unit cell. Different designs have been fabricated in the film of YBCO on LAO substrate and characterized. The experimental results were in good agreement with those of theoretical treatment.

In order to improve the stability, gain and bandwidth of Josephson parametric amplifiers, we proposed a traveling wave structure called DJTL, for realizing of parametric interaction. DJTL is an assembly of JJs in a periodic fashion over a superconducting TL. The incremental section of DJTL includes a segment of a superconducting transmission line and a lumped block of Josephson junctions. In chapter four, assuming long-wave approximation, the nonlinear PDE in time and space have been derived to describe the nonlinear wave propagation through the DJTL. Under the small amplitude assumption, DJTLs were in a linear regime and dispersion analysis was performed to see different regimes of propagation, such as bandgap and slow-wave propagation. It was demonstrated that series-connected DJTL cannot satisfy the perfect phase-matching condition which was necessary for the purpose of parametric interaction. Using dispersion engineering, open-stubs were added to overcome this issue. The wave equation in space and time has been derived again and satisfaction of the phase-matching condition has been demonstrated for several designs of DJTL structures assisted by open-stubs. Floquet analysis predicted another cut-off condition which was the consequence of the discrete nature of the structure. In other words, those waves with a wavelength greater than h/π can propagate through the DJTL. Realizability assessment based on Tichmarch's theorem has been successfully examined for this type of structure. Considering all criteria such as cut-off and long-wave approximation, a design example over a realistic DJTL structure has been carried out and the support of three phased-matched waves has been highlighted in the dispersion diagram. Impedance analysis, which was necessary in microwave implementation and excitation, has also been performed to compare the input impedance of each signal, pump and idler waves.

In chapter five, microwave behaviour of DJTLs (Discrete Josephson Transmission Line) have been investigated by time domain methods. As the governing equation was a system of nonlinear partial differential equations with mixed boundary conditions, the method of Finite Difference Time Domain (FDTD) was used to solve the equations numerically. Systematically achievable nonlinear FDTD solvers have been achieved with high stability and robustness to monitor the wave propagation through different DJTL structures. The details and numerical schemes have been fully described in this chapter. Features and characteristics such as cut-off propagation, dispersive behaviour and shock wave formation, which are expected from the wave propagation through the nonlinear DJTL, have been addressed and discussed in this section. The propagation of signal, pump and idler waves for a particular design have been also examined in this chapter. The shock wave formation was shown as a direct result of operating at in highly nonlinear regime. Shock wave examination is the simplest way to determine the nonlinearity of a waveguide. Experimental results for DJTL with HTS weak links are shown in the last section and observation of shock waves have been carried out.

With the vast knowledge of all microwave characteristics and by identifying different regimes of operation, which include impedance properties, cut-off propagation, dispersive behavior and shock-wave formation, we moved toward the study, analysis and design of a TW-JPA in chapter six. We used perturbation theory accompanied with the method of multiple scale to derive the three nonlinear coupled amplitude equations to describe the parametric interaction. The case of the phase-matching condition with slight deviation has also been addressed. The conservation of energy law has been successfully examined. The incorporation of two numerical techniques, spectral method in space and multistep Adams-Bashforth in time domain was employed to solve the complex coupled nonlinear equations. The interaction of three Gaussian pulses modulated at signal, pump and idler frequencies have been studied and led to the growth of the signal pulse. Gain enhancement has been shown when the pump is replaced by a continuous wave instead of a pulse. When contrasting the quadratures of the signals, the results show that the non-degenerate TW-JPA acts as a phase-sensitive amplifier. The TW-JPA improved the bandwidth compared to the lumped counterpart, provided the signal wave is not located at sharp-curvature parts of the dispersion diagram. Phase mismatch downgrades the performance of TW-JPA by gain degradation, bandwidth reduction and amplifier's length extension. Another effect of the phase-mismatch was seen in oscillation on the total energy profile of the DJTL. The contribution of each unit cell in gain achievement has been also addressed. In general, different aspects of the parametric amplifier such as gain, bandwidth and stability have been improved by proposing TW-JPA.

7.2 Future Directions

Having gained the knowledge about parametric interaction in JJ-based microwave networks and clear understanding of the functionality of the parametric devices studied in this thesis, the followings are suggestions to expand upon the research presented in this thesis.

Keeping with lumped parametric topology, it is desirable to implement parametric devices on a microwave platform. Thus, designing intricate microwave filters and combiners over planner transmission line structures including JJs is an essential step toward utilizing these devices in real applications.

A further improvement in gain enhancement can be achieved by cascading successive JPAs. To improve the efficiency of the device, the idler signal generated from the previous stage is to be used as a pump signal for the next JPA. Incorporation of the shunt resistance of JJ element into our analytical modeling influences the gain of the circuit and also enables one to calculate the thermal noise arising from JJs into the system.

Mixing, down-conversion, up-conversion and sub-harmonic pumping are other regimes of operation with certain applications that can be followed by parametric devices. Moreover, configurations such differentially pumped scheme improve the noise characteristics and also reduce the need for the pump filters. Further designs of elaborate lumped devices, their verification with jSPICE, and simulation of their corresponding microwave implementations with a full-wave simulator can be done before fabrication and experimental set-up to ensure their functionality.

Using biased JJs, the phase-matching condition will change from a four photon process to a three photon process. This might suggest another types of parametric devices, lumped or particularly traveling-wave, with improved performance. Moreover, using nonlinear devices such as SQUIDs instead of a single JJ offers another topic of investigation since they increase the capacity of the structure to inject a higher power of pump waves.

Instead of TL modeling, the matrix representation of each unit cell of TW-JPA with the multiplication property to find the matrix description of the total structure is another attempt to pursue. Also, by numerical methods such as Chebyshef spectral method, boundary conditions including the source of excitation can be captured into the simulation.

Integration of JPAs with sensitive devices including superconducting qubits and superconductive single photon detectors are other area of research than one can explore.

Finally, investigation of the traveling-wave parametric devices with a quantum description could open up a variety of applications and research directions, including the study of generating squeezed quantum states and microwave entangled photons in circuit QED, as well as the study of photon-photon interactions suitable for quantum signal generation and detection, and quantum information processing. Having quantum description, we can capture the issue of the quantum zero-point fluctuation which becomes significant at ultra-low temperatures.

Appendix A

Ladder Network Equations for DJTL

By dividing a series-connected DJTL into *N* identical unit cells, we can have another view of DJTL as illustrated in Fig.A.1. Instead of continuous variable *z*, index *n* designated for each unit cell.

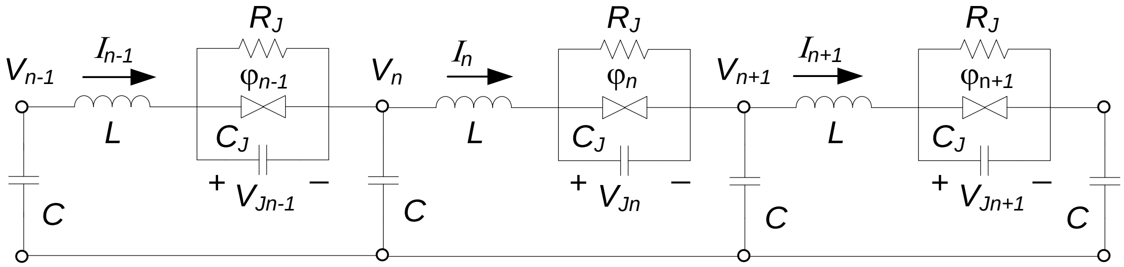

Fig. A.1. Discrete circuit model of DJTL.

To the analogy of parallel-connected [116], we attain the following equation to express flux propagation in the structure

$$\begin{gathered}\frac{L_{J0}}{R_J}(\dot{\varphi}_{n-1}-2\dot{\varphi}_n+\dot{\varphi}_{n+1})+(\sin\varphi_{n-1}-2\sin\varphi_n+\sin\varphi_{n+1})\\ +L_{J0}C_J(\ddot{\varphi}_{n-1}-2\ddot{\varphi}_n+\ddot{\varphi}_{n+1})= \\ \frac{LCL_{J0}}{R_J}\varphi_n^{(3)}+LC\frac{d^2}{dt^2}[\sin\varphi_n]+LCL_{J0}C_J\varphi_n^{(4)}+CL_{J0}\ddot{\varphi}_n\end{gathered}\tag{A-1}$$

where φ_n is the flux associated to the Josephson junction in the *n*th segment. In above equation the first, second, third and fourth derivatives of φ_n with respect to time are denoted by $\dot{\varphi}_n$, $\ddot{\varphi}_n$, $\varphi_n^{(3)}$ and $\varphi_n^{(4)}$, respectively. Considering a particular harmonic solution $\varphi_n = A_0e^{j(\omega t-\kappa n)}$ and small amplitude approximation ($\sin\varphi_n \sim\varphi_n$), substituting this into the equation (A-1), this yields following dispersion relation

$$4\sin^2(\kappa/2)=\frac{LCL_{J0}C_J\omega^4-C\left(L+L_J\right)\omega^2-j\dfrac{LCL_J}{R_J}\omega^3}{L_JC_J\omega^2-1-j\dfrac{L_J}{R_J}\omega}.\tag{A-2}$$

If L and C are distributed inductance and capacitance associated to the transmission line, they must be multiplied by the factor Δz before substitution in equations (A-1) and (A-2). Parameter κ in (A-2) is a complex number accounting for the attenuation and phase difference between two subsequent cells. If the phase constant and period of the uniform structure is γ and Δz, parameter κ will be equal to $\gamma\Delta x$. This equation is a modified version of equation (4.8) in a sense that the effect of equi-spaced discrete Josephson element is taken into account. However, the uniform model of DJTL is a very good approximation in low frequency regime. As frequency approaches the Bragg cut-off frequency, $\sin^2(\kappa/2) = 1$, the wave becomes dispersive, and these two dispersion relations deviate from each other.

If the long wave approximation $(\Delta x/\lambda \to 0)$ holds, κ is very small and by using $2\sin^2(\kappa/2) \sim \kappa^2/2$ two dispersion relations in (4.8) and (A-2) match very well. Note that when we are in a small amplitude approximation and temperature is low enough, most of the current mostly consists the Cooper pairs, so the normal and displacement currents are very small, so $C_J \to 0$ and $R_J \to \infty$. By this assumption, the fluxon dynamics given by equation (A-1) and dispersion relation of (A-2) reduces to

$$(\sin\varphi_{n-1} - 2\sin\varphi_n + \sin\varphi_{n+1}) = L_{J0}C\frac{d^2\varphi_n}{dt^2} + LC\frac{d^2}{dt^2}[\sin\varphi_n] \tag{A-3}$$

$$\sin^2(\kappa/2) = \frac{1}{4}\omega^2 C\left(L + L_{J0}\right). \tag{A-4}$$

Therefore, to have a wave propagation condition, the following condition must be met

$$\omega \leq \frac{2}{\Delta z\sqrt{C\left(L + L_J/\Delta x\right)}} \tag{A-5}$$

as distributed elements L and C have been substituted by $L\Delta x$ and $C\Delta x$, respectively. The right hand side of this inequality is the Bragg cut off frequency. The phase constant corresponding to Bragg cut off frequency is $k = \pi/\Delta x$ and this is in a quite good agreement with the fact that the first stopped band edge in periodic structures occurs at the half wavelength of the wave.

Appendix B

Nonlinear Kinetic Inductance

It has been demonstrated that the kinetic inductance associated with a superconducting film is a function of applied current, I. The current dependence of the kinetic inductance can be derived by Ginzburg-Landau theory for the case of uniform current distribution [137], [138]. The relation describing the kinetic inductance of a superconducting film is given by

$$L_K = L_{K0}\left[\frac{1}{1-\xi\chi^2(\kappa)}\right] \tag{B-1}$$

where L_{K0} is the kinetic inductance of the film in the absence of current. For superconducting thin film ($\lambda_L \gg t$) with thickness t, width w, and penetration depth λ_L, the zero-current kinetic inductance is typically equal to $L_{K0} = \mu_0\lambda_L^2(T)/wt$. Parameter κ is the ratio of the current density to the critical current density, i.e. $\kappa = J/J_c$, and χ is an implicit function of κ, given by

$$\chi^3 - 3\chi + 2\kappa = 0; \qquad -1 \le \kappa \le 1. \tag{B-2}$$

Parameter ξ indicates how fast the order parameter is adjusted by the velocity of Cooper pairs. At two extreme cases, ξ is 1 with the assumption of instant relaxation time and 1/3 with the assumption of infinite relaxation time. Since $\kappa < 1$, it can be shown that equation (B-2) always has three solutions for χ, but only one of them falls between -1 and 1. This is the acceptable value to be substituted for χ in (B-1). The typical value of critical current density J_c for YBCO superconductor material with $\lambda_L(0) = 250$ nm is 10^6 A/cm^2 [90]. Therefore, the critical current for a film of YBCO with cross area of 100 nm × 100 nm would be 0.1 A.

A nonlinear guiding system in frequency domain can be modeled by an iterative procedure using a suitable linear analysis tool as a basic routine [139]. The equivalent linear model and the original nonlinear structure are related to each other by an elementary self-consistency relation. The flowchart of Fig B.1. describes the procedure of implementation of this nonlinear method.

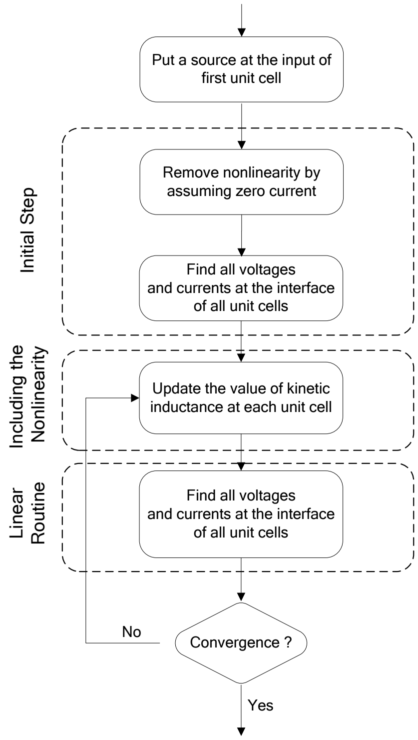

Fig. B.1 The general flowchart of analyzing a nonlinear system by the self-consistent method.

Appendix C

Multiple Scale Derivatives

In this appendix, the derivative of the function with respect to slow-varying variables are presented. They are obtained based on the chain rule in differentiation. The relation between each variables is sketched in Fig C.1.. In following formula parameter θ is equal to $\theta = \epsilon\tau$.

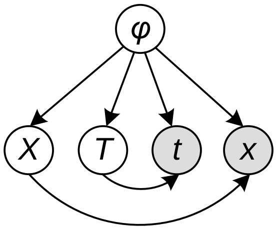

Fig. C.1. Interconnection between φ and four slow- and fast-varying variables.

$$\tilde{\varphi}_t = \varphi_t + \epsilon\varphi_T \tag{C-1}$$

$$\tilde{\varphi}_{tt} = \varphi_{tt} + 2\epsilon\varphi_{tT} + \epsilon^2\varphi_{TT} \tag{C-2}$$

$$\tilde{\varphi}_{ttt} = \varphi_{ttt} + 3\epsilon\varphi_{ttT} + 3\epsilon^2\varphi_{tTT} + \epsilon^3\varphi_{TTT} \tag{C-3}$$

$$\tilde{\varphi}_{tttt} = \varphi_{tttt} + 4\epsilon\varphi_{tttT} + 6\epsilon^2\varphi_{ttTT} + 4\epsilon^3\varphi_{tTTT} + \epsilon^4\varphi_{TTTT} \tag{C-4}$$

$$\tilde{\varphi}_x = \varphi_x + \epsilon\varphi_X \tag{C-5}$$

$$\tilde{\varphi}_{xx} = \varphi_{xx} + 2\epsilon\varphi_{xX} + \epsilon^2\varphi_{XX} \tag{C-6}$$

$$\tilde{\varphi}_{txx} = \varphi_{txx} + \epsilon(2\varphi_{xXt} + \varphi_{xxT}) + \epsilon^2(\varphi_{XXt} + 2\varphi_{xXT}) + \epsilon^3\varphi_{XXT} \tag{C-7}$$

$$\begin{gathered}\tilde{\varphi}_{ttxx} = \varphi_{ttxx} + 2\epsilon(\varphi_{xXtt} + \varphi_{xxtT}) + \epsilon^2(\varphi_{XXtt} + 4\varphi_{xXtT} + \varphi_{xxTT}) \\ + 2\epsilon^3(\varphi_{XXtT} + \varphi_{xXTT}) + \epsilon^4\varphi_{XXTT}\end{gathered} \tag{C-8}$$

$$\tilde{\varphi}_t^{(t-2\tau,T-2\theta)} = \varphi_t^{(t-2\tau,T-2\theta)} + \epsilon\varphi_T^{(t-2\tau,T-2\theta)} \tag{C-9}$$

$$\tilde{\varphi}_{tt}^{(t-2\tau,T-2\theta)} = \varphi_{tt}^{(t-2\tau,T-2\theta)} + 2\epsilon\varphi_{tT}^{(t-2\tau,T-2\theta)} + \epsilon^2\varphi_{TT}^{(t-2\tau,T-2\theta)} \tag{C-10}$$

$$\begin{gathered}\tilde{\varphi}_{ttt}^{(t-2\tau,T-2\theta)} = \varphi_{ttt}^{(t-2\tau,T-2\theta)} + 3\epsilon\varphi_{ttT}^{(t-2\tau,T-2\theta)} + 3\epsilon^2\varphi_{tTT}^{(t-2\tau,T-2\theta)} \\ + \epsilon^3\varphi_{TTT}^{(t-2\tau,T-2\theta)}\end{gathered} \tag{C-11}$$

$$\begin{aligned}\tilde{\varphi}_{tttt}^{(t-2\tau,T-2\theta)} &= \varphi_{tttt}^{(t-2\tau,T-2\theta)} + 4\epsilon\varphi_{tttT}^{(t-2\tau,T-2\theta)} + 6\epsilon^{2}\varphi_{ttTT}^{(t-2\tau,T-2\theta)} \\ &\quad + 4\epsilon^{3}\varphi_{tTTT}^{(t-2\tau,T-2\theta)} + \epsilon^{4}\varphi_{TTTT}^{(t-2\tau,T-2\theta)}\end{aligned} \tag{C-12}$$

$$\tilde{\varphi}_{x}^{(t-2\tau,T-2\theta)} = \varphi_{x}^{(t-2\tau,T-2\theta)} + \epsilon\varphi_{X}^{(t-2\tau,T-2\theta)} \tag{C-13}$$

$$\tilde{\varphi}_{xx}^{(t-2\tau,T-2\theta)} = \varphi_{xx}^{(t-2\tau,T-2\theta)} + 2\epsilon\varphi_{xX}^{(t-2\tau,T-2\theta)} + \epsilon^{2}\varphi_{XX}^{(t-2\tau,T-2\theta)} \tag{C-14}$$

$$\begin{aligned}\tilde{\varphi}_{txx}^{(t-2\tau,T-2\theta)} &= \varphi_{txx}^{(t-2\tau,T-2\theta)} + \epsilon\left(2\varphi_{xXt}^{(t-2\tau,T-2\theta)} + \varphi_{xxT}^{(t-2\tau,T-2\theta)}\right) \\ &\quad + \epsilon^{2}\left(\varphi_{XXt}^{(t-2\tau,T-2\theta)} + 2\varphi_{xXT}^{(t-2\tau,T-2\theta)}\right) + \epsilon^{3}\varphi_{XXT}^{(t-2\tau,T-2\theta)}\end{aligned} \tag{C-15}$$

$$\begin{aligned}\tilde{\varphi}_{ttxx}^{(t-2\tau,T-2\theta)} &= \varphi_{ttxx}^{(t-2\tau,T-2\theta)} + 2\epsilon\left(\varphi_{ttxX}^{(t-2\tau,T-2\theta)} + \varphi_{xxtT}^{(t-2\tau,T-2\theta)}\right) \\ &\quad + \epsilon^{2}\left(\varphi_{XXtt}^{(t-2\tau,T-2\theta)} + 4\varphi_{xXtT}^{(t-2\tau,T-2\theta)} + \varphi_{xxTT}^{(t-2\tau,T-2\theta)}\right) \\ &\quad + 2\epsilon^{3}\left(\varphi_{XXtT}^{(t-2\tau,T-2\theta)} + \varphi_{xXTT}^{(t-2\tau,T-2\theta)}\right) + \epsilon^{4}\varphi_{XXTT}^{(t-2\tau,T-2\theta)}.\end{aligned} \tag{C-16}$$

Appendix D

Combination of Asymptotic and Derivative Expressions

This appendix includes the simplified expressions for the derivatives of φ after asymptotic series and multiple scale derivatives are inserted. Only first order of each are substituted.

$$\tilde{\varphi}_t \cong \varphi_t^{(0)} + \epsilon\varphi_t^{(1)} + \epsilon\varphi_T^{(0)} \tag{D-1}$$

$$\tilde{\varphi}_{tt} \cong \varphi_{tt}^{(0)} + \epsilon\varphi_{tt}^{(1)} + 2\epsilon\varphi_{tT}^{(0)} \tag{D-2}$$

$$\tilde{\varphi}_{ttt} \cong \varphi_{ttt}^{(0)} + \epsilon\left(\varphi_{ttt}^{(1)} + 3\varphi_{ttT}^{(0)}\right) \tag{D-3}$$

$$\tilde{\varphi}_{tttt} \cong \varphi_{tttt}^{(0)} + \epsilon\left(\varphi_{tttt}^{(1)} + 4\,\varphi_{tttT}^{(0)}\right) \tag{D-4}$$

$$\tilde{\varphi}_x \cong \varphi_x^{(0)} + \epsilon\left(\varphi_x^{(1)} + \varphi_X^{(0)}\right) \tag{D-5}$$

$$\tilde{\varphi}_{xx} \cong \varphi_{xx}^{(0)} + \epsilon\left(\varphi_{xx}^{(1)} + 2\varphi_{xX}^{(0)}\right) \tag{D-6}$$

$$\tilde{\varphi}_{txx} \cong \varphi_{txx}^{(0)} + \epsilon\varphi_{txx}^{(1)} + \epsilon\left(\varphi_{xXt}^{(0)} + \varphi_{xxT}^{(0)}\right) \tag{D-7}$$

$$\tilde{\varphi}_{ttxx} \cong \varphi_{ttxx}^{(0)} + \epsilon\varphi_{ttxx}^{(1)} + 2\epsilon\left(\varphi_{xXtt}^{(0)} + \varphi_{xxtT}^{(0)}\right) \tag{D-8}$$

$$\tilde{\varphi}_t^{(t-2\tau)} \cong \tilde{\varphi}_t^{(0)(t-2\tau,T)} + \epsilon\left[\varphi_T^{(0)(t-2\tau,T)} - 2\tau\tilde{\varphi}_{tT}^{(0)(t-2\tau,T)} + \tilde{\varphi}_t^{(1)(t-2\tau,T)}\right] \tag{D-9}$$

$$\tilde{\varphi}_{tt}^{(t-2\tau)} \cong \varphi_{tt}^{(0)(t-2\tau,T)} + \epsilon\left[-2\tau\tilde{\varphi}_{ttT}^{(0)(t-2\tau,T)} + 2\varphi_{tT}^{(0)(t-2\tau,T)} + \varphi_{tt}^{(1)(t-2\tau,T)}\right] \tag{D-10}$$

$$\tilde{\varphi}_{ttt}^{(t-2\tau)} \cong \tilde{\varphi}_{ttt}^{(0)(t-2\tau,T)} + \epsilon\left[3\varphi_{ttT}^{(0)(t-2\tau,T)} - 2\tau\tilde{\varphi}_{tttT}^{(0)(t-2\tau,T)} + \tilde{\varphi}_{ttt}^{(1)(t-2\tau,T)}\right] \tag{D-11}$$

$$\tilde{\varphi}_{tttt}^{(t-2\tau)} \cong \tilde{\varphi}_{tttt}^{(0)(t-2\tau,T)} + \epsilon\left[4\varphi_{tttT}^{(0)(t-2\tau,T)} - 2\tau\tilde{\varphi}_{ttttT}^{(0)(t-2\tau,T)} + \tilde{\varphi}_{tttt}^{(1)(t-2\tau,T)}\right] \tag{D-12}$$

$$\tilde{\varphi}_x^{(t-2\tau)} \cong \tilde{\varphi}_x^{(0)(t-2\tau,T)} + \epsilon\left[\varphi_X^{(0)(t-2\tau,T)} - 2\tau\tilde{\varphi}_{xT}^{(0)(t-2\tau,T)} + \tilde{\varphi}_x^{(1)(t-2\tau,T)}\right] \tag{D-13}$$

$$\tilde{\varphi}_{xx}^{(t-2\tau)} \cong \tilde{\varphi}_{xx}^{(0)(t-2\tau,T)} + \epsilon\left[2\varphi_{xX}^{(0)(t-2\tau,T)} - 2\tau\tilde{\varphi}_{Txx}^{(0)(t-2\tau,T)} + \tilde{\varphi}_{xx}^{(1)(t-2\tau,T)}\right] \tag{D-14}$$

$$\tilde{\varphi}_{txx}^{(t-2\tau)} \cong \tilde{\varphi}_{txx}^{(0)(t-2\tau,T)} + \epsilon\Big[2\varphi_{xXt}^{(0)(t-2\tau,T)} + \varphi_{xxT}^{(0)(t-2\tau,T)} - 2\tau\tilde{\varphi}_{tTxx}^{(0)(t-2\tau,T)} + \tilde{\varphi}_{txx}^{(1)(t-2\tau,T)}\Big] \tag{D-15}$$

$$\tilde{\varphi}_{ttxx}^{(t-2\tau)} \cong \tilde{\varphi}_{ttxx}^{(0)(t-2\tau,T)} + \epsilon\Big[2\varphi_{ttxX}^{(0)(t-2\tau,T)} + 2\varphi_{xxtT}^{(0)(t-2\tau,T)} - 2\tau\tilde{\varphi}_{ttTxx}^{(0)(t-2\tau,T)} + \tilde{\varphi}_{ttxx}^{(1)(t-2\tau,T)}\Big] \tag{D-16}$$

Appendix E

Derivatives of the Zero-Order Solution

$$\varphi_t^{(0)} = \frac{1}{2}\sum_{i=1}^{3}\left\{j\omega_i A_i e^{j\theta_i} + c.c.\right\} \qquad \text{(E-1)}$$

$$\varphi_T^{(0)} = \frac{1}{2}\sum_{i=1}^{3}\left\{\frac{\partial A_i}{\partial T} e^{j\theta_i} + c.c.\right\} \qquad \text{(E-2)}$$

$$\varphi_{tt}^{(0)} = \frac{1}{2}\sum_{i=1}^{3}\left\{-\omega_i^2 A_i e^{j\theta_i} + c.c.\right\} \qquad \text{(E-3)}$$

$$\varphi_{tT}^{(0)} = \frac{1}{2}\sum_{i=1}^{3}\left\{j\omega_i \frac{\partial A_i}{\partial T} e^{j\theta_i} + c.c.\right\} \qquad \text{(E-4)}$$

$$\varphi_{ttT}^{(0)} = \frac{1}{2}\sum_{i=1}^{3}\left\{-\omega_i^2 \frac{\partial A_i}{\partial T} e^{j\theta_i} + c.c.\right\} \qquad \text{(E-5)}$$

$$\varphi_{tttT}^{(0)} = \frac{1}{2}\sum_{i=1}^{3}\left\{-j\omega_i^3 \frac{\partial A_i}{\partial T} e^{j\theta_i} + c.c.\right\} \qquad \text{(E-6)}$$

$$\varphi_x^{(0)} = \frac{1}{2}\sum_{i=1}^{3}\left\{-j\beta_i A_i e^{j\theta_i} + c.c.\right\} \qquad \text{(E-7)}$$

$$\varphi_{xx}^{(0)} = \frac{1}{2}\sum_{i=1}^{3}\left\{-\beta_i^2 A_i e^{j\theta_i} + c.c.\right\} \qquad \text{(E-8)}$$

$$\varphi_{xX}^{(0)} = \frac{1}{2}\sum_{i=1}^{3}\left\{-j\beta_i \frac{\partial A_i}{\partial X} e^{j\theta_i} + c.c.\right\} \qquad \text{(E-9)}$$

$$\varphi_{xXtt}^{(0)} = \frac{1}{2}\sum_{i=1}^{3}\left\{j\omega_i^2 \beta_i \frac{\partial A_i}{\partial X} e^{j\theta_i} + c.c.\right\} \qquad \text{(E-10)}$$

$$\varphi_{xxtT}^{(0)} = \frac{1}{2}\sum_{i=1}^{3}\left\{-j\omega_i\beta_i^2\frac{\partial A_i}{\partial T}e^{j\theta_i} + c.c.\right\} \tag{E-11}$$

$$\varphi_{t}^{(0)(t-2\tau,T)} = \frac{1}{2}\sum_{i=1}^{3}\left\{j\omega_i e^{-j2\omega_i\tau}A_i e^{j\theta_i} + c.c.\right\} \tag{E-12}$$

$$\varphi_{T}^{(0)(t-2\tau,T)} = \frac{1}{2}\sum_{i=1}^{3}\left\{e^{-j2\omega_i\tau}\frac{\partial A_i}{\partial T}e^{j\theta_i} + c.c.\right\} \tag{E-13}$$

$$\varphi_{tt}^{(0)(t-2\tau,T)} = \frac{1}{2}\sum_{i=1}^{3}\left\{-\omega_i^2 e^{-j2\omega_i\tau}A_i e^{j\theta_i} + c.c.\right\} \tag{E-14}$$

$$\varphi_{tT}^{(0)(t-2\tau,T)} = \frac{1}{2}\sum_{i=1}^{3}\left\{j\omega_i e^{-j2\omega_i\tau}\frac{\partial A_i}{\partial T}e^{j\theta_i} + c.c.\right\} \tag{E-15}$$

$$\varphi_{ttT}^{(0)(t-2\tau,T)} = \frac{1}{2}\sum_{i=1}^{3}\left\{-\omega_i^2 e^{-j2\omega_i\tau}\frac{\partial A_i}{\partial T}e^{j\theta_i} + c.c.\right\} \tag{E-16}$$

$$\varphi_{tttT}^{(0)(t-2\tau,T)} = \frac{1}{2}\sum_{i=1}^{3}\left\{-j\omega_i^3 e^{-j2\omega_i\tau}\frac{\partial A_i}{\partial T}e^{j\theta_i} + c.c.\right\} \tag{E-17}$$

$$\varphi_{ttttT}^{(0)(t-2\tau,T)} = \frac{1}{2}\sum_{i=1}^{3}\left\{\omega_i^4 e^{-j2\omega_i\tau}\frac{\partial A_i}{\partial T}e^{j\theta_i} + c.c.\right\} \tag{E-18}$$

$$\varphi_{x}^{(0)(t-2\tau,T)} = \frac{1}{2}\sum_{i=1}^{3}\left\{-j\beta_i e^{-j2\omega_i\tau}A_i e^{j\theta_i} + c.c.\right\} \tag{E-19}$$

$$\varphi_{xx}^{(0)(t-2\tau,T)} = \frac{1}{2}\sum_{i=1}^{3}\left\{-\beta_i^2 e^{-j2\omega_i\tau}A_i e^{j\theta_i} + c.c.\right\} \tag{E-20}$$

$$\varphi_{xxT}^{(0)(t-2\tau,T)} = \frac{1}{2}\sum_{i=1}^{3}\left\{-\beta_i^2 e^{-j2\omega_i\tau}\frac{\partial A_i}{\partial T}e^{j\theta_i} + c.c.\right\} \tag{E-21}$$

$$\varphi_{xX}^{(0)(t-2\tau,T)} = \frac{1}{2}\sum_{i=1}^{3}\left\{-j\beta_i e^{-j2\omega_i\tau}\frac{\partial A_i}{\partial X}e^{j\theta_i} + c.c.\right\} \tag{E-22}$$

$$\varphi_{xXtt}^{(0)(t-2\tau,T)} = \frac{1}{2}\sum_{i=1}^{3}\left\{j\omega_i^2\beta_i e^{-j2\omega_i\tau}\frac{\partial A_i}{\partial X}e^{j\theta_i} + c.c.\right\} \tag{E-23}$$

$$\varphi_{xxXtt}^{(0)(t-2\tau,T)} = \frac{1}{2}\sum_{i=1}^{3}\left\{\omega_i^2\beta_i^2 e^{-j2\omega_i\tau}\frac{\partial A_i}{\partial X}e^{j\theta_i} + c.c.\right\} \tag{E-24}$$

$$\varphi_{xxtT}^{(0)(t-2\tau,T)} = \frac{1}{2}\sum_{i=1}^{3}\left\{-j\omega_i\beta_i^2 e^{-j2\omega_i\tau}\frac{\partial A_i}{\partial T}e^{j\theta_i} + c.c.\right\}$$

Appendix F

Coefficients of the Main Harmonics Generated by Cubic Nonlinearity

The nonlinear term $J\left(\varphi^{(0)}\right)$ in equation (6.48) of chapter 6 consists of four nonlinear terms as follows

$$J\left(\varphi^{(0)}\right) = \frac{\pi^2 LCh}{4L_J\Phi_0^2}(8NL1 + 16NL2 + 8NL3 + 16NL4). \qquad \text{(F-1)}$$

In this appendix, we present the coefficients of resonant forcing terms for each nonlinear $NL1$, $NL2$. $NL3$ and $NL4$ term, after applying phase-matching relation. All expressions have been calculated by applying the phase matching conditions.

First nonlinear term $NL1$ is

$$\boxed{NL1 = \left[\varphi_{tt}^{(0)} - \frac{1}{LC}\varphi_{xx}^{(0)} + \frac{1}{ChZ_0}\varphi_{t}^{(0)}\right]\left[\varphi^{(0)}\right]^2}. \tag{F-2}$$

TABLE F.1

COEFFICIENTS OF SIGNAL, PUMP AND IDLER HARMONICS AFTER MIXING DUE TO THE FIRST NONLINEAR TERM

θ_1	$\left(\frac{3\beta_1^2}{LC} - 3\omega_1^2 + \frac{j\omega_1}{ChZ_0}\right)A_1\lvert A_1\rvert^2$ $+\,2\left(\frac{\beta_1^2 + 2\beta_2^2}{LC} - \omega_1^2 - 2\omega_2^2 + \frac{j\omega_1}{ChZ_0}\right)A_1\lvert A_2\rvert^2$ $+\,2\left(\frac{\beta_1^2 + 2\beta_3^2}{LC} - \omega_1^2 - 2\omega_3^2 + \frac{j\omega_1}{ChZ_0}\right)A_1\lvert A_3\rvert^2$ $+\left(\frac{\beta_3^2 + 2\beta_2^2}{LC} - 2\omega_2^2 - \omega_3^2 + \frac{j\omega_1}{ChZ_0}\right)A_2^2A_3^*$
θ_2	$2\left(\frac{\beta_2^2 + 2\beta_1^2}{LC} - 2\omega_1^2 - \omega_2^2 + \frac{j\omega_2}{ChZ_0}\right)A_2\lvert A_1\rvert^2$ $+\left(\frac{3\beta_2^2}{LC} - 3\omega_2^2 + \frac{j\omega_2}{ChZ_0}\right)A_2\lvert A_2\rvert^2$ $+\,2\left(\frac{\beta_2^2 + 2\beta_3^2}{LC} - \omega_2^2 - 2\omega_3^2 + \frac{j\omega_2}{ChZ_0}\right)A_2\lvert A_3\rvert^2 +$ $2\left(\frac{\beta_1^2 + \beta_2^2 + \beta_3^2}{LC} - \omega_1^2 - \omega_2^2 - \omega_3^2 + \frac{j\omega_2}{ChZ_0}\right)A_1A_2^*A_3$
θ_3	$2\left(\frac{\beta_3^2 + 2\beta_1^2}{LC} - 2\omega_1^2 - \omega_3^2 + \frac{j\omega_3}{ChZ_0}\right)A_3\lvert A_1\rvert^2$ $+\,2\left(\frac{\beta_3^2 + 2\beta_2^2}{LC} - 2\omega_2^2 - \omega_3^2 + \frac{j\omega_3}{ChZ_0}\right)A_3\lvert A_2\rvert^2$ $+\left(\frac{3\beta_3^2}{LC} - 3\omega_3^2 + \frac{j\omega_3}{ChZ_0}\right)A_3\lvert A_3\rvert^2$ $+\left(\frac{\beta_1^2 + 2\beta_2^2}{LC} - \omega_1^2 - 2\omega_2^2 + \frac{j\omega_3}{ChZ_0}\right)A_1^*A_2^2$

Second nonlinear term $NL2$ is

$$\boxed{NL2=\left\{\left[\varphi_t^{(0)}\right]^2-\frac{1}{LC}\left[\varphi_x^{(0)}\right]^2\right\}\varphi^{(0)}}. \qquad \text{(F-3)}$$

TABLE F.2

COEFFICIENTS OF SIGNAL, PUMP AND IDLER HARMONICS AFTER MIXING DUE TO THE SECOND NONLINEAR TERM

θ_1	$\left(\omega_1^2-\frac{\beta_1^2}{LC}\right)A_1\lvert A_1\rvert^2+2\left(\omega_2^2-\frac{\beta_2^2}{LC}\right)A_1\lvert A_2\rvert^2$ $+2\left(\omega_3^2-\frac{\beta_3^2}{LC}\right)A_1\lvert A_3\rvert^2$ $+\left(-\omega_2^2+2\omega_2\omega_3-\frac{2\,\beta_2\beta_3-\beta_2^2}{LC}\right)A_2^2A_3^*$
θ_2	$2\left(\omega_1^2-\frac{\beta_1^2}{LC}\right)A_2\lvert A_1\rvert^2+\left(\omega_2^2-\frac{\beta_2^2}{LC}\right)A_2\lvert A_2\rvert^2$ $+2\left(\omega_3^2-\frac{\beta_3^2}{LC}\right)A_2\lvert A_3\rvert^2$ $+2\left(\omega_1\omega_2+\omega_2\omega_3-\omega_3\omega_1+\frac{\beta_3\beta_1-\beta_2\beta_3-\beta_1\beta_2}{LC}\right)A_1A_2^*A_3$
θ_3	$2\left(\omega_1^2-\frac{\beta_1^2}{LC}\right)A_3\lvert A_1\rvert^2+2\left(\omega_2^2-\frac{\beta_2^2}{LC}\right)A_3\lvert A_2\rvert^2$ $+\left(\omega_3^2-\frac{\beta_3^2}{LC}\right)A_3\lvert A_3\rvert^2$ $+\left(2\omega_1\omega_2-\omega_2^2+\frac{\beta_2^2}{LC}-\frac{2\,\beta_1\beta_2}{LC}\right)A_2^2A_1^*$

Third Nonlinear Term :

$$\boxed{NL3 = \left[\varphi_{tt}^{(0)(t-2\tau,T)} - \frac{1}{LC}\varphi_{xx}^{(0)(t-2\tau,T)} - \frac{1}{ChZ_0}\varphi_{t}^{(0)(t-2\tau,T)}\right]\left[\varphi^{(0)(t-2\tau,T)}\right]^2.} \qquad \text{(F-4)}$$

TABLE F.3

COEFFICIENTS OF SIGNAL, PUMP AND IDLER HARMONICS AFTER MIXING DUE TO THE THIRD NONLINEAR TERM

θ_1	$\left(\frac{3\beta_1^2}{LC} - 3\omega_1^2 - \frac{j\omega_1}{ChZ_0}\right)e^{-j2\omega_1\tau}\lvert A_1\rvert^2 A_1$ $+ 2\left(\frac{\beta_1^2 + 2\beta_2^2}{LC} - \omega_1^2 - 2\omega_2^2 - \frac{j\omega_1}{ChZ_0}\right)e^{-j2\omega_1\tau}\lvert A_2\rvert^2 A_1$ $+2\left(\frac{\beta_1^2 + 2\beta_3^2}{LC} - \omega_1^2 - 2\omega_3^2 - \frac{j\omega_1}{ChZ_0}\right)e^{-j2\omega_1\tau}\lvert A_3\rvert^2 A_1$ $+\left(\frac{2\beta_2^2 + \beta_3^2}{LC} - 2\omega_2^2 - \omega_3^2 - \frac{j\omega_1}{ChZ_0}\right)e^{-j2\omega_1\tau}A_2^2 A_3^*$
θ_2	$2\left(\frac{2\beta_1^2 + \beta_2^2}{LC} - 2\omega_1^2 - \omega_2^2 - \frac{j\omega_2}{ChZ_0}\right)e^{-j2\omega_2\tau}\lvert A_1\rvert^2 A_2$ $+\left(\frac{3\beta_2^2}{LC} - 3\omega_2^2 - \frac{j\omega_2}{ChZ_0}\right)e^{-j2\omega_2\tau}\lvert A_2\rvert^2 A_2$ $+ 2\left(\frac{\beta_2^2 + 2\beta_3^2}{LC} - 2\omega_3^2 - \omega_2^2 - \frac{j\omega_2}{ChZ_0}\right)e^{-j2\omega_2\tau}\lvert A_3\rvert^2 A_2$ $+2\left(\frac{\beta_1^2 + \beta_2^2 + \beta_3^2}{LC} - \omega_1^2 - \omega_2^2 - \omega_3^2 - \frac{j\omega_2}{ChZ_0}\right)e^{-j2\omega_2\tau}A_1 A_2^* A_3$
θ_3	$+2\left(\frac{2\beta_1^2 + \beta_3^2}{LC} - 2\omega_1^2 - \omega_3^2 - \frac{j\omega_3}{ChZ_0}\right)e^{-j2\omega_3\tau}\lvert A_1\rvert^2 A_3$ $+ 2\left(\frac{2\beta_2^2 + \beta_3^2}{LC} - 2\omega_2^2 - \omega_3^2 - \frac{j\omega_3}{ChZ_0}\right)e^{-j2\omega_3\tau}\lvert A_2\rvert^2 A_3$ $+\left(\frac{3\beta_3^2}{LC} - 3\omega_3^2 - \frac{j\omega_3}{ChZ_0}\right)e^{-j2\omega_3\tau}\lvert A_3\rvert^2 A_3$ $+\left(\frac{\beta_1^2 + 2\beta_2^2}{LC} - \omega_1^2 - 2\omega_2^2 - \frac{j\omega_3}{ChZ_0}\right)e^{-j2\omega_3\tau}A_1^* A_2^2$

Fourth Nonlinear Term:

$$\boxed{NL4=\left\{\left[\varphi_t^{(0)(t-2\tau,T)}\right]^2-\frac{1}{LC}\left[\varphi_x^{(0)(t-2\tau,T)}\right]^2\right\}\varphi^{(0)(t-2\tau,T)}}. \qquad \text{(F-5)}$$

TABLE F.4

COEFFICIENTS OF SIGNAL, PUMP AND IDLER HARMONICS AFTER MIXING DUE TO THE FOURTH NONLINEAR TERM

θ_1	$-\left(\frac{\beta_1^2}{LC}-\omega_1^2\right)e^{-j2\omega_1\tau}\lvert A_1\rvert^2A_1$ $-2\left(\frac{\beta_2^2}{LC}-\omega_2^2\right)e^{-j2\omega_1\tau}\lvert A_2\rvert^2A_1$ $-2\left(\frac{\beta_3^2}{LC}-\omega_3^2\right)e^{-j2\omega_1\tau}\lvert A_3\rvert^2A_1$ $+\left(\frac{\beta_2^2-2\beta_2\beta_3}{LC}-\omega_2^2+2\omega_2\omega_3\right)e^{-j2\omega_1\tau}A_2^2A_3^*$
θ_2	$-2\left(\frac{\beta_1^2}{LC}-\omega_1^2\right)e^{-j2\omega_2\tau}\lvert A_1\rvert^2A_2-\left(\frac{\beta_2^2}{LC}-\omega_2^2\right)e^{-j2\omega_2\tau}\lvert A_2\rvert^2A_2$ $-2\left(\frac{\beta_3^2}{LC}-\omega_3^2\right)e^{-j2\omega_2\tau}\lvert A_3\rvert^2A_2$ $-2\left(\frac{\beta_1\beta_2+\beta_2\beta_3-\beta_3\beta_1}{LC}-\omega_1\omega_2-\omega_2\omega_3+\omega_3\omega_1\right)e^{-j2\omega_2\tau}A_1A_2^*A_3$
θ_3	$-2\left(\frac{\beta_1^2}{LC}-\omega_1^2\right)e^{-j2\omega_3\tau}\lvert A_1\rvert^2A_3-2\left(\frac{\beta_2^2}{LC}-\omega_2^2\right)e^{-j2\omega_3\tau}\lvert A_2\rvert^2A_3$ $-\left(\frac{\beta_3^2}{LC}-\omega_3^2\right)e^{-j2\omega_3\tau}\lvert A_3\rvert^2A_3$ $+\left(\frac{\beta_2^2-2\beta_1\beta_2}{LC}+2\omega_1\omega_2-\omega_2^2\right)e^{-j2\omega_3\tau}A_2^2A_1^*$

Bibliography

[1] Bradley, R, et al., "Microwave cavity searches for dark-matter axions." Review of modern physics, June 2003, Issue 3, Vol. 75.

[2] Lanting, T. M., et al., "Frequency-domain multiplexing for large-scale bolometer arrays." Proceedings of the SPIE, 2003, Vol. 4855, pp. 172-181.

[3] Bader, S. D., "Colloquium: opportunities in nanomagnetism." Reviews of modern physics, January 2006, Vol. 78.

[4] Augustinea, M, TonThat, D. M. and Clarke, John., "SQUID detected NMR and NQR." Solid State Nuclear Magnetic Resonance, March 1998, Issue 1-2, Vol. 11, pp. 139-156.

[5] Krithivasan, R, et al., "Half-terahertz operation of SiGe HBTs." IEEE Electron Device Letters, 2006, Issue 7, Vol. 27.

[6] Muck, M, Andre, M.-O. and Clarke, J., "Radio-frequency amplifier based on a niobium dc superconducting quantum interference device with microstrip input coupling." Applied physics letter, June 1998, Issue 22, Vol. 72.

[7] Yrke, Bernard and Buks, Eyal., "Performance of cavity-parametric amplifiers, employing kerr nonlinearity in the presence of two photon loss." Jounal of lightwave technology , December 2006, Issue 12, Vol. 24.

[8] Tholen, Erik A., et al., "Nonlinearities and parametric amplification in superconducting coplanar waveguide resonators." Applied Physics Letters, June 2007, Vol. 90, pp. 253509 (1-3). 253509 .

[9] Defeo, M. P., et al., "Microstrip superconducting quantum interference device amplifiers with submicron Josephson junctions: Enhanced gain at gigahertz frequencies." Applied physics letters, Sepetember 2010, Vol. 97.

[10] Siddiqi, I, et al., "Direct Observation of Dynamical Bifurcation between Two Driven Oscillation States of as Josephson Junction." Physical Review Letters, January 2005, Vol. 94, pp. 027005(1-4).

[11] Yurke, B, et al., "A low-noise series-array Josephson junction parametric amplifier." Applied Physics Letters, November 1996, Issue 20, Vol. 69, pp. 3078-3080.

[12] Castellanos-Beltran, M A, et al., "Amplification and squeezing of quantum noise with a tunable Josephson metamaterial." Nature Physics, October 2008, Vol. 4, pp. 929 - 931 .

[13] Clarke, John and Branginski, Alex I., *The SQUID Handbook.* Weinheim : Wiley-VCH. p. Chapter 8. Vol. II.

[14] Weinstock, H and Nisenoff, M., *Microwave Superconductivity.* s.l. : Kluwer Academic, 2001.

[15] Vijay, R, Devoret, M. H. and Siddiqi, I., "Review of scientific instruments." 2009, Vol. 80, pp. 111101 (1-17).

[16] Collin, R E., *Foundations for Microwave Engineering.* New York : McGraw-Hill Book Company, 1992.

[17] Blackwell, Lawrence A and Kotzebue, Kenneth L., *Semiconductor-Diode Parametric Amplifiers.* Englewood Cliffs : Prentice-Hall, 1961.

[18] Yariv, A and Pearson, J.E., *Parametric processes.* Oxford ; New York : Pergamon Press, 1969.

[19] Boyd, Robert W., *Nonlinear Optics.* Amsterdam, Boston : Academic Press, 2003.

[20] Craik, A. D. D., *Wave interactions and fluid flows.* Cambridge : Cambridge university press, 1985.

[21] Scott, Alwyn., *Active and Nonlinear Wave Propagation in Electronics.* New York : Wiley-Interscience , 1970.

[22] Feldman, M J, Parrish, P T and Chiao, R Y., "Parametric amplification by unbiased Josephson junctions." Journal of Applied Physics, September 1975, Issue 9, Vol. 46, pp. 4031-4042.

[23] Mohebbi, H R and Majedi, A H., "Small and large signal analyses of Josephson nonlinear inductance for superconductive parametric amplifier." Toronto : s.n., 2009. TIC-STH'09: 2009 IEEE Toronto International Conference . pp. 1015-1018.

[24] Mohebbi, H. R. and Majedi, A. H., "Current- and voltage-based Josephson parametric amplifiers." Submitted to IEEE Transaction on Microwave Theory and Techniques, 2011.

[25] Mohebbi, H. R. and Majedi, A. H., "CAD model for circuit parameters of superconducting-based hybrid planar transmission lines." Superconductor Science and Technology, Nov 2009, Vol. 22, pp. 125028 (1-12).

[26] Mohebbi, H. R. and Majedi, A. H., "Periodic superconducting microstrip line with nonlinear kinetic inductance." IEEE Transaction on Applied Superconductivity, June 2009, Issue 3, Vol. 19, pp. 930 - 935 .

[27] Mohebbi, H. R. and Majedi, A. H., "Analysis of the periodic superconducting CPW transmission line with stepped-impedance for on-chip microwave filter applications." 2010. Journal of Physics: Conference Series. Vol. 234, pp. 042022 (1-10).

[28] Mohebbi, H. R. and Majedi, A. H., "Analysis of series-connected discrete Josephson transmission line." IEEE Transaction on Microwave Theory and Techniques, August 2009, Issue 8, Vol. 57, pp. 1865 - 1873 .

[29] Mohebbi, H. R. and Majedi, A. H., "Shock wave generation and cut off condition in nonlinear series connected discretejosephson transmission line." IEEE Transaction on Applied Superconductivity, June 2009, Issue 3, Vol. 19, pp. 891-894.

[30] Heffner, H and Wade, G., "Gain, band width, and noise characteristics of the variable-parametric amplifier." Journal of Applied Physics, September 1958, Issue 9, Vol. 29, pp. 1321-1331.

[31] Zimmer, H., "Parametric amplification of microwaves in superconducting Josephson tunnel junctions." Applied Physics Letters, April 1967, Issue 7, Vol. 10, pp. 193-195.

[32] Kanter, H., "A novel parametric negative-resistance effect in Josephson junctions." Applied Physics Letters, June 1973, Vol. 23, pp. 350-352.

[33] Russer, Peter., "General energy relations for Josephson junctions ." Proceedings of the IEEE, February 1971, Issue 2, Vol. 59, pp. 282- 283.

[34] Mygind, J, et al., "Low-noise parametric amplification at 35 GHz in a single Josephson tunnel junction." Applied physics letter, April 1979, Issue 1, Vol. 35, pp. 91-93.

[35] Chiao, R Y and Parrish, P T., "Operation of the SUPARAMP at 33 GHz." Journal of applied physics, June 1976, Issue 6, Vol. 47, pp. 2639-2644.

[36] Louisel, William Henry., *Coupled Mode and Parametric Electronics.* New York : Wiley, 1960.

[37] Damgov, Vladimir., *Nonlinear and Parametric Phenomena : Theory and Applications in Radiophysical and Mechanical Systems.* Hong Kong : Singapore, 2004.

[38] Likharev, K K., *Dynamics of Josephson junctions and circuits.* New York : Gordon and Breach science , 1986.

[39] Barone, A and Paterno, G., *Physics and applications of the Josephson effect.* New York : John Wiley and Sons, 1982.

[40] Hyart, T, Shorokhov, A V and Alekseev, K N., "Theory of Parametric Amplification in Superlattices." Physical review letters, June 2007, Issue 22, Vol. 98.

[41] Gray, B., Kenney, J.S. and Melville, R., " Behavioral modeling and simulation of a parametric power amplifier ." 2009. Microwave symposium digest, IEEE MTT-S International . pp. 1373-1376.

[42] Magierowski, S., Chan, H and Zourntos, T., "subharmonically pumped RF CMOS paramps." IEEE Transactions on Electron Devices, February 2008, Issue 2, Vol. 55, pp. 601-608.

[43] Yan, J and Geiger, R., "A high gain CMOS operational amplifier with negative conductance gain enhancement." 2002. proceedings of IEEE Custom Integrated Circuits Conference. pp. 337-340.

[44] Siddiqi, Irfan, et al., "RF-Driven Josephson Bifurcation Amplifier for Quantum Measurement." Physical Review Letters, November 2004, Issue 20, Vol. 93, pp. 207002-1-.

[45] Kain, A Z and Fetterman, H R., "Parametric interaction in high-Tc superconducting step edge junctions at X-band." Physica C, April 1993, Issue 1-3, Vol. 209, pp. 281-285.

[46] Kanter, H and Silver, A. H., "Self-pumped Josephson parametric amplification." Applied Physics Letters, December 1971, Issue 12, Vol. 19, pp. 515-517.

[47] Kanter, Helmut., "Two-idler parametric amplification with Josephson junctions." Journal of Applied Physics, September 1975, Issue 9, Vol. 46, pp. 4018-4025.

[48] Russer, P., Arch. El. Ubertr, 1969, Vol. 23, p. 417.

[49] Solymer, L., *Superconductive Tunnelling and Applications.* London : Chapman & Hall , 1972.

[50] Sweeny, M and Mahler, R., "A Traveling-wave Parametric Amplifier Utilizing Josephson Junctions." IEEE Transactions on Magnetics, March 1985, Issue 2, Vols. MAG-21, pp. 654-655.

[51] Hilbert, C and Clarke, J., "DC SQUIDs as radiofrequency amplifiers." Low Temperature Physics, November 1985, Issue 3, Vol. 61, pp. 263-280.

[52] Brown, J., "Proof of the Manley-Rowerelations from quantum consideration." Electronic letters, Feb 1965, Issue 1, Vol. 1, pp. 23-24.

[53] Saleh, B. E. A. and Teich, M. C., *Fundamentals of photonics.* New York : Wiley-Interscience, 2007.

[54] Cripps, Steve C., *RF power amplifiers for wireless communications.* Norwood, MA : Artech House Inc., 2006.

[55] Bahl, Inder J., *Fundementals of RF and microwave transistor amplifiers.* New Jersy : Wiley, 2009.

[56] Van Duzer, T and Turner, C W., *Principles of Superconductive Devices and Circuits.* New Jersey : Prentice Hall Inc, 1999.

[57] Spiegel, Murray R., *Mathematical handbook of formulas and tables.* New York : Schaum's outline series, 1968.

[58] Pozar, D., "Microwave engineering." New York : John Wiley & Sons, 2005.

[59] Niknejad, Ali M., *Electromagnetics for high-speed analog and digital communication circuits.* Cambridge : Cambridge University Press, 2007.

[60] Griffiths, D. J., *Introduction to quantum mechanics.* Upper Saddle River, NJ : Pearson Prentice Hall, 2005.

[61] Yohannes, Daniel, et al., "Characterization of HYPRES' 4.5KA/CM2 & 8KA/CM2 Nb/ALOx/Nb Fabricatiob Process." IEEE Transaction on Applied Superconductivity, June 2005, Issue 2, Vol. 15, pp. 90-93.

[62] Munk, B. A., *Frequency selective surfaces theory and design.* New York : Wiley, 2000.

[63] Collin, R. E. and Zucker, F. J., *Antenna Theory vol.2.* New York : McGraw-Hill , 1969.

[64] Joannopoulos, J. D., *Photonic Crystals: Molding the Flow of Light.* Princeton : Princeton university press, 1995.

[65] Sievenpiper, D, et al., "High-impedance electromagnetic sutfaces with a forbidden frequency band." IEEE Transaction on Microwave Theory and Techniques, November 1999, Issue 11, Vol. 47, pp. 2059-2074.

[66] , "Special issue on metamaterials." IEEE Transaction on Antenna and Propgation, October 2003, Issue 10, Vol. 51.

[67] Yang, F. R., et al., "Analysis and application of photonic band-gap (PBG) structures for microwave circuits." Electromagnetics, special issue on theory and applications of photonic band-gap materials, May-June 1999, Vol. 19, pp. 241-254.

[68] Radisic, V, Qian, Yongxi and Itoh, T., "Broad-band power amplifier using dielectric photonic bandgap structure." IEEE Microwave and Guided Wave Letters, Jan 1998, Issue 1, Vol. 8, pp. 13-14.

[69] Yeh, A Pochi., *Optical Waves in Layered Media.* New York : Wiley, 1988.

[70] Yablonovitch, E., "Photonic band-gap structures." Journal of the optical society of America B, Feb 1993, Issue 2, Vol. 10, pp. 283-295.

[71] Gupta, K. C., et al., *Microstrip Lines and Slotlines.* Norwood : Artech House, 1996.

[72] Simons, R. N., *Coplanar waveguide circuits, components, and systems.* New York : J. Wiley and Sons, 2001.

[73] Mansour, Raafat R., "Microwave Superconductivity." IEEE Transaction on Microwave Theory and Techniques, March 2002, Issue 3, Vol. 50, pp. 750-759.

[74] Lancaster, M J., *Passive Microwave Device Applications of High-Temperature Superconductors.* Cambridge : Cambridge University Press, 1997.

[75] Orlando, T P and Delin, K A., "Foundations of Applied Superconductivity." Massachusetts : Addison-Wesley, 1990, 4.

[76] Mazierska, J., "Superconducting cryogenic front end receivers." Warszawa, Poland : s.n., 2004. Microwaves, Radar and Wireless Communications. pp. 351-353.

[77] Simon R.W., Hammond R.B., Berkowitz S.J. Willemsen B.A., "Superconducting microwave filter systems for cellular telephone base stations ." Proceedings of the IEEE , Oct 2004, Issue 10, Vol. 92, pp. 1585-1596.

[78] Cameron, R. J., Mansour, R. R. and Kudsia, C. M., *Microwave filters for communication systems : fundamentals, design and applications.* Hoboken N.J. : John Wiley Sons, 2007.

[79] Lancaster, M. J., et al., "Miniature superconducting filters." IEEE Transactions on Microwave Theory and Techniques, Issue 7, Vol. 44, pp. 1339-1346.

[80] Rafique, M R, et al., "Miniaturized superconducting microwave filters." Superconductor and Science Technology, 2008, Vol. 21, pp. 1-7. 075004.

[81] Tsuzuki, G., Ye, Shen and Berkowitz, S., "Ultra Selective HTS Bandpass Filter for 3G Wireless Application." IEEE Transaction on Applied Superconductivity, June 2003, Issue 2, Vol. 13, pp. 261-264.

[82] K, Likharev K., *Dynamics of Josephson junctions and circuits* . Philadelphia : Gordon and Breach Science , 1986.

[83] Majedi, Amir Hamed, Chaudhuri, S K and Safavi-Naeini, S., "Optical-Microwave Interaction modeling in high-temperature superconducting films." IEEE Transaction on Microwave Theory and Technique, October 2001, Issue 10, Vol. 49, pp. 1873-1881.

[84] Majedi A. H., Saeedkia D. , Chaudhuri S.K. ,Safavi-Naeini S., "Physical Modeling and Frequency Response Analysis of A High-Temperature Superconducting THz Photomixer." IEEE Trans. Microwave Theory & Techniques, Oct 2004, Issue 10, Vol. 52, pp. 2430-2437.

[85] Wadell, B. C., *Transmission Line Design Handbook.* Norwood : Artech House Inc., 1991.

[86] Dib, N., "Comprehensive study of CAD models of several coplanar waveguide (CPW) discontinuities." IEE Proceedings, Microwaves, Antenna and Propagation, April 2005, Issue 2, Vol. 152, pp. 69-76.

[87] Getsinger, J. W., "Circuit duals on planar transmission media." Boston : s.n., 1983. IEEE MTT-S International Microwave Symposium Digest. pp. 154-156.

[88] Gevorgian, S, et al., "CAD model of a gap in a coplanar waveguide." International Journal of Microwave and Millimeter-wave Computer-Aided Engineering, April 1996, Issue 5, Vol. 6, pp. 369-377.

[89] Hasnain, G, Dienes, A and Whinnery, J. R., "Dispersion of Picosecond Pulses in Coplanar Transmission Lines." IEEE Transaction on Microwave Theory and Techniques, June 1986, Issue 6, Vol. 34, pp. 738-741.

[90] Rauch, W and E.Gornik, E., "Microwave properties of YBa2Cu3O7-x thin films studied with coplanar transmission line resonators." Journal of applied Physics, Febriary 1993, Issue 4, Vol. 73, pp. 1866-1872 .

[91] Valenzuela, A. A., et al., "Microwave characterization of structured YBa2Cu3O7-x thin films ." Material science forum, 1993, Vols. 130-132, pp. 349-372.

[92] Caloz, Christophe and Tatsuo, Itoh., *Electromagnetic Materials: Transmisson Line Theory and Microwave Applications.* New Jersy : John Wiely & Sons, 2006.

[93] Griffiths, David J and Steinke, Carl A., "Waves in locally periodic media." American Journal of Physics , February 2001, Issue 2, Vol. 69, pp. 137-154 .

[94] Majedi, A H., "Multilayer Josephson Junctions as Quantum Well Structure." IEEE Transactions on Applied Superconductivity, June 2007, Issue 2, Vol. 17, pp. 617-620.

[95] , *Theva.* [Online] http://www.theva.com/user/eesy.de/theva.biz/dwn/Datasheet_Coatings.pdf.

[96] Utz, B, et al., "Deposition of YBCO and NBCO films on areas of 9 inches in diameter." IEEE Trans. Appl. Supercond., 1997, Issue 2, Vol. 7, pp. 1272-1277.

[97] Sydoru, O, Kalinin, V and Shamonina, E., "Parametric amplification of magnetoinductive waves supported by metamaterial arrays." phys. stat. sol, March 2007, Issue 4, Vol. 244, pp. 1176–1180.

[98] Rajo-Iglesias, E., Zaman, A. U. and Kildal, P-. S., "Alternative ridge gap waveguide design using a mushroom-type EBG surface." Charleston, SC : IEEE Antennas and Propagation Society International Symposium, 2009.

[99] Lind-Johansen, O., Seip, K. and Skaar, J., "The perfect lens on a finite bandwidth." Journal of mathematical physics, January 2009, Vol. 50, p. 012908 (9pp).

[100] Arfken, G. B., *Mathematical Methods for Physicists.* Amsterdam : Elsevier Academic Press .

[101] Ramo, S., Whinnery, J. R. and Van Duzer, T., *Fields and waves in communication electronics.* New York : John Wiley & Sons, 1984.

[102] Skaar, J. and Seip, K., "Bounds for the refractive indicies of metamaterial." J. Phys. D. Appl. Phys., March 2006, Vol. 39, pp. 126-1229.

[103] Gustafsson, M. and Sjoberg, D., "Sum rules and physical bounds on passive metamaterials." New Journal of Physics, April 2010, Vol. 12, p. 043046 (18pp).

[104] Mackay, T. G. and Lakhtakia, A., "Comment on ‘‘Criterion for Negative Refraction with Low Optical Losses from a Fundamental Principle of Causality." PRL, November 2007, Vol. 99, p. 189701 (1pp).

[105] Lotkhov, S V, et al., "Self-shunted Al/AlOx/Al Josephson junctions." arXiv:cond-mat/0605532v1, Feb 2008.

[106] Taflove, A and Hagness, S C., *Computational Electrodynamics: The Finite-Difference Time-Domain Method.* Boston : Artech House Inc, 2005.

[107] Davidson, D B., *Computational Electromagnetics for RF and Microwave Engineering.* Cambridge : Cambridge University Press, 2005.

[108] Strikwerda, John C., *Finite difference schemes and partial differential equations.* Philadelphia : Society for Industrial and Applied Mathematics, 2004.

[109] McOwen, R. C., *Partial differential equations : methods and applications.* Upper Saddle, N.J. : Prentice Hall, 2003.

[110] Smith, G D., *Numerical solution of partial differential equations.* Oxford : Clarendon Press, 1985.

[111] Sullivan, D M., *Electromagnetic Simulation Using The FDTD Method.* New York : IEEE Press , 2000.

[112] HYPRES, Inc., *Niobium Integrated Circuit Fabrication.* [Online] January 2008. http://www.hypres.com/pages/download/designrules/DesignRules.pdf.

[113] Jakcel, L D, et al., "Decay of the zero-voltage state in a small area, high-current density Josephson junctions." Physical Review Letters, August 1981, Issue 9, Vol. 47, pp. 697 - 700.

[114] Kaplunenko, V and Fischer, Gerd M., "Josephson junction arrays as a variable inductor in RF circuits and tunable filters." Supercondor Science and Technology, February 2004, Vol. 17, pp. 145-149.

[115] Kadin, Alan M., *Introduction to Superconducting Circuits.* New York : Wiley and Sons, 1999.

[116] Ustinov, A V and Cirillo, M., "Fluxon dynamics in one-dimensional Josephson-junction arrays." Physica Review B, April 1993, Issue 13, Vol. 47, pp. 8357-8360.

[117] Keterson, J B and Song, S N., *Superconductivity.* London : Cambridge University press, 1999. pp. J. B. Keterson & S. N. Song, “Superconductivity”, , 1999.

[118] Chen, George J and Beasley, M R., "Shock-wave generation and pulse sharpening on a series array Josephson junction transmission line." IEEE Transaction on Applied Superconductivity, September 1991, Issue 3, Vol. 1, pp. 140-144.

[119] Montoya, T P., "Improved 1-D FDTD modeling of parallel and series RLC loads in a lossless transmission line." Albuquerque : s.n., 2006. Antennas and Propagation Society International Symposium. pp. 1583- 1586.

[120] Landauer, R., "Shock Waves in Nonlinear Transmission Lines and Their Effect on Parametric Amplification." IBM Journal, October 1960, pp. 391-401.

[121] Jager, D and Tegude, F. J., "Nonlinear wave propagation along periodic-loaded transmission line." s.l. : Appl. Phys., 1978, Vol. 15. 393-397.

[122] Landauer, R., "Parametric Amplification along Nonlinear Transmission Lines." Journal of applied physics, March 1960, Issue 3, Vol. 31, pp. 479-484.

[123] Roe, G. M. and Boyd, M. R., "Parametric Energy Conversion in Distributed Systems." Proceedings of the IRE, July 1959, Vol. 47, pp. 1213-1218.

[124] Tien, P. K., "Parametric amplification and frequency mixing in propagating circuits." Journal of Applied Physics, September 1958, Issue 9, Vol. 29, pp. 1347-1357.

[125] Cullen, A. L., "A traveling-wave parametric amplifier." Nature, February 1958, Vol. 181, p. 332.

[126] Cassedy, E. S. and Oliner, A. A., "Dispersion relations in time-space periodic media: part I stable interactions." Proceedings of the IEEEE, October 1963, Vol. 51, pp. 1342-1359.

[127] Cassedy, E. S., "Dispersion relations in time-space periodic media part II—Unstable interactions." Proceedings of the IEEE , July 1967, Issue 7, Vol. 55, pp. 1154 - 1168 .

[128] Sorenssen, A., "A theoritical investigation of a travelling wave parametric amplifier." s.l. : Appl. sci. res.

[129] Armstrong, J. A., et al., "Interactions between light waves in a nonlinear dielectric." Physical review, September 1962, Issue 6, Vol. 127.

[130] Lamb, K. G., "Tidally generated near-resonant internal wave triads at a shelf break." Geophysical research letters , 2007, Vol. 34, pp. L18607 (1-5).

[131] Manley, J. M. and Rowe, H. E., "Some general properties of nonlinear elements part I: general energy relation." Proceedings of the IRE, July 1956, Issue 7, Vol. 44, pp. 904-913.

[132] Lin, C. C. and Segel, L. A., *Mathematicas applied to deterministic problems in the natrual science.* New York : Macmillan publishing Co., 1974.

[133] Nayfeh, A. H., *Introduction to pertrurbation techniques.* New York : John Wiley & Sons Inc., 1981.

[134] Trefethen., *Spectral Methods in Matlab.* Philadelphia : Society for Industrial and Applied Mathematics, 2000.

[135] Leveque, R., *Finite Difference Methods for Ordinary and Partial Differential Equations: Steady-State and Time-Dependent Problems.* Philadelphia : Society for industrial and applied mathematics, 2007.

[136] Masne, Q. L., *Asymmetric current fluctuations and Andreev states probed with a Josephson junction.* Research Group in Quantum Electronics, CEA-Saclay. 2009. PhD Thesis.

[137] Anlage, S M, Snortland, H J and Beasley, M R., "A current controlled variable delay superconducting transmission line." IEEE Transactions on Magnetics, March 1989, Issue 2, Vol. 25, pp. 1388-1391.

[138] Tinkham, Michael., *Introduction to superconductivity.* New York : McGraw Hill, 1996.

[139] Tong, C E, Chen, L and Blundell, R., "Theory of distributed mixing and amplification in a superconducting quasi-particle nonlinear transmission line." IEEE Transactions on Microwave Theory and Techniques, July 1997, Issue 7, Vol. 45, pp. 1086-1092.